A Study of X-ray Narrow Emission Lines from Ionised Gas in Active Galactic Nuclei

Megan Rhianna Whewell

Thesis submitted for the degree of

Doctor of Philosophy (PhD)

of

University College London

Mullard Space Science Laboratory

Department of Space and Climate Physics

University College London

May 2017

I, Megan Rhianna Whewell, confirm that the work presented in this thesis is my own. Where information has been derived from other sources, I confirm that this has been indicated in the thesis.

_____

_____

"Look at who you want to be
and start sculpting yourself into that person.
You may not get exactly where you thought you'd be,
but you will be doing things that suit you,
in a profession you believe in.
Don't let life randomly kick you
into the adult you don't want to become"
Chris Hadfield, 2013

Abstract

This thesis presents a study of X-ray narrow emission lines from ionised gas within Active Galactic Nuclei (AGN) and is based on the analysis of high-resolution X-ray spectra from *XMM-Newton*'s Reflection Grating Spectrometer.

I have investigated the location, ionisation level and chemical abundances of the gas producing X-ray narrow emission lines in NGC 5548 and NGC 1365. Using observations during an unusual time when the nuclear emission of NGC 5548 is obscured by cool absorbing material, I show that the emission lines are consistent with being absorbed by further ionised gas within the AGN system. This is supported by the location I derive for the emission line gas, within those of the known warm absorbers in this system. With NGC 1365 spectra I demonstrate that these emission lines can be used to derive metal abundances within AGN systems; this can be especially important in obscured objects where usual methods of deriving abundances from UV spectra are unavailable due to the large degree of absorption. Finally, leading on from the results on individual objects, I explore outflow-inflow velocities of emission lines in a large sample of AGN, testing whether these velocities are distributed differently for different categories of AGN. With current observations it is not possible to detect population velocity differences in the X-ray narrow emission lines of the magnitude previously seen in optical studies. Through this study, I significantly increase the number of O VII f line detections using a uniform method across a sample of AGN. These three studies show the variety of insights into AGN environments enabled by the study of X-ray narrow emission lines. The thesis closes with a forward look to what could be achieved in this area with the next generation of X-ray observatories.

Acknowledgements

"It's not enough to just live.
You have to have something to live for"
Commander William Adama

There are many people I owe thanks to for their help and support during this PhD. Firstly, to my supervisor Prof. Graziella Branduardi-Raymont: I would not have been able to do all this without you. Thank you for helping me find a path through this process. I always left our meetings with renewed confidence, enthusiasm and a way to keep going, no matter how stuck I had felt beforehand. I cannot thank you enough for your constant support; you helped more than you know.

I would also like to thank members of the NGC 5548 consortium who took me in as a new student and taught me an immeasurable amount. Especially Dr. Missagh Mehdipour who couldn't escape my questions even after leaving MSSL, and always found time to answer emails amazingly quickly, no matter how small or large the request.

Thanks also to my secondary supervisor, Prof. Mat Page, for the ideas, feedback and discussions, and to the other members of the Astro Group who I have talked to about science and life in general. Special thanks to Dr. Daisuke Kawata, who is a fantastic Postgraduate Tutor, always taking the time to listen and improve student life at MSSL.

Those I've shared lunch, office space and the student flat with have formed the majority of my day-to-day life through this process. Everyone has added a new perspective to my life and your company will be missed. I hope we keep in touch.

Massive thanks to Helen for being a wonderful friend. Thanks also to the Astronomy Team of the Royal Observatory Greenwich for their company on more than a year's worth of Thursdays.

Many thanks to my family for their unconditional support and love. I had an idea that my thesis would become your Christmas presents this year, but you will all be happy to know I'm a touch late for that!

Finally to Sami, thank you for the confidence you give me, the worlds you have introduced me to, and for everything else you do. Minä rakastan sinua.

Contents

Publications

First-authored

Whewell, M., Branduardi-Raymont, G., Kaastra, J. S., Mehdipour, M., Steenbrugge, K. C. and et al. (2015), Anatomy of the AGN in NGC 5548: V. A clear view of the X-ray narrow emission lines, *Astronomy & Astrophysics* **581**, A79–14.

Whewell, M., Branduardi-Raymont, G. and Page, M. J. (2016), X-ray narrow emission lines from the nuclear region of NGC 1365, *Astronomy & Astrophysics* **595**, A85–15.

Co-authored

Kaastra, J. S., Kriss, G. A., Cappi, M., Mehdipour, M., Petrucci, P. O., . . . and **Whewell, M.** (2014b), A fast and long-lived outflow from the supermassive black hole in NGC 5548, *Science* **345**(6192), 64–68.

Mehdipour, M., Kaastra, J. S., Kriss, G. A., Cappi, M., Petrucci, P. O. . . . and **Whewell, M.** (2015), Anatomy of the AGN in NGC 5548: I. A global model for the broadband spectral energy distribution, *Astronomy & Astrophysics* **575**, A22–18.

Arav, N., Chamberlain, C., Kriss, G. A., Kaastra, J. S., Cappi, M. . . . and **Whewell, M.** (2015), Anatomy of the AGN in NGC 5548: II. The spatial, temporal, and physical nature of the outflow from HST/COS Observations, *Astronomy & Astrophysics* **577**, A37–27.

Di Gesu, L., Costantini, E., Ebrero, J., Mehdipour, M., Kaastra, J. S. ... and **Whewell, M.** (2015), Anatomy of the AGN in NGC 5548. IV. The short-term variability of the outflows, *Astronomy & Astrophysics* **579**, A42.

Ebrero, J., Kaastra, J. S., Kriss, G. A., Di Gesu, L., Costantini, E. ... and **Whewell, M.** (2016), Anatomy of the AGN in NGC 5548. VI. Long-term variability of the warm absorber, *Astronomy & Astrophysics* **587**, A129.

Mehdipour, M., Kaastra, J. S., Kriss, G. A., Cappi, M., Petrucci, P. O. ... and **Whewell, M.** (2016), Anatomy of the AGN in NGC 5548: VII. Swift study of obscuration and broadband continuum variability, *Astronomy & Astrophysics* **588**, A139–12.

Cappi, M., De Marco, B., Ponti, G., Ursini, F., Petrucci, P.-O. ... **Whewell, M.** ... and et al. (2016), Anatomy of the AGN in NGC 5548. VIII. XMM-Newton's EPIC detailed view of an unexpected variable multilayer absorber, *Astronomy & Astrophysics* **592**, A27.

List of Figures

List of Tables

Chapter 1

Introduction to Active Galactic Nuclei

"All models are wrong, but some are useful"

George Box

The name Active Galactic Nucleus (AGN) is used when the compact central part (nucleus) of a galaxy is comparable in luminosity to or outshines stellar emission from the host galaxy. This nuclear emission has high luminosity, up to $10^{48}\,\mathrm{erg\,s^{-1}}$ (Krolik 1999) integrated over a large wavelength range (hard X-ray to infrared, plus radio for radio-loud AGN; Krolik 1999), strong and fast variability (Peterson 1999), and with features that cannot be associated with star formation, such as strong emission lines which are signatures of multi-temperature photoionised gas (see Fig. 1.1; Netzer 2006).

1.1 Classifications of AGN

AGN are classified by their observed characteristics, therefore while there is a large range of potential classifications, the distinctions between them are not absolute. This is an artefact of the history of AGN studies, as different types were traditionally discovered using different observational methods. A basic summary of the main types of AGN is shown in Fig. 1.2 and short explanations are contained in the following paragraphs.

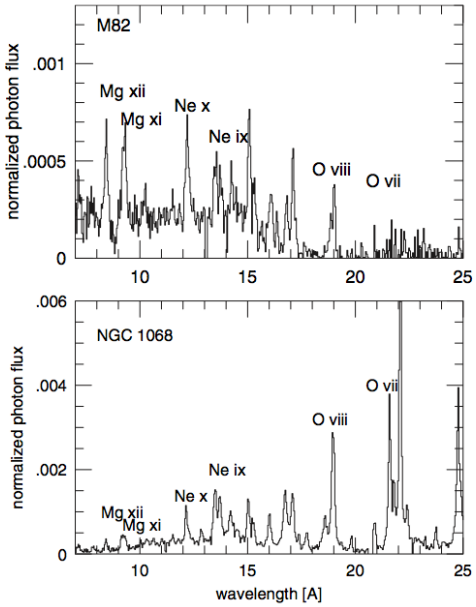

Fig. 1.1: Comparison of a typical X-ray starburst galaxy spectrum (M 82), representing collisional plasma, and a Seyfert 2 AGN spectrum (NGC 1068), representing photoionised plasma. From Netzer (2006)

	Emission Lines	High Luminosity → Low Luminosity			
Radio Quiet	Broad & Narrow		RQ Quasar	Sy 1 & NL Sy 1	LINER
	Narrow			Sy 2	
	None				
Radio Loud	Broad & Narrow	FSRQ (Blazars)	RL Quasar	BLRG	
	Narrow			NLRG	
	None	BL Lac (Blazars)			

Fig. 1.2: Basic observational classifications of AGN. Broad emission lines have velocity widths of a few thousand km s^{-1}. Narrow emission lines have velocity widths of up to 1000 km s^{-1}. RQ stands for radio quiet, RL for radio loud, Sy for Seyfert, NL Sy for narrow line Seyfert, FSRQ for flat-spectrum radio quasar, BLRG for broad line radio galaxy and NLRG for narrow line radio galaxy. For details of each type of object, see text. Adapted primarily from information in Krolik (1999), Peterson (1999) and Osterbrock and Ferland (2006), plus additional references in Sect. 1.1.

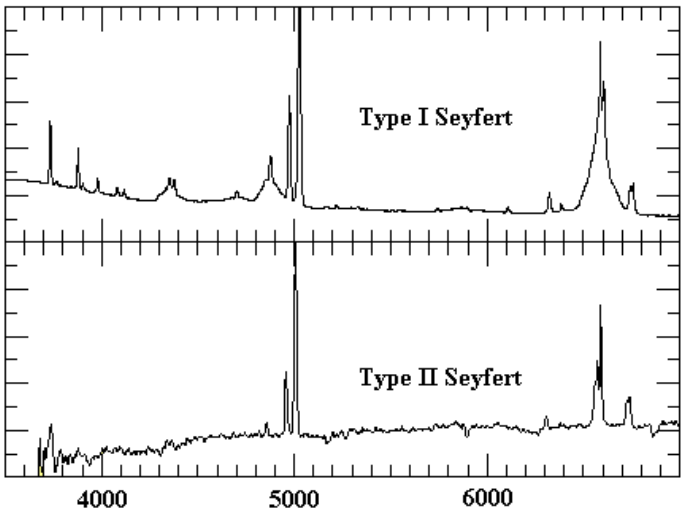

Fig. 1.3: Comparison of Seyfert 1 (upper panel) and Seyfert 2 (lower panel) optical spectra. The X-axis is wavelength (Å). Adapted from Bill Keel's comparison of AGN optical spectra (Keel 2002)

Seyfert galaxies

The first AGN to be recognised as different from 'standard' galaxies were those classified by Carl Seyfert as "extragalactic nebulae with high excitation nuclear emission lines" (Seyfert 1943). In this paper Seyfert discusses six 'nebulae' thought to be part of this new class of object, and lists twelve in total known to have similar characteristics.

The observational characteristics, found in optical spectra, distinguishing them from 'standard' galaxies are:

1. domination of high-excitation nuclear emission lines
2. broad emission lines; up to 8500 km s^{-1} at zero intensity

Khachikian and Weedman (1974) were the first to propose two subclasses of Seyfert galaxies; type 1 has the typical broad permitted emission lines as well as narrow emission lines, whereas type 2 has only the narrow components. These are now known as Seyfert 1s and Seyfert 2s. Characteristic spectra of these types can be seen in Fig. 1.3. There are also intermediate type Seyferts (1.5, 1.8, 1.9) introduced by Osterbrock (1981), where progressively weaker broad lines correspond to the larger classification number.

One more subset of Seyfert galaxies are discussed in the literature, Narrow Line Seyfert 1s (NLSy1s). These have the same properties as Seyfert 1 galaxies, such as a [O III] $\lambda 5007\,\text{Å}$ / Hβ ratio > 3 (Boller et al. 1996; Shuder and Osterbrock 1981), but with additional characteristics, such as strong Fe II emission, the narrowest 'broad' Balmer lines (transitions in Hydrogen ions from excited levels to $n = 2$), often with 500-1500 km s^{-1} widths (Véron-Cetty et al. 2001; Boller et al. 1996), and extremely variable and intense soft X-ray emission and steep soft X-ray spectra (Boller et al. 1996). This last feature may indicate a higher accretion rate and smaller black hole mass compared to other Seyfert galaxies (Pounds et al. 1995).

It can be considered in basic terms that Broad Line Radio Galaxies and Narrow Line Radio Galaxies are radio-loud counterparts of Seyfert 1s and 2s respectively, as shown in Fig. 1.2.

Quasars

Quasars were the second type of AGN to be discovered (after Seyferts) by radio surveys such as the third Cambridge (3C) catalogue in the late 1950s (Edge et al. 1959). They tend to be more luminous, and at higher redshift, and can be both radio-loud or radio-quiet (compared to Seyfert galaxies which are generally radio-quiet).

Other than the potential for high radio emission, the main distinction between Quasars and Seyfert galaxies is that Quasars are generally point sources while for Seyfert galaxies the host galaxy is clearly resolvable (Krolik 1999).

LINERs

LINER stands for "Low-Ionisation Nuclear Emission Region", and these objects have lower luminosity nuclei than Seyfert galaxies, initially defined by Hα emission line luminosities of 10^{38} - 10^{41} erg s^{-1}, compared to typical Seyfert values of 10^{41} - 10^{43} erg s^{-1} (Heckman 1980). They also show similar emission lines to Seyfert 2s, although in different ratios, with the low-ionisation lines

being stronger in LINERs (see Fig. 1.4). Some LINERs may be low-luminosity Seyfert 2s, but LINER spectra can also be produced in different environments e.g. starburst-driven winds and shock-heated gas (Peterson 1999). As LINER is an observational classification, the origin of the low-ionisation emission is not guaranteed to be the same in all objects (Heckman 1987; Gonzalez-Martin et al. 2006; Singh et al. 2013).

Radio Loud AGN

Radio loud AGN often have strong jet features; the radio emission can come from close to the core, the jets themselves, or large radio lobes situated at the ends of those jets. Radio quiet AGN can still have some faint radio emission, usually confined to a small region, close to the core of the galaxy. The work in this thesis focusses on radio quiet AGN, so this is a very general summary of the different classifications within the radio loud AGN population.

There are many different classes of radio loud AGN, based on both spectral and spatial distinguishing features. Flat-Spectrum Radio Sources (FSRSs) and Steep-Spectrum Radio Sources (SSRSs) are categories describing the power law slope of the synchrotron radio emission from the jet. This corresponds well to whether the radio source is compact (FSRSs) or extended (SSRSs), but does not correspond to the FR I and FR II Fanaroff and Riley (1974) classes. FR I and FR II classifications are given to lower and higher luminosity radio sources, respectively, with the dividing luminosity at L_ν (1.4 GHz) = 10^{32} erg s^{-1} Hz^{-1} (Bridle and Perley 1984). FR I objects are brightest in the core, with decreasing surface brightness towards the edges, while FR II objects are brightest at the edges, often with 'hot-spots' of bright emission at the end of the jet features (Fanaroff and Riley 1974). The spectrum of the compact core of an object from either class is usually flat, whilst the spectrum from the extended regions is usually steep (Peterson 1999). Radio loud AGN can also be categorised by the excitation level of their optical spectra, leading to the classes of High Excitation Radio Galaxy (HERG) and Low Excitation Radio Galaxy (LERG), which are also correlated with high and low radio luminosities

respectively. HERGs and LERGs do not have a one-to-one connection with the FR I and FR II classes.

All of the above classes fall under a general description of radio loud Quasars, and as shown in Fig. 1.2 the classifications of Broad Line Radio Galaxy (BLRG) and Narrow Line Radio Galaxy (NLRG) can be used for lower luminosity objects as the radio loud equivalents of Seyfert 1s and 2s. The final main group of radio loud AGN is the Blazar class, with the sub-classes BL Lac objects and Flat-Spectrum Radio Quasars (FSRQs).

Blazars are thought to correspond to the case of looking directly down the jet of a Quasar, which causes relativistic amplification of the jet-emitted non-thermal radiation from radio to γ-ray (e.g. Blandford and Rees 1978; Urry and Padovani 1995). This is the most energetic of the AGN classes, with characteristically 'double-humped' spectral energy distributions. The first hump is attributed to synchrotron emission from electrons accelerated along the jet, peaking in the infrared-optical (up to soft X-ray) range (Abdo et al. 2010). The second hump is at higher energies (X-ray to γ-ray) and thought to be produced by synchrotron self-Compton scattering of jet photons by the same electrons that produce the synchrotron emission, although this is less well established (see review by Böttcher 2007, and references therein). The initial observational classification of either BL Lac or FSRQ was made based on the presence of optical emission lines with equivalent widths greater than 5 Å. If lines were present then a FSRQ classification was given, while BL Lac objects traditionally have featureless spectra (see e.g. Ghisellini et al. 2011; Urry and Padovani 1995). BL Lacs are then divided into three subclasses; low-, intermediate- and high-synchrotron peaked sources (LSPs, ISPs and HSPs) depending on the peak location of their synchrotron emission, and FSRQs can also be included in the LSP subcategory (Abdo et al. 2010).

The standard theory of all AGN types is that they are powered by accretion onto a supermassive black hole (SMBH). The combination of very high luminosities and short timescale variability in AGN gives evidence that the source should have high mass (by using the Eddington limit criterion) and yet

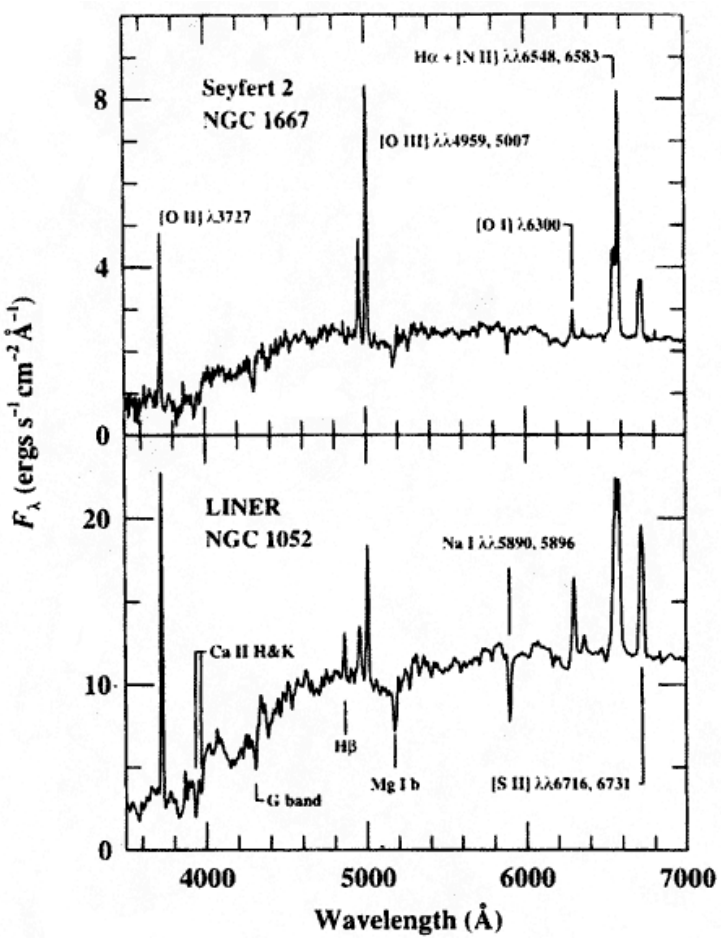

Fig. 1.4: The difference between Seyfert 2 (upper panel) and LINER (lower panel) optical spectra. For example, compared to Seyfert 2 spectra, the low-ionisation lines in LINERs (such as [O I] λ6300) are relatively strong. From Peterson (1999)

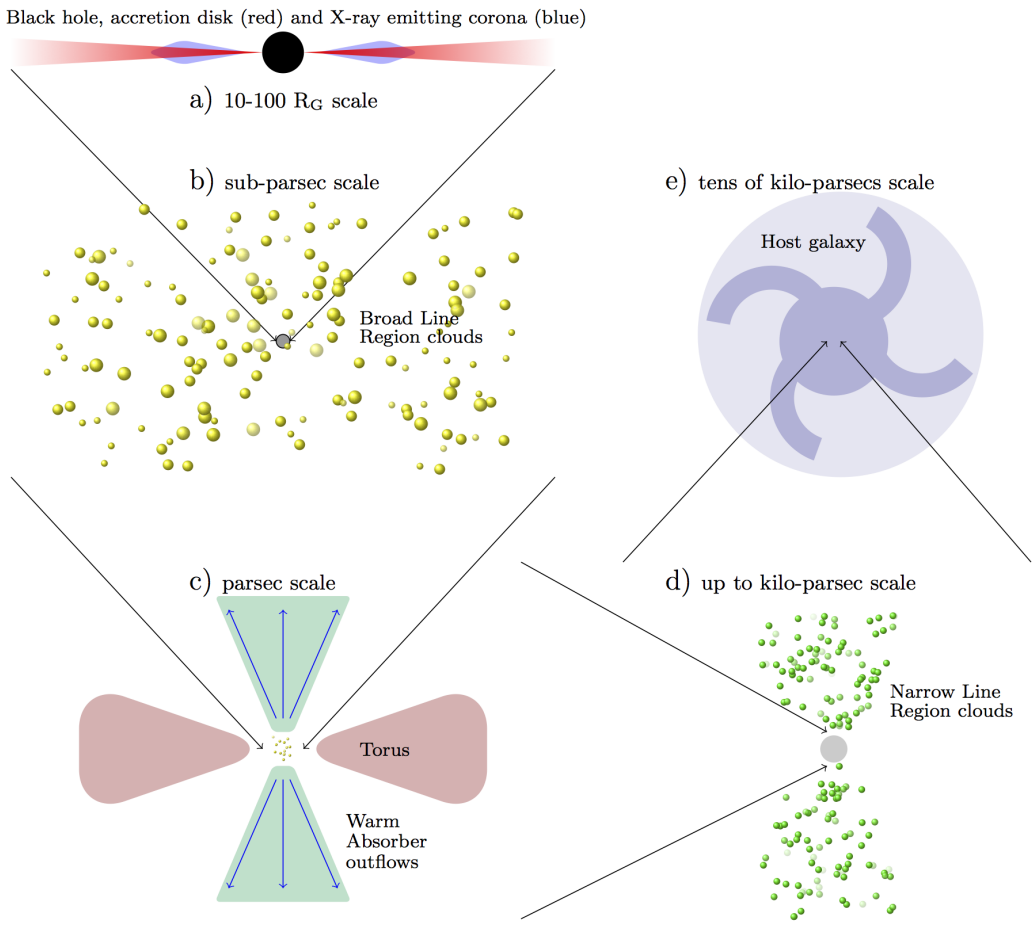

Fig. 1.5: Illustration showing the general paradigm of AGN structure. See text for details.

be very small (by using the variability timescale to constrain light travel time across the source) (see Krolik 1999, and references therein). A basic picture of an AGN is shown in Fig. 1.5.

The following paragraph describes this general picture of AGN structure, but detail about the emission mechanisms, atomic processes and how they relate to the observed spectra, specifically with regard to Seyfert galaxies, is covered in Sect. 1.3.

In the generally accepted paradigm, immediately surrounding (10-100 gravitational radii; Netzer 2006) the central SMBH ($\sim 10^6$-10^9 $M_\odot$) is an accretion disk whose inner parts are emitting in the UV band, an X-ray corona (panel a, Fig. 1.5), and in some cases the base of a radio jet which can extend out into the intracluster medium between galaxies. The hot corona is where the UV photons from the disk are inverse Compton scattered by energetic elec-

trons to X-ray energies although it is difficult to determine the geometry and location any further. The necessary and sufficient conditions for the presence of a jet in an AGN are not well understood, and neither are the launching mechanism or location (see Worrall 2009, for a review of AGN jets from an X-ray perspective). On sub-parsec scales (panel b, Fig. 1.5), Broad Line Region clouds are thought to surround the SMBH, and are the location where the broad components of emission lines originate. Further still from the central source, at parsec scales (panel c, Fig. 1.5), are a torus of dusty obscuring material and ionised gas in conical outflows (called 'warm absorbers' in the X-ray literature; Halpern 1984). At greater distances (up to kiloparsec scales; panel d, Fig. 1.5) the Narrow Line Region clouds are located, and finally (panel e) the host galaxy surrounds the whole AGN structure.

1.2 Unified Models of AGN

The great variety in spectra of all the AGN types described above cannot yet be completely explained by this basic picture. For example, there are two ways to think about the differences between Seyfert 1 and Seyfert 2 characteristics, under the assumption that they are both caused by accretion onto a SMBH; either the intrinsic emission is different (and may represent e.g. different evolution stages of these objects) or the intrinsic emission is the same but the viewing angle causes them to look different.

The latter of these two ideas gave rise to what is known as the AGN Unification Theory (Urry and Padovani 1995), where the inclination (viewing) angle determines which types of emission are seen and therefore which type of AGN. In the radio quiet version of this scheme, Seyfert 1s are viewed by looking directly into the centre of the AGN system, so both the inner broad line emission and the outer narrow line emission can be seen. In contrast, Seyfert 2s are seen from a greater inclination angle (more of a side-on view) so the dusty torus obscures the inner broad line emission, and only the outer narrow line emission can be seen.

In X-ray literature, Seyfert galaxies can also be referred to as unobscured and obscured, which are similar classifications to Seyfert 1 and Seyfert 2 al-

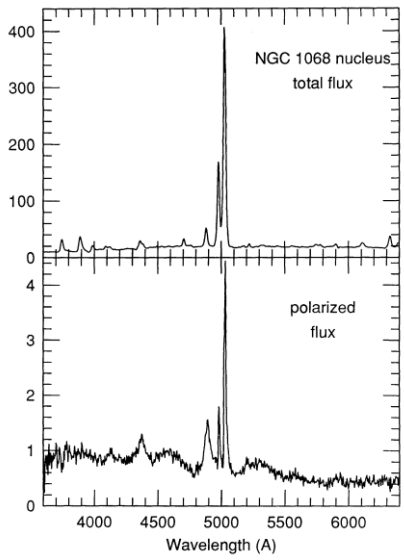

Fig. 1.6: Comparison between total flux and polarized flux for the nucleus of NGC 1068 in the optical band. Broad lines are visible in the polarized flux that cannot be seen in the total flux. From Miller et al. (1991)

though the optical and X-ray classifications do not always line up as expected (se e.g. Gonzalez-Martin et al. 2014). Within the group of obscured Seyferts, another two terms are often used: Compton-thin and Compton-thick. An AGN is considered Compton-thick when the intrinsic neutral absorbing column density observed to affect the X-ray spectrum is above $1.5 \times 10^{24}\,\mathrm{cm}^{-2}$; in this case X-rays emitted from the nucleus are effectively destroyed before they exit the system, by both Compton scattering and photoelectric absorption. In these objects only indirect reflected or scattered X-rays from the system are visible to us (Alloin 2006).

One of the most famous pieces of evidence for the Unification Theory comes from observations of NGC 1068 (Antonucci and Miller 1985). This is a traditional Seyfert 2 galaxy in both the optical (see Fig. 1.6; Miller et al. (1991)) and the soft X-ray band (see Fig. 1.7; Kinkhabwala et al. (2002)), with many narrow emission lines easily visible above a low continuum. The above Unification Theory suggests that a 'scattering medium' lies above the hole in the torus, and light from the inner broad line region can be scattered back into our view by this medium. The evidence for this theory appears when you look at the linear polarization spectrum (see Fig. 1.6), where you can see

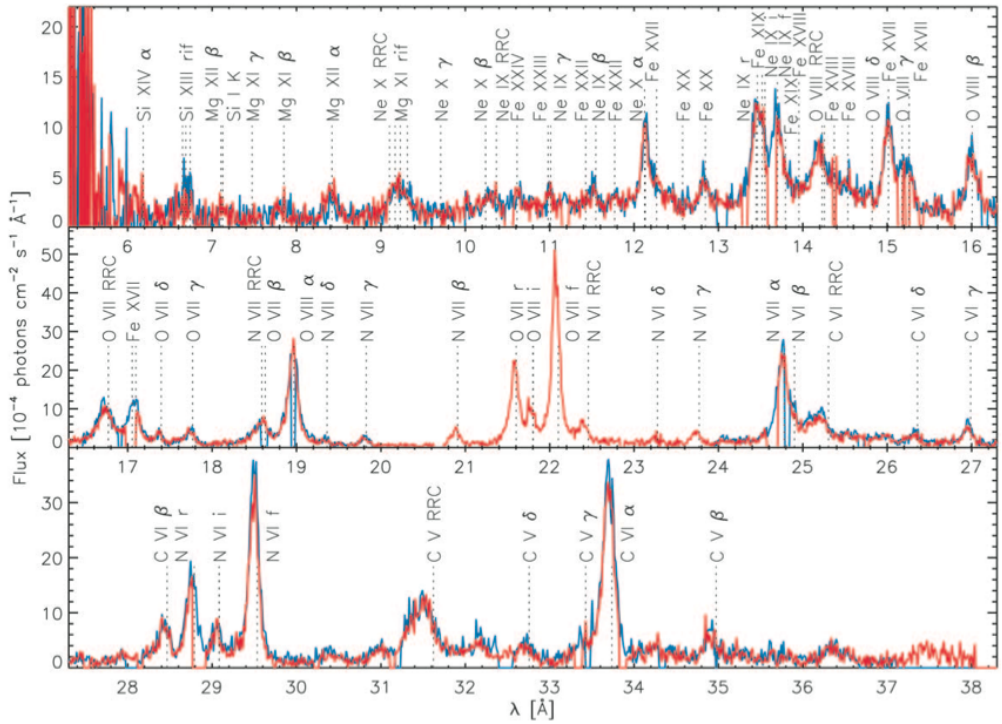

Fig. 1.7: 110 ks observation of NGC 1068 using XMM-Newton RGS, taken in July 2000. Shown are the effective area-corrected, first-order RGS 1 (red) and RGS 2 (blue) spectra shifted to the galaxy's rest frame ($z = 0.00379$). The strong narrow emission lines are clearly seen over the observed low continuum. From Kinkhabwala et al. (2002).

broad Fe II, Hγ and Hβ lines. This is interpreted as photons from the inner broad line region being scattered back into our line of sight.

This 'hidden' Broad Line Region, found by polarisation, does not appear to be present in all Seyfert 2 objects (Tran 2001), giving evidence that the above Unification Theory based on viewing angle may not be applicable to all Seyferts.

There are also observations suggesting some AGN can move between the Seyfert 1 and Seyfert 2 classifications. For example, Denney et al. (2014) find that over almost 40 years of observations (1973-2014), Mrk 590 changed classification from a Seyfert 1.5, to a Seyfert 1, and then to a Seyfert 2 (see Fig. 1.8) as the optical band broad lines appear to get stronger and then disappear.

There are two ways to explain these "changing look" AGN. Either i) there is variable obscuration of the broad lines, they are always produced, but whether they are observed or not depends on the level of absorption/obscuration that occurs, or ii) there is a variable accretion rate onto the central SMBH, so that the structure, level of emission, and to a certain extent the existence of the BLR are dependent on the accretion rate.

Denney et al. (2014) suggest that the changes in classification of Mrk 590 are caused by variable accretion, as they see the same general trends in flux variations of the optical continuum, optical broad lines (particularly Hβ) and optical narrow lines (particularly [O III] λ5007), although on differing timescales. The authors conclude from this that the classification type for at least some AGN may be more an insight into the immediate environment of the black hole, rather than an outcome of viewing angle.

Clearly, while the model for the basic structure of AGN environments is generally accepted, questions remain about the specific differences between objects as well as between observations of the same object separated by decades.

Recently, due to these differences, alterations to the Unification Theory have been proposed. Netzer (2015) suggests three main modifications: changes to the physics and structure of the torus with the presence of a more central obscurer in some objects, recognition that there are genuine differences between

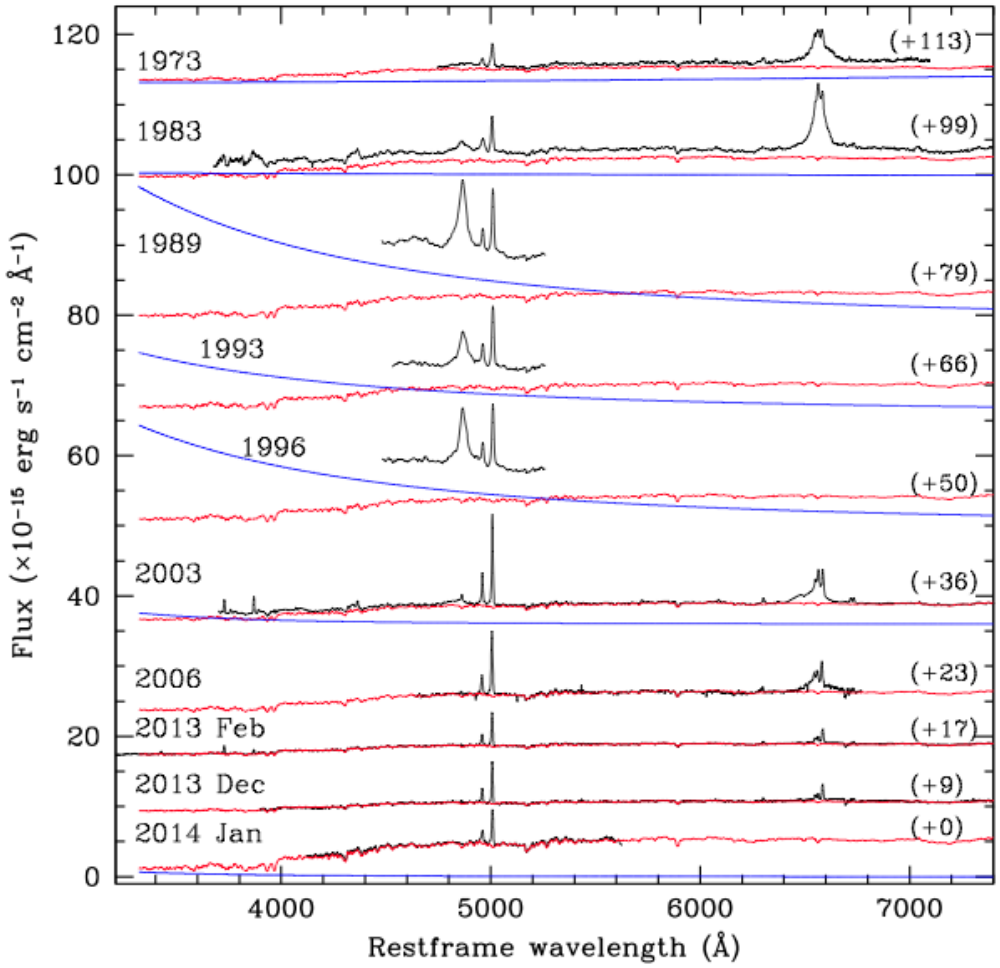

Fig. 1.8: Rest frame optical spectra of Mrk 590 spanning more than 40 years. The black curves show the observed spectra, the red curves show a host galaxy starlight template that was fit to the 2013 spectrum and has been scaled to all other spectra, and the blue curves show power law continuum fits for the epochs in which the stellar component could not account for all the observed continuum flux. All spectra are on the same flux scale, given in the ordinate axis label, but a constant has been added (given in parentheses to the right of each spectrum) to all but the most recent epoch to clearly visualize observed changes between epochs. From Denney et al. (2014).

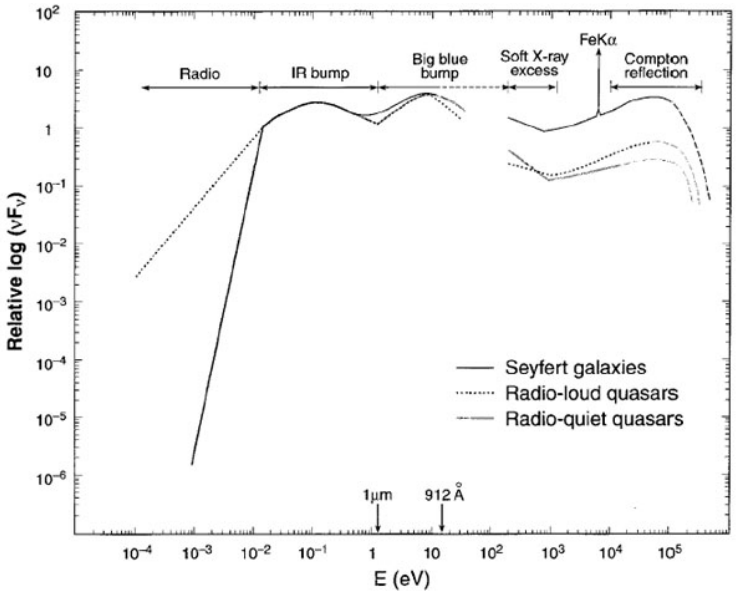

Fig. 1.9: Average broadband spectrum for three different AGN types, illustrating their common features. From Koratkar and Blaes (1999)

sub-classifications of AGN (independent of luminosity and inclination), and ability to take into account evolution of the host galaxy, particularly in terms of merger history. Central to these modifications is the separation of torus absorption from the presence (or not) of broad emission lines, and minimising the use of broad emission lines as a major classification feature.

1.3 Emission and Absorption from AGN

Defining a detailed average spectral energy distribution (SED) of AGN is a difficult task, although most AGN have a variety of similar features. Figure 1.9 illustrates these common features, and Figure 1.10 shows a more detailed view of features in X-ray spectra of Seyfert galaxies.

Radio loud and quiet classifications are usually based on a ratio between of $R = \frac{F_r}{F_o}$ where F_r and F_o are radio and optical flux measurements at 5000 MHz and 2500 Å respectively (Sramek and Weedman 1980). $R > 10$ has been traditionally used to distinguish radio loud sources (Stocke et al. 1992; Sramek and Weedman 1980), although recent work suggests that radio loudness is not defined by a strict loud/quiet split, but rather a gradual transition (Mingo et al. 2016).

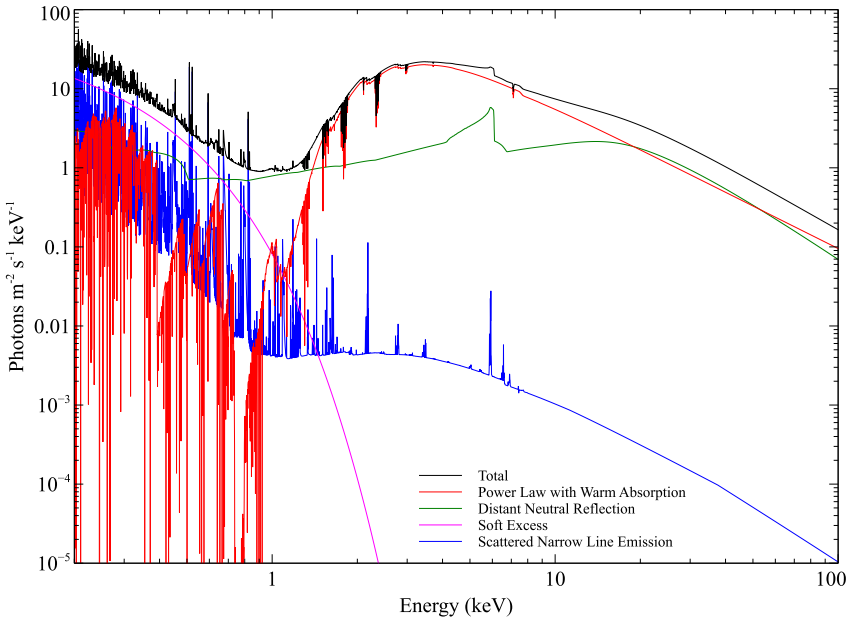

Fig. 1.10: Simplified illustration of the main components thought to make up X-ray emission from AGN, modelled with SPEX.

The infrared (IR) bump in the SED is thought to be produced by thermal emission from dust heated by the primary continuum, potentially in the torus region. The big blue bump (BBB) in the optical/UV region is also believed to be thermal emission but from hotter material, possibly in the accretion disk. Most AGN also show a local minimum in their SED around $\sim 1\mu$m, between these two bump-like features (Peterson 1999).

The break in the SEDs in Figure 1.9 between the BBB and the 'soft X-ray excess' labels shows the spectral region where the interstellar medium in our own Milky Way causes too much extinction for extragalactic observations to be possible.

At higher energies than this unobservable range is the X-ray and γ-ray emission. X-rays are split into two regions; soft X-rays are normally defined as covering the band 0.1 keV - 2 keV and hard X-rays 2 keV - 100 keV (even higher energies are γ-rays). Different detector techonologies are needed to observe in the soft X-ray, hard X-ray and γ-ray regimes (Peterson 1999). Figure 1.10 is a more detailed view of the X-ray emission of a typical Seyfert 1 spectrum.

The power law component (shown as absorbed by a warm absorber in

Fig. 1.10) is well explained by Comptonization processes. Comptonization occurs when photons and electrons scatter off each other within a gas, changing the resulting spectrum of the light. If energy is transferred from photons to electrons the process is called Compton scattering, which lowers the energy of photons in the spectrum. The reverse process (energy transfer from electrons to photons) is called inverse Compton scattering, and the photons are up-scattered to higher energies. Inverse Compton scattering in a hot corona, where photons from the disk collide with high energy electrons, can explain the power law observed above ∼2 keV within AGN spectra; the sum of the scattering events, over the distribution of both the photons and electrons, produces a smooth power law shape (Fabian et al. 1986; Osterbrock and Ferland 2006).

Some of this X-ray power law emission then interacts with other material within the AGN structure such as the disk, the torus and the BLR/NLR. As it irradiates other material it produces back-scattered radiation in our line of sight, known as a reflection spectrum. If that material is neutral and distant (e.g. at the far edge of the disk) then the main components of the (cold) reflection spectrum are a narrow Fe Kα line at ∼6.4 keV and a Compton hump at high energies (see Fig. 1.10). In some objects a broad asymmetric component to the Fe Kα emission line has been observed, interpreted as a reflection signature from the inner part of the accretion disk, where extreme gravity has distorted the shape of the emission line (for an extensive discussion of X-ray reflection in AGN systems see the review by Fabian and Ross 2010, and references therein).

The physical origin of the soft excess feature, seen in the soft X-ray spectra of some AGN to emerge above the extrapolation of the power law below 2 keV, is still debated (e.g. Mehdipour et al. 2011). Various models have been put forward, including interpreting it as the high energy tail of the thermal emission causing the BBB (e.g. Arnaud et al. 1985; Pounds et al. 1986), the result of strong, relativistically smeared, partially ionised aborption in a wind from the inner disk (Gierlinski and Done 2004), part of the relativistically blurred, photoionised, disk reflection as in the model by Ross and Fabian

(2005) (e.g. Nardini et al. 2011) or 'warm' Comptonisation, where a corona with lower temperature and higher optical depth than that used to explain the origin of the X-ray power law, up-scatters disk photons to higher energies (see Mehdipour et al. 2011, and references therein).

Identifying a physical origin for the soft excess is complicated by the presence of 'warm absorbers' that imprint absorption features in the same soft X-ray region of particularly Seyfert 1 spectra (the continuum in this region of Seyfert 2 spectra is usually too low to allow detection of absorption features) (Reynolds 1997). Warm absorbers were first proposed by Halpern (1984) to explain signatures of variable absorption in the Radio Quiet Quasar, MR 2251-178. In this paper the author discusses two models to potentially explain this variation; one with a 'cold' (neutral) absorber crossing the line of sight and the other with a 'warm' (ionised) absorber with varying ionisation levels. The warm absorber model gave a better fit to the data, and more recently the first detection of narrow absorption lines from the warm absorber in NGC 5548 has confirmed this scenario (with some surprise because absorption edges had been fitted traditionally and were expected, not narrow absorption lines; Kaastra et al. 2000).

There is now an extensive body of literature reporting on warm absorbers detected in many AGN; the vast majority show blue-shifted absorption lines, which identifies them with outflowing ionised gas moving towards the observer (see Cappi et al. 2013, and references therein). The origin of warm absorbers is not well determined, and has been argued to be from the inner edge of the torus (Krolik and Kriss 2001) or the accretion disk (Bottorff et al. 2000; Elvis 2000). In addition, there are detections of 'ultra fast outflows' (UFOs) in a growing sample of AGN (Cappi 2006; Tombesi et al. 2010). These are detected as blueshifted absorption lines at rest frame energies above 7 keV, and identified with Fe XXV and/or Fe XXVI (He-like and H-like iron) resonant absorption lines at mildly relativistic velocities (up to 0.4c) (Tombesi et al. 2010). The origin of UFOs is also uncertain (see Tombesi et al. 2012, and references therein), as well as whether they are extreme versions of the same phenomena as warm absorber outflows, or have a completely different origins

(see Tombesi et al. (2013) and Laha et al. (2014) for differing views).

Gas producing narrow absorption lines in our line of sight has also been detected using UV data (see e.g. Kriss 2001; Kriss et al. 2003). Gas which produces observable absorption lines in the UV may contain ions which should produce absorption transitions observable in the soft X-rays too, although current soft X-ray instrumentation is not generally sensitive enough to the low column densities of those associated X-ray absorbing ions. Absorber phases in the UV are usually characterised by their velocity, whereas in the soft X-rays they are usually characterised by ionisation state as the data in this band have a much lower velocity resolution. The general picture so far is that some (but not all) of the UV velocity phases are detected as X-ray absorber phases, and some (but not all) of the X-ray ionisation phases can be detected as UV absorber phases (Blustin et al. 2005; Arav et al. 2015).

There are two distinct emission line regions thought to occur close to the core of AGN systems. These emission lines are produced from recombination after photoionisation of the gas has taken place. The broad line region (BLR) is close (for NGC 5548, studied in Chapter 5 of this thesis, within five light days, from Pancoast et al. 2013) to the central source and consists of dense (10^{10} cm^{-3}) gas (Detmers et al. 2009), potentially in the form of clouds, streams or filaments (Peterson et al. 2013). The narrow line region (NLR) is further out from the ionising source (1-3 pc radius for the optical NLR of NGC 5548, from Peterson et al. 2013), more spatially extended, less dense (Peterson et al. 2013, estimates 10^5 cm^{-3}, again for NGC 5548's optical NLR) and produces narrow emission lines including forbidden lines, with widths less than 1000 km s^{-1}. The X-ray BLR and NLR emission can further complicate studies of the soft excess and warm absorbers, due to its presence in the same region of the soft X-ray spectrum.

The line of sight velocity of the optical NLR has been investigated using the [O III] λ5007 emission line, which is often either blueshifted (moving towards us) or at rest, relative to the low ionisation optical narrow lines, or stellar absorption lines from the host galaxy (Boroson 2005; Bae and Woo 2014). The [O III] velocity shift has been used as an orientation indicator by

Boroson (2011), in conjunction with Fe emission which is thought to originate from the BLR.

Studies of outflowing emitting gas complements those of absorbing gas as they probe gas outside our direct line of sight towards the nucleus. For objects such as the 'bare' Seyfert 1 galaxy Ark 120, which has no intrinsic X-ray absorbing gas along our line of sight, studying the X-ray narrow emission lines is the best way to investigate gas intrinsic to the AGN (Reeves et al. 2016b).

In Seyfert 2 systems, the optical and X-ray NLR regions have been shown to be co-spatial using HST and *Chandra* images (Bianchi et al. 2010), but the same analysis is more difficult for Seyfert 1 galaxies due to the higher continuum relative to the soft X-ray narrow lines.

Narrow emission lines from AGN are historically thought to remain constant, given they are produced at large distances from the central engine, which makes a rapid response to its variability unlikely. However, there is growing evidence that, at least in some cases where repeated observations are available, these narrow emission lines vary over timescales of years. This has been presented by Detmers et al. (2009), using O VII f in the X-rays, and both Peterson et al. (2013) and Denney et al. (2014), using [O III] in the optical (the three papers refer to NGC 5548 in the former two cases and Mrk 590 in the third).

As well as studies attempting to connect UV and X-ray observations of warm absorbers, there have also been studies linking the X-ray warm absorber gas to the X-ray narrow-line emitting gas (e.g. Krolik and Kriss 1995; George et al. 1998; Sako et al. 2000; Blustin et al. 2003; Armentrout et al. 2007). These investigations have shown qualitively similar properties between the absorbing and emitting gas phases, but have not yet conclusively proven the same gas is responsible for both.

Overall there is no clear picture of how optical and X-ray narrow line regions, and UV and X-ray warm absorbers are related to each other (or not) within an entire AGN system.

1.4 Chemical Abundances of AGN Outflows

Abundance measurements for AGN outflows are usually made using broad emission lines in UV (e.g. Hamann et al. 2002) or narrow absorption lines in UV (e.g. Arav et al. 2007). In both types of UV based abundance measurements (emission and absorption), 2-4 times solar abundances have typically been found (see Hamann et al. 2007; Arav et al. 2007, and references therein), and in one case as high as 15 times solar (Q 0353-383; Baldwin et al. 2003).

Optical narrow emission lines can also be studied for abundance measurements; Groves et al. (2006) used line ratio diagnostics ([N II] λ6584 Å / [O II] λ3727 Å and [O III] λ5007 Å /[O II] λ3727 Å) to determine that only 40 AGN from an Sloan Digital Sky Survey (SDSS) sample of 23000 are clear candidates for sub-solar NLR abundances.

In some cases narrow absorption lines in X-ray (e.g. Steenbrugge et al. 2011) are used. X-ray spectra do not include any hydrogen transitions, and the level of bound-free hydrogen absorption only alters the perceived continuum level, so is degenerate with the flux level of the object. Therefore only relative abundances can be determined using X-ray spectra, with no direct comparison to the hydrogen abundance possible.

There are few studies estimating AGN abundances using X-ray narrow emission lines in a small number of objects. Jimenez-Garate and Khu (2004) looked at three AGN and determined that NGC 1068 (Seyfert 2) has a ≤ 2 times overabundance of nitrogen, NGC 4051 (Narrow Line Seyfert 1) has an overabundance of neon and NGC 4507 (Seyfert 2) is consistent with solar abundances. Both Kinkhabwala et al. (2002) and Brinkman et al. (2002) have also found evidence for 2-3 times overabundance of nitrogen in the emission line spectrum of NGC 1068 (using RGS and *Chandra* LETGS data, respectively). RGS observations of starburst galaxies have been used to estimate metal abundances from the soft X-ray collisional emission lines. In M 82, Read and Stevens (2002) find supersolar abundances of magnesium, silicon, neon and nitrogen (between 2 and 5 times solar), and Origlia et al. (2004) also find supersolar abundances of magnesium, silicon and sulphur, although to a lesser extent (up to 1.5 times solar).

1.5 Effects of AGN on Galaxy Evolution

A major question of interest connecting AGN accretion and outflow processes with wider astrophysics is: "To what extent can AGN affect the evolution of their host galaxies and wider surroundings?". This has been the subject of many books, review articles, theses and papers, so it is not possible to do it justice in such a short section. Here is a very brief summary of some points relevant to this thesis.

Following Mo, H., van den Bosch, F. and White, S. (2010), the power of a single AGN energy output can be described as:

$$\frac{dE}{dt} = \epsilon \dot{M}_{BH} c^2 \tag{1.1}$$

where $\dot{M}_{BH}$ is the mass accretion rate of the black hole, c is the speed of light and ϵ is the efficiency factor, quantifying how much of the accretion power of the SMBH is released.

This can be integrated over the entire history of that AGN, giving the total energy output:

$$E = \bar{\epsilon} M_{BH} c^2 \tag{1.2}$$

where $\bar{\epsilon}$ is the mean efficiency. This can then be compared with the binding energy of the host galaxy, to see if the AGN can have a significant impact on that galaxy's evolution.

Using the virial theorem, the gravitational binding energy of a galaxy is roughly:

$$W \sim -M_{gal} \sigma^2 \tag{1.3}$$

where M_{gal} and σ are the mass and velocity dispersion of the host galaxy respectively.

Observationally $\frac{M_{BH}}{M_{gal}} \sim 10^{-3}$ (Kormendy 2001, of course this varies for each galaxy/SMBH combination), so dividing equation 1.2 by equation 1.3 gives, for a massive galaxy with $\sigma \sim 300\,\mathrm{km\ s^{-1}}$, the ratio $\frac{E}{|W|} \sim 10^3 \bar{\epsilon}$.

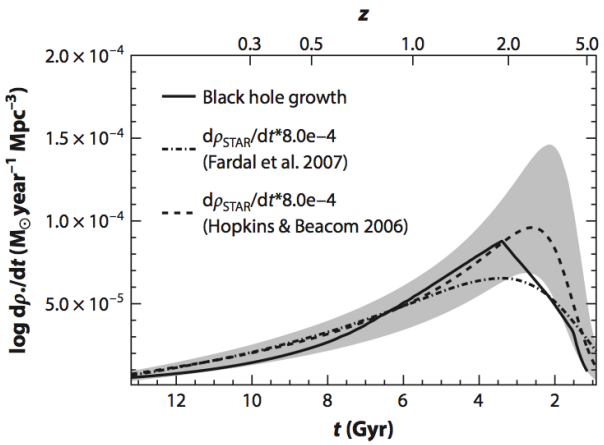

Fig. 1.11: Black hole growth and stellar mass growth as a function of redshift. The average black hole accretion rate is compared to the star-formation rates from Hopkins and Beacom (2006) (including their 3σ uncertainty region in gray) and Fardal et al. (2007), scaled by the factor 0.8×10^3. Figure from Shankar et al. (2008).

Therefore it is clear that, depending on the accretion efficiency of the AGN, it is certainly possible for this process to affect the host galaxy evolution. The questions that remain are what this efficiency value is in reality, and whether the energy output from the AGN is effectively coupled to the environment within the host galaxy and its wider surroundings.

Observational evidence suggests that AGN and their host galaxies co-evolve. Figure 1.11 shows the evolution of galaxies (traced by star formation rates) and of their central SMBHs (traced by AGN activity). The trends in both populations show remarkable similarities; peaks at $z \sim 2-3$, gradual declines by roughly a factor of 10 from $z = 2-3$ to 0 and steeper declines at higher redshifts.

In the local Universe, the empirical $M - \sigma$ relation (correlating the mass of the central SMBH with the stellar velocity dispersion within the galactic bulge, see Section 6 of the review by Kormendy and Ho 2013, and references therein) further implies this co-evolution, and has been interpreted as showing the SMBH and the galaxy regulate each other's growth (e.g., Gebhardt et al. 2000; Ferrarese and Merritt 2000). This picture is becoming more complicated with further studies suggesting there are some types of galaxies with less strong correlations between these two parameters, for example those galaxies with

pseudobulges, but this still requires co-evolution between SMBHs and galaxies at certain stages of their lifetime (Kormendy and Ho 2013). Evidence such as this shows that SMBHs and galaxies undergo similar evolutions, but the causal link between them is not yet fully established.

This is where studying individual AGN can help. One of the ways AGN can release energy into their surroundings is through 'winds' of outflowing material. Outflows have been detected in many AGN and over many energy bands, so their ubiquity is well known, see e.g. the reviews by Fabian (2012), Crenshaw et al. (2003) and Cicone et al. (2014) (the latter for a recent sub-millimeter survey). Further sub-millimeter results will become available in the near future, as the capabilities of the Atacama Large Millimeter/Sub-Millimeter Array (ALMA) are used to investigate galaxy scale molecular outflows in a greater number of objects.

Outflows may be able to prevent further star formation and black hole growth by heating and/or removing the interstellar medium within the host galaxy (e.g. Silk and Rees 1998; King 2003). For the impact on the host galaxy to be large enough to produce the observed $M-\sigma$ relation (Ferrarese and Merritt 2000; Gebhardt et al. 2000), the kinetic luminosity of the outflows must be 0.5% - 5% of the bolometric luminosity of the AGN (Hopkins and Elvis 2010; Di Matteo et al. 2005). Over the last few years, observations have begun to show that winds with this power exist (see e.g. Borguet et al. 2012), and warm absorber outflows, seen in the soft X-rays, are interpreted as low power versions of these winds. Nearby Seyfert AGN where warm absorbers are common are then an ideal place to study AGN winds in detail. Increasing our understanding of all outflowing material from AGN, whether seen in absorption or emission, will help us get closer to a coherent picture of interactions between AGN and different scales of their surroundings, therefore advancing the overall theory of galaxy evolution through time.

Chapter 2

X-ray Emitting Gas and Atomic Physics

"You can't know, you can only believe - or not"

C.S. Lewis

The focus of this thesis is X-ray line emission from gaseous environments of AGN. For X-ray lines to be produced, atomic inner shells must have electron vacancies, i.e. high charge state ions in an excited state are required, from which they decay via transitions leading to emission lines of specific energies. Among the processes leading to excited high charge state ions in gas, those relevant to the work in this thesis are photoionisation and photoexcitation (following irradiation by an external source), collisional ionisation and excitation (mechanically induced through collisions), charge exchange (see Sect. 2.8), and a combination of multiple processes in a hybrid gas.

If an electron in an atom or ion receives enough energy from an outside source, it will escape the atom or ion in a process called ionisation. If the outside source does not have enough energy to cause ionisation, it may excite the electron to a higher level shell of the atom or ion instead, as an excitation process.

The outside source could be photons from a radiation field (for photoinisation), or other electrons (for collisional ionisation). If the outside source is a radiation field, and the radiation appears to come from behind the ionised

gas in an observer's line of sight, then this produces an absorption line in the observed radiation.

The freed electron can also recombine with an ion, and therefore release a photon in any direction. The photon energy corresponds to the initial energy of the electron minus the energy of the shell it recombines into. If the electron recombines to a high level shell of the ion, it can cascade to a lower shell, releasing another photon with the specific energy of that transition. These released photons produce emission lines.

Photoionised gas produces X-ray line emission through recombination processes and radiative cascade after photoionisation, as well as radiative decay after photoexcitation; these processes have been found in to take place in X-ray binaries (Cottam et al. 2001), cataclysmic variables (Mukai et al. 2003), components of stellar winds (e.g. in Sako et al. 1999; Schild et al. 2004) and, most importantly for this work, in X-ray narrow line regions of AGN (e.g. Sako et al. 2000; Kinkhabwala et al. 2002; Nucita et al. 2010, among others).

Collisional gas, on the other hand, produces X-ray line emission mainly through radiative decay after electron impacts upon ions (hence the name 'collisional'). Collisional plasmas have been found in stellar coronae, shock-heated environments and the intracluster medium in galaxy clusters (Kahn et al. 2002). The critical density for a species is defined as the density at which collisional and radiative de-excitation rates are equal; for O VII this is $10^9 - 10^{10}$ cm^{-3} (Porquet and Dubau 2000).

For photoionised gas, as the radiation field is the major cause of ionisations, the electron temperature can be much lower than the ionisation potential. For collisionally ionised gas, the electron temperature is comparable to the ionisation potential, because the electrons have enough energy to cause those ionisations. This is why collisionally ionised gas has a higher temperature than photoionised gas with an equivalent ionisation level.

The following sections describe parameters, notations and processes relevant to the gaseous environments investigated in this thesis.

2.1 Ionisation Parameter

A quantity known as the ionisation parameter is employed to characterise photoionised gas, both in absorption and emission. Within AGN studies, two types of ionisation parameter are commonly used for this purpose, U and ξ.

The first is:

$$U = \frac{1}{4\pi r^2 cn} \int_{\nu_0}^{\infty} \frac{L_\nu}{h\nu} \, \mathrm{d}v \tag{2.1}$$

where L_v is the luminosity of the source per unit frequency interval, r is the distance from the ionising source, n is the gas density and the integral is evaluated above the ionisation threshold of hydrogen ($\nu_0 = 13.6\,eV$) (Osterbrock and Ferland 2006; Costantini 2010).

The second is:

$$\xi = \frac{L}{nr^2} \tag{2.2}$$

where L is the ionising luminosity in the 1-1000 Ryd (13.6 eV - 13.6 keV) band, n is the gas density and r is the distance from the ionising source (Tarter et al. 1969).

These definitions imply that U is a dimensionless parameter, whereas ξ has units of $\mathrm{erg\,cm\,s^{-1}}$.

It is possible to convert between values of U and ξ for the same source, as long as the SED of that source is known; the luminosity values over the different energy ranges used in the definition of the two parameters must be consistently calculated from the same SED.

2.2 Electron Configuration Notation

To describe the configuration of electrons within any shell of an atom or ion, the following notation can be used:

$$nl^x \tag{2.3}$$

where n is the principal quantum number (the main energy level, or shell), l is the orbital angular momentum quantum number (describing the shape of the electron orbits) and x is the number of electrons in that subshell. The orbital angular momentum quantum number l is represented by s, p, d, f

(and then onwards in alphabetical order) for $l = 0$, 1, 2, 3 etc. These first four letters seem random, but were originally chosen to stand for *sharp*, *principal*, *diffuse* and *fundamental* as they were associated with different groups of lines observed in the spectra of alkali metals. The total number of electrons allowed in each subshell (x) can be calculated by $2(2l + 1)$, giving a maximum of 2 electrons in s, 6 in p, 10 in d etc. Atoms (and ions) can be described using the full electron configuration, or simply by the final state of the outer subshell (in which case the inner subshells are assumed to be full).

To be more specific, an atom or ion can also be described using its overall energy state, representing the sum of all its electrons. In this case the notation is as follows:

$$^{2S+1}L_J \tag{2.4}$$

where:

- L is the total orbital angular momentum (represented by capital letters following the S, P, D, F sequence described above),
- S is the total spin,
- J is the total angular momentum (which ranges between $L + S$ and $|L - S|$).

For example, an ion with two electrons in the configuration $1s^1\,2p^1$ has $L = 1$, $S = 0, 1$, $J = 1$ (when $S = 0$), $J = 0, 1, 2$ (when $S = 1$), and therefore can have four different energy states: $^1P_1$ (when $S = 0$) or $^3P_0$, $^3P_1$ or $^3P_2$ (when $S = 1$).

Within this thesis this notation is used only to distinguish between different energy states in the important case of He-like triplet emission (see Section 2.6.1).

2.3 Spectroscopic Notation

Spectroscopic notation is slightly different to other notations used for ions. For historical reasons, the ground state of each element, known usually as X^0 (e.g. Fe^0 for iron), is referred to as X I (e.g. Fe I for iron). Therefore the first ionisation state of each element, or X^{1+}, is called X II (e.g. Fe^{1+} and Fe

II respectively). This continues through all ionisation states, so the number of electrons an ion has lost is $n - 1$, where n is the roman numeral after the element code in spectroscopic notation.

To complicate things further, X-ray spectroscopic notation is, for more historical reasons, different to that of other wavelengths (Osterbrock and Ferland 2006). In increasing energy order, these shells are: [X-ray notation (standard notation, where n is the principle quantum number describing the distance of the electron from the nucleus)] K ($n = 1$, the ground state), L ($n = 2$), M ($n = 3$). This notation will not be used substantially in this thesis, apart from references to the FeKα emission line, which represents electrons 'jumping' down to the hole left after removing a $1s$ electron from an ion of iron and the subsequent photon emitted to conserve energy. The exact energy of the FeKα emission line depends on the ionisation state of the iron ion; the higher the ionisation state, the higher the line energy (this is not a linear relationship, see Osterbrock and Ferland 2006). For example for Fe^{16+} the line energy is ∼6.4 keV, while for Fe^{20+} the line energy is ∼6.5 keV and for Fe^{23+} is ∼6.62 keV (Osterbrock and Ferland 2006).

2.4 Isoelectronic Sequences

An isoelectronic sequence is made up of a neutral atom and ions of different elements that have the same number of electrons. For example N VI, O VII, Ne IX and neutral helium all have two electrons, and are therefore all in the He-like isoelectronic sequence. Ions in the same isoelectronic sequence can be thought to be very similar as, because of their shared electron configuration, they produce similar spectra although at different energies.

The isoelectronic name can be used when describing electron transitions within ions. The transition names are made by combining two pieces of information: which isoelectronic sequence the ion is on, and which energy levels the electrons are transitioning between. If the electrons are transitioning between the n = 2 and n = 1 levels then the transition is called α, and if this is occuring in an He-like ion then the full name is Heα. If (in the same ion) the electrons are transitioning between the n = 3 and n = 1 levels, then the

transition is called Heβ, and so on through the Greek alphabet as the higher level of n increases.

When these transitions occur within H-like ions (those with one electron, like hydrogen) then, for historical reasons, these are called Lymanα (Lyα), Lymanβ (Lyβ) and so on.

2.5 Line Broadening

Spectral emission and absorption lines have a width related to various processes, both physical and instrumental. For an example of instrumental broadening, see Sect. 3.1.1. Three important physical processes are: 1) natural, 2) Doppler and 3) turbulent broadening.

Natural broadening is a result of the Uncertainty Principle, which dictates that any energy level within an atom or ion does not have a specifically defined energy, but instead a small range of possible energies. Therefore transitions of electrons between any two energy levels correspond not to one specific energy difference between those levels, but a small range of energy differences. This causes the line, whether emission or absorption, to have stronger wings and weaker peak than in a Gaussian profile, in fact presenting a Lorentzian (or natural) profile. This is a small broadening affect; for allowed transitions this may lead to a width of 10^{-6} Å.

Doppler broadening is caused by the velocity distribution of the atoms or ions involved in line emission (or absorption). Any gas at a given temperature T, where the velocity distribution is driven by collisions, will have a Maxwellian velocity distribution. Individual particles will have a range of energies (and therefore velocities) centered around the mean value of $(3/2)kT$. The higher the temperature, the greater the mean velocity and the greater the spread in velocities. When thinking about emission (or absorption) lines, the important velocity component is that in our line of sight, as this causes blue- or red-shifts in the observed spectrum. For particles of mass m at temperature T, the Doppler width (in terms of velocity v) of the observed line corresponds to (see e.g. Kutner, Marc. L 2003):

$$v = \left(\frac{3kT}{m}\right)^{\frac{1}{2}} \tag{2.5}$$

which can be converted into wavelength units using the relation (valid for small v):

$$\frac{v}{c} = \frac{\Delta\lambda}{\lambda} \tag{2.6}$$

For example, an oxygen ion at 10^6K would have $v = 40\,\mathrm{km\ s^{-1}}$, corresponding to a broadening of $0.003\,\text{Å}$ at $22.1\,\text{Å}$ (the rest wavelength of the O VII forbbidden line).

The same effect can occur on a much larger scale when bulk gas motions cause a large range of velocities in our line of sight, for example when gas is orbiting an object such as an AGN.

Turbulent broadening is defined to be the combination of other effects which broaden emission and absorption lines. As a physical process for this combination is not well defined, it is often represented by a Gaussian function. This can therefore be combined with the Gaussian function used for Doppler broadening (as the combination of two Gaussians is another Gaussian) to give a function which combines both Doppler and turbulent broadening. In this case the width of both Doppler and turbulent broadening (in terms of velocity $v_{dopp+turb}$) is represented as: $v^2_{dopp+turb} = v^2_{dopp} + v^2_{turb}$

2.6 Distinguishing Photoionised and Collisional gas

2.6.1 He-like Triplets

Ions within the He-like isoelectronic sequence have intense emission lines corresponding to transitions between the $n = 2$ shell and $n = 1$ ground state (see Fig. 2.1). They take the form of triplets, composed of the resonance, forbidden and intercombination lines:

- The resonance line (r or W): 1s 2p ^{1}P$_1$ - 1s^2 ^{1}S$_0$
- The intercombination line (i), made up of two individual transitions:
  - X: 1s 2p ^{3}P$_2$ - 1s^2 ^{1}S$_0$
  - Y: 1s 2p ^{3}P$_1$ - 1s^2 ^{1}S$_0$
- The forbidden line (f or Z): 1s 2s ^{3}S$_1$ - 1s^2 ^{1}S$_0$

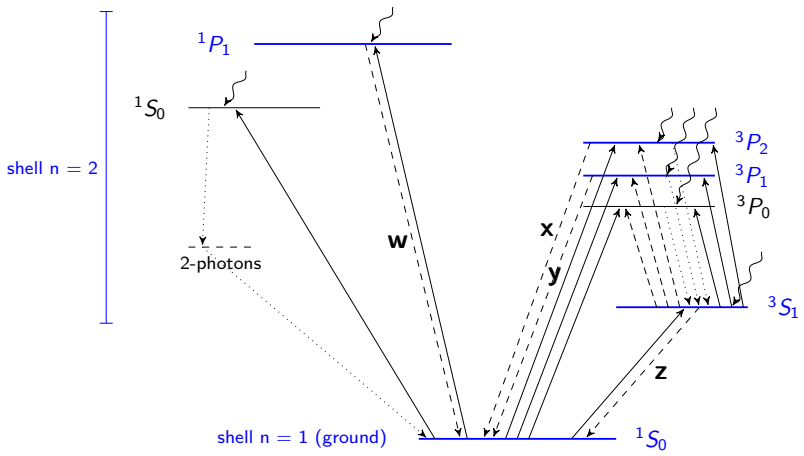

Fig. 2.1: Simplified Grotrian diagram for He-like ions. The ground state is at the base of the diagram, with increasing energy upwards. The main levels involved in the He-like triplet transitions are coloured in blue. W (or r), X, Y (or i) and Z (or f) are the resonance, intercombination and forbidden lines, respectively. *Upward arrows* correspond to the electron collisional excitation transitions (solid) and to the photo-excitation from 2^3S_1 to $2^3P_{0,1,2}$ levels (dashed). *Downward arrows* correspond to the radiative transitions (including 2-photon continuum from the 2^1S_0 to the ground level) (dotted) and recombination (radiative and dielectronic) plus cascade processes (dashed). The *curly arrows* represent electrons recombining to that level of the ion. Adapted from Porquet and Dubau (2000).

The name of 'forbidden' for transitions such as the last one mentioned above is not strictly true; while these transitions do not fulfill the selection criteria of quantum mechanics, there is a small probability of them occuring spontaneously. In low density environments (below the critical density of that ion, for example a few $\times 10^9$ cm^{-3} for O VII; Porquet et al. 2010) it is very unlikely for that state to decay in another way (e.g. collisionally), so forbidden lines of high intensity can be observed.

The different types of transitions associated with the He-like triplet and their dependency on different processes enable us to use the ratios between fluxes of these lines as a diagnostic. The standard ratios used are:

$$R(n_e) = \frac{Z}{X+Y} \tag{2.7}$$

$$G(T_e) = \frac{Z+(X+Y)}{W} \tag{2.8}$$

These ratios were developed for use with collisional (solar coronal, optically thin) gas (Gabriel and Jordan 1969), but have also been investigated in relation to photoionised gas (Porquet et al. 2010). In a photoionised gas the dominant process is recombination, which favours the populations of the $^3P_{0,1,2}$ and $^3S_1$ levels and therefore increases the intensity of the intercombination and forbidden lines. When the value of G is above 4, the forbidden and intercombination lines are enhanced relative to the resonance line, and this can indicate that the gas is predominantly photoionised (Porquet and Dubau 2000). For G to be used, Porter and Ferland (2007) show that the column density of the emitting gas must be constrained first, as the value of G can change over two orders of magnitude as the column density changes from $10^{17}\,\mathrm{cm}^{-2}$ to $10^{24}\,\mathrm{cm}^{-2}$ (see Fig. 2.2).

The density sensitivity (value of R) occurs because the $^3S_1$ level can be collisionally excited to the ^3P levels. When the electron density is high (above the critical density), this process removes electrons from the $^3S_1$ level without the radiative decay of the forbidden line being able to occur. Therefore the ratio R reduces above the critical density (see Fig. 2.3). This is not the only way R can be affected; the $^3S_1$ level can also be photoexcited to the ^3P

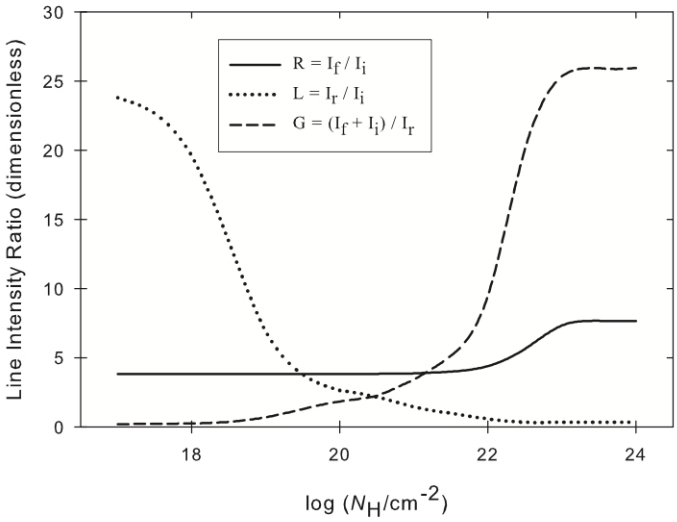

Fig. 2.2: Variation of the He-like triplet ratios at different column densities for a pure photoionised gas. From Porter and Ferland (2007).

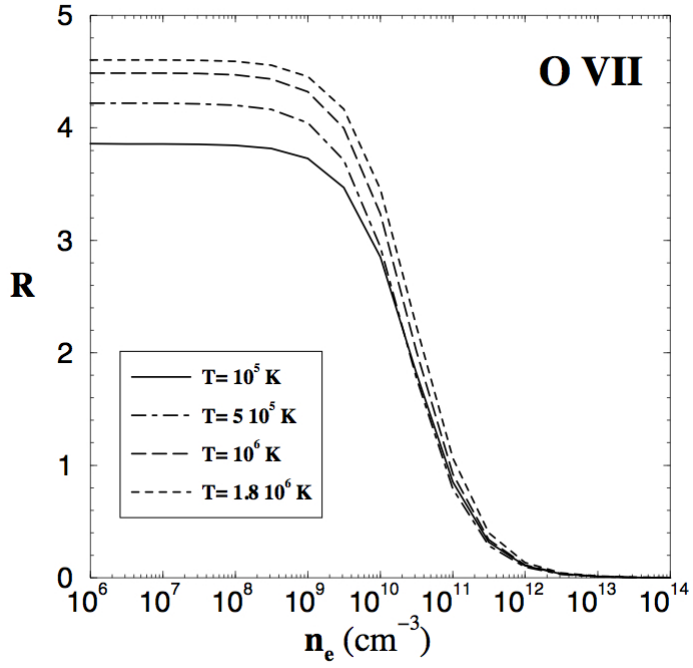

Fig. 2.3: Behaviour of the R ratio at different densities and temperatures for a pure photoionised gas. From Porquet and Dubau (2000).

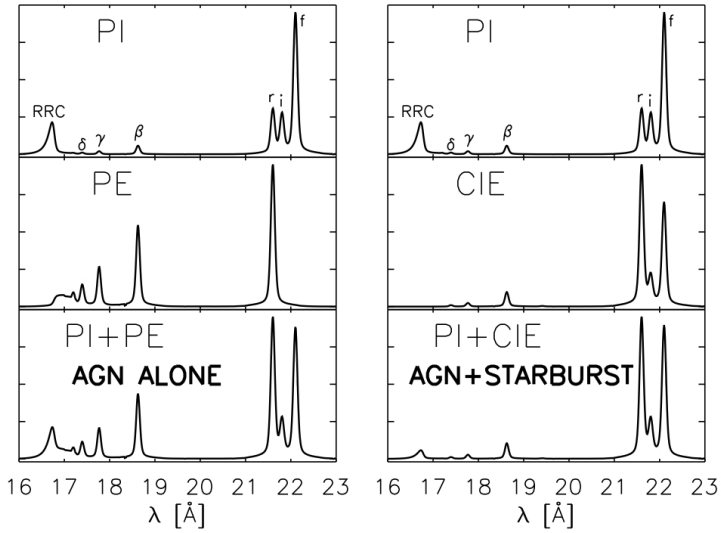

Fig. 2.4: Figure from Kinkhabwala et al. (2002), showing the difference in the O VII series between entirely photoionised (PI) emission, photoexcitation (PE) and collisionally ionised (CIE) emission, and hybid gas with multiple components.

levels if incident UV intensity is high enough at the relevant energies for those transitions. This suppresses the forbidden line, enhances the intercombination lines and mimics a high electron density (Porter and Ferland 2007).

The bottom two panels of Figure 2.4 show that these triplet ratios can sometimes be ambiguous when comparing between photoionisation plus photoexcitation and photoionisation plus collisionally ionised gas. The relative strength of RRC features (see Section 2.6.3) and higher order lines can distinguish between these two scenarios.

2.6.2 Dielectronic Recombination

Dielectronic recombination (DR) is shown in Fig. 2.5 as a two stage atomic process. The first stage is a free electron being 'caught' into a highly excited state within an ion, and while doing so exciting an existing electron of that ion into another excited state. This is (usually) an unstable configuration, therefore one electron (most often the inner of the two excited states) falls back to the ground level to increase stability (this is shown in the second stage of Fig. 2.5). The presence of the outer excited electron slightly alters the energy of this stabilising transition, causing 'satellite' emission lines to surround the normal energy of that particular emission line in the spectrum. The multiple

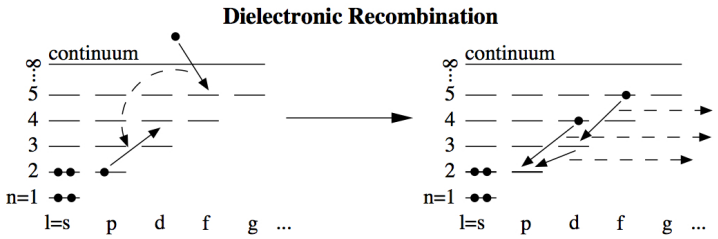

Fig. 2.5: Highly simplified Grotrian diagram showing the two-step process of dielectronic recombination. In the first stage a free electron is 'caught' and an inner electron is excited, and in the second stage both these electrons fall to lower energy levels, releasing photons. Adapted from Kinkhabwala et al. (2003).

Table 2.1: Rest wavelengths for the He-like oxygen triplet and important surrounding DR satellite lines. From Audard et al. (2001).

Line type	Rest wavelength ($\AA$)
O VII r	21.60
DR satellite line	21.63
DR satellite line	21.70
O VII i	21.80
DR satellite line	22.02
O VII f	22.10
DR satellite line	22.11

satellite lines arise because of the multiple possibilities for the position of the outer excited electron. The final part of dielectronic recombination is the outer electron radiatively decaying to the ground state (also shown within stage two in Fig. 2.5).

The strength of the DR satellite lines has a steep temperature sensitivity (Audard et al. 2001), and they are expected to be significant in collisional gas and negligible for the temperatures expected of photoionised gas (Porquet et al. 2010). Therefore the presence of DR satellite lines can also give an indication of whether the gas contains any collisional components. As an example, Table 2.1 shows the rest wavelengths of the O VII triplet lines and surrounding DR satellite lines.

2.6.3 Radiative Recombination Continua

Radiative recombination continuum (RRC) features are generated when free electrons directly recombine into the bound state of an ion. The free electrons can have a range of energies therefore the RRC features are asymmetrical, extending in energy above the ionisation threshold, and can be very broad. The width of these features gives a direct measurement of the energy of the electrons and therefore of the temperature of the gas. Broad (narrow) RRCs indicate a large (small) range of electron energies, and therefore are observed from high (low) temperature gas.

The edge energies (E) of all the RRC features and the temperatures (ΔE) can be compared in a ratio $\Delta E/E$ to separate photoionised and collisional gas. A ratio $\Delta E/E << 1$ is evidence for dominating photoionised conditions.

2.7 Resonance Scattering

When an ion is radiatively excited (it absorbs a photon, and enters an excited state), it is possible that the ion will de-excite afterwards by emitting a photon of the same energy as was absorbed. This process is called resonance scattering and the subsequent photon can be emitted in any direction, therefore is likely to be travelling in a different direction compared to the initial photon.

Resonance scattering preferentially affects transitions with the highest probability of occurring, as these transitions more readily lead to absorption. For example, the resonance line has higher probability of being absorbed than the forbidden or intercombination lines within the same He-like triplets (e.g. for the O VII r line, the transition probablility is $3.467 \times 10^{12}\,\mathrm{s}^{-1}$, leading to a timescale of $2.88 \times 10^{-13}\,\mathrm{s}$; Porquet and Dubau 2000), therefore the resonance lines are more greatly affected by resonance scattering (as also indicated by the name of this effect!).

Depending on the geometry of the observed emitting gas, resonance scattering can increase or decrease the observed strength of the resonance lines, therefore values of the He-like triplet diagnostic G and R ratios (explained in Sect. 2.6.1) are not always reliable. Other spectral diagnostics, for example the width of radiative recombination continuum features (see Sect. 2.6.3),

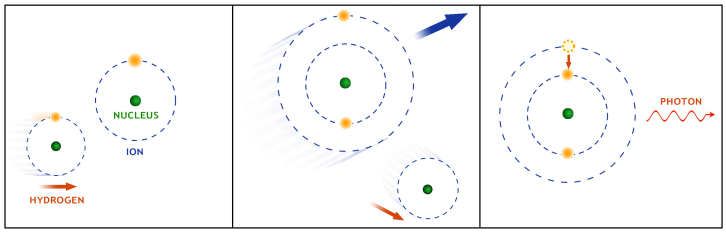

Fig. 2.6: Illustration of charge exchange. Credit: NASA/CXC/M.Weiss

should be used to confirm dominant conditions in the emitting gas.

2.8 Charge Exchange

Charge exchange emission is caused by the transfer of electrons from neutral atoms (or molecules) to ions (Fig. 2.6). The neutral atom and the ion collide with each other, with the ion usually carrying more speed into the collision. The energy levels of both species are distorted as they collide, and energy levels from both can overlap so that an electron from the neutral atom can be transferred to the ion without releasing radiation. If the ion is highly charged the electron it receives is captured into a high energy level, and it then decays back to the ground state, releasing an X-ray photon as it does so. This can also happen between ions, but the electrostatic repulsion between the two nuclei in that case causes the cross-section to be very small (Wargelin et al. 2008).

Charge exchange has been observed to produce X-rays within our Solar System, for example where the Solar Wind interacts with cometary comae, and the Earth's magnetosphere, and in Jupiter's aurorae (Dennerl 2010), but recently evidence is building that this mechanism may be important in star formation regions as well (Liu and Mao 2015; Wang and Liu 2012).

Charge exchange can be distinguished from collisionally ionised and photoionised emission using a variety of features. The He-like triplet line ratios produced by charge exchange are easily distinguishable from those produced from collisionally ionised gas as the forbidden line is strong relative to the intercombination and resonance lines, giving a high G ratio (see Sect. 2.6.1, and for a discussion of this ratio relative to charge exchange see Dennerl et al. 2006). RRC features (see Sect. 2.6.3) are not produced from charge exchange

because free electrons are not involved in charge exchange processes, therefore the presence of narrow, asymmetrical RRC features distinguishes photoionised emission from charge exchange.

Chapter 3

X-ray Observatory Satellites

"I wanted to see what no one had yet observed"

Jules Verne

As the Earth's atmosphere absorbs X-ray light before it reaches the ground, all X-ray observations of cosmic sources must be made from space. The first satellite launched for the sole purpose of X-ray astronomical observations was NASA's Uhuru, in 1970. The UK's first involvement in cosmic X-ray observations came with Copernicus, launched in 1972, which carried X-ray instruments alongside the main UV telescope.

In the four and a half decades since the early 1970s, great progress has been made in both X-ray imaging and spectroscopic observational capabilities, with high spatial resolution mirrors, CCD imaging with good energy resolution, and high-resolution grating spectrometers on the current generation of X-ray satellites.

The focus of this thesis is on analysis of data from one of these high-resolution spectrometers, the Reflection Grating Spectrometer (RGS) onboard the European Space Agency's (ESA) *XMM-Newton* observatory. The remainder of this chapter contains details of this satellite, the RGS instrument in particular, and finally describes plans for new X-ray observatories moving into the 2020s and beyond.

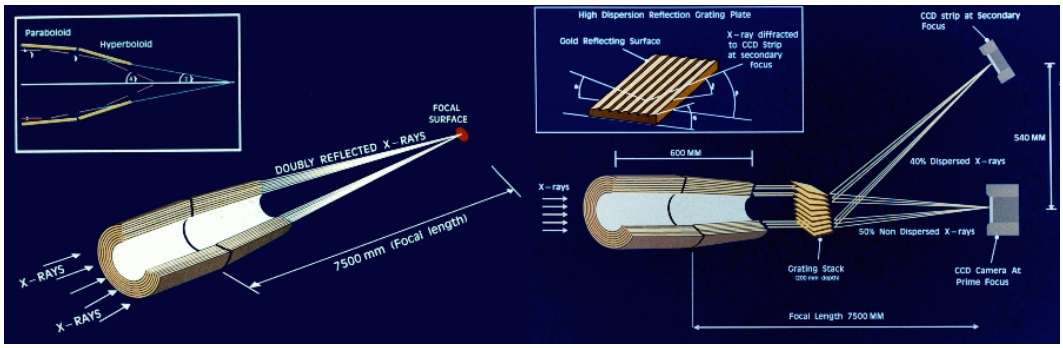

Fig. 3.1: Simplified schematic of the light paths through one of the *XMM-Newton* mirror arrays. The left diagram shows the light paths for the telescope with the EPIC-pn camera, and the right diagram shows the equivalent for the telescopes associated with both EPIC-MOS and RGS instruments. Lengths are not to scale. Image copyright: ESA

3.1 *XMM-Newton*

ESA's 10 m long and 3.8 tonnes *X-ray Multi-Mirror* mission, the second mission of ESA's cornerstone Horizon 2000 programme, was launched on an Ariane 5 rocket on 10 December 1999. After launch it was renamed *XMM-Newton*, in honour of Isaac Newton, one of Europe's most famous and influential scientists.

The orbit of *XMM-Newton* is highly eccentric, with an initial perigee and Southern apogee of 7 000 km and 114 000 km respectively. The orbital parameters evolve over the mission, for example, the perigee altitude has varied between 7 000 km and 28 000 km, while the apogee altitude has varied between 114 000 km and 100 000 km.

For roughly 8 hours of the 48 hour period, *XMM-Newton* is below the minimum observing altitude (46 000 km), therefore observations are possible for about 40 hours of each orbit. This minimum observing altitude is set to protect the instruments from radiation background damage during passage through the radiation belts around Earth.

XMM-Newton carries one optical-UV (Optical Monitor; OM) and three X-ray telescopes. The three X-ray telescopes focus light towards the three European Photon Imaging Cameras (EPIC) and the Reflection Grating Spectrometer (RGS). The RGS instrument is described in more detail below, in Sect. 3.1.1.

The X-ray telescopes are grazing-incidence Wolter Type-I, each com-

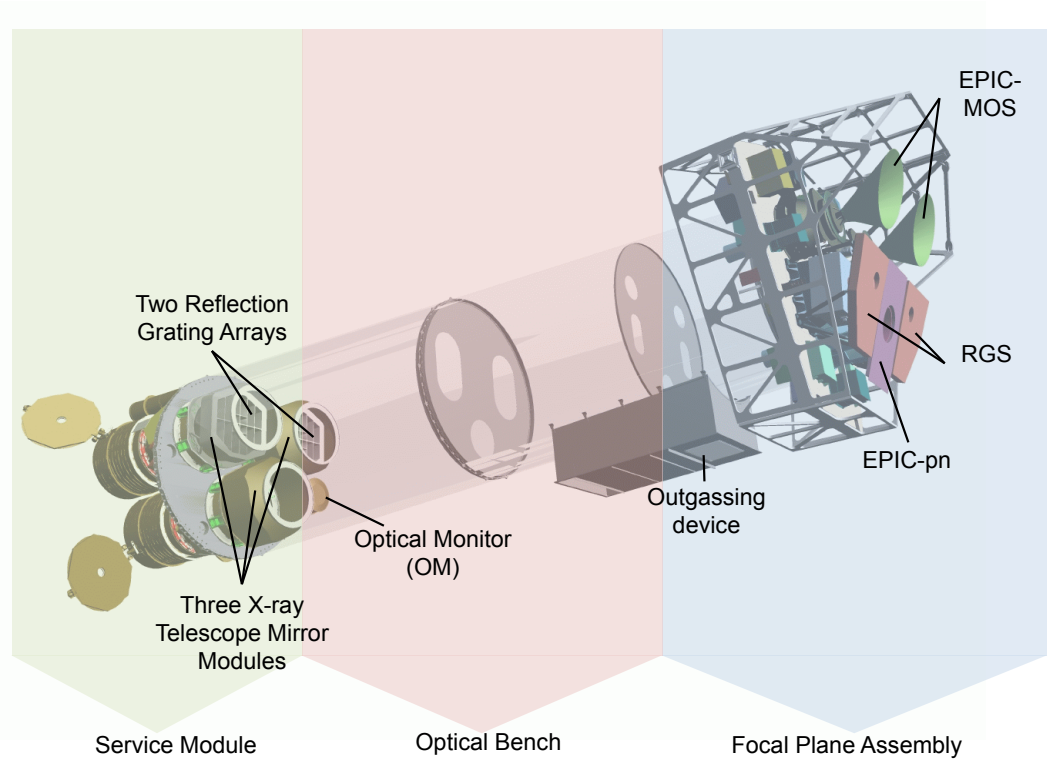

Fig. 3.2: Open view of the main parts of XMM-Newton, for details see text. Image courtesy of Dornier Satellitensysteme GmbH and ESA with additional labels and coloured bands.

posed of 58 gold-coated mirrors nested in a coaxial and confocal configuration (Jansen et al. 2001), therefore all the mirrors within one telescope are mounted on the same axis and have the same focus. The telescope focal length is 7.5 m, with a outer mirror diameter of 70 cm. A simplified diagram of the light paths through the *XMM-Newton* telescopes is shown in Fig. 3.1.

The mirror arrays are located within the Service Module at one end of a long (6.8 m) carbon fibre tube, which is the telescope optical bench, and at the other end the Focal Plane Assembly is located, mounted on which are the RGS and EPIC cameras and associated radiators. The Service Module also incorporates the OM, star trackers, and most of the spacecraft sub-systems (Jansen et al. 2001). All aspects of the spacecraft mentioned so far can be seen in Fig. 3.2. The solar-array wings, Telescope Sun Shield and antennas are attached to the outer part of the Service Module.

The EPIC instrument incorporates three CCD arrays, two of which are made from Metal Oxide Semiconductor and so are referred to as the EPIC-

Table 3.1: Key performance parameters for *XMM-Newton* RGS. From den Herder et al. (2001)

Parameter	Performance
Wavelength range (first order)	6-38 Å
Resolution (line separation) $\lambda/\Delta\lambda$(FWHM)	100-500
Resolution (weak line detection) $\lambda/\Delta\lambda$(HEW)	100-800
Peak effective area (A_{eff})	140 cm^2
Wavelength accuracy ($\delta\lambda$)	8 mÅ

MOS cameras (Turner et al. 2001), and the third uses implanted p-n junction semiconductor technology so is therefore referred to as EPIC-pn (Strüder et al. 2001). The RGS gratings are installed behind two of the three X-ray telescopes, directing about half the focused flux towards the two RGS cameras; the remaining flux from these two telescopes is directed towards the EPIC-MOS cameras. EPIC-pn has an unobstructed view of the entire flux from the third X-ray telescope. The EPIC cameras operate in photon counting mode, and produce simultaneous imaging and non-dispersive spectroscopy using the CCD detectors' intrinsic energy resolution. Over a field of view of 30 arcmin and an energy range 0.15-12 keV, EPIC gives moderate spectral ($E/\Delta E \sim 20 - 50$) and angular resolution (on-axis full width half maximum: FWHM $\sim$ 6 arcsec and half energy width: HEW $\sim$ 15 arcsec, set by the telescope, and a little dependent on energy).

The Optical Monitor (OM; Mason et al. 2001) is an optical-UV telescope, co-aligned with the X-ray telescopes, and the first to be flown on an X-ray satellite. OM incorporates a filter wheel so the user can choose between six broadband filters (V, B, U, UVW1, UVM2, UVW2) for photometry, a white light filter, a UV or an optical grism (a grating-prism combination) for low resolution spectroscopy or a magnifier lens for higher spatial resolution (3800-6500 Å). The final filter wheel position is blanked off and can serve as a shutter.

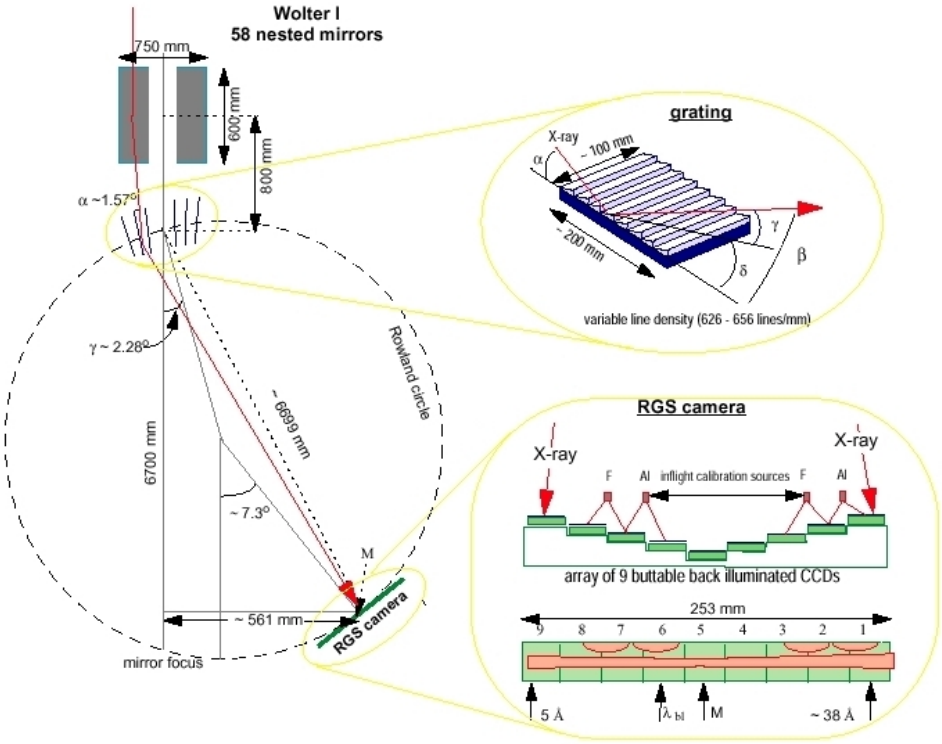

Fig. 3.3: Schematic layout of RGS, from Brinkman et al. (1998)

3.1.1 Reflection Grating Spectrometer

The Reflection Grating Spectrometer (RGS; den Herder et al. 2001) operates in the wavelength range 5-38 Å, with a spectral resolution ($\lambda/\Delta\lambda$) of 100-500 (see Table 3.1). This wavelength range includes a large number of diagnostic spectral lines from hydrogen- and helium-like ions of C, N, O, Ne, Mg and Si. The RGS is made up of two spectrometer chains, intercepting X-ray photons from two of the three X-ray telescopes onboard *XMM-Newton*. Each one uses a Reflection Grating Array (RGA) to deflect and disperse around 53 % (ignoring obstruction by telescope structures) of the light towards one of the RGS focal plane cameras (RFCs). An RGA is a grating stack composed of 182 identical gratings, each 10 cm × 20 cm. The gratings are located on a toroidal surface along the Rowland circle (which also passes through the telescope main focus and the RGS first order blaze focus). This is shown in Fig. 3.3. The gratings are mounted at grazing incidence to the X-ray beam in the classical in-plane configuration, so the incident and diffracted X-rays are in a plane perpendicular to the grating grooves. The X-rays hit the grating at an angle

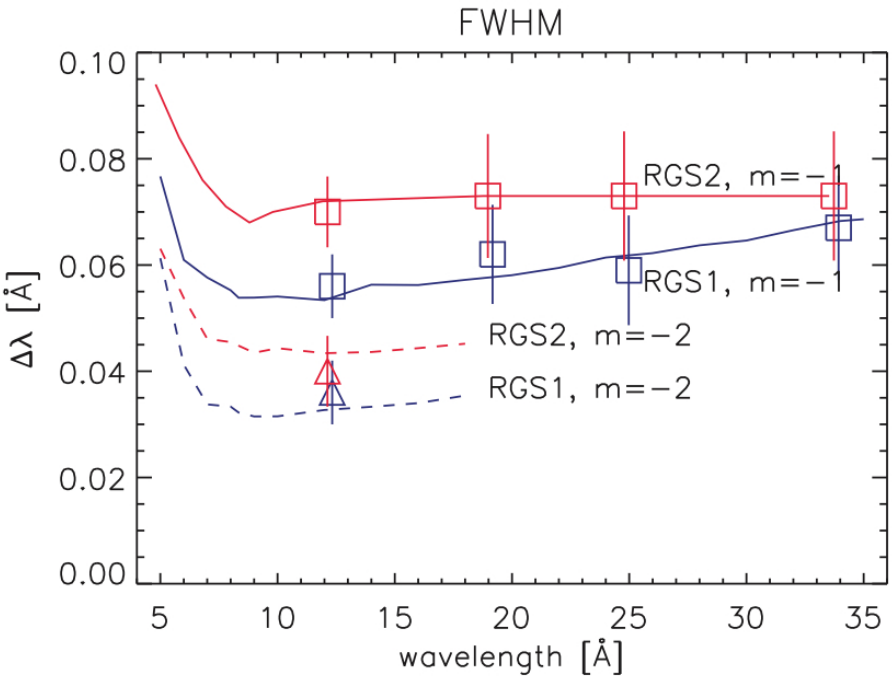

Fig. 3.4: Comparison of predicted and measured FWHM resolution for RGS. From den Herder et al. (2001).

α with respect to the plane of the grating, which has triangular grooves tilted at an angle δ with respect to that plane. The X-rays are dispersed towards the RGS camera at an angle β with respect to the grating plane (Fig. 3.3).

From the event position on the detector, the wavelength of the X-ray photon (λ) is calculated using the dispersion equation:

$$\cos\beta = \cos\alpha + \frac{m\lambda}{d} \tag{3.1}$$

where m is the spectral order (-1, -2,...), d is the groove spacing and α and β are the angles between the incoming ray and the grating plane or the outgoing ray and the grating plane respectively (ESA XMM-Newton SOC 2016). Note that $\beta = \gamma + \delta$, where γ and δ are shown in Fig. 3.3.

The spectral resolution of a reflection grating spectrometer is (see e.g. Porter, F. S. and Brown, G. V. and Cottam, J. 2005):

$$\Delta\lambda = \frac{d}{m}\sin\alpha\Delta\alpha \tag{3.2}$$

where $\Delta\alpha$ = the intrinsic angular resolution of the telescope. Therefore small angular resolution $\Delta\alpha$ and groove spacing d contribute to a high spectral

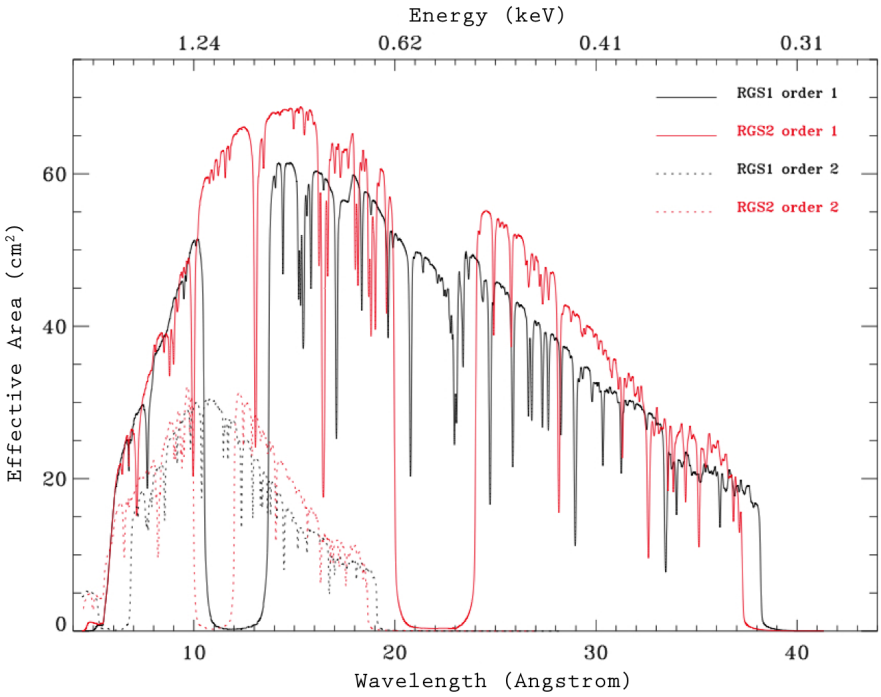

Fig. 3.5: The in-flight effective area for RGS1 in black and RGS2 in red. The gaps between the CCDs and the failing read-out of CCD7 in RGS1 and CCD4 in RGS2 are clearly visible, the narrow drops in the curves are due to corrections for cosmetic blemishes. From the July 2015 XMM-Newton Calibration Technical Note.

resolution. The FWHM spectral resolution for both RGS chains, first and second spectral orders, is shown in Fig. 3.4 (about 0.06 Å for the first order RGS1 spectra).

In addition, the spectral resolution for extended sources is affected by the extent of the source:

$$\Delta\lambda(ext) = 0.138\frac{\theta(ext)}{m} \tag{3.3}$$

where $\Delta\lambda(ext)$ is the resolution in Å for an extended source, and $\theta(ext)$ is the source extent in arcminutes (ESA XMM-Newton SOC 2016). For moderately extended sources RGS still has a superior spectral resolution to EPIC. For example, the 2' angular extent of 1E 0102.2-7219 (a supernova remnant in the Small Magellanic Cloud) gives a resolution ($\lambda/\Delta\lambda$) of 80 at 22 Å in first order.

The two RFCs each incorporate nine back illuminated CCDs, which operate in single photon counting mode, and are mounted in a row along the curvature of the Rowland circle (see Fig. 3.3). The CCDs are cooled to -110°C, reduced in November 2002 from the launch value of -80°C. This reduction in temperature decreases the dark current and the effect of charge transfer inefficiency (CTI) consequent to radiation damage on the energy resolution of the CCDs (de Vries et al. 2015). Cooling is achieved by a two-stage radiator, and three nested thermal shells, the first of which also contains four internal calibration sources (den Herder et al. 2001).

One CCD from each RFC failed shortly after launch, so in the 10.6-13.8 Å (RGS1) and 20.0-24.1 Å (RGS2) wavelength ranges the effective area is roughly half of the original. Unfortunately, the failed RGS2 CCD covers the wavelength range including the O VII He-like triplet for nearby objects. The redundancy built into RGS by having two chains means that this important spectral feature can still be measured, but the signal to noise is smaller than if both detectors were working. The interchip gap between adjacent CCDs is about 0.5 mm, corresponding to 85 mÅ and 45 mÅ at short and long wavelengths respectively. Both the failed CCDs and interchip gaps can be seen in the effective area plot, Fig. 3.5. The maximum effective area achievable when combining RGS1 and RGS2 first order spectra is 125 cm^{-2} at 15 Å, with a wavelength accuracy of 6 mÅ (July 2015 XMM-Newton Calibration Technical

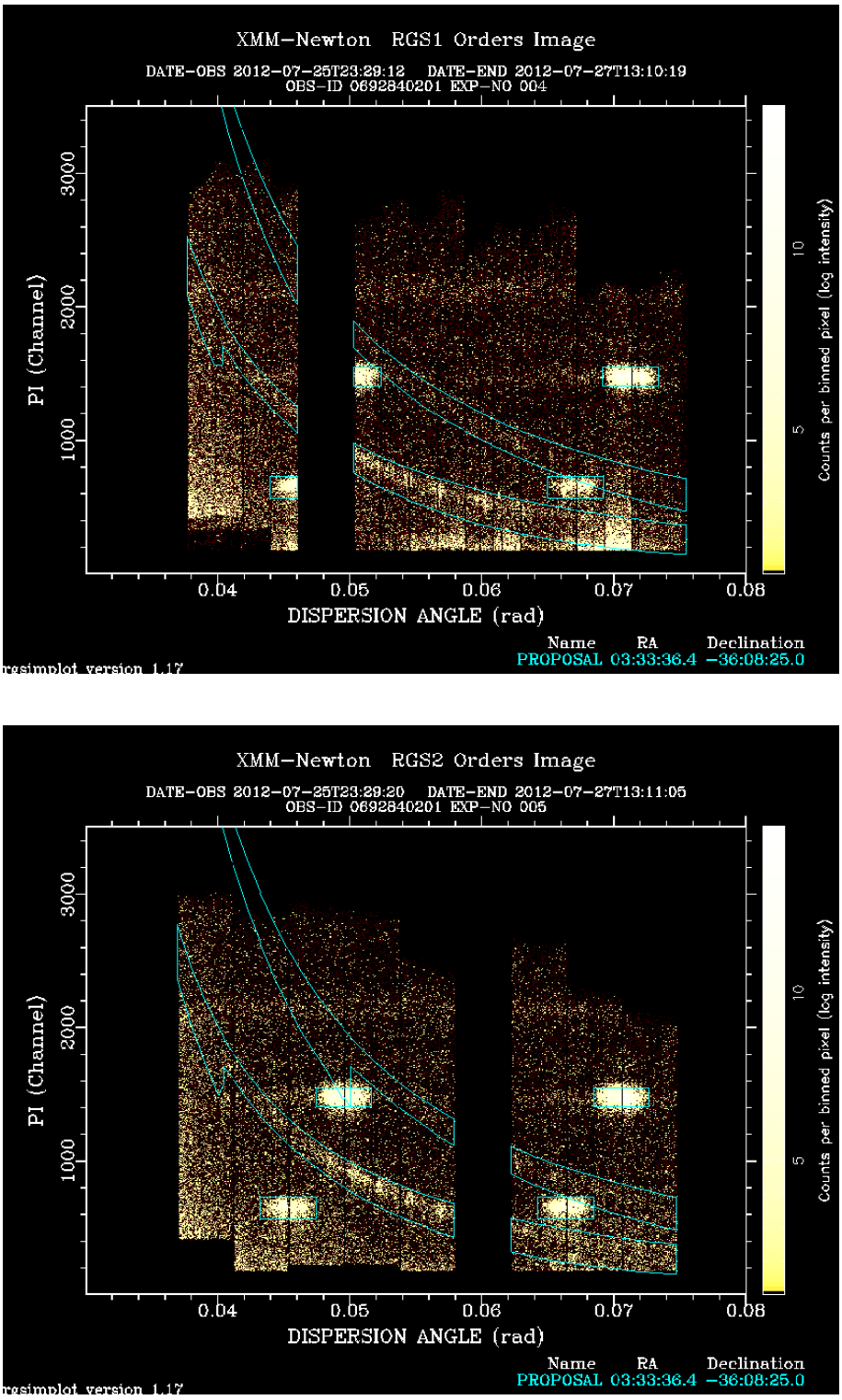

Fig. 3.6: The RGS1 and RGS2 'banana plots' from observation 0692840201 of NGC 1365. The X-ray events from first and second order spectra can be seen within the curved regions, the calibration sources show up as brighter rectangles and the failed CCDs as vertical black stripes.

Note).

The intrinsic energy resolution of the CCDs allows to separate the first and second order spectra from each other (den Herder et al. 2001), and from the calibration sources, as shown in Fig. 3.6 where for each X-ray photon the CCD energy channel is plotted against dispersion angle beta. These plots are known as 'banana plots' because of the curved shape of the first and second order spectra.

RGS has three operating modes for science data acquisition: Spectroscopy, Spectroscopy HCR and Small Window. The vast majority of data are acquired in Spectroscopy mode, in which all CCDs are read out every 4.8 s for RGS1 and every 9.6 s for RGS2. Only objects with expected high count rates need to be observed in either of the other two modes. The standard Spectroscopy mode simultaneously takes science data (which are processed on-board in order to select only true X-ray events for telemetry) and diagnostic images (one full CCD image of each RGS is telemetred every 1500 s). The latter is not done in Spectroscopy HCR (high count rate) mode so that bright sources can be observed without data loss. In Small Window mode only the central 32 of the 128 CCD rows in the cross dispersion direction are read out, allowing the effects of pile up in very bright sources to be mitigated. This is only relevant for roughly the 20 brightest X-ray sources (XMM-Newton Science Operations Centre Team 2014). Finally, there is a Multipointing Mode in which multiple exposures of the target are taken, each with the spacecraft pointing slightly offset so that important spectral features fall on different pixels of the detectors and out of the gaps between the CCDs. This reduces the effect of any pixel sized defects on the final (combined) spectrum (XMM-Newton Science Operations Centre Team 2014).

3.2 Future of X-ray Satellites

The future of X-ray astronomy is focused on ESA's future mission *ATHENA*, and the new observational possiblities it brings (see Sect. 3.2.1 below). Before that, the field will rely on the continuation of current observatories, and possibly on new missions such as:

- *Astro-H2*: After the loss of *Hitomi* (*Astro-H*; Takahashi et al. 2014) in 2016, JAXA and NASA are discussing[1] the financial and logistical aspects of building another telescope to recover the science aims from *Hitomi*. This would include a copy of the Soft X-ray Spectrometer (SXS) instrument enabling non-dispersive spectroscopy with spectral resolution comparable to RGS over 0.3-12 keV. Proposed launch date: 2020

- *Arcus*: This is a proposal for NASA's Midex call, using an *ATHENA* style telescope (silicon pore optics, with 12 m focal length) and a reflection grating style spectrometer to deliver a resolution 10 times better than RGS ($R \sim 3000$) over 8-50 Å and an effective area more than four times greater (>500 cm^2; Smith et al. 2016). Proposed launch date: 2023.

- *X-ray Surveyor*:[2] X-ray Surveyor is a large (strategic) mission concept identified in the 2013 NASA Astrophysics Roadmap. This is currently in a Mission Concept Study phase, which will likely be used to inform NASA's 2020 Decadal Survey (along with other studies). The concept of *X-ray Surveyor* is to have 50 times larger effective area than *Chandra* (which has 800 cm^{-2} at 0.25 keV), with similar angular resolution, a spectral resolution from gratings of 5000 in the soft X-ray range, and a much larger field of view than *Chandra*. This mission is in early stages of planning, so there is no proposed launch date yet.

3.2.1 *ATHENA*

Much of the information in this section is from the '*ATHENA* mission proposal' (Nandra et al. 2014).

ATHENA was chosen by ESA's Science Programme Committee (SPC) in June 2014 to be ESA's L2 mission (the second large class mission within its Cosmic Vision 2015-2025 programme), due to launch in 2028. Technology development and planning are already underway and construction will start in 2019, subject to review and final approval by the SPC that year.

The mission name is an acronym for "**A**dvanced **T**elescope for **H**igh-

[1] As quoted by spacenews.com, 21 July 2016

[2] http://wwwastro.msfc.nasa.gov/xrs/

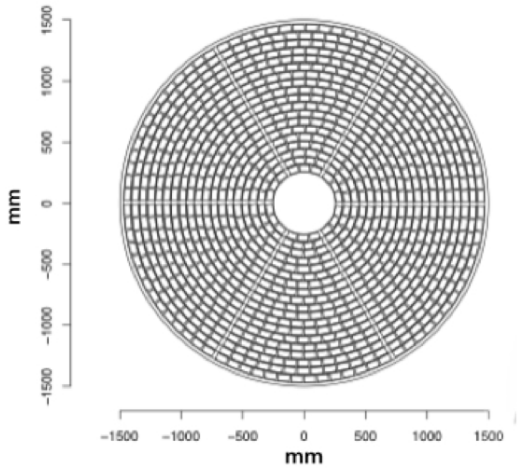

Fig. 3.7: Arrangement of *ATHENA* pores: modules are arranged in six sectors and nineteen rings are needed to populate the aperture. From Nandra et al. (2014).

ENergy **A**strophysics", as well as sharing the name of the Ancient Greek goddess of wisdom and daughter of Zeus.

The X-ray telescope is planned to have a 12 m focal length, and be made using silicon pore optics (SPO) technology, which enables a high collecting area to mass ratio (Willingale et al. 2013). In SPO, each 'pore' is effectively a small sector of a Wolter type-I telescope, where two reflections from the inner surfaces of the pore direct the X-rays to a common focus point. Overall there will be 19 rings of these pores, manufactured in six sectors (see Fig. 3.7). The baseline effective area is $2\,\mathrm{m}^2$ at 1 keV as originally proposed, although a possible descope to $1.4\,\mathrm{m}^2$ has been considered to reduce mission costs (by reducing the telescope diameter) (Athena Science Working Group 2.3, Feedback in Local AGN and Star Forming Galaxies 2015).

ATHENA will have two instruments, the X-ray Integral Field Unit (X-IFU) and the Wide Field Imager (WFI). The X-IFU will be an X-ray microcalorimeter spectrometer, capable of spatially resolved high-resolution spectroscopy over a limited field of view. As a calorimeter, it will detect the heat pulses generated by X-ray photons when they are absorbed by the detector. The temperature increase is proportional to the photon energy, and measured as the change in electrical resistance of the detector (den Herder et al. 2012). The X-IFU requirements (as of July 2016) are shown in Table 3.2 (from Bar-

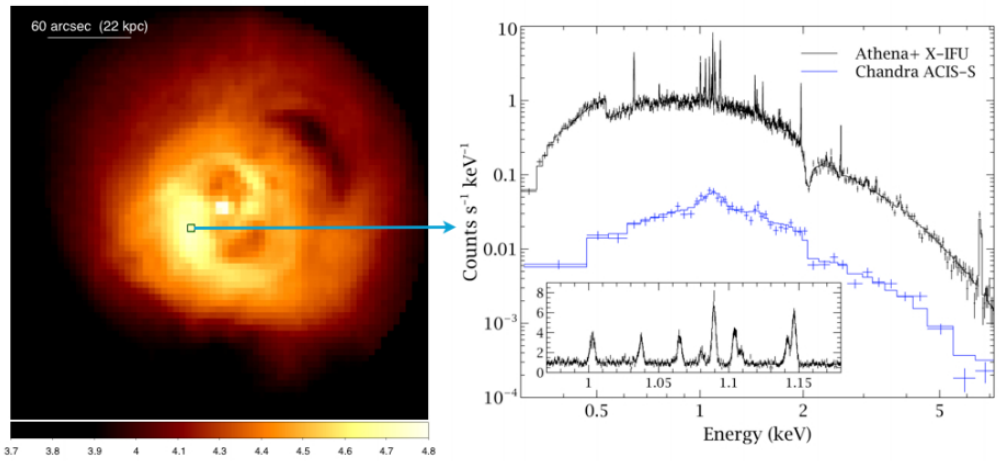

Fig. 3.8: Simulated *ATHENA* observations of the Perseus cluster, highlighting the advanced capabilities for revealing the intricacies of the physical mechanisms at play. The left panel shows a simulated 50 ks X-IFU observation ($0.5 - 7$ keV), displayed on a colour log scale. The spectrum on the right is from the single $5" \times 5"$ region marked by the box, with the existing *Chandra* ACIS spectrum for comparison. The inset shows the region around the iron L complex. This figure was originally published in Croston et al. (2013)

Table 3.2: Key performance requirements for the *ATHENA* X-IFU. TES stands for Transition Edge Sensors. From Barret et al. (2013)

Parameter	Requirements
Energy range	0.3-12 keV
Energy resolution: E $<$ 7 keV	2.5 eV ($240 \times 250\,\mu$m TES pixel)
Energy resolution: E $>$ 7 keV	E/ΔE = 2800
Field of View	5' (diameter) (3840 TES)
Detector quantum efficiency at 1 keV	$>$60 %
Detector quantum efficiency at 7 keV	$>$70 %
Time resolution	10 μs
Non X-ray background	$< 5\ 10^{-3}$ counts s^{-1} cm^{-2} keV^{-1}

ret et al. 2013) and as an example the simulated image and spectrum of the Perseus cluster of galaxies are shown in Fig. 3.8. The final details of the X-IFU may alter before launch (2028).

ATHENA was chosen to address the 'Hot and Energetic Universe' science theme, and therefore to answer two key astrophysical questions:

1. How does ordinary matter assemble into the large-scale structures we see today?

2. How do black holes grow and shape the Universe?

To answer the first question, *ATHENA* will map large scale hot gas structures throughout the Universe and track how they evolved as the Universe evolved. The second question is more relevant to the topics in this thesis, as it requires understanding the inflows and outflows of supermassive black holes as they grow over time.

Part of answering this second question is quantifying the energy contained in AGN outflows, and understanding how they interact with their host galaxy. *ATHENA*'s collecting area together with the high spectral resolution of the X-IFU will combine to give key insights into absorbing and emitting outflows within AGN.

Chapter 4

Data Reduction and Analysis Techniques

"Nothing ever happens like you imagine it will"

John Green

4.1 Data Reduction: RGS

The Observation Data Files (ODFs) for each RGS observation are processed with the Science Analysis Sytem (SAS) metatask *rgsproc* to produce background-subtracted spectra and response matrices for each spectral order (1st and 2nd) and each chain (RGS1 and RGS2). This therefore gives four source spectra per observation. The background-subtracted spectra still include information on the background level for each bin. High-background time intervals were filtered out by imposing a threshold of $0.15\,\mathrm{counts\,s^{-1}}$ on the lightcurve extracted from a background region of CCD-9, the CCD closest to the optical axis and therefore most affected by background flares.

Using the standard data reduction pipeline, SAS, it is possible to combine spectra from the same or both RGS chains (RGS1 and/or RGS2), over many observations, as long as they are all the same spectral order (1st or 2nd). It is not possible to combine all data from both detectors and both spectral orders over many observations.

The following data reduction section is based on work done by Jelle Kaastra, as an extension of Kaastra et al. (2011). The data used in Chapters 5 and

6 of this thesis were reduced following this method. This also allows combinations of spectra with different occurrences of bad pixels and from the multi-pointing mode (such as for the NGC 5548 campaign, described in Mehdipour et al. 2015).

While the data reduction process within Kaastra et al. (2011) allows both spectral orders and chains from RGS observations to be combined, the authors state that only χ^2 statistics may be used to analyse the spectra produced, as information on the background level is not carried through the process. This is because fluxed RGS spectra created by SAS do not include background information for each bin. Cash statistics (C-statistic) cannot be used correctly without this information and therefore is not appropriate for use on any spectra produced this way.

Individual spectra used in this thesis have low numbers of counts per bin (the average number of source and background counts per bin can be as low as 5), and therefore χ^2 is not the appropriate goodness-of-fit parameter. In order to use C-statistics the data reduction process had to be altered from that described in Kaastra et al. (2011), so the background and source count information is retained.

The spectra from the SAS are converted into SPEX (Kaastra et al. 1996) format using the auxiliary program *trafo*, then the first order spectra from both detectors are fitted together with a preliminary model using SPEX. This model only needs to empirically describe the data, it does not need to be physically motivated.

At this point the empirical model is used to convert all four spectra for that observation into fluxed spectra (in photons $\mathrm{s}^{-1}\,\mathrm{m}^{-2}\,\mathrm{\AA}^{-1}$, instead of the previous counts $\mathrm{s}^{-1}\,\mathrm{m}^{-2}\,\mathrm{\AA}^{-1}$, and including information on background). Then they can be combined, taking into account the detector and spectral order combinations. The second order spectra are weighted differently to the first orders, to reflect the greater signal to noise and number of counts in the first order spectra.

Now there is one spectrum for each observation, which can be combined with others to provide a stacked spectrum, using a process very similar to the

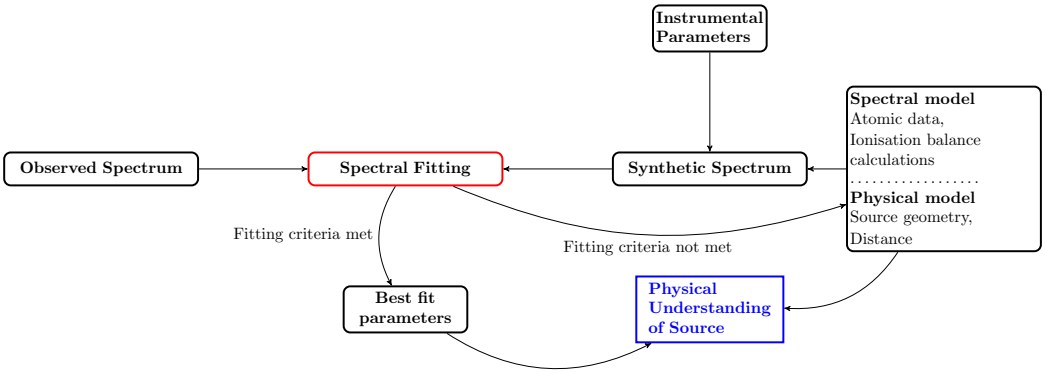

Fig. 4.1: Simple flowchart representing the main stages of spectral fitting. Adapted from the SPEX Reference Manual, version 3.

rgsfmat auxilary function in SPEX. This also creates the relevant response files for both the stacked and individual observations.

4.2 Spectral Fitting

When fitting astronomical spectra, the aim is to understand physical parameters of the source. This is done by comparing the expected spectrum, given a physical model convolved with an instrument response, with the observed spectrum. The instrument's response can alter the observed spectra in many ways, for example the continuum shape will depend on how the reflectivity of the mirror and efficiency of the detector vary over different energies (effective area), background components may be added (instrumental noise) and spectral lines may be blurred by the spectral resolution.

Figure 4.1 shows a simplified flowchart of the whole spectral fitting process (based on the SPEX manual). Important elements of the 'physical model', 'spectral model', 'instrumental parameters' and 'fitting criteria' are described within this thesis in Chapters 1, 2, 3 and below respectively.

4.2.1 Goodness of Fit Measures

χ^2 fitting is the default method to test how well a model fits to data within X-ray spectral packages. This method assumes that each bin contains enough counts that the underlying distribution of the difference between the expected and observed number of counts is Gaussian. This is fundamentally untrue when the number of counts in each bin is low (under 15: Humphrey et al.

2009) because then the underlying distribution is Poissonian, not Gaussian. When fitting with the χ^2 method, the function being evaluated is:

$$S = \sum_{i=1}^{N} \frac{(n_i - e_i)^2}{e_i} \tag{4.1}$$

where N = the number of bins, n_i = the observed number of counts in bin i and e_i = the expected (or modelled) number of counts in bin i. This allows us to minimise the *square* of the distances between the model and data (expected and observed).

The C-statistic (named after Webster Cash, who described this method in Cash 1979) is the equivalent function derived from an underlying Poisson distribution, giving:

$$C = -2 \sum_{i=1}^{N} (n_i \ln e_i - e_i - \ln n_i!) \tag{4.2}$$

which allows the minimisation of the *natural log* of the distances between the model and data (expected and observed).

In spectral fitting packages, this C-statistic equation is altered by approximating the $\ln n_i!$ term as $n_i \ln n_i + n_i$ (Sterling's approximation). As these modifications are to terms that only depend on the data, they do not alter the best fit parameters which minimise the C-statistic function. Finally the minus sign is brought inside the brackets, to help the reader, so the final function which is evaluated in spectral fitting packages (such as SPEX) is:

$$C = 2 \sum_{i=1}^{N} (-n_i \ln e_i + e_i - n_i + n_i \ln n_i) \tag{4.3}$$

At high counts (within bins) the Poisson distribution tends towards the Gaussian distribution, therefore the C-statistic is an appropriate method to use also in this regime.

When using C-statistic to fit models in SPEX, as well as the calculated C-statistic value, SPEX also gives the expected C-statistic value and its standard deviation (also called root mean square uncertainty, or r.m.s.) to help the user determine the goodness-of-fit (see SPEX manual).

The mean, or expected, C-statistic (C_e) for each bin is calculated by:

1. Taking the observed number of counts per bin as the expected value (n) of a Poisson distributed variable

2. Calculating the C-statistic for a certain number of counts in that bin (k): $2(n - k + k \ln k - k \ln n)$

3. Weighting this by the probability of that number of counts, i.e. multiplying by the probability of k given the Poisson distribution is centered on n ($P_k(n)$)

4. Summing over every possible value of k (0 to ∞)

The equation used to calculate this is then:

$$C_e = 2 \sum_{k=0}^{\infty} P_k(n)(n - k + k \ln k - k \ln n) \tag{4.4}$$

This can be summed over all bins to give the overall expected C-statistic for the spectrum.

The variance of the expected C-statistic for each bin (C_v) is calculated by using the Poisson distribution outcome that:

$$\text{r.m.s}^2 = \text{variance} = \bar{m^2} - \bar{m}^2 \tag{4.5}$$

which states that the variance (which equals r.m.s.^{2}) can be calculated by taking the square of the mean value of m ($\bar{m}^2$) away from the mean value of the square of m ($\bar{m^2}$), if m is the measured value in a Poisson distribution, and $\bar{m}$ is the average (mean) m over many observations.

The expected C-statistic per bin, C_e, as calculated above is $\bar{m}$, and similarly $\bar{m^2}$ is:

$$\bar{m^2} = 4 \sum_{k=0}^{\infty} P_k(n)(n - k + k \ln k - k \ln n)^2 \tag{4.6}$$

Therefore C_v is $\bar{m^2} - C_e^2$.

Humphrey et al. (2009) demonstrate that in multiple situations, including when fitting physical models to X-ray spectral data, the C-statistic is a less biased estimator than χ^2, even at high numbers of counts per bin.

Humphrey et al. (2009) defined a value they called 'fractional bias', f_b:

$$f_b = \frac{\text{bias}}{\text{statistical error}} = \frac{p_{obs} - p_{real}}{\text{standard deviation of } p_{obs}} \tag{4.7}$$

where p_{obs} and p_{real} are the observed and real values of the interesting parameter.

They simulated an X-ray emitting, collisional gas for 1000 different combinations of temperature, metal abundance and total counts in the spectrum. The simulated spectra were regrouped to ensure at least 20 photons per bin, and then the authors proceeded to use both χ^2 and C-statistic to fit the data, trying to recover the correct gas temperature. The results show that even in this nominal χ^2 regime, the χ^2 derived gas temperatures had a $|f_b|$ of 0.5-1 when the total counts in the spectrum were above 10^4. The C-statistic derived gas temperatures consistently have $|f_b| \ll 0.2$, and in this case $|f_b|$ is not a function of the total number of counts in the spectrum, making C-statistics a less biased estimator to use than χ^2 for at least this class of problem.

The high spectral resolution of RGS ($\lambda/\Delta\lambda \sim 340$ at 22 Å; den Herder et al. 2001) compared to lower resolution X-ray spectrometers leads to more detailed models being needed to fully describe the data. Knowledge of many aspects of these models is not yet complete (for example presence of additional astrophysical components in the line of sight towards the source and imperfect atomic data) as well as the continued existence of imperfect instrumental calibration, systematic effects and statistical fluctuations, so there will necessarily be differences between the data and the best physical model that can be found. As discussed in Blustin et al. (2002), the use of goodness-of-fit statistics when modelling RGS data must be coupled with careful consideration of the physical meaning of the models, as physical self-consistency is more important than reaching a nominally "acceptable" goodness-of-fit value.

4.2.2 SPEX

All spectral fitting in this thesis has been done using SPEX (versions 2.6-3.0, stated where necessary). The name SPEX stands for **SPE**ctral **X**-ray, and refers to a software package for modelling and analysing both X-ray and UV spectra. SPEX includes a number of physical models of X-ray and UV emitting and absorbing gas, including more than a million spectral lines from 30 elements (H to Zn).

The standard abundances used in SPEX, and for all the work in this thesis,

are those published by Lodders et al. (2009). These are proto-Solar abundances because they were measured from carbonaceous meteorites rather than the Solar photosphere, therefore avoiding abundance changes since the beginning of our Solar System from both nucleosynthesis and settlement within the Sun.

The main SPEX models used for the work in this thesis are:

- *hot*: a collisional ionisation equilibrium absorption model which mimicks the absorption of a neutral gas when set to a low electron temperature. This is used to model the Galactic absorption column density in the relevant line of sight by setting the correct column density value and a temperature of 0.5 eV.

- *reds*: a redshift model. If a photon is emitted at energy E, this model shifts it to energy $(1 + z)E$, where z is the redshift value.

- *pow*: a power law model. This model can also be used to fit a broken power law, but the only parameters varied in this thesis are the slope and normalisation of a single, unbroken power law.

- *xabs*: a photoionised absorption model, where all ionic column densities are linked through a photoionisation model represented by the ionisation parameter ξ. The column density, velocity, covering factor and abundances can also be varied.

- *cie*: a collisionally ionised emission model. The emission is calculated for collisional ionisation equilibrium at a given gas temperature, by first calculating the ionisation balance and then the X-ray spectrum. The abundances of the gas can also be varied.

- *gaus*: a Gaussian emission line model. The normalisation, energy (or wavelength) and width of the line can be varied. The width parameter is the full width half maximum (FWHM), which relates to the Gaussian width σ by FWHM $= 2.3548\sigma$.

- *vgau*: a Gaussian velocity broadening model, which can be applied to any emission models. Characterised by the Gaussian sigma value in km s^{-1}.

- *rrc*: a simplified model to calculate radiative recombination continua features. The emission measures of each ion are fitted separately, without connecting them via an ionisation balance.

- *file*: a model read from a user input. The filename for the input and normalisation of this model are the only variables. Within this thesis, this model was used to fit CLOUDY simulated spectra to data within SPEX.

4.3 CLOUDY

CLOUDY is a microphysics code, designed to simulate physical conditions within photoionised clouds. To do this it simultaneously solves equations of statistical and thermal equilibrium, ionisation-neutralisation balance and heating-cooling processes to model the ionisation, chemical and thermal state of material within those clouds. This section, describing how CLOUDY works, uses information from the code's documentation (the Quickstart guide, and Hazy 1 and 2) and website[1]. CLOUDY was last described in academic literature by Ferland et al. (2013).

Given an input, CLOUDY will output the predicted emission-line spectrum. This output spectrum is over the range 100MeV (gamma-rays) - 10m (radio) and the calculations are valid within a temperature range of 2.7 K (CMB) - 10^{10} K. The upper limit to the temperature range is caused by the effects of electrons travelling at relativistic speeds at temperatures above this limit. There is no low density limit to these calculations, although they become computationally demanding below 100 cm^{-3}. At high densities the Saha-Boltzmann equation is recovered as local thermodynamic equilibrium (LTE) is reached.

The input must describe three items, simply summarised as: i) the amount of energy hitting the cloud, ii) what the cloud is made from and iii) the geometry of the cloud. These three items are more accurately described as: i) the shape (SED) and intensity of the external radiation field striking a cloud, ii) the chemical composition and grain content of the gas, and iii) the geometry

[1] www.nublado.org

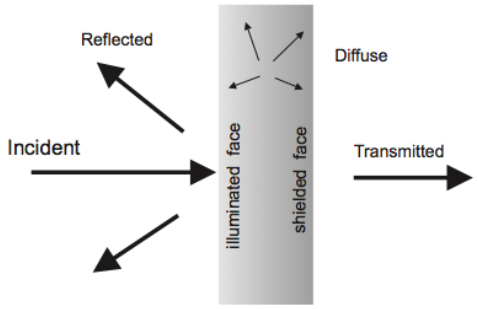

Fig. 4.2: Illustration of radiation fields used or computed by CLOUDY. From Hazy 1 (Cloudy Documentation)

of the gas, including cloud radius limits and dependence of density on radius. The intensity can be defined in multiple ways, for the work in this thesis it has been specified by the ionisation parameter of the illuminated face of the cloud.

CLOUDY makes two main assumptions for its calculations: energy is conserved over the entire wavelength range, and atomic processes have reached a steady state. The first assumption means that any energy absorbed by the cloud will be re-emitted by an appropriate process, therefore may be re-emitted in a different wavelength band. The second assumption is only valid if the cloud has existed longer than the longest timescale for atomic processes within that cloud. This can be checked as, within the CLOUDY output, the longest timescale for relevant atomic processes is given. This should be compared with the observed timescale of variation of the cloud.

The photoionised cloud is then divided into a set of thin concentric shells, called zones. The calculations begin at the illuminated face of the cloud, and once they have reached the end of the cloud the whole process is iterated so that the zones are thin enough for the physical conditions across each of them to be approximated as constant. Typically 100-200 zones are computed in a cloud.

There are numerous possible outputs from CLOUDY because, depending on the geometry of the system, the user may want to model emission in different directions.

Several different radiation fields are computed during these calculations; these are shown in Fig. 4.2. The incident radiation field is specified by the input, and is the radiation field striking the illuminated face of the cloud. The diffuse radiation field is emitted by gas and grains within the cloud and consists mainly of emission lines.

In terms of emission from the cloud, there are two directional components: reflected and transmitted. The reflected emission is from the illuminated face of the cloud (illuminated by the source), travelling back towards the source. The transmitted emission is the emission from the shielded face of the cloud and travels outwards (away from the source).

Each computed CLOUDY reflected spectrum includes diffuse emission from within the cloud and scattered (absorbed and re-emitted) radiation from the intrinsic continuum, therefore it includes only narrow emission lines and a scattered continuum. The transmitted spectrum is computed as total emission in that direction, therefore includes the attenuated incident radiation as well as diffuse emission from the cloud. These components are also output directly from CLOUDY as separate spectra.

After completing the relevant work in this thesis it was discovered (through the Cloudy Yahoo Discussion Group; Topic 2624) that the ionisation parameter ξ value used by CLOUDY v.13.03 is defined over a different energy range (13.6 eV to the high energy limit of the code) compared to the one used in the X-ray literature (13.6 eV - 13.6 keV). Applying another form of the ionisation parameter (U) that CLOUDY uses I converted it into the usual 'X-ray literature ξ' and found that the CLOUDY values are systematically 0.2 higher (in log ξ) than the standard formulation used in X-ray literature (for the main SED used in this thesis). This discrepancy between the two formulations of ξ will be resolved in later versions of CLOUDY, as the next version of CLOUDY will be made to match the standard X-ray literature. The values currently quoted in this thesis are the 'CLOUDY ξ values', for ease of comparison to any other work based on CLOUDY version 13.03 or previous.

One implication of this discrepancy is that previous work comparing AGN warm absorber phases in the X-ray and UV regimes may benefit from being

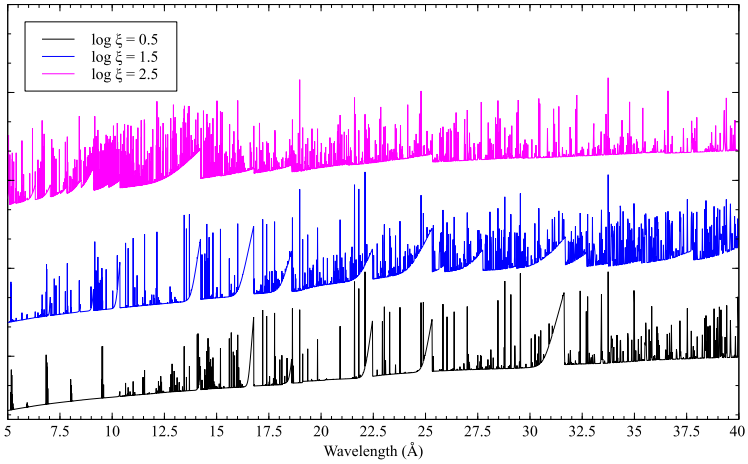

Fig. 4.3: Example reflected outputs from CLOUDY with different ionisations. The different ionisation outputs are offset from each other along the y-axis (shown in log format, not linear) for viewing purposes.

revisited, if CLOUDY was used to calculate ξ values for gas at only one of these energies.

4.3.1 Using CLOUDY Spectra within SPEX

CLOUDY calculates the spectrum for each of its output options over a grid of input values. The modelling and spectral fitting work in Chapters 5 and 6 uses a parameter range of $\log \xi = 0.1$-3.3 (17 steps of 0.2), hydrogen column density $= 10^{21}$-$10^{24}\,\mathrm{cm}^{-2}$ (13 steps of $10^{0.25}$) and turbulent velocity $= 10^{1}$-$10^{3.5}\,\mathrm{km\ s}^{-1}$ (six steps of $10^{0.5}$). This gives ($13 \times 17 \times 6$) 1326 simulated spectra in total. Example output from CLOUDY are shown in Figure 4.3

These are output from CLOUDY as XSPEC *table* models, which can then be converted into SPEX *file* models[2]. These spectra can then be compared with the data one by one, using an automated fitting process. For the work in this thesis, the automated fitting process is run using PYTHON. Throughout this process there is no interpolation applied between the CLOUDY generated spectra.

[2]This step will be superfluous in future, as with SPEX v.3.02.00 onwards it is possible to read in and use XSPEC *table* models directly

Chapter 5

NGC 5548: X-ray Narrow Emission Lines (2013-14)

"The more you learn, the more you realize how little you know.
Still, the struggle itself is worthwhile"
Joe Abercrombie

5.1 NGC 5548 - Observational History

NGC 5548 is a well studied, nearby ($z = 0.017175$) AGN historically showing typical Seyfert 1 behaviour, with strong broad emission lines and a small number of narrow emission lines across its optical, UV and X-ray spectra (e.g. Korista et al. (1995), Peterson et al. (1994), Chiang et al. (2000) and Kaastra et al. (2000)).

NGC 5548 is included in Carl K. Seyfert's first work discussing "extra-galactic nebulae with high excitation nuclear emission lines" (Seyfert 1943); not as one of the 6 focussed on, but mentioned as another 'known' nebula of that proposed type. Since then this object has continued to reveal new AGN science over a series of observations and campaigns.

Branduardi-Raymont (1989) found, from *EXOSAT* data, a consistent soft-excess component in the X-ray band, present at all times except when the source was weakest. Correlated spectral variability was also seen over X-ray, UV and optical observations. NGC 5548 then became the first 'AGN watch' target, where a co-ordinated campaign of optical and UV observations

over eight months allowed reverberation mapping of the BLR to be feasible, showing evidence for ionisation stratification of this region (see Peterson (1993) and references therein).

More recently, with the advances in X-ray spectroscopy from *Chandra* and *XMM-Newton*, NGC 5548 was the first Seyfert 1 galaxy to be observed using high-resolution (E / ΔE $\sim$ 100-500) spectroscopy in the soft X-ray band. These data showed the presence of narrow X-ray absorption lines in AGN spectra for the first time (Kaastra et al. 2000). This also allowed details such as Doppler shifts and line broadening to be detected for the first time, showing that these X-ray narrow absorption lines are produced by ionised outflowing material, referred to as warm absorbers. Evidence for warm absorber signatures have been found in roughly half of observed Seyfert galaxies (Blustin et al. 2005). In particular, NGC 5548's warm absorbers show evidence of long-term stability in ionisation and kinematics (Steenbrugge et al. 2005).

More recent optical and UV observations of NGC 5548 have continued to produce new results; dynamical modelling based on reverberation mapping data from 2008 has given the most detailed picture of the geometry of the BLR, estimating a distance of $\sim$2-5 light days from the central source and an observed inclination angle of $\sim 32^o$ (Pancoast et al. 2013).

5.1.1 2013-2014 Multi-Wavelength Campaign: Main Result

Between June 2013 and February 2014, a multi-wavelength monitoring campaign targeted NGC 5548, using six space and two ground based observatories (*XMM-Newton*, *Chandra*, *HST*, *NuSTAR*, *Swift*, *INTEGRAL*, *Wise Observatory*, Israel (*WO*) and *Observatorio Cerro Armazones* (*OCA*)). The timeline of this campaign is shown in Fig. 5.1, the observation log in Table 5.1 and details of each instrument's data reduction is presented in Mehdipour et al. (2015).

As shown in Fig. 5.2 the soft X-ray flux in the first 2013 observation was 25 times weaker than the typical median in grating observations taken by Chandra in 2002. This suppression of the soft X-ray spectrum continued throughout all 14 XMM-Newton observations within the campaign.

The 2013 hard X-ray flux (above 10keV) shows a characteristic powerlaw

Table 5.1: Observation log for the NGC 5548 campaign. For the *Swift*, OCA and WO monitorings, the Obs. numbers correspond to days in which observations were taken. The *Swift* lengths in ks are the total length of the observations in each year.

			Start time (UTC)		Length				Start time (UTC)		Length
Observatory	Obs.	ID	yyyy-mm-dd	hh:mm	(ks)	Observatory	Obs.	ID	yyyy-mm-dd	hh:mm	(ks)
XMM-Newton	1	0720110301	2013-06-22	03:53	50.5	HST COS	1	lc7001	2013-06-22	13:25	13.0
XMM-Newton	2	0720110401	2013-06-29	23:50	55.5	HST COS	2	lc7002	2013-07-12	02:23	14.2
XMM-Newton	3	0720110501	2013-07-07	23:28	50.9	HST COS	3	lc7003	2013-07-24	16:43	8.9
XMM-Newton	4	0720110601	2013-07-11	23:11	55.5	HST COS	4	lc7004	2013-07-30	15:15	16.0
XMM-Newton	5	0720110701	2013-07-15	22:56	55.5	HST COS	5	lc7005	2013-08-01	03:21	12.3
XMM-Newton	6	0720110801	2013-07-19	22:40	56.5	HST COS	6	lc7006	2013-12-20	02:49	13.0
XMM-Newton	7	0720110901	2013-07-21	22:32	55.5	*NuSTAR*	1	60002044002	2013-07-11	09:50	51.6
XMM-Newton	8	0720111001	2013-07-23	22:24	55.5			60002044003	2013-07-12	00:10	52.2
XMM-Newton	9	0720111101	2013-07-25	22:15	55.5	*NuSTAR*	2	60002044005	2013-07-23	14:25	97.2
XMM-Newton	10	0720111201	2013-07-27	22:06	55.5	*NuSTAR*	3	60002044006	2013-09-10	21:25	97.5
XMM-Newton	11	0720111301	2013-07-29	21:58	50.4	*NuSTAR*	4	60002044008	2013-12-20	08:30	98.1
XMM-Newton	12	0720111401	2013-07-31	21:49	55.5	*Chandra*	1	16369	2013-09-01	00:01	29.7
XMM-Newton	13	0720111501	2013-12-20	14:01	55.3	*Chandra*	2	16368	2013-09-02	10:33	67.5
XMM-Newton	14	0720111601	2014-02-04	09:33	55.5	*Chandra*	3	16314	2013-09-10	08:17	122.0
INTEGRAL	1	10700010001	2013-06-29	21:34	100.0	*Swift* (2013) [a]	1–160	[b]	2013-01-04	00:24	326.6
INTEGRAL	2	10700010002	2013-07-11	21:13	102.0	*Swift* (2014) [c]	161–291	[d]	2014-01-02	14:53	182.5
INTEGRAL	3	10700010003	2013-07-15	23:31	106.5	OCA [e]	1–27	-	2013-05-20	03:17	[e]
INTEGRAL	4	10700010004	2013-07-23	03:54	128.9	WO (2013) [f]	1–93	-	2013-06-02	07:22	[f]
INTEGRAL	5	11200110003	2014-02-09	10:00	38.2	WO (2014) [g]	94–150	-	2013-12-16	14:38	[g]

[a]The *Swift* monitoring in 2013 ended on 2013-12-31 18:19.

[b]The *Swift* target IDs of NGC 5548 in 2013: 30022, 80131, 91404, 91711, 91737, 91739, 91744, 91964.

[c]The *Swift* monitoring up to 2014-07-01 00:00 is reported here. The *Swift* monitoring of NGC 5548 is currently ongoing in 2014–2015.

[d]The *Swift* target IDs of NGC 5548 in 2014: 30022, 33204, 91964.

[e]The OCA monitoring ended on 2013-07-25 01:13. Observations taken in the B, V, R filters, with 150 s exposure in each filter.

[f]The WO monitoring ended on 2013-09-24 04:59. Observations taken in the B, V, R, I filters, with 300 s exposure in each filter.

[g]The WO monitoring ended on 2014-04-14 08:25. Observations taken in the B, V, R, I filters, with 300 s exposure in each filter.

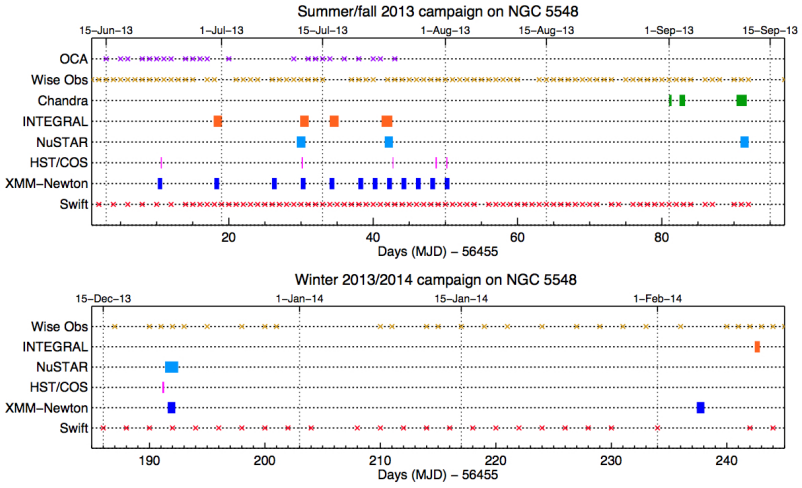

Fig. 5.1: Timeline of the 2013-2014 multi-wavelength campaign on NGC 5548 undertaken by Kaastra et al. (2014). The thickness of each rectangular symbol on the time axis is indicative of the length of that observation. The days in which Swift, Wise observatory and OCA made observations are indicated by crosses. From Mehdipour et al. (2015)

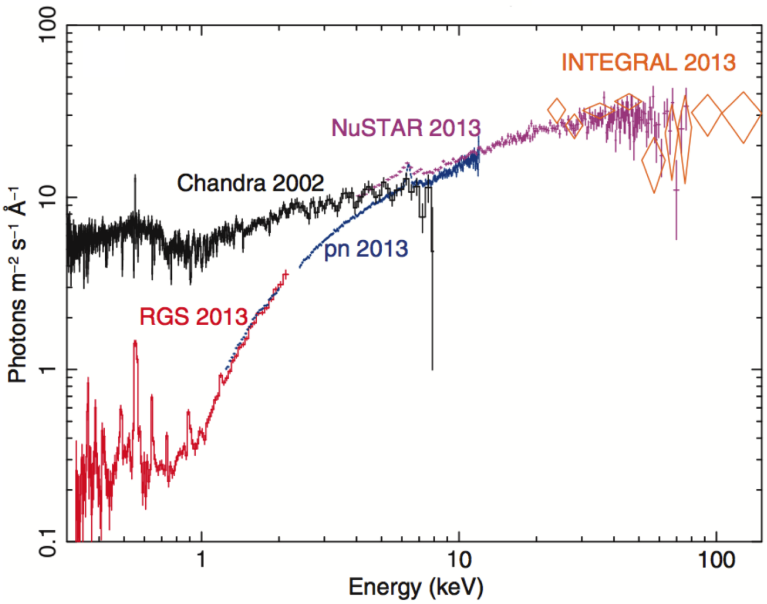

Fig. 5.2: The heavily obscured X-ray spectrum during summer 2013. The unobscured Chandra LETGS spectrum taken in 2002 is shown for comparison. The 2013 spectrum is obtained from 12 *XMM-Newton*, two *NuSTAR*, and four INTEGRAL observations. 'pn' stands for *XMM-Newton* EPIC-pn. From Kaastra et al. (2014)

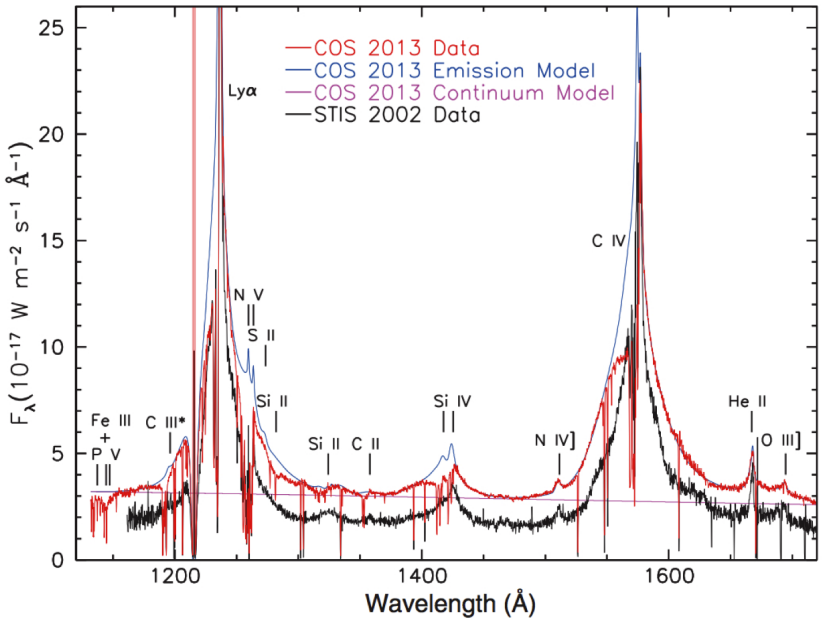

Fig. 5.3: Averaged 2013 HST COS spectrum in F_λ as a function of wavelength compared with the 2002 STIS spectrum, showing the broad UV absorption lines in 2013. From Kaastra et al. (2014)

shape, consistent with the median flux level of the 2002 Chandra observation. Below 10 keV the spectrum is cut off, and reaches a very hard effective photon index, before flattening again below 1 keV. In this flattened range there are clear narrow emission lines and radiative recombination continua from photoionised gas. The intensity of the strongest emission line, the O VII forbidden line, appears only slightly below its 2002 intensity.

Kaastra et al. (2014) conclude that obscuring material is absorbing the soft X-ray continuum. This obscuring material must be inside the X-ray narrow line region because the narrow emission features are not suppressed compared to historical data.

Six of the 14 XMM-Newton observations were taken simultaneously with UV spectra from the Hubble Cosmic Origins Spectrograph (COS).

These UV observations show many narrow absorption lines at the same velocities as previously known warm absorber components (see Fig. 5.3), but from gas with a lower ionisation. This shows that the warm absorber is now being irradiated by a less ionising flux from the central source.

The UV spectra also show broad, blue-shifted absorption troughs at ion-

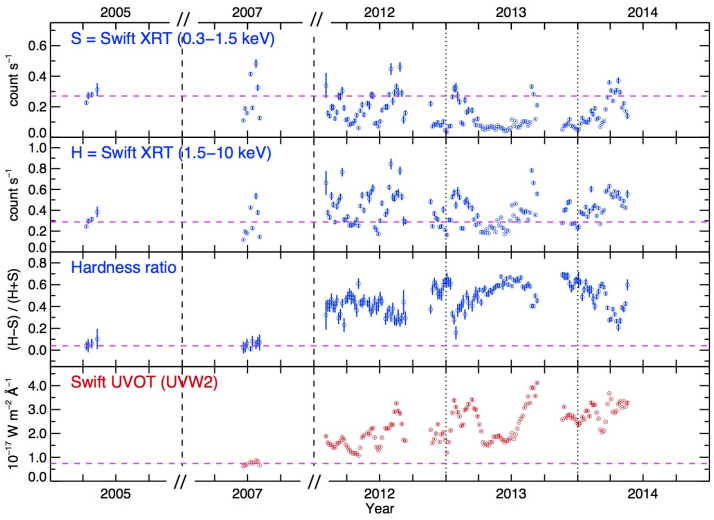

Fig. 5.4: X-ray and UV light curves of NGC 5548 obtained with Swift between 2005 and 2014. Vertical lines separate the five years shown here. Horizontal dashed lines show the average flux or hardness ratio measured with Swift during 2005 and 2007 in an unobscured and optically low state. The data have been averaged over five days. Error bars are ±1 SD. From the supplementary material to Kaastra et al. (2014)

isation levels similar to those needed to explain the X-ray obscuration. The strength of these individual absorption features is correlated with the strength of the X-ray obscuration, indicating that this UV absorption and the X-ray obscuration are effects of the same gas.

The new obscuration lowers the ionization of the previously known warm absorber components. This lower ionisation also means the warm absorber components will become more opaque to X-rays, therefore Kaastra et al. (2014) modelled the new 2013-14 warm absorber parameters as well as modelling the obscurer parameters.

With the new 2013-14 warm absorber model, two obscuring components were needed to properly fit the spectrum. Two obscuring components are required, rather than just one, because of constraints from the unobscured high-energy NuSTAR data, showing the importance of a multi-satellite campaign to the analysis of these results.

Lightcurve data from *Swift* give an indication of when this obscuration

began. The hardness ratio can be an indicator of absorption, and is defined as $(HS)/(H + S)$ with H and S the count rates in the 1.5-10 and 0.3-1.5 keV bands, respectively. As absorption increases, the observed soft X-ray flux level decreases while the observed hard X-ray flux level remains reasonably constant, causing the hardness ratio to increase. By comparing the hardness ratio of a source with that in its 'normal' state, the level of absorption can be estimated.

Looking at the *Swift* data from 2005 and 2007 in Fig. 5.4, the hardness ratio is at a 'normal' value, shown by the horizontal dashed lines. The higher hardness ratio during 2012-14, despite the hard X-ray flux staying consistent with previous measurements, indicates that the obscuration of the soft X-ray flux was ongoing over this period.

As the obscuration reduces the ionisation level of the warm absorber outflows, the obscuring material must be closer to the source than these outflows are, giving an upper limit to the distance of $\sim 10^{17}$ m. The obscurer partially covers the broad UV emission lines, therefore it is further out than the UV broad line region, giving a lower limit to the distance of $\sim 10^{14}$ m. The velocities observed in the UV absorption (strongest at -1000 km s^{-1}, but extending out to -5000 km s^{-1}) also support a location just outside the broad line region (Kaastra et al. 2014).

5.2 NGC 5548: X-ray Narrow Emission Lines (2013-14)

The following work in this chapter is based on Whewell et al. (2015).

As presented above and in Kaastra et al. (2014), NGC 5548 has recently undergone a drastic change in its observed spectrum, with the soft X-ray flux 25 times lower than the typical median in observations taken by *Chandra* in 2002 (when last observed with a high-resolution spectrometer). Kaastra et al. (2014) conclude this is due to the presence of a new "obscurer" located closer to the source than the classical warm absorbers (WA) and narrow-line region (NLR). Using *Swift* observations, the authors conclude that the "obscurer" must have entered the line of sight between 2007 and 2011. This "obscurer" directly causes the additional absorption in the soft X-ray band and the broad

absorption features in the UV. The classical WAs known in this source (in both X-ray and UV) are shielded from the ionising UV/X-ray radiation by the "obscurer" so are now at lower ionisations than their historical values. The 2013-14 ionisation parameters derived for each component of the X-ray WAs are shown in Table 5.2.

The view of the soft X-ray band (0.1-2 keV) during this obscuration event has revealed a rich emission spectrum dominated by narrow emission lines and radiative recombination continuum (RRC) features, never previously observed this clearly in NGC 5548.

This work is part of a series of investigations exploring different aspects of the 2013-14 observational campaign (summerised by Mehdipour et al. 2015). Here I focus on the revealed soft X-ray narrow emission lines and RRC features, as they are excellent probes of the physical characteristics of the emitting region.

In the remainder of this chapter I first detail the observations used for this work (Sect. 5.3) and data analysis techniques (Sect. 5.4), including the He-like triplet diagnostics (Sect. 5.4.3). The overall best fit spectrum is presented in Sect. 5.4.4. I then build a consistent photoionisation model using CLOUDY (Sect. 5.5). The physical implications of the analysis are discussed in Sect. 5.6. Finally, the conclusions of this work are summarised in Sect. 5.7.

5.3 Observations

The data used for this chapter were taken as part of a large multi-wavelength campaign aimed at characterising in detail the WA in NGC 5548; the structure, data reduction techniques used and other results of this campaign are explained in Kaastra et al. (2014); Mehdipour et al. (2015); Arav et al. (2015); Ursini et al. (2015); Di Gesu et al. (2015); Ebrero et al. (2016); Mehdipour et al. (2016) and Cappi et al. (2016). All spectra shown in this chapter are in the observed frame.

The redshift value $z = 0.017175$ has been used for this work, determined from the 21 cm hydrogen line (de Vaucouleurs et al. 1991), as given in the NASA/IPAC Extragalactic Database (NED), which is slightly different to

Table 5.2: Parameters of the 2013-14 warm absorber components (WA comp.) from Kaastra et al. (2014)

WA comp.	$\log \xi$ (10^{-9} Wm)	N_H (10^{20} cm^{-2})	v (km s^{-1})	σ_v (km s^{-1})	WA comp.	$\log \xi$ (10^{-9} Wm)	N_H (10^{20} cm^{-2})	v (km s^{-1})	σ_v (km s^{-1})
A	0.33	2.0±0.6	−588±34	210±40	D	1.91	10.7±11.6	−254±25	68±14
B	1.06	7.0±0.9	−547±31	61±15	E	2.48	28±8	−792±25	24±12
C	1.70	15±3	−1148±20	19±6	F	2.67	57±17	−1221±25	34±13

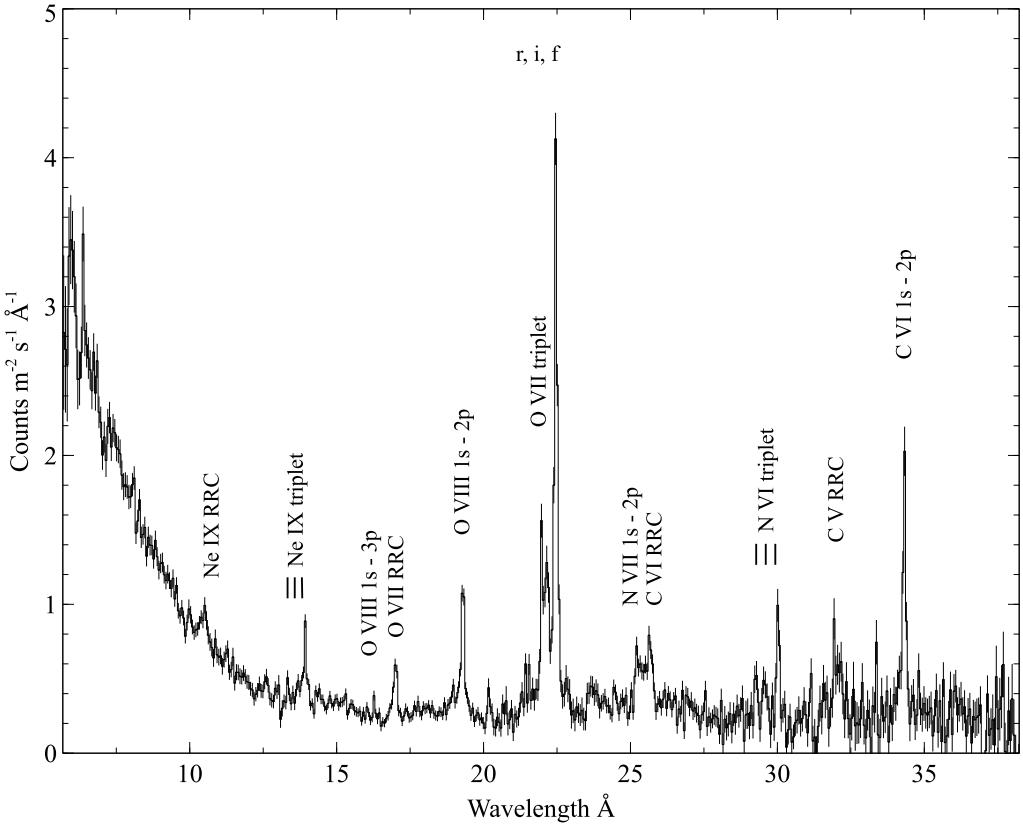

Fig. 5.5: The 2013-14 770 ks stacked RGS spectrum of NGC 5548 (observed frame). The strongest emission lines are labelled. There are ∼60 counts in each of the continuum bins around 20 Å. The data are shown in black and are binned by a factor of two for clarity.

some previous work that used a redshift value $z = 0.01676$ determined from the optical lines (e.g. used in Steenbrugge et al. 2003).

This chapter presents a study of the narrow emission lines in the spectra of NGC 5548 obtained by RGS (see Chapter 3 for details). I focus on the 770 ks stacked spectrum in the range 5.7-38.2 Å(see Fig. 5.5), created from combining fourteen observations of ∼50 ks by the method described in Chapter 4; twelve of these were taken each a few days apart between 22 June and 31 July 2013, with two other *XMM-Newton* observations taken a few months later (December 2013 and February 2014).

The fourteen individual observations have also been examined separately, by fitting each narrow emission line in each spectrum with an individual gaussian, and they show no significant variability in flux or width of the narrow emission features. Therefore analysing the stacked spectrum of 770 ks for the remainder of this work is justified in order to increase data counts and signal to noise levels within the spectrum.

The long wavelength part of the spectrum (in Fig. 5.5, around 35-38 Å) has noticeably larger uncertainties, due to the decrease in effective area of RGS in this range (den Herder et al. 2001). There is also a decrease in effective area at the short wavelength part of the spectrum (5-10 Å) but the much higher photon count from the source at these wavelengths slightly reduces the effect this has on the observed spectrum.

5.4 Data Analysis

In order to analyse accurately the narrow emission features of this spectrum, a good model for the continuum and absorption was needed. Kaastra et al. (2014) conclude that the classical WA previously observed in NGC 5548 is not sufficient to explain the unexpected degree of absorption shown in this spectrum, and identify two new "obscurer" components needed to fit the intrinsic and reflected continuum well, in addition to six WA components (named from A to F; parameters shown in Table 5.2). The continuum was modelled with a combination of a modified black body and power-law, including reflection from distant material and an exponential cut-off at high energies. The details

of this are in the supplementary materials of Kaastra et al. (2014). The exact physical interpretation of this continuum does not affect this work on the narrow emission features as it is used only as a continuum level above which the emission features are measured. Galactic neutral absorption is included with H I column density in the line of sight set to $N_H = 1.45 \times 10^{20}\,\mathrm{cm}^{-2}$ (Wakker et al. 2011). This continuum and absorption model is used throughout the analysis in this chapter.

As with all work in this thesis, I use the C-statistic (Cash 1979) parameter for all analysis in this chapter (see Chapter 4). The expected C-statistic for the full 770 ks spectrum is 1087 ± 47, for the O VII triplet range used in Sect. 5.4.3 is 50 ± 10, and for the range around the O VIII Ly-α and C VI Ly-α broad lines discussed in Sect. 5.4.1 the expected C-stat values are also both 50 ± 10. The errors used in this paper are all at the 1σ (68%) confidence level unless stated otherwise.

All the spectral fitting in this paper was done with the SPEX[1] spectral fitting program (Kaastra et al. 1996) version 2.05.02. Additional analysis compares simulated photoionisation spectral models from CLOUDY (version 13.03; Ferland et al. 2013) with the observational data (Sections 5.5 and 5.5.1). The adopted cosmological parameters are $H_0 = 70$ km s^{-1} Mpc^{-1}, $\Omega_\Lambda = 0.70$ and $\Omega_m = 0.30$.

5.4.1 Broad Emission Lines

Although broad emission lines are difficult to identify in the 2013-14 spectrum, Kaastra et al. (2014) include four of these in their model (C VI Lyα, O VII Heα, O VII Heβ, O VIII Lyα). All of their parameters (FWHM, luminosity and outflow velocity) were initially taken from the Steenbrugge et al. (2005) analysis of the *Chandra* LETGS 2002 spectrum, when the continuum was higher, and the broad lines are initially fixed to those values, using a *Gaussian* model for each. The broad line source is taken to be interior to the obscurer, as expected from the results of Kaastra et al. (2014), therefore (as the fitted model parameters are different to the 2002 analysis) the new luminosities differ from those found previously. The 2002 parameters were estimated from knowledge

[1] http://www.sron.nl/spex

Table 5.3: Broad emission line parameters from the 2013-14 RGS spectra. All values without error bounds were fixed during fitting. The outflow velocities and widths of both O VII lines were chosen to be the same as those used by the Steenbrugge et al. (2005) analysis of 2002 LETGS data.

Line	Rest λ ($\AA$)	λ [a] ($\AA$)	Outflow Velocity (km s^{-1})	FWHM ($\AA$)	Luminosity (10^{33} W)
O VII 1s-3p	18.63	18.63	0	0.50	<1.8
O VIII 1s-2p	18.97	18.89±0.06	−1200±900	0.12±0.08	$10.3^{+23.9}_{-7.4}$
O VII 1s-2p	21.60	21.60	0	0.58	8.5±4.4
C VI 1s-2p	33.74	33.65±0.03	−800±300	$0.24^{+0.12}_{-0.05}$	32.6±12.1

[a]measured values in the rest frame

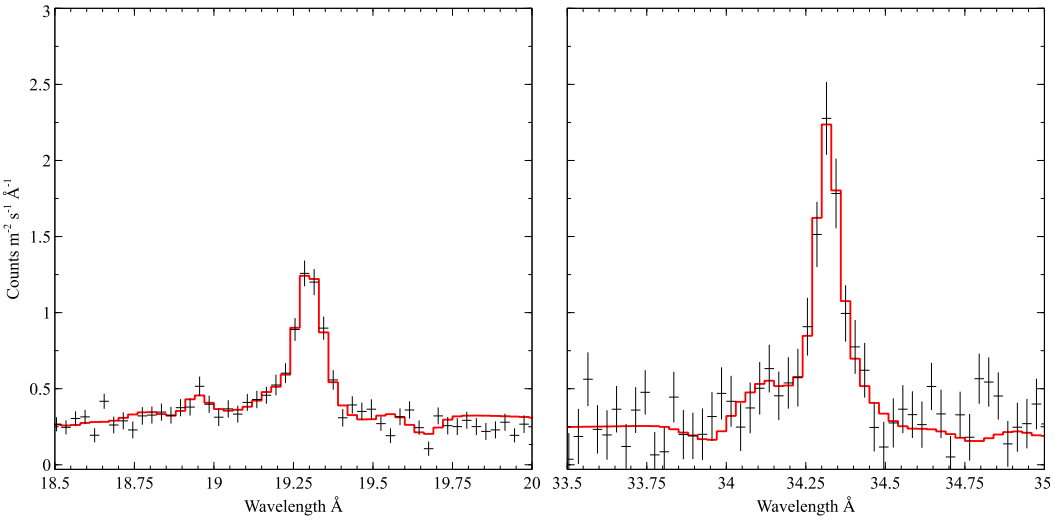

Fig. 5.6: The two broad emission lines that are well fitted; O VIII Lyα (18.5-20 Å) and C VI Lyα (33.5-35 Å). Both can be seen as shoulders on the blue side of their corresponding narrow emission line. Shortwards of O VIII Lyα, the O VII Heβ narrow emission line can also be seen. See text for details.

of the UV broad line parameters in this source as they could not be directly fitted. I left these parameters (FWHM, outflow velocity and luminosity of each line) free to vary where possible while fitting the 2013-14 770 ks spectrum (see Table 5.3). The best fits to the broad O VIII Lyα line (over the range 18.5-20 Å; C-stat = 80) and the broad C VI Lyα line (33.5-35 Å; C-stat = 75) in the 2013-14 data, are shown in Fig. 5.6. The measured widths of these lines indicate that their location is in the broad line region, as expected. It is interesting to note that the outflow velocities of these broad lines are similar to the strongest velocities seen in the UV absorption of the newly detected obscuring material, especially as the obscurer is thought to be located at a similar distance from the source as the broad line region (Kaastra et al. 2014).

Difficulties fitting new values for both of the O VII broad lines (Heα and Heβ) in the 2013-14 spectrum led to using the simplifying assumption that their FWHM and outflow velocity values have not changed since the values derived for the 2002 spectrum. Therefore these two lines are set to their rest wavelength (i.e. assuming no outflow velocity), as they are in Steenbrugge et al. (2005). For the O VII Heα line this gives a luminosity estimate, but for the O VII Heβ this only gives an upper limit to the luminosity (see Table 5.3), therefore the broad O VII Heβ line is not included in any further analysis.

The parameters for the O VIII Lyα, O VII Heα and C VI Lyα lines are fixed at the values in Table 5.3 throughout the rest of the analysis in this chapter.

5.4.2 Initial Fit and He-like Triplet Diagnostics

There are He-like emission line triplets of oxygen, nitrogen and neon within the NGC 5548 stacked spectrum. The O VII triplet is the strongest and the O VII forbidden line component is the highest flux emission line in the data. For this reason, the diagnostics in this chapter are concentrated on the O VII triplet.

All three emission lines within any triplet (four if taking into account the intercombination line as an unresolved doublet) from any individual phase of gas have consistent velocities. When fitting the He-like oxygen triplet in these NGC 5548 data by using three simple *Gaussian* models in SPEX, the

Table 5.4: Initial parameters for the O VII triplet from the 770 ks spectrum. C-statistic (21.5-23 Å) = 48

Line [a]	Rest λ (Å)	Measured λ [b] [c] (Å)	Flow velocity (km s^{-1})	FWHM (Å)	FWHM (km s^{-1})
O VIIr	21.602	21.601±0.004	-20 ± 50	<0.002	<30
O VIIi	21.807	21.772±0.020	-480 ± 160	0.151±0.024	2100±330
O VIIf	22.101	22.077±0.002	-320 ± 40	0.064±0.007	870±100

[a] r, i and f represent the resonance, intercombination and forbidden lines, respectively

[b] NGC 5548 rest frame values

[c] There is an additional $\pm 0.004\,\AA$ error on these values due to RGS absolute wavelength uncertainty

forbidden and intercombination lines are found to have outflow velocities of -320 ± 40 km s^{-1} and -480 ± 160 km s^{-1} respectively, while the resonance line has a best fit velocity consistent with being at rest (-20 ± 50 km s^{-1}; all values shown in Table 5.4). This discrepancy is not the case for the N VI He-like triplet (at ∼29 Å) where the three measured line velocities are consistent, and cannot be determined for the Ne IX He-like triplet (at ∼13.5 Å) because the resonance and intercombination line velocities are not constrained by this data.

A collaborator looked at whether calibration issues could have caused this apparent velocity discrepancy in the O VII He-like triplet by comparing with a 68 ks exposure of Capella taken close in time to the NGC 5548 data, on 31-08-2013 (ObsID: 0510781201), and reduced the same way as the NGC 5548 data. They compared the line centroids of 8 strong emission lines between 6.64 and 33.74 Åwith laboratory wavelengths and found the weighted mean difference to be -2.7 ± 0.4 mÅ, corresponding to -17 ± 2 km s^{-1} at 20 Å. This very small offset is compatible with the typical orbital velocity of 30 km s^{-1} of the binary components of Capella, and shows that the uncertainties on the absolute wavelength scale are much smaller than the offsets found for the forbidden and intercombination lines in the NGC 5548 data. In the Capella data, between 15 and 25 Å, the centroids of the five strongest lines

were consistent within the error bars with the weighted mean and all had uncertainties of less than 30 km s^{-1}. In conclusion, there is no instrumental reason to doubt the measured line centroids of the O VII triplet in the NGC 5548 spectrum.

Further evidence that this velocity discrepancy is a real effect can be found in historical data; the same apparent velocity difference is seen in 1999 *Chandra* data, analysed by Kaastra et al. (2000) and Kaastra et al. (2002), where the O VII resonance line appears ∼300 km s^{-1} redshifted with respect to the O VII forbidden and intercombination lines, i.e. displaced in the same direction as found in the 2013-14 spectrum. This previous work focussed on the narrow absorption lines that could be seen in the data, therefore those authors did not investigate the velocity discrepancy between these emission lines.

5.4.3 Investigation into O VII Triplet Velocity Discrepancy

After calibration effects were ruled out, I investigated various scenarios to explain the velocity discrepancy between the O VII triplet lines. First I explored the case in which we observe the combined emission from two ionised cones propagating out from the central source in opposite directions. Then I investigated the possibility that the velocity discrepancy is due to absorption.

Two Cone Model

It is possible that the velocity discrepancy between the O VII triplet lines is caused by the presence of two contributing O VII triplets of different line ratios, one redshifted and one blueshifted with respect to the host galaxy. This could be the case if the narrow emission lines are being produced in two opposing cone shaped regions, each illuminated by and expanding away from the central source, with more gas in the cone closer to (and outflowing towards) the observer. In this case, the optically thin lines (such as forbidden and intercombination lines) would be seen from all of the gas and therefore would have one average (measured) velocity, dominated by that of the closer region with more gas. If the optically thick lines (such as the resonance line) are mainly produced at the illuminated face of the gas and shielded by the cooler gas, then the observer would preferentially see the lines formed in the

gas facing towards them (the farther cone, outflowing away from the observer, and therefore redshifted). This would cause an apparent velocity difference between the resonance and both the intercombination and forbidden lines.

This theory was tested in SPEX by modelling each narrow emission line as a combination of two separate *Gaussian* components, one blueshifted and one redshifted, to represent the two opposing conical regions. The velocity difference between these components must be small enough that the observed emission lines retain their single peak appearance; this restriction is more important at longer wavelengths. The narrow emission line observed in the data with the longest rest wavelength is C VI 1s-2p (33.736 Å), therefore the single peak appearance of this line sets a limit on the velocity difference between the two conical regions in this model.

The best fit to the C VI 1s-2p line had ouflow velocities of -305 ± 40 and $+125 \pm 50\,\mathrm{km\ s^{-1}}$ for the blueshifted and redshifted components respectively. This model (with the outflow velocities fixed to those values) was then extended to fit all the emission lines in the spectrum, leaving widths and normalisations free. Finally the outflow velocities of the *Gaussian* components were left free to vary to find the final best fit for this model. The final best fit outflow velocities in this case are -320 ± 30 and $+190 \pm 30\,\mathrm{km\ s^{-1}}$ respectively, with a C-statistic of 1832 over the whole spectrum.

This model is not without problems, as the statistical best fit does not physically match the two cone model explained above. In this model the observed O VII forbidden line should be a combination of O VII forbidden emission from both the blueshifted and redshifted emission cones (as it is an optically thin line), whereas in the best fit model described above, the O VII forbidden line only has a contribution from the blueshifted Gaussian component (see Fig. 5.7). In contrast, the Ne IX and N VI forbidden lines in this model do have contributions from both the blue- and redshifted components, as expected. As discussed in Chapter 4, physical self-consistency of the best fit model is an important factor for acceptance, so for this reason the two emission cone model is not favoured as a physical explanation of the apparent O VII velocity discrepancy.

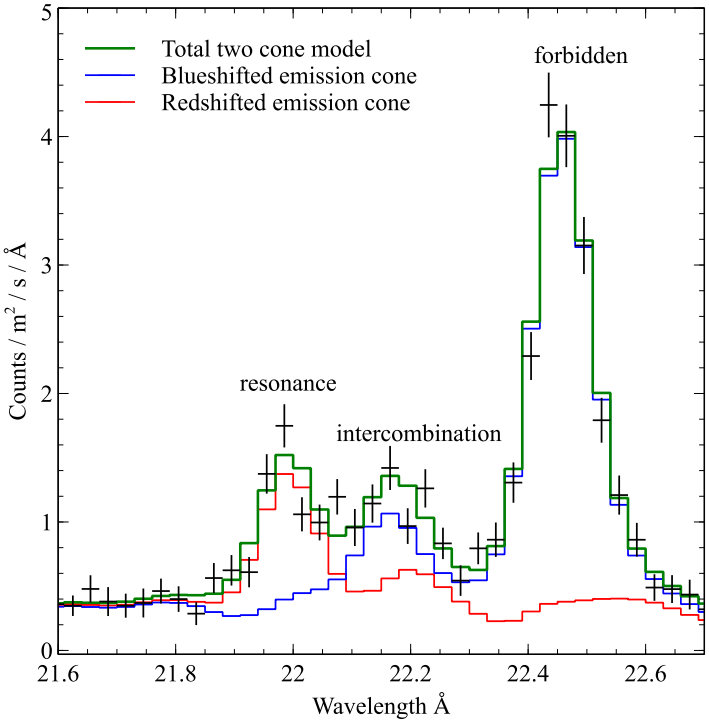

Fig. 5.7: Final two cone model fit of the O VII triplet. Each emission line is fitted with two Gaussian components, one at velocity of $-320\,\mathrm{km\ s^{-1}}$ (shown in blue) and the other at velocity of $+190\,\mathrm{km\ s^{-1}}$ (shown in red). The data are shown in black and the overall fit is shown in green. Clearly, the O VII forbidden line (on the right) only requires the blueshifted Gaussian component but this does not match the physical requirements of the two cone model (see text for details).

For completeness, this scenario is explored further in Sect. 5.5.1 when investigating possible geometries for the narrow-line emitting gas using self-consistent photoionization models from CLOUDY (this is not tried with SPEX as it does not yet include photoionisation emission models).

Absorption

It is also possible that the velocity shift in the resonance line with respect to the other components of the O VII triplet is due to absorption on its blue side. This could then allow the true velocity of the resonance line to match the outflow velocity of around $-300\,\mathrm{km\ s^{-1}}$ measured for the intercombination and forbidden lines. The resonance line could be more strongly affected by absorption than the other components of the triplet due to resonant scattering and the possible geometry of the region (see Chapter 2 and Porquet et al. 2010).

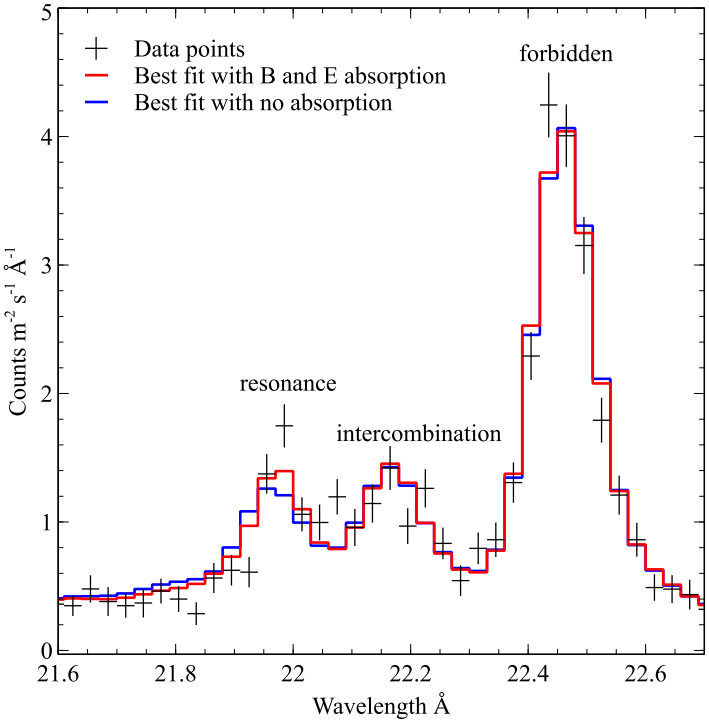

Fig. 5.8: Best fit model to the O VII triplet. The data are shown in black. Shown in red is the best fit including absorption from X-ray WA components B & E (C-statistic = 82). Shown in blue is the best fit with no absorption (C-statistic = 104). In both models the outflow velocities and line widths of all three triplet lines are coupled together. The outflow velocity, line width and normalisations were left free to vary to find the best fit for each scenario.

The comparative widths of these three lines, when simply fitted with *Gaussian* models, are already an indication that absorption may be playing a role in the appearance of the resonance line. As shown in Table 5.4, the measured width of the O VII resonance line is extremely small, especially compared to the intercombination and forbidden lines within that same O VII triplet. As all three of these lines should have very similar widths, this implies that part of the resonance line is not being observed for some reason; absorption could cause this effect.

I tested whether absorption of the triplet by any of the six WA components applied by Kaastra et al. (2014) (see Table 5.2) could explain the shift of the resonance line in this way, as all WA components are found to have blueshifted velocities. Previous distance estimates for both the X-ray WA components

(at least one component <7 pc; Detmers et al. 2008) and X-ray NLR (1-15 pc; Detmers et al. 2009) are similar, but the "obscurer" components discovered by Kaastra et al. (2014) are known to be located much closer to the ionising source than the NLR. Therefore these "obscurer" components were not included in this absorption test. Parameters of the WA components can be seen in Table 5.2. For this test the normalisations of the three O VII triplet lines were left free to vary after being placed inside each of the WA components in turn. The FWHM values for each of the O VII triplet lines were coupled and left free to vary. The outflow velocities for the three O VII triplet lines were also coupled and initially fixed to $-300\,\mathrm{km\ s^{-1}}$ (the approximate outflow velocity of the forbidden line), to reduce the number of free parameters at this stage. This led to the C-statistic listed in Table 5.5. The outflow velocity is left free to vary after this test.

When comparing different, non-nested best fit models with the same number of degrees of freedom, as in this case, standard tests (such as the F-test) are not applicable, so another method must be used to determine if any improvement in the C-statistic is significant. In this case, given the tight relation between χ^2 and C-statistic, the significance is tested by taking the square root of the Δ C-statistic (measuring the improvement in C-statistic when comparing one model to another) and this gives us the significance of that improvement in σ. For example, ΔC of 9 corresponds to a 3σ improvement.

As shown in Table 5.5 the C-statistic values for each scenario were also calculated over the whole spectrum. I focus on the results using only the O VII triplet wavelength range, as the C-stat of this region is not affected by any other regions where the continuum model does not match the data exactly (for example the excess of data over model in the range 35-38 $\mathring{A}$). One model is an improvement over another when the C-stat improves by $\geq$9, relating to a 3σ improvement.

Initially absorption was considered by each WA component in turn; absorption by WA component B improved the fit substantially, and more so than the other components (from a C-stat of 104 to 93 for the O VII triplet). Further absorption components were added to this fit, one by one, and including

Table 5.5: C-statistic values for fitting the O VII triplet, and the whole RGS spectrum, with WA absorption of narrow emission lines (and RRCs when looking at the whole data range). The parameters of all the WA components were fixed to the best-fit values from Kaastra et al. (2014), as they are for all the analysis within this work. For each of these fits, all three O VII triplet lines had fixed outflow velocities of $-300\,\mathrm{km\ s^{-1}}$ and the widths of all three triplet lines were coupled and fitted together.

Absorption applied [a]	C-stat value for O VII triplet [b]	C-stat value for all RGS data [c]
None	104	1865
A	103	1864
B	93	1856
C	102	1861
D	114	1882
E	94	1879
F	100	1863
B & E	83	1870
B, E & D	85	1878
B, E & F	78	1871
A, B & C	90	1853
A, B, C & D	96	1864
A, B, C, D & E	80	1866
A, B, C, D, E & F	78	1868

[a] Letters refer to Kaastra et al. (2014) WA components as described in Table 5.2
[b] Data range 21.5-23 $\mathring{A}$
[c] Data range 5.68-38.23 $\mathring{A}$

absorption by component E decreased the C-stat (by 10, to 83). Adding a third absorbing component (F) also decreased the C-stat around the triplet range again, but this time only by 5, so it is not considered enough improvement to justify use of this model over the previous one. A different absorption scenario was also tested, by using components A, B and C to absorb the narrow emission lines. This gave a better C-statistic when fit to the whole spectrum, but a worse value for only the O VII triplet range (see Table 5.5). As this test focuses on how well the O VII triplet is fitted, the scenario using absorption by B and E only is marginally prefered because it requires a smaller number of absorbing components.

The outflow velocity of the triplet lines (still coupled together) was left to vary freely, using absorption from WA components B and E, giving a best fit outflow velocity of $-300 \pm 30\,\mathrm{km\ s^{-1}}$ (the C-statistic reduced by 1, to 82). This fit, compared to the fit with coupled O VII triplet line velocities but no absorption, is shown in Fig. 5.8. Clearly, the inclusion of absorption shifts the fitted peak of the O VII resonance line towards the peak seen in the data.

The evidence from these tests so far implies that WA components B and E are doing most of the absorbing of the O VII r line; I explored how important the outflow velocities of these components are to this determination. To do this I took each of the other WA components and fixed their velocity to that of B and E in turn. Absorption by component A had very little effect on the fit around the O VII triplet, whichever velocity I fixed it at, becasue the measured velocities of components A, B and E are similar ($-588 \pm 34\,\mathrm{km\ s^{-1}}$, $-547 \pm 31\,\mathrm{km\ s^{-1}}$ and $-792 \pm 25\,\mathrm{km\ s^{-1}}$ respectively, taken from Kaastra et al. 2014). When the other components (C, D and F) were set to the velocities of components B and E, absorption by them caused a substantial improvement in the fit of the O VII triplet, compared to when they were set to their measured velocities. The C-statistic improved by between 5 and 29 for each case.

The above indicates that having well determined outflow velocities for these warm absorber components is vital to calculate the effect that absorption by each one would have on the fit of the O VII triplet. Therefore the details of this absorption scenario for the narrow emission lines should be

seen as strongly dependent on the determined warm absorber properties; this work tests the concept that the narrow emission lines could be absorbed by some warm absorber components, not the specific order of the involved warm absorber components.

While this absorption scenario does not give a perfect fit, it is the only physically plausible explanation for the O VII velocity discrepancy so far. Therefore absorption by WA components B and E is used as the best fit scenario for the remainder of this work.

Using this absorption scenario for the O VII triplet, the parameters of all narrow emission lines and RRCs (using the *RRC* model in SPEX, see Sect. 4.2.2 and 5.4.4) were recalculated assuming that all are absorbed by the same combination of WA components. The results of this can be seen in Table 5.5. Absorbing all the narrow lines and RRCs by WA components B and E led to the best fit for the O VII triplet (following the above method), but not for the whole spectrum. The best fit for the whole data range (5.7-38.2 Å) is obtained when the narrow lines and RRCs are all absorbed by WA components A, B and C; while this could be another physically acceptable scenario, the improved fit around the O VII triplet when absorbed by WA components B and E leads to the decision to focus on the latter for the rest of the work in this chapter.

The best fit values for the narrow-line and RRC parameters over the whole spectrum, after absorption from WA components B and E, are presented in Sect. 5.4.4 and in Tables 5.6 and 5.7 respectively. These parameters are of course dependent on which scenario is used; here the simplest absorption scenario is adopted that gives the best fit to the O VII triplet region (with $\Delta C \geq 9$ from any simpler scenario).

5.4.4 SPEX Best Fit for the 770 ks Stacked Spectrum

There are 14 narrow emission lines detected and an upper limit to one further narrow emission line in the stacked spectrum; their best-fit parameters are in Table 5.6. These were obtained using the absorption scenario (B and E absorption) described in detail in Sect. 5.4.3. If absorption from WAs A-C, instead of B and E, had been used to measure the parameters in Tables 5.6 and 5.7, the values would all be within 3σ of those provided. This shows that, for

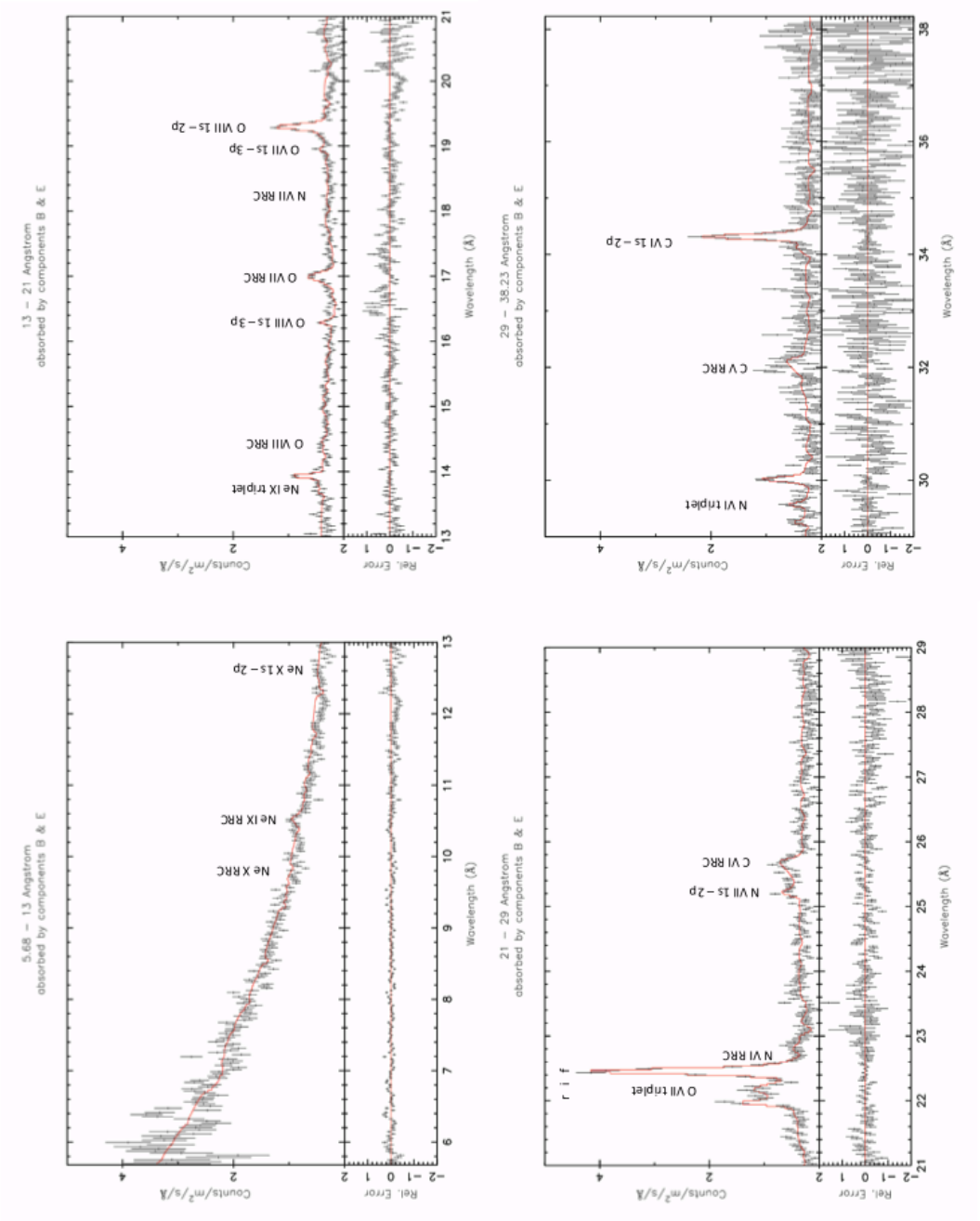

Fig. 5.9: Best fit using individual Gaussian lines and RRC model within SPEX. Warm absorber components B and E are absorbing the narrow emission lines and RRCs. The data are shown in black and the best fit model in red. A selection of emission lines are named. See text for detail.

Table 5.6: Narrow emission line best fit parameters from the 770 ks spectrum when absorption from WA components B and E is applied. Parameters without errors were fixed during fitting. Overall C-statistic = 1870.

Line [a]	Rest λ (Å)	Measured λ [b] [c] (Å)	Flow velocity [d] (km s^{-1})	FWHM [e] (Å)	FWHM (km s^{-1})	Unabsorbed Flux (photons m^{-2} s^{-1})	Previous detections [f]
Ne X 1s-2p	12.138	12.138	-	10^{-4}	-	<0.013	-
Ne IXr	13.447	13.447	-	0.056±0.002	1230±40	0.035±0.008	-
Ne IXi	13.553	13.553	-	0.056±0.002	1230±40	0.016±0.007	S05
Ne IXf	13.699	13.695±0.004	-90±90	0.056±0.002	1230±40	0.115±0.008	K02, S05
O VIII 1s-3p	16.006	16.003±0.006	0±110	<0.068	<1280	0.049±0.006	-
O VII 1s-3p	18.627	18.612±0.015	-240±240	<0.086	<1390	0.047±0.014	-
O VIII 1s-2p	18.969	18.969±0.001	0±20	0.079±0.028	1250±440	0.238±0.100	K02
O VIIr	21.602	21.580±0.002	-300±30	0.082±0.006	1130±80	0.307±0.027	K02
O VIIi	21.807	21.785±0.002	-300±30	0.082±0.006	1130±80	0.222±0.024	K02, S05
O VIIf	22.101	22.079±0.002	-300±30	0.082±0.006	1130±80	0.822±0.030	K02, S05, D09
N VII 1s-2p	24.781	24.806±0.011	300±130	0.177±0.028	2140±340	0.169±0.023	-
N VIr	28.787	28.753±0.011	-350±110	0.058±0.014	600±140	0.136±0.027	-
N VIi	29.084	29.060±0.013	-250±130	0.058±0.014	600±140	0.086±0.017	S05
N VIf	29.534	29.511±0.006	-230±60	0.058±0.014	600±140	0.176±0.018	S05
C VI 1s-2p	33.736	33.734±0.005	-20±50	<0.063	<800	0.339±0.069	-

[a] r, i and f represent the resonance, intercombination and forbidden lines, respectively

[b] NGC 5548 rest frame values

[c] There is also 0.004 Åuncertainty on these values due to RGS absolute wavelength uncertainty

[d] The O VII triplet outflow velocity values were coupled together

[e] The Ne IX, O VII and N VI triplets each had the FWHM values of their three lines coupled together

[f] K02 represents Kaastra et al. (2002). S05 represents Steenbrugge et al. (2005). D09 represents Detmers et al. (2009)

the X-ray narrow lines in this source, choosing a different specific absorption scenario does not significantly alter the overall results. The presence of this absorption is more important than which specific components are causing it.

Three complete emission triplets, of forbidden, intercombination and resonance lines (O VII, N VI & Ne IX) are present, plus four Lyα (Ne X, N VII, O VIII & C VI), O VII Heα and O VIII Lyβ lines. These lines, with a few exceptions, were fitted using the simple *Gaussian* model in SPEX with the outflow velocity, FWHM and normalisation kept as free parameters. The exceptions to this are the Ne IX, O VII and N VI triplet lines, which had some values coupled together (see Table 5.6 for details), and the Ne X Lyα and the Ne IX resonance and intercombination lines, which were fixed at their NGC 5548 rest frame wavelengths. The rest wavelengths were all taken from the internal SPEX line list.

Table 5.6 also shows which of these narrow lines have been previously detected in NGC 5548 (Kaastra et al. 2002; Steenbrugge et al. 2005; Detmers et al. 2009).

Eight RRC features are detected in this spectrum; the final best fit parameters are presented in Table 5.7. All eight RRC features were simultaneously fitted with one *RRC* model in SPEX, which uses one temperature and allows different emission measures for each ion. This first *RRC* model gives an electron temperature in eV which is shown (along with the emission measures for each ion) in Table 5.7 (third column). The RRC features were then split into element pairs (e.g. O VII and O VIII together) and fitted with one *RRC* model for each pair. The carbon, oxygen and neon *RRC* models all give temperatures of the same order of magnitude (Table 5.7). The nitrogen RRC features are very weak in this spectrum, therefore the temperature for the nitrogen *RRC* model was fixed at the best fit value for that of the oxygen *RRC* model as the O VII RRC is the strongest, non-contaminated RRC feature in this spectrum. Nitrogen RRC emission measure values using this temperature are shown in Table 5.7. Fitting the RRC features in this 'paired' way marginally improved the overall C-statistic by ΔC = 10 compared to using just one *RRC* model (and therefore one temperature) for all features. The best-fit temperatures

Table 5.7: RRC parameters for the 770 ks spectrum, including absorption from WA components B and E, as discussed in Sect. 5.4.3. Overall C-statistic = 1870.

RRC name	Recombining ion	Emission Measure [a] for overall fit (10^{64} m^{-3})	Temperature for pair fit eV (K)	Emission Measure [a] for pair fit (10^{64} m^{-3})
C V	C VI	1500^{+200}_{-190}	4.1 ± 0.7	1110±200
C VI	C VII	900^{+100}_{-90}	$(4.8 \pm 0.8 \times 10^4)$	620±110
N VI	N VII	130±70	6.6 [b]	130±80
N VII	N VIII	60±30	(7.7×10^4)	70±30
O VII	O VIII	650±40	6.6±0.6	700±50
O VIII	O IX	130±20	$(7.7 \pm 0.7 \times 10^4)$	140±20
Ne IX	Ne X	60±10	9.4±0.3	80±20
Ne X	Ne XI	20±10	$(10.9^{+0.4}_{-0.3} \times 10^4)$	30±20
	Overall Temperature	5.9 ± 0.5 eV $(6.8 \pm 0.5 \times 10^4$ K)		

[a] of recombining ion

[b] Fixed to oxygen best fit value, see text for details

Table 5.8: Results from automated fitting of the 770 ks stacked spectrum with CLOUDY simulated spectra. For each fit the CLOUDY spectra are given an outflow velocity of -300 km s^{-1}, in order to match the O VII f line (the strongest in the spectrum). The emboldened rows show the best-fits to both absorption scenarios when using the fine grid of unobscured CLOUDY models.

SED	Spectrum range	Absorption [a]	C-statistic	Best fit CLOUDY parameters		
				log ξ	log v_{turb}	log N_H
	Å				km s^{-1}	cm^{-2}
obscured	5.7-38.2	B, E	2213	2.3	2.5	22.5
obscured	5.7-38.2	A-C	2178	2.3	2.5	22.5
unobscured	5.7-38.2	B, E	2298	1.5	2.0	23
unobscured	5.7-38.2	A-C	2272	1.5	2.0	22.5
unobscured	21.5-23	B, E	97	1.7	2.5	23.25
unobscured	21.5-23	A-C	106	1.7	2.0	22.25
unobscured	**5.7-38.2**	**B, E**	**2273**	**1.45**	**2.25**	**22.9**
unobscured	**5.7-38.2**	**A-C**	**2243**	**1.45**	**2.25**	**22.9**

[a]Letters refer to Kaastra et al. (2014) WA components shown in Table 5.2

for the carbon and neon RRC pairs are inconsistent with each other at the 3σ level (the uncertainties in Table 5.7 represent 1σ), which gives some evidence for stratification of the emission regions producing these RRC features.

The threshold energies (E) of all the RRC features are of the order of several hundred eV, and the electron temperatures (ΔE) are measured to be of the order of a few eV, therefore $\Delta E/E << 1$ which is strong evidence for photoionised conditions dominating within the emitting gas.

5.5 Testing the Absorption Model using CLOUDY

In order to fit the spectrum with physically self-consistent models (as SPEX does not include a photoionised emission model) the spectral synthesis program CLOUDY (Ferland et al. 2013) was used. A number of simulated spectra for a range of physical parameters were created, and compared to the NGC 5548 data using the absorption scenario described above. A plane parallel geometry is assumed, with the central source illuminating the inner face of the

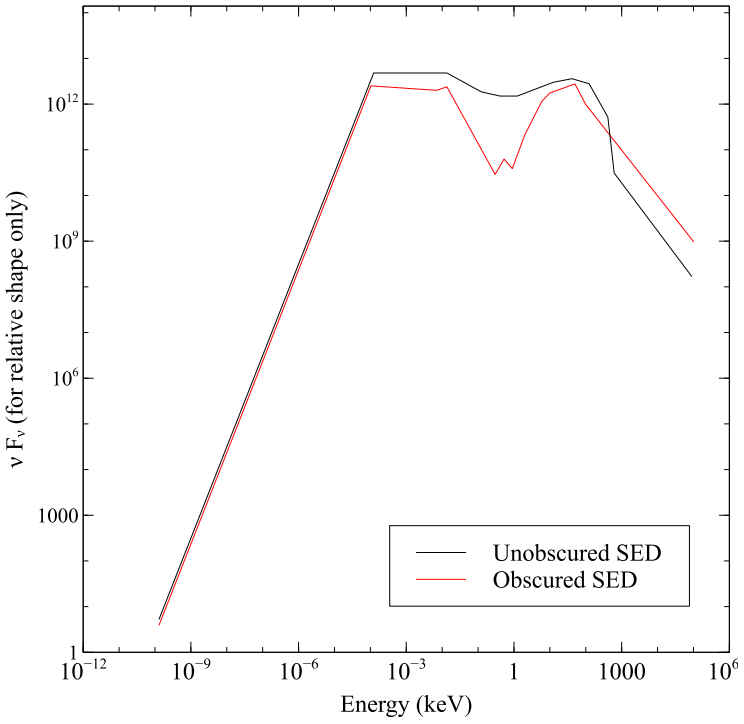

Fig. 5.10: The two SED shapes used as input for CLOUDY. CLOUDY scales the input SEDs using either luminosity or intensity values, so absolute values on the y-axis are not relevant.

cloud and with a flux density dependent on a chosen ionisation parameter, ξ.

The spectrum produced by photoionisation processes strongly depends on the shape of the ionising continuum, described by the SED. Two sets of CLOUDY results were compared with the 770 ks RGS spectrum; one was generated using the historical unobscured SED of NGC 5548 and one used the new obscured SED from 2013-14, both shown in Fig. 5.10. These SEDs are smoothed and simplified compared to those presented in Mehdipour et al. (2015), but qualitatively very similar in shape, which is enough for this analysis. Both sets of CLOUDY spectra were compared with the data in order to determine which gave the best fit. If the unobscured SED gives a better fit to the data, this would be evidence for the X-ray NLR still receiving and reacting to the unobscured flux from the central source. If the obscured SED gives a better fit, then this would suggest that the NLR is located close enough to the central source that it is visibly receiving and reacting to the obscured flux.

For both SEDs, the CLOUDY simulated spectra explored a parameter

range of log ξ = 0.1-3.3 (with 0.2 step size), hydrogen column density = 10^{21}-10^{24} cm^{-2} (with $10^{0.25}$ step size) and turbulent velocity = 10^{1}-$10^{3.5}$ km s^{-1} (with $10^{0.5}$ step size). The electron density was set to 10^{8} cm^{-3} because as long as this remains under the critical density[2] its value is unconstrained by the data.

The 1326 simulated spectra within this parameter grid for each SED were compared with the stacked 770 ks spectrum.

Each one of the CLOUDY generated spectra was imported into a SPEX *file* model and compared with the data using an automated fitting process, with the normalisation of the simulated spectra left free to vary. This fitting process used a Python script to run SPEX and generate a C-statistic value for each one of the simulated spectra. Throughout this process there is no interpolation between the 1326 CLOUDY models in the grid specified above. Unless otherwise stated, the CLOUDY spectra were all given an outflow velocity of -300 km s^{-1} to match the measured value of the strongest emission line in the data, the O VII f line.

There are numerous possible outputs from CLOUDY which are described in Chapter 4. For this first test the reflected spectrum output was used to model the narrow emission lines (as done in e.g. Bianchi et al. 2010; Guainazzi et al. 2009). This is of course only one potential geometry of the NLR region; more geometrical possibilities are explored in Sect. 5.5.1.

Each CLOUDY reflected spectrum includes diffuse emission from within the cloud and scattered (absorbed and re-emitted) radiation from the intrinsic continuum, i.e. it includes only the narrow emission lines and a scattered continuum, therefore the incident continuum itself, WAs, obscurer and broad emission lines must be modelled separately. The observed continuum, WAs and obscurer are modelled as in Kaastra et al. (2014) and the 2013-14 broad emission line parameters from Sect. 5.4.1 in this chapter are used.

The narrow emission lines CLOUDY produces are intrinsically narrower than those seen in the RGS data because, while CLOUDY takes the effect of turbulence within the gas into account for the line strengths, it does not use

[2]see Chapter 2 and Porter and Ferland (2007) for details

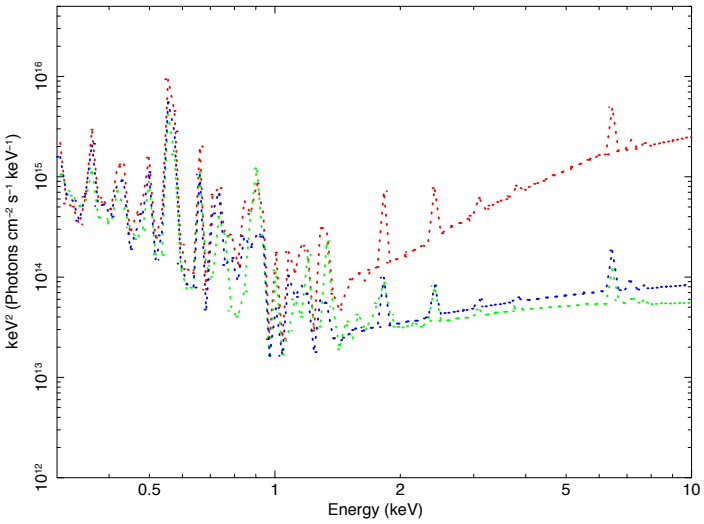

Fig. 5.11: Comparison of emission from CLOUDY models using the obscured (red) and unobscured (blue) SEDs. Emission from a CLOUDY model using a generic AGN SED is also shown in green.

this to broaden the lines in the produced spectra[3]. Therefore for the absorption to be applied properly, the narrow emission lines in the CLOUDY spectra must be broadened. This was done using the *vgau* model in SPEX, set to a sigma velocity of 450 km s^{-1} as this was manually found to be the best overall fit to the data; it is also consistent with the average Gaussian sigma broadening value (460 ± 30 km s^{-1}) found for all the narrow emission lines in Kaastra et al. (2014) and overall with the FWHM values in Table 5.6.

When fitting the whole 770 ks spectrum, with absorption from WA components B and E applied, the CLOUDY results based on the obscured and unobscured SEDs gave best C-statistic values of 2213 and 2298 respectively. All the C-statistic values from the CLOUDY fits are collected in Table 5.8.

At this point results from using the CLOUDY models from obscured and unobscured SEDs were compared (see Fig. 5.11). In the RGS data range the CLOUDY simulated spectra using the obscured SED gave a better fit to the data ($\Delta C = \sim 90$). The compatibility of this with the rest of the NGC 5548 spectrum extending to the hard X-rays was tested, by applying the best fit model for the RGS band to the EPIC-pn data from the same campaign

[3]See Hazy 1 documentation, page 162

(see Cappi et al. 2016 for details of the analysis of the EPIC-pn data). This showed a severe excess of flux in the higher energy (>2 keV) range of the obscured SED CLOUDY model in comparison to the EPIC-pn spectrum, and led to the conclusion that the CLOUDY results from the unobscured SED are more physically appropriate, despite the slightly worse statistical quality of the fit in the RGS band.

The narrow line-emitting gas is also expected to be reacting to the unobscured SED because the O VII forbidden line flux has not changed as substantially as the more drastic change in the soft X-ray continuum (see the later discussion in Section 5.6.2). If the narrow line-emitting gas is reacting to the new, obscured SED then a much greater change would be expected.

In order to derive the errors in the best fit parameters for the emitting gas a finer grid of models with CLOUDY were created, using the unobscured SED.

From this grid, uncertainties on the parameters of the emitting gas were calculated for both absorption scenarios investigated above (B, E and A, B, C), giving $1\,\sigma$ uncertainties of $\log\,\xi = 1.45\pm0.05$, $\log\,N_H = 22.9\pm0.4\,\mathrm{cm}^{-2}$ and $\log\,v_{turb} = 2.25\pm0.5\,\mathrm{km\ s}^{-1}$.

This model is plotted in Fig. 5.12.

5.5.1 Testing Further Geometries with CLOUDY

In the previous section the 770 ks spectrum has been fitted with simulated spectra from CLOUDY models. As stated above, this is only one geometrical possibility for the NLR region, and so this section looks into other potential geometries using different CLOUDY outputs[4].

Four main different geometries are compared to draw some simple conclusions; this is by no means a full investigation into all possible geometries of this system. These tests were all done with the CLOUDY grid of models used in the previous section, but with varying outputs used.

Geometry 1) The simplest interpretation of the reflected output, adopted in the previous section, is that emission is observed from the illuminated face of NLR clouds, which could be on the opposite side of the source to the observer's

[4]For detailed information of CLOUDY's geometry see Chapter 4 and Hazy 1, page 6

line of sight, or on the near side of the the source but out of the observer's line of sight.

Geometry 2) Emission could be observed from the shielded face of NLR clouds on the same side of the source as the observer. The CLOUDY outputs of transmitted lines and diffuse emission were additively combined to approximate this geometry. The best fit parameters for this geometry gave a C-stat value of ∼300 larger than the best fit for geometry 1), with smaller N_H, but very similar ξ and v_{turb} values ($\log \xi = 1.5$, $\log N_H = 22$ and $\log v_{turb} = 2.5$).

Geometry 3) Emission from a combination of two ionisation cones, one either side of the source, could be observed, i.e. emission from both the illuminated face of NLR clouds on the far side of the source and the shielded face of NLR clouds on the near side of the source, with respect to the observer. This is similar to the 'Two cone model' discussed in Sect. 5.4.3, and was modelled using a combination of the outputs used for geometries 1) and 2) above. To restrict the permutations of this geometry, and therefore reduce computational time, the simplifying assumption was made that both the near and far NLR ionisation cones have the same parameters (ξ, N_H and v_{turb}). The reflected output (representing emission from clouds on the far side of the source) was given a positive velocity shift (+300 km s^{-1}) and the transmitted outputs (representing emission from clouds on the near side of the source) were given a negative velocity shift of (-300 km s^{-1}), so that both are outflowing away from the source. This geometry was tested in three ways: i) with no absorption of either emission components, ii) with absorption of the far clouds' emission (the reflected output) by WA components B and E and no absorption of the near clouds' emission, and iii) with absorption of the far clouds' emission (the reflected output) by all WA components (A-F) and no absorption of the near clouds' emission. In all three cases, i), ii) and iii), the best fit parameters were: $\log \xi = 1.5$, $\log N_H = 22.25$ and $\log v_{turb} = 2.5$. The best of these cases, in terms of C-statistic value, is ii), but even in this case the C-statistic value is ∼200 larger than the best fit for geometry 1).

Geometry 4) Emission from both the illuminated and shielded faces of the NLR clouds within one ionisation cone, on the near side of the source, could

be observed. In this case, the illuminated faces of clouds out of the observer's line of sight and the shielded faces of clouds within the observer's line of sight are both seen. Again, the simplifying assumption was made that both types of outputs correspond to the same input parameters, which would be expected as both are coming from the same ionisation cone. This geometry also combines the outputs used for geometries 1) and 2) above, but differently to geometry 3), as all the gas in this scenario is outflowing towards the observer, so all outputs are given a velocity shift of -300 km s^{-1}. In this test, emission from outside the observer's line of sight is absorbed by WA components B and E while emission from the observer's line of sight is not absorbed by any intrinsic WA components. This geometry gives an improved C-statistic (ΔC of $\sim$50) with very similar best fit parameters of $\log \xi = 1.5$, $\log N_H = 22.5$ and $\log v_{turb} = 2.5$, and 80% of the emission line luminosity coming from the illuminated face of the cloud. The best fit parameters found in this test are within the uncertainties calculated when only the reflected output was used to model the line emission, demonstrating the robustness of these values.

These tests have shown that, when comparing these simple geometries, the observed emission is likely to originate in the ionisation cone on the near side of the source, with the illuminated face of the cloud (as modelled in Cloudy) producing the majority of the X-ray narrow line emission from NGC 5548. However, it is very likely that the geometry in this system is more complex than the plane-parallel clouds assumed in Cloudy.

5.6 Discussion

As previously stated, the 2013-14 770 ks RGS spectrum shows the largest number of soft X-ray narrow emission lines and RRC features ever observed in NGC 5548. In total, fourteen narrow lines and eight RRCs are detected, with an upper limit for one more narrow emission line. Due to the low soft X-ray continuum flux during these observations, six narrow lines and six RRCs are identified that had not previously been detected in NGC 5548. New parameters are also presented for eight narrow emission lines and two RRCs identified in previous observations of this source.

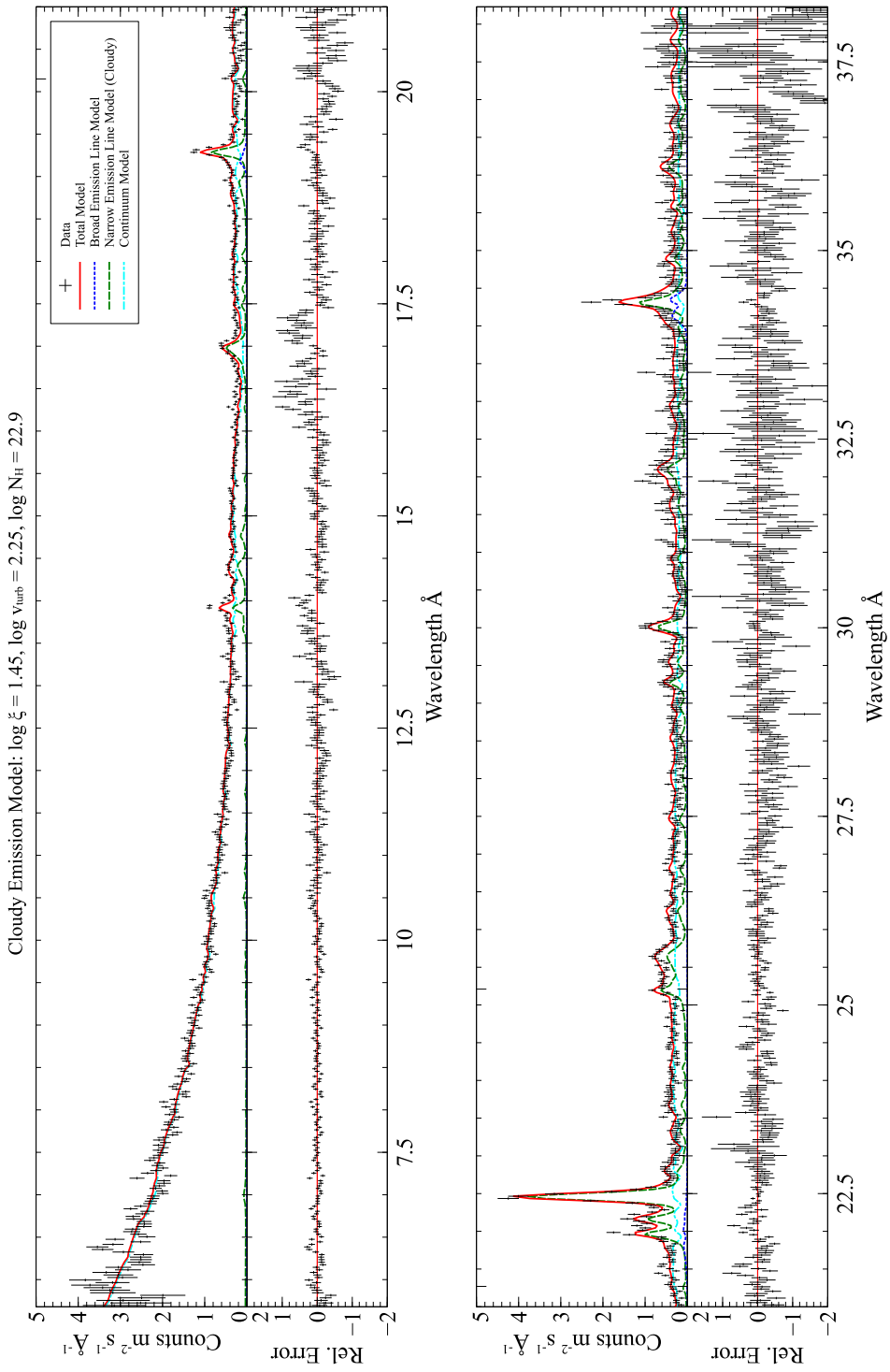

Fig. 5.12: Best fit self-consistent photoionisation model from CLOUDY for all emission features (5.7 - 38.2Å), including absorption from X-ray WA components B & E (see Kaastra et al. 2014 for details). C-statistic: 2273. The data are shown in black, the best fit model is shown in red and the components of this model are shown in different colours and line styles. The relative error between the data and best fit model is shown underneath each of the main plots.

Six of the ten narrow lines found by Steenbrugge et al. (2005) are detected; one of their lines (C V f) falls outside the RGS wavelength range, and the other three (Mg XI f, Al XII f & Si XIII f) are in the steep, noisy short wavelength part of the spectrum, so it is very difficult to set stringent limits to their parameters using these data.

Using photoionisation models from CLOUDY, the emitting gas has been parameterised by an ionisation parameter of $\log \xi = 1.45 \pm 0.05$, column density of $\log N_H = 22.9 \pm 0.4\,\mathrm{cm}^{-2}$ and turbulent velocity of $\log v_{turb} = 2.25 \pm 0.5\,\mathrm{km\ s}^{-1}$. Using the same conversion between the ionisation parameters of ξ and U as in Arav et al. (2015) for the historical SED of NGC 5548 ($\log \xi = \log \mathrm{U} + 1.6$), gives an estimate for the emitting gas of $\log \mathrm{U} = -0.15 \pm 0.05$. The ionisation parameter and column density from this work can now be compared to similar work on other Seyfert objects (see Table 5.9 for a summary of previous work). The column density value ($10^{22.9 \pm 0.4}\,\mathrm{cm}^{-2}$) is similar to the highest values found for other objects. For example NGC 4051, NGC 4151 and NGC 1365 (by Nucita et al. 2010; Armentrout et al. 2007; Guainazzi et al. 2009, respectively) are all found to need emitting gas with column densities of the order of $10^{23}\,\mathrm{cm}^{-2}$ in order to model their X-ray NLR emission. The NGC 5548 narrow line-emitting gas ionisation parameter, converted to $\log \mathrm{U} = -0.15 \pm 0.05$, is lower than for most other Seyfert galaxies, except for the low ionisation component of the three phase model for NGC 4151 (Armentrout et al. 2007). As expected, the ionisation parameter is higher than that needed to model the UV narrow emission lines in NGC 5548 itself (Kraemer et al. 1998). Due to the much higher soft X-ray continuum flux in previous observations of NGC 5548, and therefore a much smaller number of measurable X-ray narrow emission lines, this is the first time photoionisation modelling has been used to constrain the ionisation parameter and column density of the X-ray narrow-line emitting gas in this galaxy.

5.6.1 Warm Absorption of the NLR

The initial fit (using a *Gaussian* model in SPEX for each narrow line) to the 2013-14 stacked spectrum of 770 ks shows a difference in velocity between the O VII resonance line ($-20 \pm 50\,\mathrm{km\ s}^{-1}$) and the forbidden and intercombina-

Table 5.9: Previously reported results of Seyfert galaxy narrow line region modelling using CLOUDY

Reference	Galaxy	Type	Wavelength Band	CLOUDY parameters of emitting gas		
				No. of Phases	Ionization $\log U$	Density (cm^{-3}) $\log n_H$
Kraemer et al. 1998	NGC 5548	Seyfert 1	UV	2	-1.5	7
					-2.5	4
Reference	Galaxy	Type	Wavelength Band	CLOUDY parameters of emitting gas		
				No. of Phases	Ionization $\log U$	Column Density (cm^{-2}) $\log N_H$
Armentrout et al. 2007	NGC 4151	Seyfert 1.5	X-ray	3	1.3	23
					0	23
					-0.5	20.5
Longinotti et al. 2008	Mrk 335	Seyfert 1	X-ray	2	0.4	≤ 22
					0.8	≤ 22
Guainazzi et al. 2009 [a]	NGC 1365	Seyfert 1.8	X-ray	1	$1.6^{+0.3}_{-0.4}$	≥ 22
Nucita et al. 2010	NGC 4051	Seyfert 1	X-ray	2	$0.6 < \log U < 1.9$	21.77-22.72
Marinucci et al. 2010	NGC 424	Seyfert 2	X-ray	2	$0.23 < \log U < 1.41$	21.77-22.11

[a]These authors also found strong evidence for a contribution from collisional components, related to the known ring of starburst activity in this object and not specified here

tion lines (-320 ± 40 km s^{-1} and -480 ± 160 km s^{-1}, respectively). This result is hard to interpret physically; the triplet lines should all be formed by the same gas and therefore have consistent velocities. The work in this chapter investigates possible explanations for this mismatch of velocities such as calibration effects, emission from two ionisation cones, and absorption, concluding that absorption is most likely (as detailed in Sect. 5.4.3).

An alternative hypothesis could be considered, that the O VII triplet may be a superposition of emission by photoionised and collisional plasmas, such as found in star forming regions. However, this is very unlikely; NGC 5548 does not have a high star formation rate, and the AGN is too bright to allow any star formation rate contribution to be detected unless it were a very significant one (Doroshenko et al. 1998). To test this interpretation a collisionally excited emission model was fitted on top of a non-absorbed photoionised emission model, showing that the upper limit for contributions from collisionally excited line emission is 4% of the luminosity of the photoionised emission (calculated over the RGS wavelength range).

The main result of this chapter, which resolves the velocity discrepancy of the O VII triplet, is by having the narrow emission lines absorbed by at least one of the six X-ray WA components found by Kaastra et al. (2014). The implications of this in terms of the distance of the NLR from the source are discussed in Sect. 5.6.3 below.

A similar result has been obtained for the UV narrow emission lines in NGC 7469, where Kriss et al. (2003) found that the best fit to their Far Ultraviolet Spectroscopic Explorer (FUSE) data included absorption of the narrow emission line components by the UV warm absorbers, at the same covering fraction as the absorption of the broad emission lines and continuum.

Using the best fit model from the scenario with absorption of both the narrow emission lines and RRC features by WA components B and E, the ratio of the unabsorbed flux of O VII RRC to the O VII forbidden line (RRC/f) was calculated, as was done in Kaastra et al. (2002). The 2013-14 absorption scenario RRC/f value is 0.44 ± 0.05, much closer to (and consistent within 3σ to) the value of 0.57 from Behar et al. (2002) photoionisation models for

an adopted temperature of 5 eV [5] than to the value from the 1999 observations (0.07 ± 0.12; Kaastra et al. 2002). Kaastra et al. (2002) suggest that their smaller than expected RRC/f value may be due to a combination of limited statistics and nearby WA absorption features contaminating the RRC flux measurement. Without WA absorption of either narrow emission lines or RRCs, a smaller than expected RRC/f value is also observed in the 2013-14 data (0.28 ± 0.03), which again is not consistent with the model value. Therefore including the absorption by WA components B and E of both the RRCs and the narrow emission lines greatly reduces the tension between observed and modelled O VII RRC/f values, further supporting this absorption scenario.

5.6.2 NLR Reacting to Unobscured SED

Fitting simulated spectra from Cloudy (see Sect. 5.5) to both RGS and EPIC data shows that the narrow-line emitting gas is still reacting to the unobscured SED. This implies that no additional variation in the narrow lines should be expected compared to previous observations and levels of variability between them. As previous analysis of historical observations did not take into account any absorption of the narrow lines by the WAs, the same assumptions as in previous analyses must be made in order to compare appropriately. The 2013-14 O VII f unabsorbed flux, calculated without including any absorption by WA components, is $0.65^{+0.01}_{-0.05}$ photons $\mathrm{m}^{-2}\,\mathrm{s}^{-1}$, which is between values from observations between 1999 and 2001 (4 observations, with flux values 0.81 ± 0.16, 0.82 ± 0.18, 1.3 ± 0.2 and 1.1 ± 0.1 photons $\mathrm{m}^{-2}\,\mathrm{s}^{-1}$, in chronological order), and the 2005 and 2007 values (0.35 ± 0.06 and 0.27 ± 0.06 photons $\mathrm{m}^{-2}\,\mathrm{s}^{-1}$ respectively), when the source was seen in an unobscured but intrinsically low-flux state (these historical measurements of O VII f fluxes are collated in Detmers et al. 2009). The unabsorbed flux of the O VII f line in 2002 (0.75 ± 0.07 photons $\mathrm{m}^{-2}\,\mathrm{s}^{-1}$) is the historical value closest to the 2013-14 measurement, still differing from it by just over the 1σ level. In conclusion,

[5] As the temperature dependence of this ratio is weak (Kaastra et al. 2002), and the best fit temperature from the pair of oxygen RRCs (O VII and O VIII) is 6.6 ± 0.06 eV, this is a reasonable comparison to make

there is marginal evidence for variability between 2013-14 and some previous epochs, which is well within the expected range for this source (Detmers et al. 2009). This supports the claim that the NLR is still reacting to the unobscured SED, as it would have been during all these previous epochs.

5.6.3 Distance and Density Estimates of NGC 5548's X-ray NLR

In the best fit absorption scenario, the emitting gas (determined from CLOUDY modelling) has the parameters: $\log \xi = 1.45 \pm 0.05$, $\log N_H = 22.9 \pm 0.4$ and $\log \mathrm{v}_{turb} = 2.25 \pm 0.5$.

Using this result, and the definition of ξ ($\xi \equiv L/nr^2$, see Chapter 2), a lower limit to the distance of the emitting gas from the source can be determined (I take $n < 5 \times 10^9\,\mathrm{cm}^{-3}$, because this is the critical density for O VII (Porquet and Dubau 2000) and as this gas is known to be photoionised by the presence of narrow RRCs, the density must be below this value). The luminosity of the unobscured 2013-14 SED L ($= 11.7 \times 10^{43}\,\mathrm{ergs\,s}^{-1}$) is taken from Mehdipour et al. (2015), and ξ ($\log \xi = 1.45$) is taken from the CLOUDY best fit to the data. This gives a (not very restrictive) lower limit to the distance of the emitting gas of $r > 9.3 \times 10^{-3}\,\mathrm{pc}$.

For another distance estimate, the column density, N_H, can be written as:

$$N_H = \int_{r_{min}}^{r_{max}} n_H dr = \frac{n_H}{n_e}\frac{L}{\xi}\left(\frac{1}{r_{min}} - \frac{1}{r_{max}}\right) \tag{5.1}$$

which, using the same method as Behar et al. (2003) and assuming $r_{max} \gg r_{min}$, can be rewritten as:

$$r_{min} \simeq (r_{min}^{-1} - r_{max}^{-1})^{-1} = \frac{n_H}{n_e}\frac{L}{\xi N_H}. \tag{5.2}$$

Using the simplifying relation $n_e = 1.2 n_H$ (for a fully ionized cosmic plasma), and the values of L, ξ and N_H (see previous paragraph), $r_{min} = 13.9 \pm 0.6\,\mathrm{pc}$ is calculated. While this is consistent with the previous distance estimate of 1-15 pc for the X-ray NLR by Detmers et al. (2009), if the gas is clumpy or consists of compact clouds (i.e. $\Delta \mathrm{r} = \mathrm{r}_{max} - \mathrm{r}_{min} \ll \mathrm{r}$) then the location derived here will move inwards.

Spectral modelling has determined the velocity broadening of the emitting gas to be $460 \pm 30\,\mathrm{km\ s}^{-1}$ (measured by Kaastra et al. 2014, and consistent with

the CLOUDY modelling in this work). This broadening can be assumed to be from Keplerian motion of the gas (potentially not the case if some broadening arises from the outflow), and then the Virial Theorem can be used to calculate the distance r:

$$v^2 = \frac{GM}{r} \tag{5.3}$$

where v = velocity broadening, G = the gravitational constant, and M = mass of the central black hole ($6.54 \pm 0.25 \times 10^7 M_\odot$; Bentz et al. 2007). This gives an estimate that the distance of the emitting gas is 1.3 ± 0.1 pc from the central source.

Using this distance, and the definition of the ionisation parameter ξ (see Chapter 2), the density of the gas can also be estimated to be $2.4 \times 10^5\,\mathrm{cm}^{-3}$, consistent with the upper limit given by the O VII critical density (above).

Combining this density with the column density of $\log N_H = 22.9 \pm 0.4\,\mathrm{cm}^{-2}$, from the CLOUDY modelling in Section 5.5, gives a size estimate for the emitting gas of Δr = 0.13 pc.

As the emitting gas is still reacting to the unobscured SED, this lack of response to the obscured SED for at least one year can be used to approximate another distance. Using light crossing arguments (r > c Δt, where Δt = one year, the time since the continuum altered, from which the gas has not yet responded, and c = speed of light), this gives a lower limit estimate of 0.3 pc, supporting the parsec scale expectations from the previous calculations.

The other possibility is that the O VII emitting gas has not yet recombined after the decrease in continuum intensity. Recombination time is related to the gas density, by t $\sim \frac{1}{\alpha n_e}$, where α is the recombination coefficient. Using the temperature measured from the RRCs (see Sect. 5.4.4) α is determined to be $7 \times 10^{-12}\,\mathrm{cm}^3\,\mathrm{s}^{-1}$ for O VII (see Nahar and Pradhan 2003, for the calculation), and the recombination time can be assumed to be at least one year. This gives a density estimate of $4.5 \times 10^3\,\mathrm{cm}^{-3}$ which, using the definition of ξ, leads to a distance estimate of 9.8 pc.

Finally, using the emission measure from the RRC features and assuming a quasi-spherical distribution of emitting gas clouds, the volume filling factor of the gas can be estimated from the integral of $\mathrm{n}^2\,d\mathrm{V}$ (as done in Reeves et al.

2016a):

$$\text{Emission Measure} = \int n_e n_H V = \int n^2 V \sim \frac{4}{3}\pi \mathrm{r}^3 \mathrm{V}_f n^2 \tag{5.4}$$

where V_f = the volume filling factor. Assuming the distance of the gas is on the parsec scale and the gas density is of the order of $10^4\,\mathrm{cm}^{-3}$, supported by the calculations above, gives $\mathrm{V}_f = 5 \times 10^{-4}$. This is consistent with the emitting gas being clumpy.

Both the distance of a few parsecs and density of the order of $10^4\,\mathrm{cm}^{-3}$ are in line with expectations for optical NLR gas (see Chapter 1).

It should be also noted that the $\log \xi$ value of the emitting gas found from CLOUDY analysis, 1.45 ± 0.05, is consistent with the 2002 $\log \xi$ value of WA component B (1.51 ± 0.05, when the WAs were reacting to the unobscured ionizing flux). Combining this with the consistent distance estimates for the X-ray NLR ($r_{min} = 13.9 \pm 0.6$ pc, this work; 1-15 pc, Detmers et al. 2009) and for WA component B (<40 pc, Ebrero et al. 2016), can the NLR emission gas be identified with the WA absorption gas? The column density for the emitting gas determined with CLOUDY, $\log N_H = 22.9 \pm 0.4\,\mathrm{cm}^{-2}$, is higher than the combined column densities of all WA components. However, WAs are seen along the line of sight while the X-ray NLR emission is likely coming from a much larger region, given the fact that it is still reacting to the unobscured SED, so there could be column density variations over that region. The coincidence of ionisation parameters and compatible distances of the X-ray NLR gas with one of the WA components is not seen here as enough evidence to conclusively identify any of the WA components as the same physical gas as the narrow-line emitting gas, although it is suggestive of that possibility.

5.7 Conclusions

I have used the 770 ks RGS spectrum of NGC 5548 from the 2013-14 observational campaign to show evidence that the narrow emission lines undergo absorption by at least one of the six known warm absorber (WA) components in this source. There are indications that the main absorption comes from WA component B (labelled as such by Kaastra et al. 2014), established from analysis of the O VII triplet in the wavelength range 21.5-23 Å. This solu-

tion also resolves tension between modelled and observed values of the O VII RRC/f unabsorbed flux ratio. Unfortunately the data do not allow to conclusively distinguish between competing detailed scenarios of absorption of the narrow emission lines by different combinations of WA components. The presence of this absorption is a more important result than which of the specific components are causing it.

Through comparison to simulated spectra produced by the photoionisation code CLOUDY, both RGS and EPIC-pn data are used to determine that the emitting gas can be described as reacting to the unobscured SED (i.e. to ionising radiation before the intervention of the 'obscurer' discovered in the 2013-14 observing campaign). The emitting gas has a well constrained ionisation parameter of $\log \xi = 1.45 \pm 0.05$ and column density and turbulent velocity of $\log N_H = 22.9 \pm 0.4\,\mathrm{cm}^{-2}$ and $\log v_{turb} = 2.25 \pm 0.5\,\mathrm{km\ s}^{-1}$ respectively. This is the first time the X-ray NLR emitting gas in this source has been characterised by an ionisation parameter and column density.

Chapter 6

NGC 1365: X-ray Narrow Emission Lines (2004-13)

"You always have two choices: your commitment versus your fear"

Sammy Davis, Jr.

This chapter is based on Whewell et al. (2016).

6.1 Introduction to NGC 1365

NGC 1365 (z = 0.0055) has an interesting observational classification history. Optically it has been called a Seyfert 1.5, 1.8 or 2 by different authors (e.g. Véron et al. 1980; Maiolino and Rieke 1995; Turner et al. 1993, respectively). Most recent X-ray papers have classified NGC 1365 as a Seyfert 2 owing to the column density of neutral material ($> 1.5 \times 10^{23}$ cm^{-2}, Risaliti et al. 2007, 2009a) covering its X-ray emission (intrinsic $L_{2-10\,keV} \sim 10^{42}\,\mathrm{erg\,s^{-1}}$ Risaliti et al. 2005b). NGC 1365 is also referred to as a 'changing-look' Seyfert because of the variable intrinsic obscuration ranging from Compton thin (as low as $N_H \sim 10^{22}\,\mathrm{cm^{-2}}$) to Compton thick ($N_H \sim 10^{24}\,\mathrm{cm^{-2}}$) (Matt et al. 2003).

Notably, especially for this work, there is a nuclear starburst in NGC 1365 with a diameter of 10", which is resolved in X-rays (using Chandra, Wang et al. 2009), and in optical wavelengths into multiple compact star clusters (using the HST Faint Object Camera, Kristen et al. 1997). This is often referred to as a 'ring', and it is called so in this work, although there is some evidence from radio emission that the ring is incomplete (Beck et al. 2005). Starburst

Table 6.1: *XMM-Newton* and *Chandra* observations of the nuclear region of NGC 1365 and where the data have been analysed. The final four *XMM-Newton* observations were taken simultaneously with *NuSTAR*. References as follows: (1): Risaliti et al. (2005b); (2): Risaliti et al. (2005a); (3): Risaliti et al. (2007); (4): Wang et al. (2009); (5): Guainazzi et al. (2009); (6): Risaliti et al. (2009b); (7): Risaliti et al. (2009a); (8): Risaliti et al. (2013); (9) Connolly et al. (2014); (10): Parker et al. (2014); (11): Braito et al. (2014); (12): Walton et al. (2014); (13): Nardini et al. (2015); (14): Rivers et al. (2015)

Telescope	Start of obs.	Obs. ID	Duration (ks) [a]	References
Chandra	2002-12-24	3554	15	1, 9
XMM-Newton	2004-01-17	0205590301	59.7	2, 7, 5, 10
XMM-Newton	2004-07-24	0205590401	68.8	2, 5, 10
Chandra	2006-04-17	6868	15	3, 4
Chandra	2006-04-20	6869	15	3, 4
Chandra	2006-04-23	6870	15	3, 4
Chandra	2006-04-10	6871	15	3, 4
Chandra	2006-04-12	6872	15	3, 4
Chandra	2006-04-12	6873	15	3, 4
XMM-Newton	2007-06-30	0505140201	128.9	6, 5, 10
XMM-Newton	2007-07-02	0505140401	131.1	6, 5, 10
XMM-Newton	2007-07-04	0505140501	130.9	6, 5, 10
Chandra	2012-04-09	13920	90	11, 13
Chandra	2012-04-12	13920	120	11, 13
XMM-Newton	2012-07-25	0692840201	138.5	8, 10, 12, 14
XMM-Newton	2012-12-24	0692840301	126.2	10, 12, 14
XMM-Newton	2013-01-23	0692840401	133.6	11, 10, 12, 14
XMM-Newton	2013-02-12	0692840501	134.7	10, 12, 14

[a]For *Chandra* observations the scheduled length is quoted

regions are known to produce soft X-rays primarily from collisionally excited, shock-heated gas, and hard X-rays mainly from accreting compact objects such as X-ray binaries. Any interpretation of soft X-ray emission from AGN photoionised gas in NGC 1365 must take this surrounding starburst emission into account.

Recently, four joint observations of NGC 1365 with *NuSTAR* and *XMM-Newton* have revealed evidence that is used to explain the presence of a broad Fe K line at ~ 6.4 keV and a Compton reflection component via a relativistic reflection model. Risaliti et al. (2013) analysed the first of these four observations and found that the relativisic reflection model explains the X-ray spectral features much better than an absorption-dominated model with no relativistic reflection, both on statistical and physical (comparison to emission at other wavelengths) grounds. Walton et al. (2014) extended this work and analysed all four observations in this series, finding that relativistic reflection models independently fitted to each of the four observations gave consistent parameters, futher supporting this model. In this model the reflection of hard X-rays from the inner edge of an accretion disk, coupled with rapid rotation and relativistic effects near the black hole, alters the shape of the Fe K emission line and also produces a excess of emission over the expected continuum at higher energies (10-80 keV; known as the 'Compton hump'). This is in addition to the already known 'distant' reflection component, which produces the narrow Fe K line seen in the data. The competing theory to explain the spectral shape around the narrow Fe K emission line observed in some AGN, is that absorption from gas within the source causes these features. In the case of NGC 1365, Miller and Turner (2013) argue that Risaliti et al. (2013) do not test an accurately modelled absorption scenario, but as Miller and Turner (2013) themselves do not fit their absorption model to data for NGC 1365 their model is not used in this thesis for any further analysis.

It is well established that the variability seen in the spectrum of NGC 1365 is caused by variations in photoelectric absorption. Recently, Parker et al. (2014) showed this in a model independent way by using Principal Component Analysis (PCA). Comparing PCA results of analysis of NGC 1365 to results

from model spectra, varied in different physical ways, showed that variable absorption causes $> 90\,\%$ of the variability in NGC 1365's observed spectra. The details of the complex phases of X-ray absorbing gas found in this source are summarised below.

6.1.1 Emission Line Gas

Gas photoionised by the central AGN of NGC 1365 has been studied in both optical and X-ray bands. Optical line ratios in an asymmetrical conical region suggests photoionisation by the AGN (Veilleux et al. 2003; Schulz et al. 1999).

NGC 1365 was the first AGN where high-quality, high-resolution soft X-ray spectra showed emission lines dominated by collisionally ionised gas (Guainazzi et al. 2009). In their analysis of a ∼500 ks stacked spectrum collected by RGS between 2004 and 2007, Guainazzi et al. (2009) model the emission lines with two collisional components (kT∼300 and ∼640 eV) and one loosely constrained photoionised component ($N_H \geq 10^{22}\,\mathrm{cm}^{-2}$, $\log \mathrm{U} = 1.6^{+0.3}_{-0.4}$, $n_e \leq 10^{10}\,\mathrm{cm}^{-3}$).

Studies since Guainazzi et al. (2009) have confirmed the two collisional phases of emission line gas. Characterising the photoionised emission in the presence of this collisional emission has been difficult, but restricting the spatial dimension of *Chandra* HETGS spectra allowed Nardini et al. (2015) to reduce the contribution of collisional emission from the circumnuclear starburst ring in their spectra compared to previous analyses (e.g. Guainazzi et al. 2009). They confirm the presence of photoionised emission, as well as two collisionally ionised phases with different temperatures to those found by Guainazzi et al. (2009) (∼150 eV and ∼1200 eV as opposed to ∼300 eV and ∼640 eV). Nardini et al. (2015) accept that the spectral quality of their data is limited by lack of photon counts and therefore a detailed characterisation of the photoionised emission lines cannot be done with this dataset. The authors loosely constrain the temperature and density of the emitting gas to $T < 3 \times 10^6\,\mathrm{K}$ and $n < 10^{13} - 10^{14}\,\mathrm{cm}^{-3}$ respectively. They could fit the spectrum with three photoionised emission models at ionisations of $\log \xi > 4.1, \sim 3.1 \pm 0.3$ and < 0.6 but recommend interpretation of this as simply proof of the existence of a large range of ionisation states.

Using the *Chandra* data, Nardini et al. (2015) estimated the location of the photoionised gas to be 'across the virtual BLR/NLR boundary', based on some evidence of broadening of the emission lines ($\sim 1000\,\mathrm{km\ s^{-1}}$). Guainazzi et al. (2009) tentatively suggested the inner face of the photoionised gas could be $\geq 0.75\,\mathrm{pc}$ from the source, potentially placing it within the BLR. Braito et al. (2014) use an *XMM-Newton* observation in 2013 (RGS and EPIC) and also conclude that some emission line gas is located within the BLR, as they see the Mg XII Ly-α emission line increase in strength as their measured absorption decreases. They interpret this as either the uncovering of emission from within their most variable absorber ($r < 10^{17}\,\mathrm{cm}$) or ionised gas responding to a change in its illuminating continuum, which (given the likely timescales) would have to be a compact region and then would likely be located at $r \sim 10^{15}\,\mathrm{cm}$ from the source.

Finally, Braito et al. (2014) suggest that the Mg XII emission and absorption lines in the highest flux part of their observation are reminiscent of a classical P-Cygni profile, and therefore could hint at a common origin for both from an outflowing wind.

6.1.2 X-ray Absorbers

The X-ray absorption complex within NGC 1365's nuclear region has been studied in detail. In addition to the original neutral absorber characterised by Risaliti et al. (2005b), shown to cause the main variability seen from the source (Risaliti et al. 2005b, 2009b; Parker et al. 2014), many other absorption layers have also been detected with X-ray data.

Risaliti et al. (2005a) found absorption lines between 6.7 and 8.3 keV with *XMM-Newton* EPIC data of the source in a Compton-thin state, which they attribute to an absorber originating from an accretion disk wind.

By analysing one 120 ks (2013) *XMM-Newton* observation in detail, Braito et al. (2014) find at least two ionised absorber phases (and evidence for a third), which are needed to fit the RGS spectrum, as well as a neutral absorber needed to fit the EPIC spectrum (not statistically required in the RGS band). The lowest ionisation phase of these three is found to be partially covering and variable in column density over timescales as short as 40 ks (within the

120 ks observation). The three ionised absorber phases they use are each responsible for different signatures within the data. Their highest ionisation phase ($\log \xi = 3.8$), which causes the absorption features around the Fe K line complex (the absorption lines found by Risaliti et al. 2005a), is outflowing at 3900 km s^{-1}, and is only needed by the EPIC spectrum. Their mid ionisation phase ($\log \xi = 2.1$) produces Mg, Si and S absorption lines, fitted in both RGS and EPIC spectra, and with an RGS measured outflow velocity of 1200 km s^{-1}. Their lowest ionisation phase ($\log \xi < 1$) causes spectral curvature in the EPIC spectrum and the Fe UTA in the RGS spectrum. Braito et al. (2014) propose that the three ionised absorber phases are part of a disk wind, and the lowest ionisation phase could be identified as the partially covering neutral absorber previously detected by Risaliti et al. (2005b), located around the distance of the BLR ($r < 10^{16}$ cm; e.g. Brenneman et al. 2013; Risaliti et al. 2005a).

The same four 2012-13 joint *XMM-Newton* and *NuSTAR* observations analysed by Walton et al. (2014), Risaliti et al. (2013) and Braito et al. (2014) were also studied by Rivers et al. (2015), to untangle any extra complexities and layers of neutral absorption. The Rivers et al. (2015) model also includes absorption lines to represent the ionised absorption discovered around 6-8 keV by Risaliti et al. (2005a). They observed that when the source becomes uncovered by its high column density partially covering absorber (the covering fraction decreases), such as in observations 2, 3 and 4 of this set (in Dec 2012, Jan 2013 and Feb 2013 respectively), an additional layer of fully covering neutral absorption is needed to fit the spectrum.

Their model for a partially covering layer of absorption varies substantially within and between observations 1, 3 and 4. Its behaviour during observations 1 and 4 is similar, with column density changes but no covering fraction changes, and here Rivers et al. (2015) call it a "partial-covering 'high column density' absorber". Its behaviour in observation 3 is very different, with a rapid drop of both covering factor and column density, which Rivers et al. (2015) refer to as an uncovering of the source, and call this a "patchy partial-covering" absorber instead. They argue that these two different behaviours are evidence that the one partial covering model they use actually

tracks different layers of the absorption, in reality distinct from each other.

The work in this chapter looks at the RGS data from all four of these 2012-13 *XMM-Newton* observations, and at the *XMM-Newton* observations from 2004 and 2007, in order to analyse in a uniform way and further characterise the X-ray narrow-line emitting photoionised gas. This chapter is structured as follows: Sect. 6.2 describes the observations; Sect. 6.3 presents an analysis of the emission line spectrum from NGC 1365, firstly using Gaussian line models (Sect. 6.3.1) before moving on to a combination of physically motivated emission models (Sect. 6.3.5). The implications are discussed in Sect. 6.4, and finally the work is concluded in Sect. 6.5.

6.2 Observations and Data Reduction

In this work I consider the nine *XMM-Newton* observations of NGC 1365, obtained from the *XMM-Newton* Science Archive; two from 2004, three from 2007, two from 2012 and two from 2013 (see Table 6.1). Only the RGS data from each observation are used as they are the only data of high enough resolution to study the narrow emission lines.

The data are reduced as described in Chapter 4, for one spectrum for each observation, combining both RGS chains and both spectral orders.

The RGS data are analysed in the range 11-38 Å, with a bin size of 0.033 Å, which over-samples the RGS resolution element of ∼0.07 Å. As discussed below the spectra vary between observations shortwards of 11 Å, which makes the continuum uncertain in the stacked, time-averaged spectra used in this work. All the spectra in this chapter are shown as background-subtracted and in the observed frame. The spectral analysis and modelling for this work was done with SPEX (v.2.06.01).

6.3 Analysis

The 2012-13 observations (1, 2, 3 and 4) were first compared by eye, and I determined that observations 1, 2 and 4 are very similar above 11 Å. I stacked these three observations together to begin the analysis, with a combined exposure time of ∼355 ks. Observation 3 has a lower level of absorption than the others (Braito et al. 2014).

I also reduced and stacked the five observations taken in 2004 and 2007, giving a stacked spectrum of ∼419 ks, in order to compare these results with Guainazzi et al. (2009) and to check any variation of the emission lines over time. I return to the individual observations to look for variations between their emission lines after establishing a baseline model (Sect. 6.3.2).

As already discussed in Chapter 4, when using C-statistic to fit models in SPEX, as well as the calculated C-statistic value, SPEX also gives the expected C-statistic value and its r.m.s. uncertainty to help the user determine goodness-of-fit. For the 2012-13 stacked spectrum the expected C-statistic is 911 ± 43 and for the 2004-07 stacked spectrum it is 907 ± 43.

6.3.1 Testing the 2012-13 Stacked Spectrum with Continuum Model and Gaussian Lines

As Braito et al. (2014) have previously analysed the Jan 2013 observation (Obs. 3, the least absorbed of the four 2012-13 observations), this analysis begins by using their continuum and absorption model. Their use of EPIC data allows much better contraints of the continuum than is possible using just the RGS data. As observation 3 has lower neutral absorption than the other 2012-13 observations, it reveals ionised absorber phases not previously seen. For this a power law model, absorbed by three ionised absorbers ($\log \xi$ of 3.77, 2.15 and 0.17, as in Table 4 of Braito et al. 2014) was used. The power law normalisation was left free to vary, and Γ was fixed to a value of 2.1 to match their EPIC fits. At this stage I have not fitted any of the emission lines, so have an unacceptable C-statistic value of >7000.

Gaussian lines were then fitted to the data to represent the narrow emission lines, adding a Gaussian if the best fit C-statistic improves by 6.25, corresponding to a 90% confidence level for three extra free parameters (normalisation, width and peak wavelength). These Gaussian models are only absorbed by the Galactic N_H, and none of the absorption intrinsic to NGC 1365. For the He-like triplets in this wavelength range I included three components (resonance, intercombination and forbidden) if at least one was detected at the 90% level. These 'triplets' really include four components, but at RGS resolution the two components of the intercombination line cannot be separated. I also

Table 6.2: Narrow emission line best fit intensities from the 2012-13 stacked spectrum and 2004-07 stacked spectrum. A star marks uncertainty in the assigned transition. G09 refers to Guainazzi et al. (2009). Overall C-statistic = 1445 (2012-13) and 1548 (2004-07)

Line Transition [a]	Rest λ (Å)	2012-13 Intensity (10^{-5} ph cm^{-2} s^{-1})	2004-07 Intensity (10^{-5} ph cm^{-2} s^{-1})	2004-07 (G09) Intensity (10^{-5} ph cm^{-2} s^{-1})
Ne X 1s-2p	12.14	0.85±0.11	1.12±0.11	1.0±0.2
Fe XXI *	12.29	0.20±0.09	0.21±0.08	-
Ne IX r	13.45	0.99±0.13	1.28±0.11	0.42±0.18
Ne IX i	13.55	<0.13	<0.08	<0.33
Ne IX f	13.70	0.90±0.10	$1.02^{+0.08}_{-0.02}$	0.40±0.12
O VIII RRC	14.23	0.44±0.07	0.59±0.07	0.42±0.13
Fe XVIII *	14.41	0.33±0.10	0.20±0.05	-
Fe XVII 3d-2p	15.03	1.63±0.09	1.66±0.09	1.49±0.17
O VIII 1s-4p /	15.18			
Fe XVII 3d-2p	15.26	1.18±0.10	$1.02^{+0.08}_{-0.03}$	-
O VIII 1s-3p	16.01	0.87±0.08	0.81±0.07	0.75±0.13
O VII RRC /	16.77			
Fe XVII 2s-2p	16.78	1.05±0.08	1.12±0.08	0.47±0.15
Fe XVII 3s-2p	17.07	2.31±0.12	2.73±0.11	1.89±0.19
N VI RRC /	18.59			
O VII 1s-3p	18.63	0.25±0.07	0.51±0.10	-
O VIII 1s-2p	18.97	2.65±0.13	$2.97^{+0.12}_{-0.05}$	2.5±0.2
O VII r	21.60	1.23±0.16	1.01±0.15	1.0±0.2
O VII i	21.81	0.50±0.13	0.58±0.13	0.6±0.2
O VII f	22.10	2.04±0.19	2.23±0.19	2.4±0.3
N VII 1s-2p	24.78	1.35±0.13	1.60±0.12	1.2±0.2
N VI 1s-3p	24.90	0.66±0.10	0.47±0.08	-
C VI 1s-4p	26.99	0.27±0.09	$0.12^{+0.10}_{-0.06}$	0.40±0.18
C VI 1s-3p	28.44	0.23±0.13	0.61±0.13	0.6±0.3
N VI r	28.79	0.34±0.18	0.26±0.14	0.7±0.4
N VI i	29.08	0.24±0.15	0.25±0.14	<0.6
N VI f	29.53	1.70±0.20	1.61±0.18	1.8±0.3
C VI 1s-2p	33.74	1.30±0.24	$1.86^{+0.13}_{-0.18}$	1.4±0.5

[a] r, i and f represent the resonance, intercombination and forbidden lines of an He-like triplet, respectively

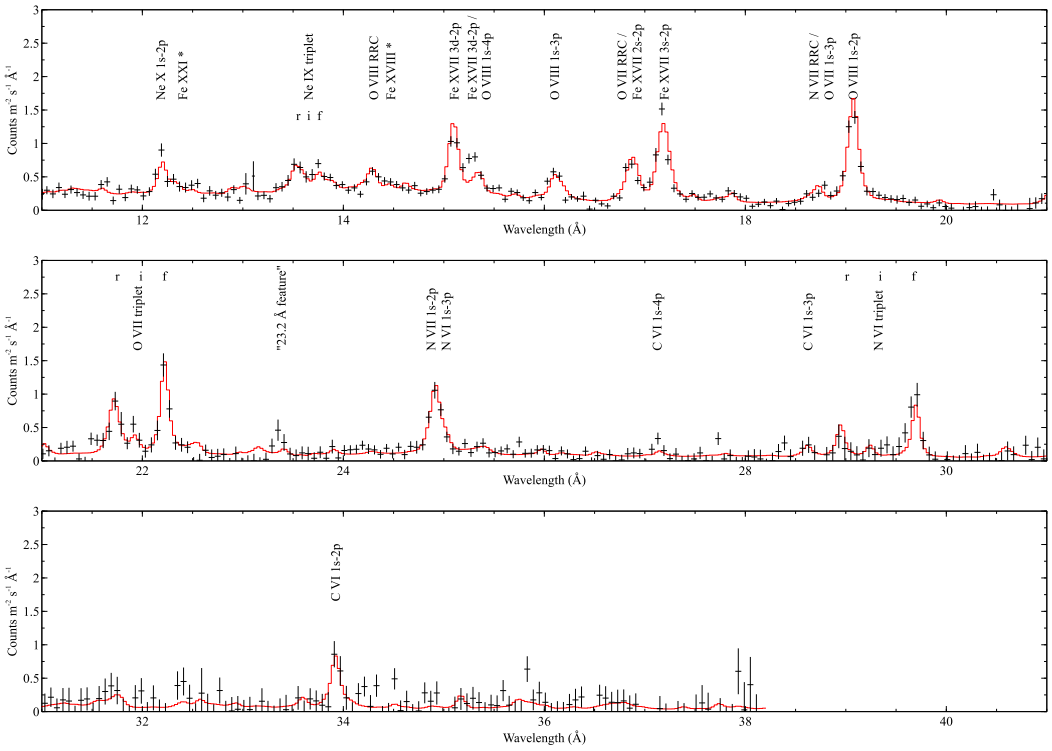

Fig. 6.1: 2012-13 RGS spectrum and line labels for detected emission lines. r, i and f represent the resonance, intercombination and forbidden lines of a He-like triplet, respectively. A * indicates uncertainty in the line identification. The data are binned by two for display purposes. The data are shown in black, and the model in red. For details of the model shown here, see Sect. 6.3.5.

included any relevant lower order transitions for an ion where a higher order transition is detected at the 90% level. For example, C VI 1s-3p (28.44 Å) is included, although its detection did not fulfil this criterion, because C VI 1s-4p (26.99 Å) is detected at the stated level.

I explored whether the parameters of the power law (Γ) and absorber components (ξ and N_H) change when they are fitted, rather than directly using Braito et al. (2014)'s values. I expect changes to the absorption, because there are visible differences between observation 3 (which Braito et al. (2014) analysed in detail) and observations 1, 2 and 4, which are stacked here. The Gaussian lines were fixed to their current best fit values and first the Γ of the power law was allowed to vary. This was unconstrained by the RGS data, as expected, so it was fixed back to 2.1. I then also allowed the ionisations or the column densities of the absorbing components (as `xabs` models) to vary. Finally both the ionisations and column densities of the `xabs` models were allowed to vary at the same time.

The highest ionisation WA component is constrained by Braito et al. (2014) using EPIC data, so it is unsurprising that this becomes very loosely constrained using only RGS data. The low and mid ionisation components increase in ionisation (from $\log \xi$ 0.17±0.1 to 0.70±0.1 and 2.15 ± 0.1 to 3.05 ± 0.4 respectively) and also change in column density (from $1.1 \pm 0.1 \times 10^{22}\,\mathrm{cm}^{-2}$ to $2.7 \pm 0.3 \times 10^{22}\,\mathrm{cm}^{-2}$ and $1.1 \pm 0.4 \times 10^{22}\,\mathrm{cm}^{-2}$ to $<0.5 \times 10^{22}\,\mathrm{cm}^{-2}$). I also find an upper limit to the presence of neutral absorption, which has a column density of $<0.023 \times 10^{22}\,\mathrm{cm}^{-2}$, and the inclusion of this is what renders the mid-ionisation WA phase statistically unnecessary. This is unsurprising as Braito et al. (2014) analysed the least absorbed of the four 2012-13 observations, and the lower neutral absorption allowed them to detect the previously unseen $\log \xi \sim 2$ absorbing phase.

So the highest ionisation absorber's ionisation and column density, as well as the mid ionisation absorber's ionisation value were fixed to the parameters reported by Braito et al. (2014) and the other ionised absorber parameters, the neutral absorber column density, as well as the power law normalisation were left free to vary. These parameters remained consistent with those in

the previous paragraph, with a C-statistic of 1445, an improvement on the previous C-statistic (including gaussian emission lines) of > 150, with only four additional free parameters.

I took this overall model for the 2012-2013 observations and refitted both the continuum, absorption and emission lines to a stacked spectrum combining the two 2004 and three 2007 observations. In this case the power law Γ value was fixed to 2.6 to better represent the intrinsic continuum at that time, as Risaliti et al. (2005a) and Risaliti et al. (2009b) show that the powerlaw Γ was steeper in the 2004 and 2007 observations (~ 2.6, compared to 2.1 during the 2012-13 observations). The same absorption parameters were allowed to vary as described above. These are the best fit models, and the emission line intensities are given in Table 6.2, where they are also compared to Guainazzi et al. (2009)'s results. This comparison is discussed in Section 6.3.3. The line identifications can be seen with the data in Fig. 6.1, and all the detections are consistent with being at rest relative to the host galaxy within 3σ uncertainties.

6.3.2 Fitting Individual Observations

The best fit models to the stacked spectra described in the above section were fitted to the relevant individual observations. First the continuum and absorption parameters were refitted (with the emission lines fixed) and then the emission lines, continuum and absorption parameters were all fitted together.

The absorption varies between observations, as expected (e.g. Parker et al. 2014). As absorption variability in this source is a well-studied and complicated phenomenon, it is not commented on further for the work in this chapter. The absorption has only briefly been modelled here to ensure there is an appropriate continuum and absorption model underlying the emission model, and each observation's model has been visually inspected to ensure the continuum and absorption are well represented.

All individual observations are fitted well, and any potential variations of the emission lines are smaller than their 3σ uncertanties within the two stacked epochs (2004-07 and 2012-13).

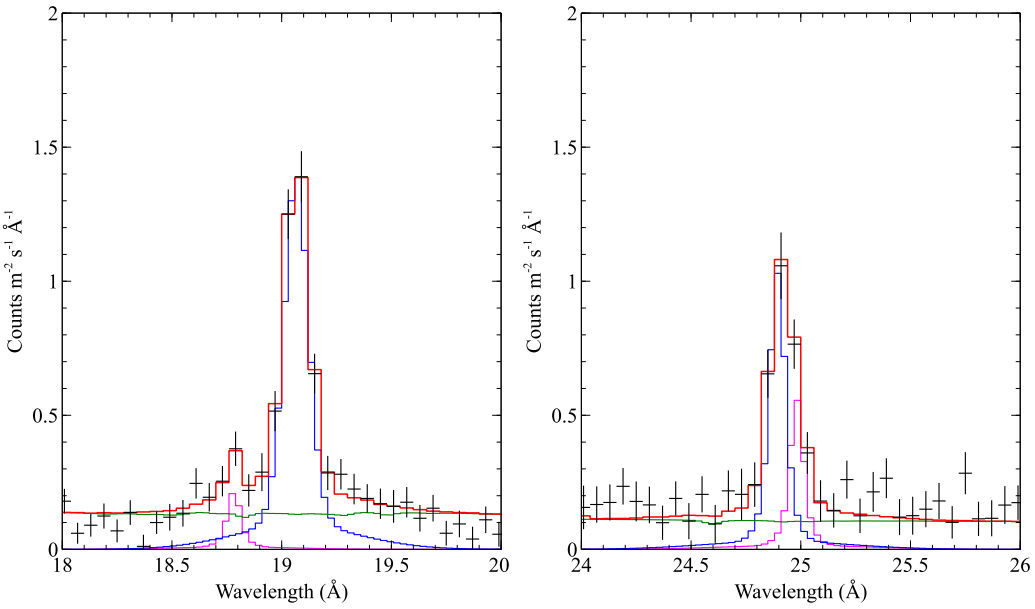

Fig. 6.2: Location of the two new 1s-3p emission lines found, with gaussian components shown. In both panels the data are shown in black, the total model in red and the absorbed powerlaw component in green. Left: Gaussian components for O VIII 1s-2p and O VII 1s-3p shown in blue and pink respectively. Right: Gaussian components for N VII 1s-2p and N VI 1s-3p shown in blue and pink respectively.

6.3.3 Emission Line Comparison

The emission lines I found in the 2012-13 (observations 1, 2 and 4) and 2004-07 stacked spectra are compared with the emission lines found by Guainazzi et al. (2009) in their 2004-07 stacked spectrum (see Table 6.2).

I have found emission lines at all wavelengths where Guainazzi et al. (2009) report emission lines, and evidence for five additional emission lines.

The additional emission lines found at $18.66^{+0.02}_{-0.08}$ Å and 24.85±0.02 Å have been labelled as O VII 1s-3p (rest wavelength: 18.63 Å) and N VI 1s-3p (rest wavelength: 24.90 Å) respectively. Both these lines suffer from blending with nearby, stronger emission lines (O VIII 1s-2p and N VII 1s-2p respectively), as shown in Fig. 6.2. There could also potentially be a nitrogen RRC contribution at 18.59 Å contaminating the O VII 1s-3p line, and this is difficult to disentangle.

The emission line at 15.22±0.01 Å could be identified with either O VIII Lyγ (rest wavelength: 15.176 Å) or Fe XVII 3d-2p (rest wavelength: 15.262 Å),

and this is likely to be a blend of both. If this line is O VIII Lyγ then a stronger intensity is measured for this than for O VIII Lyβ (rest wavelength: 16.01 Å) which is not expected. It is more reasonable that this is a blend of both O VIII Lyγ and Fe XVII 3d-2p line emission, especially as another Fe XVII 3d-2p line is detected at 15.03 Å.

I have tentatively assigned the final two newly detected emission lines (found at 12.29 and 14.41 Å) to Fe XXI and Fe XVIII emission, although there are many possible alternative Fe transitions in these regions.

Of the emission lines found here, that were also measured by Guainazzi et al. (2009), intensity values in the 2004-07 stacked spectrum match Guainazzi et al. (2009)'s values well, within 1σ uncertainties, with a few exceptions: Ne IX r, Ne IX f, O VII RRC, Fe XVII 3s-2p and O VIII 1s-2p. For all the exceptions I measure higher intensities than Guainazzi et al. (2009). This is at least in part owing to the difference in line widths assumed between the two works - Guainazzi et al. (2009) assumed the lines were all unresolved (and therefore set their line widths to zero) whereas this work allows the line widths to be free to vary. For the Ne XI He-like triplet, which appears blended, this leads the forbidden and resonance lines to broaden and account for more of the flux, and the intercombination line has a correspondingly smaller upper intensity limit than that of Guainazzi et al. (2009) in response. By fixing the widths of these lines to zero, the intensities fall much more in line with those of Guainazzi et al. (2009), and only the O VII RRC intensity is left with a discrepancy.

In the case of the O VII RRC, there is also potential contamination by the Fe XVII 2s-2p line (rest wavelength: 16.78 Å). This is discussed by Guainazzi et al. (2009) who attribute an intensity of $0.9\pm0.4\times10^{-5}$ ph s^{-1} cm^{-2} to the O VII RRC (given in their text) although their Table 2 quotes $0.47\pm0.15\times10^{-5}$ ph s^{-1} cm^{-2} for the entire feature. An intensity of $0.9\pm0.4\times10^{-5}$ ph s^{-1} cm^{-2} is consistent with result in this work for the entire feature at that position.

There are some emission lines which show hints of variation between the measured intensities in 2012-13 and 2004-07, but only at the 1σ level. I return

to comparing the two time periods in Sect. 6.3.6.

The narrow emission lines have also been studied by Nardini et al. (2015), although their statistics is very low (partially owing to extracting the spectrum from a smaller spatial area), especially over the O VII triplet region. Their best constrained lines are at higher energies (shorter wavelengths) than investigated here, but there are some emission lines measured in both. The smaller extraction region used in Nardini et al. (2015) allows cleaner detections of emission lines from the AGN NLR to be made, without as much contamination from emission from the starburst region. The intensity of the O VIII 1s-2p and Ne X 1s-2p lines is measured to be much larger in this work than in Nardini et al. (2015), implying that at least some of the emission from these lines measured here is collisionally excited emission from the nuclear starburst region. This is discussed further in Section 6.3.5.

6.3.4 Feature at 23.2 Å

In addition to the emission lines discussed in the previous section, a feature is also detected at 23.237 ± 0.020 Å in the 2012-13 stacked spectrum (see Fig. 6.1), which I initially identified as N VI 1s-5p (rest wavelength of 23.277 Å), although only tentatively. The strength of this line is much higher than expected from a collisional or photoionised gas, because the lower order N VI transitions are much weaker than this feature (except the N VI He-like triplet).

Potentially, if there was charge exchange (CX) emission, this emission line could be enhanced compared to the lower order transitions (for more information on CX, see Chapter 2). If CX emission is enhancing the N VI 1s-5p line, then the same would be expected to happen for ions of the same iso-electronic sequence in nearby elements, which is not the case; the O VII 1s-5p line (17.396 Å) and the Ne IX 1s-5p line (10.76 Å) are not enhanced. Because of this, I consider the possibility of CX emission (or any other physical mechanism enhancing this transition) causing this feature to be very unlikely.

In addition, it should be noted that the CCD on RGS2 covering this wavelength range failed shortly after launch, thus reducing the signal to noise ratio in the spectrum, and that there are known instrumental features from oxygen absorption (23.05 Å and 23.35 Å; de Vries et al. 2003) which also contribute in

this region.

Finally, the significance of this feature is estimated to be 3σ, giving a probability of 0.3% that a feature of this strength may be seen by chance. This feature is driven by its central data point that, while strong, does have a larger uncertainty than the other data points around it. The above probability corresponds to an expectation that 1/370 events will be further than 3σ from the correct model. Therefore given the number of bins, two non-physical features of this significance are expected to be present in the spectrum.

The origin of this feature is not known, and it is not considered further within this analysis.

6.3.5 Physically Motivated Emission Models

First I tested whether collisional ionisation models on their own could fit the NGC 1365 spectra, as the starburst ring has previously been shown to contribute to the RGS spectra (Guainazzi et al. 2009). Collisional emission models were added one at a time (*cie* models from SPEX; over the best fit continuum and absorption model from Sect. 6.3.1), with their normalisations and temperatures allowed to vary, until any further additions did not improve the overall fit. The overall fit is considered to be improved when the C-statistic decreases by ≥ 4.61, corresponding to 90% confidence level for two free parameters (temperature and normalisation). With this method four collisional phases were added, each giving a C-statistic decrease of 2975, 497, 32 and 40 respectively. These models correspond to best fit temperatures of 150 ± 10 eV 350 ± 50 eV, 660 ± 30 eV and 2800^{+4100}_{-1000} eV, similar to the temperature ranges of the two component collisional models in both Braito et al. (2014) and Guainazzi et al. (2009) (300 eV-700 eV and 150 eV-1200 eV, respectively) with an additional higher temperature phase. This high temperature phase is not well constrained and contributes very little to the line emission; only small contributions to O VIII 1s-2p and weak lines at the shortest wavelength range (11-12 Å) are made by this component. The total luminosity (0.3-2 keV) from the four collisional models is $6.5^{+3.0}_{-1.7} \times 10^{40}\,\mathrm{erg\,s^{-1}}$, with a C-statistic of 1972.

Although no more collisional models are needed by the data, this is still not a satisfactory fit, especially around the O VII triplet ($\sim$22 Å), because the

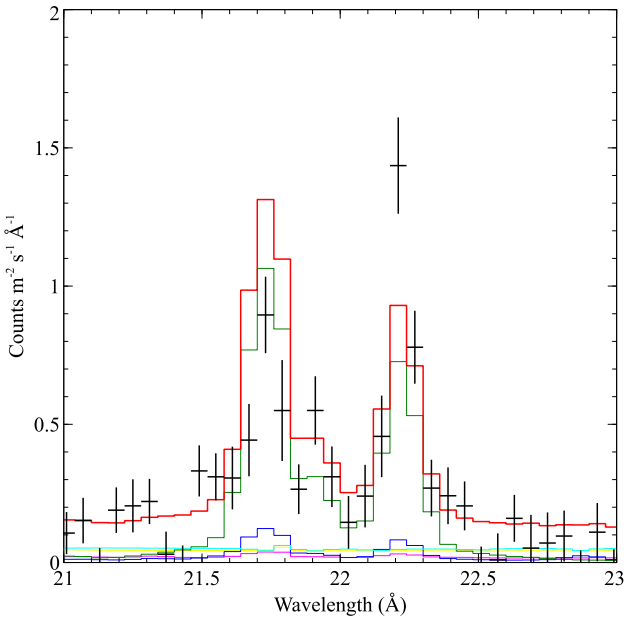

Fig. 6.3: Best fit to the O VII triplet, with absorbed power law and four collisionally ionised emission models. The data are shown in black, the total model in red and the absorbed powerlaw component in light blue. The collisional emission components at temperatures 150 eV, 350 eV, 660 eV and 2830 eV are shown in green, dark blue, pink and yellow respectively. The data are binned by two for display purposes.

resonance line is overestimated and the forbidden line is underestimated (see Fig. 6.3).

Alternatively I tried to fit the emission line spectra with only photoionised models. As SPEX does not yet include a photoionisation emission model, the photoionised emission was fit with simulated spectra from CLOUDY (Ferland et al. 2013). The CLOUDY models are generated assuming a plane parallel geometry, with the central source illuminating the inner face of the cloud and with a flux density dependent on a chosen ionisation parameter, ξ. The gas cloud has proto-solar abundances (Lodders et al. 2009). The ionisation parameter ($\log \xi = 0.1\text{-}3.3\,\mathrm{erg\,cm\,s^{-1}}$), column density ($\log \mathrm{N}_H = 21\text{-}24\,\mathrm{cm^{-2}}$) and turbulent velocity ($\log \mathrm{v}_{turb} = 1.0\text{-}3.5\,\mathrm{km\ s^{-1}}$) of the illuminated cloud are varied over the stated ranges to generate a grid of simulated spectra.

NGC 1365 is an obscured AGN, so the nucleus is likely to be observed closer to edge on than face on (by the Unification Theory), so the shielded face of the NLR gas, opposite to the illuminated face, will be seen to a lesser

degree than for a face on nucleus. As emission from the illuminated face of the NLR gas already dominates the emission lines of a face on AGN (see Chapter 5), the reflected output of CLOUDY is used as the narrow emission line model for this work.

A standard Seyfert 1 AGN SED is used as I assume the X-ray narrow-line emitting clouds see the nuclear continuum. This assumption is justified by the luminosity of the [O III] λ5007 emission line from the photoionised ionisation cone southeast of the nucleus; the photoionisation cone has a typical AGN [O III] / Hα line ratio (Veilleux et al. 2003) and an [O III] λ5007 luminosity of $\sim 4 \times 10^{40}\,\mathrm{erg\,s^{-1}}$ (Kristen et al. 1997), which together with the hard X-ray luminosity (14-195 keV) of $10^{42.68}\,\mathrm{erg\,s^{-1}}$ (Tueller et al. 2010), place NGC 1365 within the expected region on a $L_{[OIII]}$ (observed) vs $L_{14-195\,keV}$ plot (see e.g. Winter et al. 2010). If the optical NLR was seeing an absorbed nuclear SED then the optical emission line luminosities would be much smaller than observed.

It is worth noting here that Guainazzi et al. (2009) made the counter argument, as they found the total soft X-ray contribution from photoionised gas relatively weak compared to other AGN. The similarity of photoionisation parameters in final models from both the work by Guainazzi et al. (2009) and the work here implies that this difference does not alter the overall conclusion.

As these CLOUDY models only include the emission directly from the photoionised cloud, the continuum and absorption described in Section 6.3.1 is included. These components were fixed to their best fit parameters previously determined in Sect. 6.3.1. Each CLOUDY model was imported (one by one) into SPEX (as a *file* model), and broadened by a *vgau* model. As in the case of NGC 5548 in Chapter 5, the broadening is applied because while CLOUDY takes the effect of turbulence within the gas into account for the line strengths, it does not use this to broaden the line profiles in the produced spectra [1]. The normalisation of the *file* model, and sigma value of the *vgau* model are the only free parameters during this fit. Each CLOUDY model is fitted in turn to the data using this process, finding a C-statistic value appropriate for each

[1] See Hazy 1 documentation, page 162

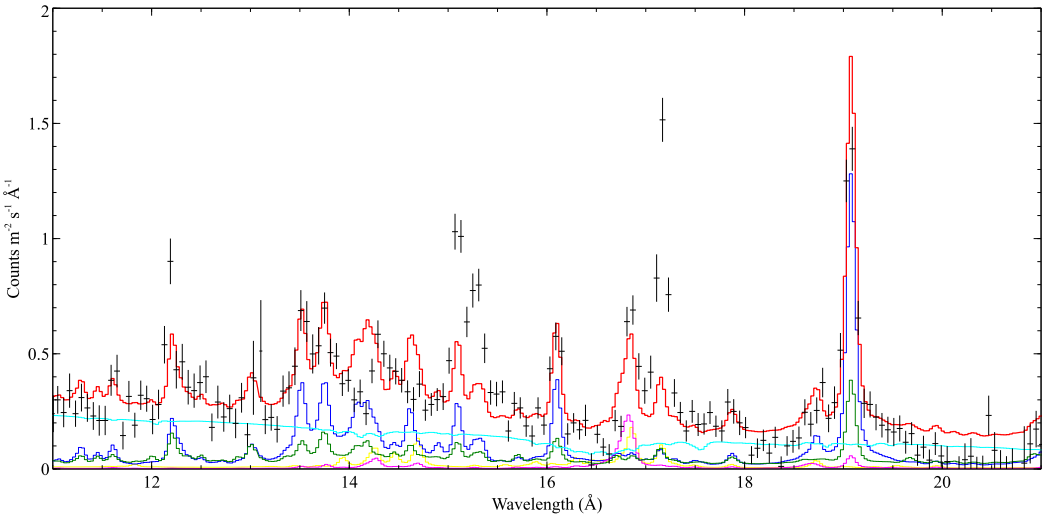

Fig. 6.4: Best fit to the data with absorbed power law and four photoionised emission models, 11-21 Å range shown. The data are shown in black, the total model in red and the absorbed powerlaw component in light blue. The photoionised emission phases 1, 2, 3 and 4 are shown in green, pink, dark blue and yellow respectively.

one. A first photoionisation model is considered to be needed if the best fit C-statistic improves by 9.24, corresponding to a 90 % confidence level for five extra free parameters (column density, ionisation parameter and turbulent velocity of the CLOUDY models, plus normalisation of that model in SPEX and broadening applied by the *file* model). Further phases of photoionised gas are considered to be needed if the best fit C-statistic improves by 7.78, corresponding to a 90 % confidence level for four additional free parameters (all of the above, without broadening applied by the *file* model as this is applied to all photoionised phases).

With this method four CLOUDY models were added, giving C-statistic decreases of 2161, 277, 116 and 52 respectively. The best fit models had $\log \xi$ values of 2.7, 1.1, 2.3 and 0.1, $\log N_H$ values of 23.5, 24, 21.25 and 24 cm^{-2} and $\log v_{turb}$ values of 3.5, 1.0, 3.0 and 1.0 km s^{-1} respectively. The total luminosity (0.3-2 keV) from the four CLOUDY models is $4.2 \pm 0.6 \times 10^{40}$ erg s^{-1}, with a C-statistic of 2909. While no more photoionised models are needed by the data, this is still not a satisfactory fit, especially around the Fe lines at $\sim$15 and 17 Å (see Fig. 6.4).

As neither collisional nor photoionised emission alone fits the data, com-

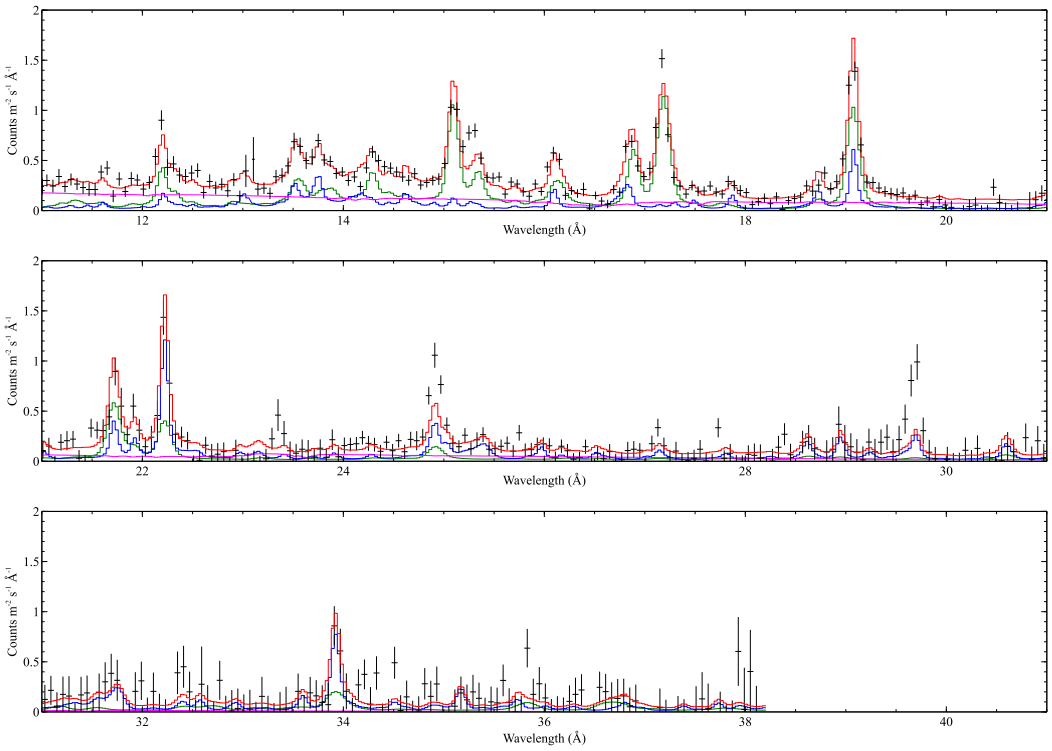

Fig. 6.5: The stacked 2012-13 spectrum with best fit continuum and absorption model, two collisional emission models and three photoionised emission models, all using solar abundances. C-statistic = 1756. The data are shown in black, the total model in red and the absorbed powerlaw component in pink. The collisional emission components are combined and shown in green. The photoionised emission phases are combined and shown in blue. The data are binned by two for display purposes. For details see text.

bination of both was tested. Gas phases were added one by one; either a collisional or photoionised phase at each stage, depending which gives a greater improvement in the C-statistic. The same criteria as above are used to determine whether a phase is necessary. The normalisations of all phases (both photoionised and collisional) are left free to vary throughout this process, along with the temperatures of the collisional phases and the broadening values.

The best fit in this case is obtained with two collisional phases (at temperatures 200±10 and 540±20 eV) and three photoionised CLOUDY phases with log ξ of 1.5, 2.5 and 1.1 erg cm s^{-1}, log N_H of 22.25, 21.75 and 22.25 cm^{-2}, each having a v_{turb} of $10^{2.5}$ km s^{-1}, giving a C-statistic of 1756. Two of the photoionised phases within this fit have very similar parameters; both have

the same column density and turbulent velocity, and have ionisation parameters (log ξ) of 1.5 and 1.1 erg cm s^{-1}. To test whether both phases are needed, the higher ionisation (log $\xi = 2.5$) phase and collisional phases were used as a baseline to add one further photoionised phase to the fit. This added a phase with log ξ of 1.3, but gave a C-statistic of 1817, with a ΔC of +61 compared to the three photoionised, two collisional phase model.

As shown in Figure 6.5, the O VII triplet is now well fitted with this combination of two collisional and three photoionised emission components. The total 0.1-2.5 keV luminosity from the collisional components of this model is $2.45\pm0.20 \times 10^{40}$ erg s^{-1}, consistent with that expected from the starburst ring in this object, given by Wang et al. (2009)'s *Chandra* analysis as $2.7^{+0.7}_{-0.6} \times 10^{40}$ erg s^{-1}.

Even though no further phases of either photoionised or collisionally ionised gas improve the statistical fit, the N VII Lyα ($\sim$ 25 Å) and N VI forbidden ($\sim$ 30 Å) lines are still underpredicted by the combined model (Fig. 6.5). These are the only two strong nitrogen emission lines in this spectrum (although there are also other, much weaker nitrogen lines), which suggests there may be an overabundance of nitrogen compared to the proto-solar abundances (Lodders et al. 2009) used within the CLOUDY model. This interpretation is supported by the detection of super-solar nitrogen abundances in other AGN outflows (e.g. Gabel et al. 2006; Arav et al. 2007, using UV absorption lines), as well as a specific suggestion of higher nitrogen abundances in the optically detected outflows of this object by Schulz et al. (1999).

Further CLOUDY models were run to test this, for the three phases already fitted, with a range of different nitrogen abundances ($\times$ 2, 5, 10 and 20 overabundant relative to the Lodders et al. (2009) values used previously). The varying nitrogen abundance alters the strength of the two nitrogen emission lines mentioned above: N VII Lyα at $\sim$25 and N VI f at $\sim$30 Å. The two nitrogen RRCs also change slightly in strength, at $\sim$19 (N VI) and $\sim$22.5 Å(N VII). The higher the nitrogen abundance, the stronger the nitrogen features, including the nitrogen RRC at $\sim$22.5 Å. As this particular feature gets stronger, the O VII f line gets weaker, which reduces the quality of the overall fit to the

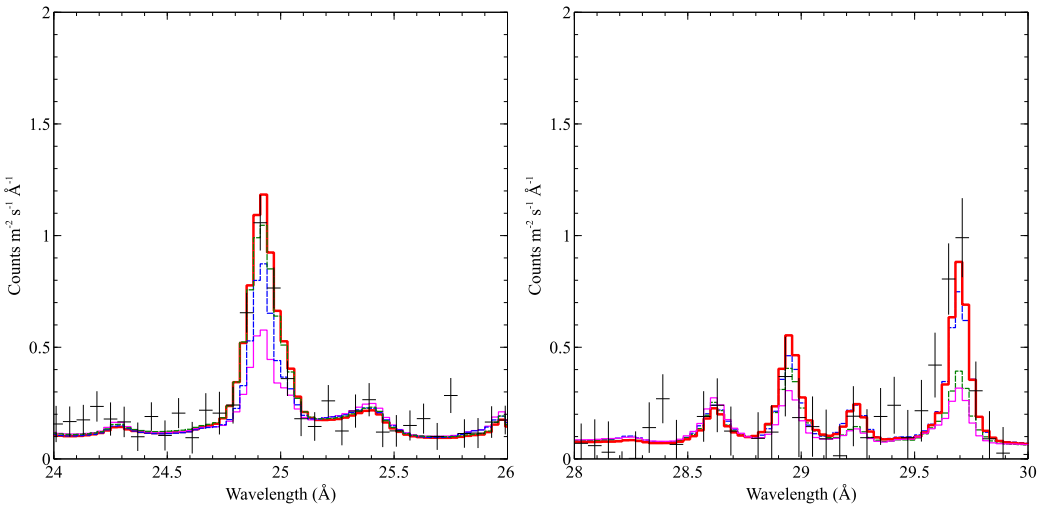

Fig. 6.6: Fits with two collisional, three photoionised emission models. Models with five times over abundance of nitrogen for intrinsic AGN gas only (dashed blue line), starburst emission lines only (dashed green line) and for both intrinsic AGN and starburst gas (thick red line), are compared to the same model with solar abundances throughout (thin pink line). The data are binned by two for display purposes. For details see text and Table 6.3. Left: Region around N VII 1s-2p and N VI 1s-3p. Right: Region around N VI He-like triplet, including C VI 1s-3p (observed at 28.6 Å).

spectrum.

If there is an overabundance of nitrogen in the nuclear region of NGC 1365 it could reasonably be expected to be present in the starburst ring surrounding the nucleus as well as in the gas intrinsic to the AGN.

Therefore 2, 5 and 10 × nitrogen abundances were tested self-consistently with the collisional emission (representing the starburst region), the CLOUDY phases (representing the photoionised AGN emission) and the intrinsic AGN absorption (the traditional warm absorber phases). A nitrogen abundance of five times proto-solar was found to fit the spectrum well, reducing the C-statistic by 120 to 1636 compared to the solar abundance model (see Table 6.3 and Fig 6.6).

As Fig. 6.7 shows, the N VII RRC at ∼22.5 Å visually seems stronger in this model than the data. This feature is from the photoionised emission phases, so one option to reduce the emission here in the total model would be to reduce the nitrogen overabundance in the AGN emission. One could

Table 6.3: Results from testing different nitrogen abundances in both the AGN and starburst spectral components. Using solar abundances in all components gives C-statistic = 1756. See text for details.

Components with non-solar abundances	2 × nitrogen	5 × nitrogen	10 × nitrogen
intrinsic AGN emission	1714	1674	1667
intrinsic AGN emission and absorption	1712	1663	1658
starburst emission	1713	1663	1701
all	1681	1636	1731

argue that leaving the AGN emission at solar abundances would help the model fit well here, but this 'solution' would reduce the goodness of fit to the N VI triplet at $28.5 - 30$ Å, because the nitrogen overabundance in AGN (photoionised) emission contributes heavily to the N VI f emission line.

To narrow down the N abundance further, 3, 4, 6, 7 and finally 4.5 × overabundance of nitrogen relative to the Lodders et al. (2009) values were tested (using the same method as above). A nitrogen abundance in the nuclear regions of NGC 1365 of 4.5 ± 0.5 × solar (Lodders et al. 2009) best fits the data, giving a C-stat of 1634, shown in Fig. 6.7. The collisional and photoionised phase parameters are contained in Table 6.4.

As this method was successful at improving the fit of the nitrogen lines, higher iron abundances were also tested to improve the fit of the Fe XVII 3s-2p line at ∼17 Å and the Fe XVII 3d-2p / O VIII 1s-4p blend at ∼15.2 Å. Statistically, an overabundance of iron indicates a worse fit ($\Delta C > 34$); the problematic iron lines remain underestimated and there are also problems fitting lines from other elements. Therefore an overabundance of iron is not included in the final model.

The final model is shown in Fig. 6.7 and includes two collisional emission phases, three photoionised emission phases, and an absorbed powerlaw continuum (as described in Sect. 6.3.1). All nuclear gas phases (both starburst

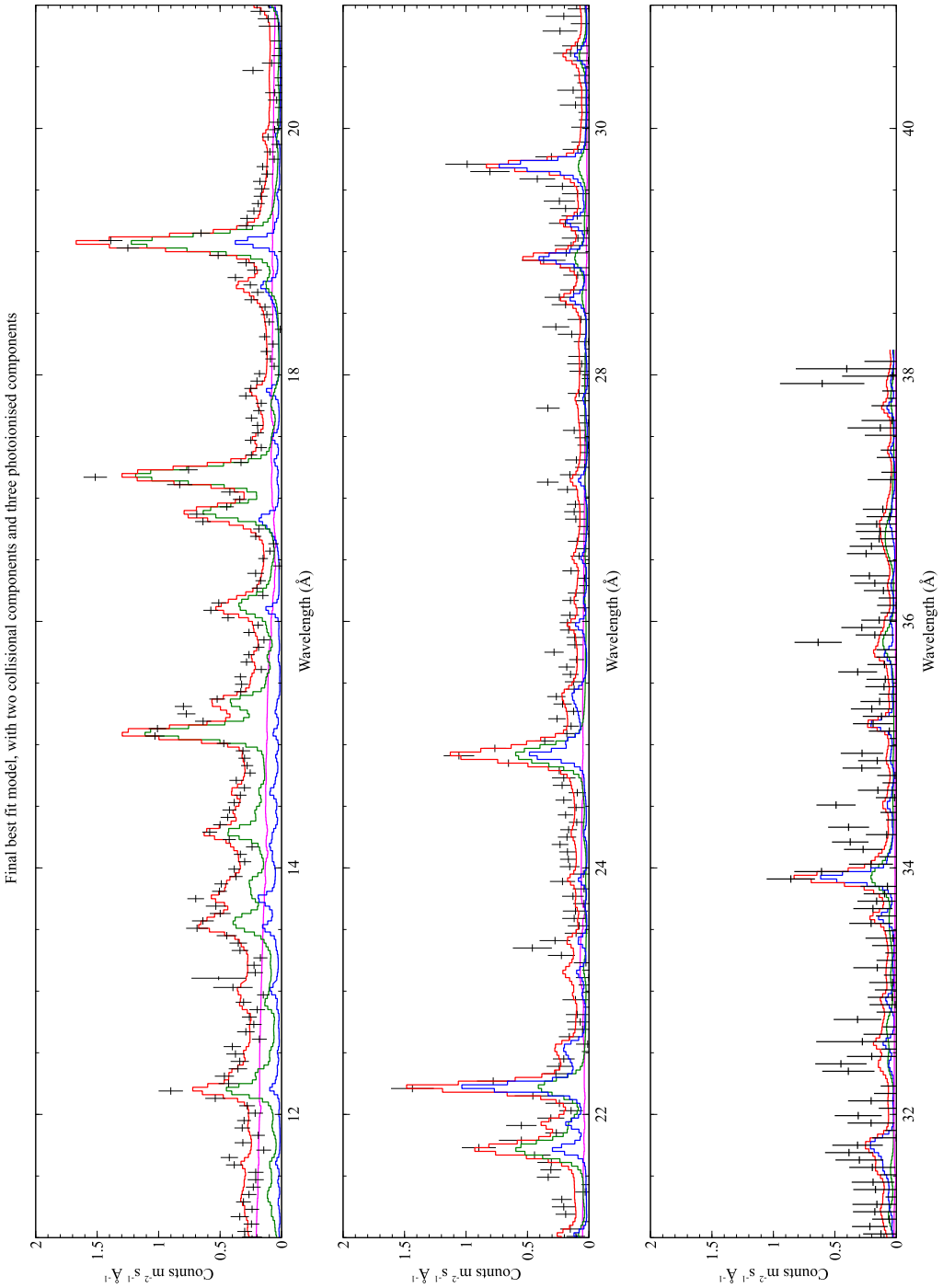

Fig. 6.7: Final best-fit model for the 2012-13 stacked spectrum of NGC 1365 with $4.5\times$ solar nitrogen abundance, two collisional emission models representing the starburst ionised gas and three photoionised emission models representing the AGN ionised gas. The data are shown in black, the total model in red and the absorbed powerlaw component in pink. The collisional emission components are combined and shown in green. The photoionised emission phases are combined and shown in blue. The data are binned by two for display purposes. For details see text and Table 6.4

Table 6.4: Parameters of the final best fit model, shown in Fig 6.7. C-statistic = 1634. All components listed here have an enhanced nitrogen abundance of 4.5 × solar.

Parameter	Phase 1	Phase 2	Phase 3
Collisional gas			
T (keV)	0.220±0.010	0.570±0.015	-
Emission measure[a]	3.77±0.37	6.71±0.34	-
Photoionised gas			
log ξ (erg cm s^{-1})	1.5±0.2	2.5±0.2	1.1±0.2
log N$_H$ (cm^{-2})	22.25±0.25	21.75±0.25	22.25±0.25
v$_{turb}$ (km s^{-1})	$10^{2.5\pm0.5}$	$10^{2.5\pm0.5}$	$10^{2.5\pm0.5}$

[a]In units of 10^{68} m^{-3}

and AGN, emission and absorption) have enhanced nitrogen abundances of 4.5 × solar. The parameters of the emission phases in this model are shown in Table 6.4. The temperatures of the collisional phases are similar but not consistent with the collisional components from Guainazzi et al. (2009). This is owing to different analysis methods, as in the work described here the collisional phases' temperatures and normalisations were allowed to vary while fitting photoionised phases to the data, whereas Guainazzi et al. (2009) kept their baseline model fixed.

In addition, a better fit (ΔC = 120) is found when both the collisional line emission models are broadened by a SPEX *vgau* model. The collisional models fit best with a broadening of $\sigma = 690 \pm 50$ km s^{-1}, while the photoionised models are broadened by σ <225 km s^{-1}. As introduced in Chapter 3, RGS spectral lines can be broadened by the extent of a non point-like source. The amount of broadening is given by the formula:

$$\Delta\lambda = \frac{0.138}{m}\Delta\theta \tag{6.1}$$

where $\Delta\lambda$ is the wavelength broadening (in Å), m is the spectral order and θ is the source extent in arcminutes (ESA XMM-Newton SOC 2016).

Using the *Chandra* images in Wang et al. (2009) the soft X-ray emission of

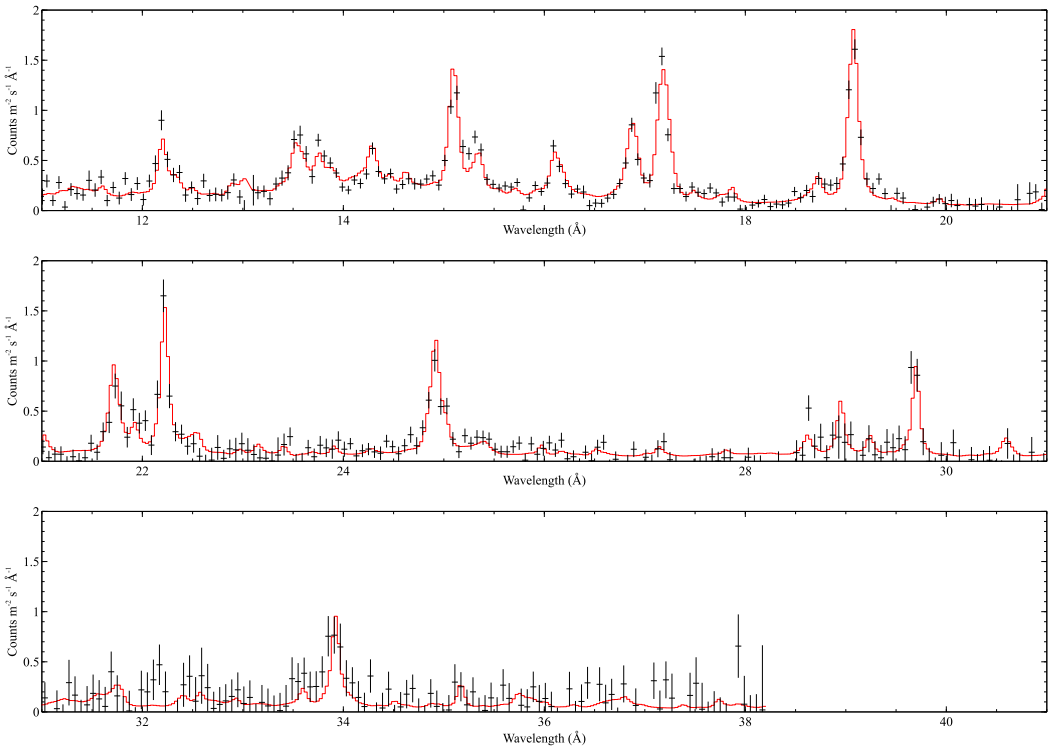

Fig. 6.8: The 2012-13 best-fit emission line model fitted to the 2004-07 stacked spectrum. Only the normalisations and broadening values of the emission line model were fitted to this spectrum. The data are shown in black and the total model in red. The data are binned by two for display purposes.

NGC 1365 is estimated to be 20 arcseconds across, corresponding to a broadening of 620 km s^{-1} at 22 Å. This is a reasonable match to the broadening of the collisional emission, and is much larger than that of the photoionised emission, indicating that most of the photoionised emission comes from a more compact region, within the starburst ring. By comparing RGS and *Chandra* ACIS spatially resolved spectroscopy, Guainazzi et al. (2009) also concluded that the bulk of the photoionised emission comes from the central nucleus unresolved by *Chandra*.

6.3.6 2012-13 Best Fit Model with 2004-07 Data

The best fit model for the 2012-13 stacked spectrum, described above, is fitted to the 2004-07 stacked spectrum, with the 2004-07 continuum and absorption model from Sect 6.3.1. Only the normalisations and broadening values for the emission models were fitted. The temperatures of the collisional models,

and the ionisation parameters, turbulent velocities and column densities of the photoionised models were all fixed to their best fit 2012-13 values. This gives a C-statistic of 1743, showing the emission is very similar between the two time periods (see Fig. 6.8). The broadening values fitted to the 2004-07 stacked spectrum are consistent with those found using the 2012-13 stacked spectrum (2004-07: 640±40 km s^{-1} and <130 km s^{-1}; 2012-13: 690±50 km s^{-1} and <225 km s^{-1}). This confirms what is reported in Sect. 6.3.1, where no strong evidence is found for emission line changes between the two time periods when using *Gaussian* models to fit the emission lines.

The same test was done with the 2012-13 stacked spectral model and the third observation in that campaign (Jan 2013; not included in the 2012-13 stacked spectrum owing to the differences in the intrinsic absorption compared to the other observations.), with a continuum and absorption model fitted to this observation, by the same method discussed in Sect 6.3.1. The emisssion line model also fits reasonably well, with a C-statistic of 1461, confirming that the emission lines remained constant even as the absorption of the continuum changed.

6.4 Discussion

The work in this chapter models the narrow line emission from NGC 1365's nuclear region in a uniform and detailed way, using *XMM-Newton* RGS data from 2004 to 2013. Firstly, using *Gaussian* models for the emission lines, the results were compared to the only other study which published individual emission line parameters in this wavelength range. Then the 2012-13 spectrum was fit with self-consistent, physical models, showing that a combination of both collisionally produced and photoionised emission lines reproduces the spectra well when the nitrogen abundance is increased by a factor of 4.5 relative to solar. This physical model also reproduces the earlier 2004-07 spectra without any temperature, ionisation parameter, turbulent velocity or column density changes in the emitting gas.

Not included in this model is photoexcitation followed by radiative decay, which Kinkhabwala et al. (2002) showed was important in enhancing

higher order resonance lines in NGC 1068's soft X-ray emission line spectrum. Kinkhabwala et al. (2002) also showed that the importance of photoexcitation decreases for higher ionic column densities, and at O VII radial column densities of $10^{19}\,\mathrm{cm}^{-2}$ the spectrum imitates that of pure photoionisation followed by recombination/radiative cascade. The CLOUDY models used show an O VII radial column density close to this $10^{19}\,\mathrm{cm}^{-2}$ value, so any photoexcitation contribution can be ignored without affecting the results.

In this section the relative contributions of the collisional and photoionised line emission and the enhanced 4.5 × solar abundance of nitrogen in the context of NGC 1365 as seen at other wavelengths are discussed.

6.4.1 Starburst and AGN Relative Contributions

The expected X-ray emission from star formation can be measured directly or estimated using measurements of infrared emission from the same region. Wang et al. (2009) measure $\mathrm{L}_{0.3-10\,keV}$ luminosity as $1.87 \pm 0.36 \times 10^{40}\,\mathrm{erg\,s}^{-1}$ from NGC 1365's nuclear starburst. Using the total IR luminosity of NGC 1365's nuclear core measured by Tabatabaei et al. (2013), and the star formation IR to X-ray relation for galaxies in the local Universe from Symeonidis et al. (2014), gives a consistent result with this direct measurement from *Chandra*. Collisional emission models at the temperatures considered here have very little emission at energies above the RGS band, so the *Chandra* 0.3-10 keV luminosity can be compared directly to the luminosity calculated from collisional emission models fitted to RGS data.

For the starburst (collisionally excited) emission in the final 2012-13 model, an RGS 0.3-10 keV luminosity of $2.26^{+0.17}_{-0.13} \times 10^{40}\,\mathrm{erg\,s}^{-1}$ is derived, consistent with the Wang et al. (2009) measurement. For the 2004-07 data, a 0.3-10 keV luminosity of $2.45 \pm 0.11 \times 10^{40}\,\mathrm{erg\,s}^{-1}$ is calculated, consistent with the Wang et al. (2009) measurement at the 2σ level

In the RGS band analysed here (11-38 Å), the photoionised emission contributes 25-46% of the total narrow line emission, with collisional emission contributing the rest. In addition, the collisional components contribute a very small amount of emission to the continuum, which is not included in the estimate above. In fact the photoionised emission is 5-15% of the total soft X-

ray emission in this range. This estimate is consistent with that of Guainazzi et al. (2009) ($\leq$ 10%) with the possibility of a slightly higher contribution. This is attributed to a slight difference in analysis method; Guainazzi et al. (2009) fix their collisional emission model first, and then estimate that the photoionised emission contributes any 'leftover' line intensities, whereas in this work the collisional emission phases are allowed to vary in both normalisation and temperature whilst fitting photoionised phases (see Sect. 6.3.5).

6.4.2 Higher Nitrogen Abundances

As the work presented in this chapter finds a best fit spectral model with 4.5±0.5 times enhanced abundance of nitrogen in the nuclear area of NGC 1365, it is natural to ask why and where this might come from.

One possibility is that the enhanced strength of nitrogen lines may be caused by the Bowen fluorescence mechanism, as described by Sako (2003), rather than a higher nitrogen abundance. Sako (2003) shows that at high optical depths, resonance line photons (e.g. O VIII Lyα doublet at 18.967 and 18.973 Å) can be absorbed by other ions, exciting an electron to a higher energy level, when the receiving transition has a very similar energy (e.g. N VII Lyζ at 18.974 Å). This electron then undergoes radiative cascade and therefore releases photons associated with lower order transitions of the receiving ion. The overall effect of this is to reduce the apparent abundance of the initial ion (in the example case, O VIII) and increase the apparent abundance of the receiving ion (in the example case, N VII). While this mechanism can enhance the strength of lower order N VII emission lines, it does not do the same for N VI emission lines, which are enhanced in NGC 1365's spectrum. Therefore Bowen fluorescence is not a satisfactory explanation for the observations in this case.

The alternative explanation for the observed enhanced nitrogen lines is that they are caused by an over abundance of nitrogen in the source. If the nitrogen abundance in NGC 1365's nucleus is enhanced, then signatures of this should be visible in data at other wavelengths too. As NGC 1365 is an obscured AGN, the UV emission is too weak for the usual types of abundance studies. However, using optical HST data, Schulz et al. (1999) modelled a

photoionised region of optical narrow-line emission in NGC 1365 and found evidence for a factor of three increase in nitrogen abundance. Their major problem with this conclusion was that they thought the 2-10 keV luminosity ($L_{2-10\,keV}$) of the AGN was too low for the number of ionising photons needed for their model, and considered the necessary absorption column of $\sim 10^{23}\,cm^{-2}$ to reconcile this to be too high. With the extended energy range and higher resolution spectra available from both *Chandra* and *XMM-Newton*, it is now clear that this level of absorption is not unusual for NGC 1365, avoiding this problem with the Schulz et al. (1999) optical narrow-line emission model, and therefore supporting the need for a higher than solar nitrogen abundance.

Most of the nitrogen in the ISM today is ejected during the AGB phase of low and intermediate mass stars (1-8 $M_{\odot}$), with negligible oxygen enrichment. During the red giant branch and asymptotic giant branch phases of intermediate mass stars, dredge up episodes can occur. The outer convective envelope reaches down to inner regions where nitrogen has been produced by the CNO cycle. This, combined with 'hot-bottom burning', which converts some or most of the carbon at the base of the convective zone to nitrogen, enhances the surface abundance of nitrogen. The nitrogen is then ejected into the ISM through winds driving mass loss from these stars. Unfortunately, stellar yields of nitrogen are still reasonably uncertain, as they are sensitive to convection models and estimates of dredge up efficiency (Pagel 2009).

For this mechanism to cause the observed higher nitrogen abundance, the star formation history of NGC 1365 would have to greatly deviate from average over a long period of time. Without any significantly unusual other features, this seems to be an unlikely explanation, especially as the N/O ratio in outer H II regions of this galaxy is measured to be consistent with solar (Bresolin et al. 2005).

The other option for increasing the nitrogen abundance is a shorter timescale, smaller scale effect. The only nucleosynthetic environment in the nucleus is the starburst region, so if the nitrogen enhancement is created in the nucleus, then the starburst region may well be the cause. The presence of Wolf-Rayet (WR) stars has been shown to correlate with a higher N/O abun-

dance ratio by Brinchmann et al. (2008), using an SDSS sample with 570 WR galaxies and more than 1000 WR galaxy candidates. WR stars are thought to descend from O stars, after losing their outer envelope (Murdin 2001). WR stars were detected by Phillips and Conti (1992) in spectra of a 'hot spot' near the nucleus of NGC 1365, so this could be enhancing the nitrogen abundance in the nuclear region.

6.4.3 Long Term Behaviour and Distance of Emitting Gas

Comparing the 2004-07 and 2012-13 spectra shows no evidence of variability of the emission lines. Each individual emission line is consistent at a 3σ uncertainty level between the two epochs (Table 6.2). The individual starburst and AGN emission components also have consistent overall luminosities (11-38 Å) between the two epochs. Therefore variability cannot be used to infer the size of the emitting region or its distance from the ionising continuum.

An estimate of the location of the bulk of the photoionised gas can also be calculated by using the line broadening of the photoionised phases. In Sect. 6.3.5, an upper limit of $< 225\,\mathrm{km\ s^{-1}}$ is found for the broadening of the photoionised gas using the 2012-13 spectrum. The 2004-07 spectrum gives us a consistent, and tighter, constraint of $< 130\,\mathrm{km\ s^{-1}}$.

Assuming that any broadening is owing to bulk motion of the gas orbiting the central source, a lower limit to the distance can be calculated. Using a black hole mass of $2 \times 10^6 M_\odot$ (Risaliti et al. 2009a), the upper limits on the line widths imply that the emitting gas must be located further than 0.5 pc from the central source.

This is consistent with the estimate by Guainazzi et al. (2009), using their best-fit ionisation parameter, that the emitting gas is located $\geq 0.75\,\mathrm{pc}$ from the central source. Our distance is inconsistent with Braito et al. (2014), who conclude that emission line gas is located at $\sim 10^{15}\,\mathrm{cm}$ ($3 \times 10^{-4}\,\mathrm{pc}$) from the central source, calculated from tentative variability of Mg XII emission lines. In fact, if the model from the work in this chapter is extended down to the Mg XII Ly-α line at 8.42 Å, it shows that the collisional emission models contribute most of the intensity of this line which then has to be produced further out. The Braito et al. (2014) much closer distance estimate is also

based on shorter term variability (within an observation) than investigated in this work, and as discussed above, evidence of variability is not found over these longer timescales. It is likely that the gas Braito et al. (2014) see dominating is from closer to the central source as the BLR scale emission was uncovered only during the period of exceptionally low obscuration. When the AGN is obscured at these wavelengths, as is usually the case, only the more distant contribution towards the emission is seen against the faint continuum, from either the starburst or NLR scale gas which is measured here.

An upper limit to the size of the photoionised emission line region can be obtained from its angular extent on the sky. From the RGS, which is a slitless spectrograph, spatially extended emission causes broadening of the emission lines, as discussed in Sect. 6.3.5. Using the 2004-07 constraint ($<$130 km s^{-1}) gives a photoionised gas extent of <4.2", and at the distance of NGC 1365 this converts to a physical projected distance of <380 pc. This is consistent with *Chandra* results from Nardini et al. (2015), who show that extracting spectra from a circular aperture of 10" diameter centred on the nucleus increases the proportion of photoionised emission and correspondingly reduces the collisional emission contribution. In addition, Wang et al. (2009) fit the starburst ring and surrounding diffuse emission with collisional emission models while photoionised emission is expected to be the dominant component in the inner region around the nucleus, within a radius of 10".

NGC 1365's nucleus is more likely to be observed side on than face on (using the unification scheme and NGC 1365's classification range of Seyfert 1.5-2). Therefore the 380 pc can be assumed to represent the maximum extent of two ionisation cones in opposite directions from the nucleus, and one half of that can be deprojected to estimate the physical distance of the bulk of the emitting gas from the central source. Using a range of viewing angles from 80°-45° (if 0° represents looking face on), a range of upper limits for the distance between the central source and the photoionised gas can be calculated as 190-270 pc (see Figure 6.9). It would be reasonable to assume the true distance of this gas is much lower than this upper limit.

This upper limit is entirely consistent with previous distance estimates for

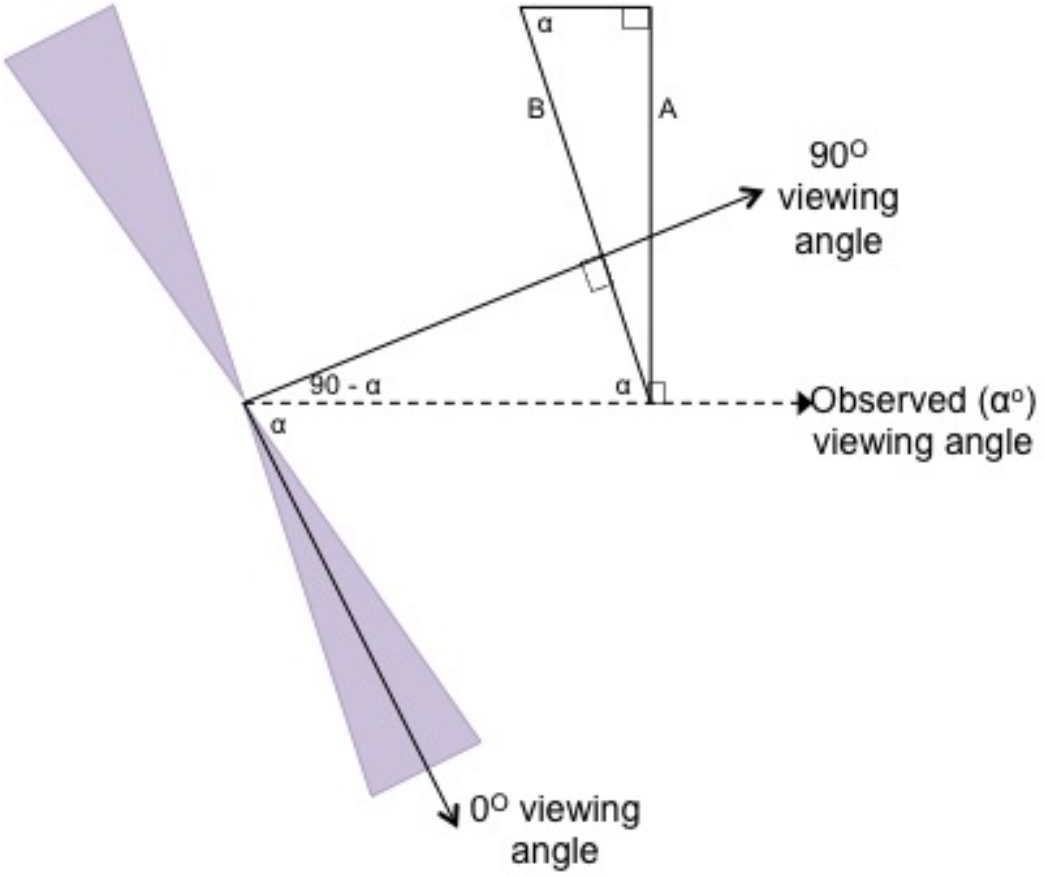

Fig. 6.9: Cartoon representing the deprojection of NGC 1365's ionisation cones (shown in purple). The viewing angle is shown as α, the observed extent of one ionisation cone is shown as A, and the calculated distance of the ionisation cone is shown as B.

the photoionised gas (discussed in Sect. 6.1.1).

6.5 Conclusion

The work reported in this chapter represents the most detailed spectral description of the emission lines from NGC 1365's nucleus so far, and has been enabled by the quantity of good quality data available in the *XMM-Newton* archive.

The X-ray narrow emission line spectrum of NGC 1365 is well represented by a combination of two collisionally ionised (kT of 220±10 and 570±15 eV) and three photoionised ($\log \xi$ of 1.5±0.2, 2.5±0.2, 1.1±0.2) phases of emitting gas, all with higher than solar nitrogen abundances. The collisionally ionised gas is attributed to the starburst surrounding the nuclear region and the photoionised gas to the Seyfert 2 nucleus in the centre.

This physical model is the best fit to the 2012-13 stacked spectrum, and yet also fits well to the 2004-07 stacked spectrum, without changing any characteristics of the emitting gas phases. The finding of 4.5±0.5 times solar nitrogen abundance in the nuclear region of this system represents the second time an over abundance of nitrogen has been suggested in this source (the first being Schulz et al. 1999, from optical measurements).

This work also finds that the photoionised X-ray emitting gas is $0.5 \leq$ distance ≤ 270 pc from the ionising continuum of the central source.

Chapter 7

Survey of O VII Forbidden Line Velocities in AGN

"If everything seems under control, you're not going fast enough"
Mario Andretti

7.1 Introduction

In the previous two chapters, two objects have been investigated in detail; Chapter 5 looks at the traditionally unobscured galaxy NGC 5548, and Chapter 6 at the more obscured (typically $N_H > 1.5 \times 10^{23}$ cm^{-2}) galaxy NGC 1365. Among the derived results are the outflow velocity values inferred from the X-ray narrow emission lines. The O VII f line found in NGC 5548 has a measured blueshifted velocity (-300$\pm$30 km s^{-1}), while that in NGC 1365 is found to be at rest (-30$\pm$70 km s^{-1}). This fact generated the idea, explored in this chapter, of testing whether there are any differences in observed outflow velocities of obscured and unobscured AGN, at the population level.

Extended ionisation cones of emission line gas photoionised by AGN have been long observed at optical wavelengths, for example in NGC 5252 (Tadhunter and Tsvetanov 1989). Their existence has also been inferred by X-ray studies, especially for nearby objects such as NGC 1068 (Kinkhabwala et al. 2002). The comparison between optical [O III] and X-ray O VII emission from Seyfert 2 galaxies by Bianchi et al. (2006), using HST and *Chandra*, showed that the regions emitting these two narrow emission lines are very well spa-

tially correlated. This fits well within the general picture of a dusty gaseous torus surrounding the AGN and determining whether we see the object as obscured or unobscured, depending on the viewing angle. This same torus is expected to restrict the gas seen by the central source, causing the biconical shape of the photoionised emission line regions, in both optical and X-ray.

In the context of the AGN Unification Theory (see Chapter 1), the hypothesis for the work in this chapter is that unobscured nuclei are more likely to have ionisation cones facing towards us, as observers, and so we are more likely to observe their emission line gas outflowing from the central source towards us. Obscured nuclei are more likely to be oriented close to edge on and to have their ionisation cones at high inclination with respect to our line of sight, so we are more likely to see their emission line gas at rest, rather than flowing towards or away from us in bulk. This may be tested by considering the velocity of the emission line gas: on average the emission line gas associated with unobscured objects should have higher velocities towards us than the emission line gas associated with obscured objects.

This hypothesis has been explored to some extent using optical narrow emission line gas, with relative success, as well as comparing the line-of-sight velocity of the emission line gas with the Eddington ratio.

Zhang et al. (2011) investigated connections between the velocity of [O III] λ5007 and other physical parameters of Type 1 objects. The authors find a velocity distribution peaking at $-47\,\mathrm{km\ s^{-1}}$ with a standard deviation of $72\,\mathrm{km\ s^{-1}}$ and a weak positive correlation between [O III] velocity and Eddington ratio of the objects in their sample. Bae and Woo (2014) looked at the velocity of [O III] λ5007 and Hα in Type 2 objects, relative to stellar absorption lines from their host galaxies, and found their velocity distribution peaks at $0\,\mathrm{km\ s^{-1}}$ with a standard deviation of $36\,\mathrm{km\ s^{-1}}$. In their sample, the [O III] velocity shift is correlated with Eddington ratio, implying that the outflow velocity of the narrow emission lines is related to ongoing black hole activity. By comparing their results to published work on Type 1 objects (e.g. Zhang et al. 2011), the authors found that the outflow fraction (for a fixed velocity offset, e.g. $50\,\mathrm{km\ s^{-1}}$) is higher in Type 1 objects than Type 2, and

attribute that to projection effects.

Boroson (2011) uses the [O III] λ5007 emission line, along with Fe II emission, to predict the orientation of a sample of quasars extracted from the Sloan Digital Sky Survey. The author argues that Fe II emission comes from inflowing gas located in the outer part of the BLR, and so has a higher inflow velocity when the disk is seen edge on, and the [O III] emission comes from polar outflows, and so has a higher outflow velocity when the disk is seen face on. The orientation predicted from the optical emission lines was supported by the (small numbers of) radio loud objects in the sample, as only those in the group defined as viewed edge on through their optical emission lines had visible double radio lobes.

Bian et al. (2005) look specifically at the blueshift of the [O III] λ5007 emission line in Narrow Line Seyfert 1s and find that there is a strong correlation between velocity shift and Eddington ratio for only the seven 'blue outliers' in their sample (velocity shifts more than 250 km s^{-1} relative to the Hβ emission). The majority of their sample shows a much weaker correlation between the two parameters.

Boroson (2005) shows that in a sample of QSOs from the SDSS survey, the [O III] λ5007 emission line is blueshifted with respect to lower ionisation optical emission lines for about half the objects, with the shifts being on average 40 km s^{-1} and reaching $>$ 400 km s^{-1}. Again, the magnitude of the blueshift was found to correlate with the Eddington ratio of the object.

Some samples of soft X-ray emission lines have also been studied. Kraemer et al. (2011) looked at the O VII f emission line in their study of AGN narrow line regions, although unfortunately only 15 of the sources in their sample had X-ray data (out of 108). They find that the O VII f line is weaker in Seyfert 2s than Seyfert 1s, attributing the difference to absorption from dusty gas (N_H of several $\times 10^{21}$ cm^{-2}) outside the NLR. This study does not look at velocities of the emission lines. Guainazzi and Bianchi (2007) were the first to focus a study on a sample of soft X-ray emission lines, in this case from *XMM-Newton* RGS archive data for 69 obscured AGN. They call their sample CIELO-AGN, and conclude that these emission lines are usually from photoionisation by

the central AGN, using line strengths to suggest a soft X-ray criterion to discriminate between AGN-photoionised sources and starburst galaxies. 23 of these objects have O VII f line detections, although the uncertainties on measured line wavelengths are up to ± 0.5 Å, and so the velocities of these (or any of the emission lines in the sample) are not investigated.

In this chapter, *XMM-Newton* RGS archive data are used for an exploratory test of the AGN Unification Theory by measuring velocities of the O VII forbidden line, and therefore probing higher ionisation gas than optical emission lines allow. This study focuses on the O VII forbidden line for two main reasons; O VII f is the strongest emission line in many AGN soft X-ray spectra and, as an optically thin forbidden line, the measured peak wavelength is unlikely to be affected by absorption intrinsic to the object (as for the O VII resonance line of NGC 5548 in Chapter 5). The sample will not be uniform or complete, but will give a preliminary assessment of the feasibility of the test and of how X-ray emission lines can be used to probe AGN orientation.

7.2 Initial Sample

I started with the *ROSAT* Bright Source Catalog and selected all objects with an AGN, Seyfert (of any type) or QSO classification in the *ROSAT* Cross-correlation Catalog. From this I searched for any *XMM-Newton* observations of those objects. The *ROSAT* Position Sensitive Proportional Counter (PSPC) instrument, used to create the *ROSAT* Bright Source Catalog operated at 0.1-2.4 keV. Hence this sample is likely to be incomplete in obscured AGN, as their continuum emission is often almost entirely absorbed at these energies. Therefore I also searched for all objects with LINER and Seyfert activity types in the NASA/IPAC Extragalactic Database (NED), and added any *XMM-Newton* observations of these to the sample, if not already included.

This inital sample consists of 1819 observations of 726 objects, and then a maximum redshift of $z < 0.65$ was applied so that the O VII f emission line rest wavelength (plus 1 Å) for all objects is within the RGS wavelength range. In addition, only observations with RGS data in the *XMM-Newton* archive were used. Therefore, the sample to be analysed has 1500 observations of 599

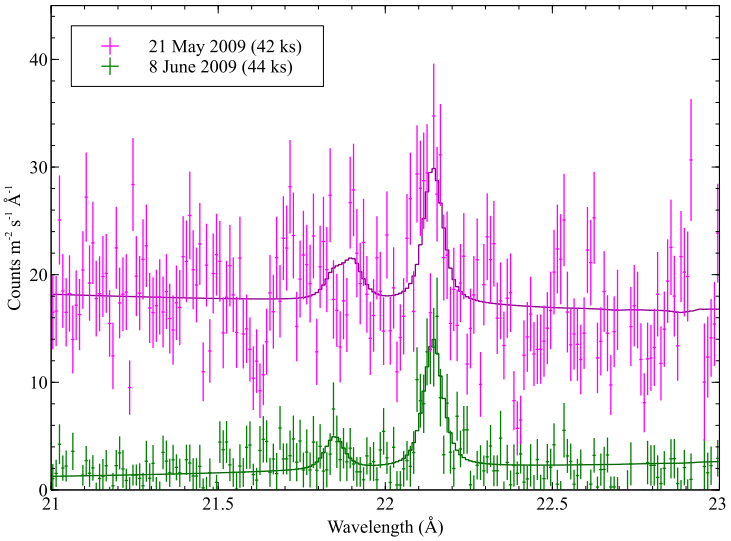

Fig. 7.1: Two observations of NGC 4051 and fits to the O VII f line (the strongest emission line in both observations). See text for details.

objects; 266 of these objects have multiple observations and 333 have been observed only once by *XMM-Newton*.

The *XMM-Newton* SAS pipeline products (PPS products) were downloaded from the *XMM-Newton* archive for each observation. All archive *XMM-Newton* observations were re-reduced in Dec 2012 for the 3XMM-DR4 serendipitous survey catalogue (Rosen et al. 2015), so the sample data have all been reduced using SAS version 12 or later.

For each observation, I used *rgscombine* (SAS) to combine the RGS1 and RGS2 first order spectra together. The second order spectra do not cover the band of interest, because they end at 17 Å. For each of the 266 objects with multiple observations I also created a stacked first order spectrum (again using *rgscombine*) of RGS1 and RGS2 combined from all individual observations of that object.

I combined all observations of each object, regardless of any spectral shape changes, as I am only analysing a small region of each spectrum (2.5 Å) and fitting only a local continuum (see Sect. 7.3). Therefore a change in spectral slope or flux level of the continuum is not expected to affect the results. Long exposure times have been shown to be important for soft X-ray emission line detections in AGN. For example, Reeves et al. (2016b) revealed the first ev-

idence of emission lines in the stacked RGS spectrum of Ark 120 (> 400 ks), which had not been seen in previous individual observations of 100 ks or less.

The only measurement I am using is the wavelength shift (if any) of the O VII emission line. Therefore by stacking the observations I am assuming that this shift is not changing. The O VII f emission line is thought to originate from the reprocessing of the nuclear radiation in the ionisation cones. There has been evidence of X-ray narrow emission lines varying in intensity over timescales of years (Detmers et al. 2009), but not of any changes in line wavelengths over these timescales. Even if the velocity of the O VII f line did change over the period covered by RGS spectra, I would then be measuring an average of the total velocity, and so it could still be considered representative of that object's properties for this exploratory study. As a test case, I used two observations of NGC 4051 with different continuum levels to check this (Obs IDs: 0606321601 and 0606322101). The measured wavelengths of the O VII f line in both observations are consistent within 1σ uncertainties (see Fig. 7.1).

For each object, the redshift, Galactic column density and classification were collected. Where possible 21 cm derived redshifts were used, and otherwise optically derived values, collected from NED. The chosen classifications are the standardised activity types given by NED, and from Simbad if no NED activity types were available. The 21 cm derived redshifts trace the neutral hydrogen in the galaxy and therefore give a more accurate standard of rest for the host galaxy than emission lines from ionised gas which could potentially be outflowing. Galactic column density values are from the LAB map, as described by Kalberla et al. (2005).

The spectral analysis and modelling for this work was done with SPEX (v.3.01.00).

7.3 Data Analysis

Each of the 599 objects (266 stacked spectra and 333 individual observations) in the sample was analysed using an automated fitting procedure, in the rest frame of each galaxy. This fitting procedure used Cash-statistics to assess the

best-fit parameters, as χ^2 is not appropriate when there are low numbers of counts per bin (see Chapter 4).

Only the data covering 2.5 Å around the O VII triplet were used because this is the only region of interest. Around the O VII triplet wavelength range there could potentially also be emission from a nitrogen radiative recombination continuum feature (RRC) just longwards of the O VII f line, or warm absorber narrow absorption lines (e.g. from O VI). The presence of these features will not be accounted for in this fitting procedure, and will reduce the overall fit quality for some objects (see the fits for NGC 1068 and NGC 3516 in Appendix A as examples). Neither of these features affects the peak wavelength measurement of the O VII f line, and this was checked after analysis by comparing to literature values derived using more detailed models (e.g. Kinkhabwala et al. 2002; Mehdipour et al. 2010).

A local continuum was fitted to the region of interest first (rest wavelength range: 20.6-23.1 Å). For each spectrum the continuum is represented by a power law model, absorbed by the local Galactic column density along that line of sight. The normalisation and spectral index of this power law model were left free in the fit. Three *Gaussian* models representing the O VII triplet, also absorbed by the local Galactic column density, were then fitted to the data together with this continuum. The wavelengths were initially fixed to the values corresponding to the redshift of the galaxy, and the normalisations were fitted. Then the wavelengths were fitted, with a $\pm 15000\,\mathrm{km\ s^{-1}}$ restriction, to ensure any 'detected' lines remain within the 2.5 Å wavelength range used in each spectrum. Each line velocity was fitted independently of the others in the triplet so that any potential absorption from the resonance line does not alter the measured velocity of the forbidden line. The intrinsic widths of the *Gaussian* models were fixed to zero throughout, to ensure that the lines remained narrow during the automated fitting procedure.

Fitting a continuum estimate first allows the continuum level to be correct for those objects with no (or very weak) emission lines, before the *Gaussian* models are included. If this step is skipped, in some cases SPEX can remain in a local C-stat minimum with no continuum and very strong *Gaussian* lines,

which is clearly incorrect. For objects with very strong emission lines (e.g. NGC 1068) the initial fit to the continuum is too high, but this reduces to the correct level once the *Gaussian* models are included.

An O VII forbidden line was considered to be 'detected' if its presence improved the ΔCash-statistic by > 9, corresponding to a 3σ detection for one parameter of interest (the line normalisation).

After analysis of the 266 objects with a stacked spectrum and the 333 objects with individual observations, 104 objects have 3σ detections of the O VII f emission line. In cases where only one line of the triplet is detected, it is assumed to be the O VII forbidden line. Six 'detections' which have emission line velocities consistent with the edge of the allowed parameter range were removed, because any uncertainties calculated for them have been artificially restricted and are therefore incorrect. Nine further 'detections' were removed after checking each of the spectra visually for spurious detections.

There are now 89 detections, 66 from stacked spectra and 23 from individual observations. These are presented in Appendix A.

For NGC 5548, NGC 1365, NGC 1068 and NGC 3516 the O VII f line velocities from this analysis were compared with values from more detailed modelling (from Chapter 5 and Chapter 6, and Kinkhabwala et al. 2002; Mehdipour et al. 2010, respectively). All measurements were consistent within 2σ uncertainties, showing that applying this analysis technique to the sample is justified.

As in previous optical studies, I plan to compare the wavelength shift (velocity) of the O VII narrow emission lines with the Eddington ratios of the source. For this I need bolometric and Eddington luminosities for the objects.

74 of the 89 objects for which there is a O VII f line detection, have 2XMM catalogue names (Watson et al. 2009), which I found using the NED database. The 3XMM catalogue is more recent, but the assigned 2XMM names are more consistently associated with objects throughout NED. To convert the 2XMM catalogue 2-12 keV fluxes into 2-10 keV luminosities, intrinsic absorption must be taken into account. Through a literature search I found intrinsic absorption column densities for 58 of the objects with 2XMM names.

I then converted the observed 2-12 keV fluxes to intrinsic 2-10 keV luminosities for these 58 objects taking into account their intrinsic column densities, following the process explained by Mingo et al. (2016), but using SPEX instead of XSPEC and HI Galactic column densities from the LAB map (Kalberla et al. 2005). As in Mingo et al. (2016), uncertainties for these luminosities were calculated by using the highest and lowest intrinsic column densities and flux values as this allows the intrinsic column density uncertainties to be taken into account, rather than simply propagating only the flux uncertainties through the calculations.

The 2-10 keV luminosity $L_{(2-10\,keV)}$ can then be converted into an estimate of the bolometric luminosity L_{bol} using the relation from Marconi et al. (2004):

$$\log[L_{bol}/L_{(2-10\,keV)}] = 1.54 + 0.24\mathcal{L} + 0.012\mathcal{L}^2 - 0.0015\mathcal{L}^3 \tag{7.1}$$

where $\mathcal{L} = \log L_{bol} - 12$ and both L_{bol} and $L_{(2-10\,keV)}$ are in units of $L_{\odot}$. Ideally a bolometric luminosity value should take into account the real emission over the whole electromagnetic spectrum, rather than using a template (as this conversion does). Using this simpler estimate allows us to calculate bolometric luminosity values for the majority of the sample objects in the same way.

55 of the 58 objects with calculated L_{bol} values also have black hole masses in the literature. For these, I calculated the Eddington luminosity L_E (Eddington 1925) using the formulation shown in Rybicki and Lightman (1979):

$$L_E = \frac{4\pi G c m_H}{\sigma_T} M = 1.25 \times 10^{38} (\frac{M}{M_{\odot}}) \mathrm{erg\,s^{-1}} \tag{7.2}$$

where G = the Gravitational constant, c = the speed of light, m_H = the mass of an hydrogen atom and σ_T = the Thompson scattering cross section

For the 55 objects where both the Eddington and bolometric luminosities are estimated, I also calculated the Eddington ratio ($\frac{L_{bol}}{L_E}$).

The 2-10 keV and bolometric luminosities, black hole masses, Eddington luminosities and ratios are all included in Appendix B.

7.3.1 Kolmogorov-Smirnov Test

As the sample under consideration is split into different AGN types, I need a method to determine if the distribution of the interesting variable (outflow

velocity of X-ray narrow emission line gas) in each part of the sample is from the same or a different parent distribution as other parts of the sample. As the parent distribution is not known, a distribution-free (nonparametric) test is required.

One such test is the Kolmogorov-Smirnov (K-S) two sample test; the following formulation is from Bohm and Zech (2010) and the *Python.scipy.stats* K-S two sample test function. This uses the cumulative distribution function of each sample ($F(x)$) and calculates the greatest vertical distance between the two (D). The test statistic calculated is:

$$D = max|F(x_1) - F(x_2)| \tag{7.3}$$

The expected distribution of D is then scaled by the sample size, to take into account that there is more information in samples of larger sizes. As discussed in Bohm and Zech (2010), for sample sizes larger than 20 this can be approximated by:

$$D^\star = D(\sqrt{N} + 0.12 + 0.11/\sqrt{N}) \tag{7.4}$$

where $N = \sqrt{\frac{n_1 n_2}{n_1+n_2}}$, and n_1 and n_2 are the two sample sizes respectively.

Fig. 7.2 shows the function which converts $D^\star$ into a probability that the two samples would be at least this different if drawn from the same parent distribution.

The K-S test is sensitive to the location, scale and shape of the underlying distributions, but its main weakness is that it is not very sensitive to differences in the tails of the distributions. This particular weakness is not a problem when addressing the question set out in this chapter, as the main difference between the distributions is expected to be the locations of their peaks.

7.4 Results and Discussion

I first compared the sample with detected O VII f lines (89 objects) with the initial sample of 599 objects (see Fig. 7.3). From a basic interpretation of the Unification theory, the Seyfert 2 emission line detection rate would be expected to be higher than the Seyfert 1 detection rate, as the soft X-ray continuum for

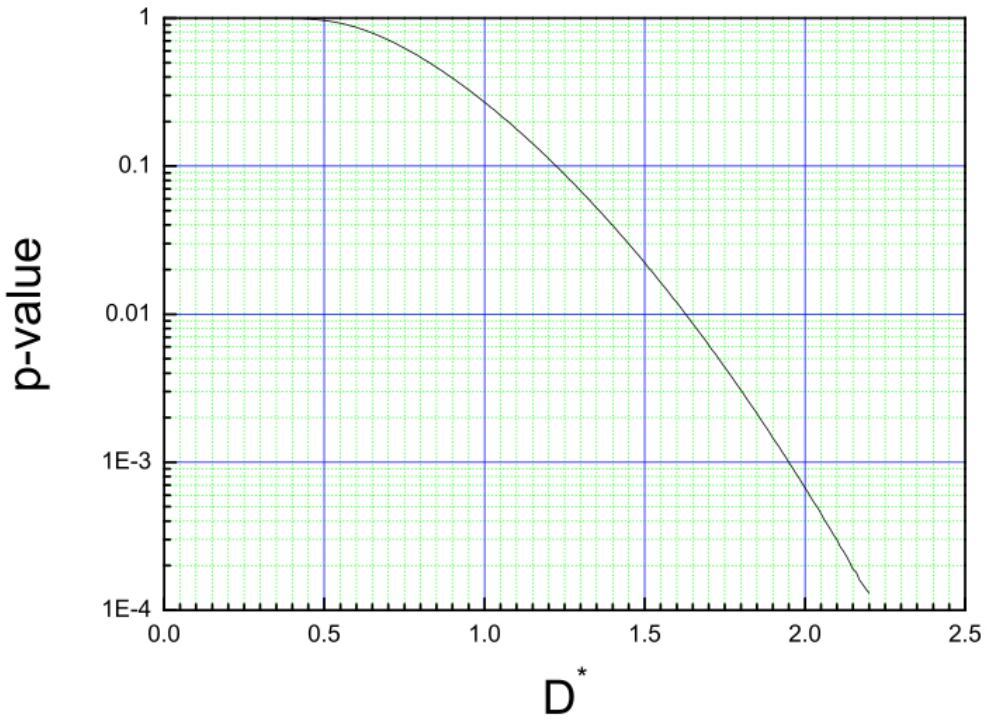

Fig. 7.2: Probability as a function of the Kolmogorov-Smirnov test statistic D*. From Bohm and Zech (2010)

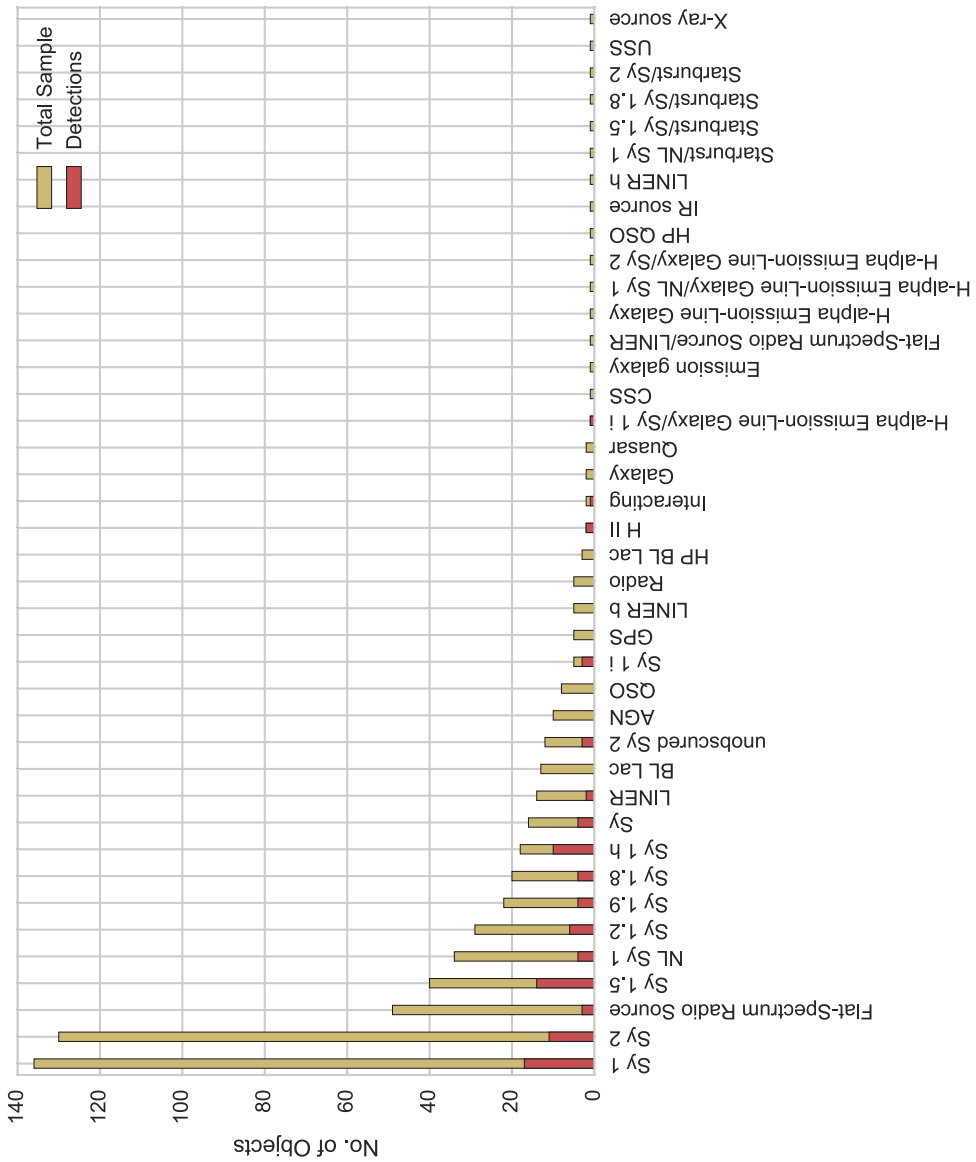

Fig. 7.3: Number of objects in initial sample (total: 599) and number of objects with line detections (total: 89), shown as classified in NED

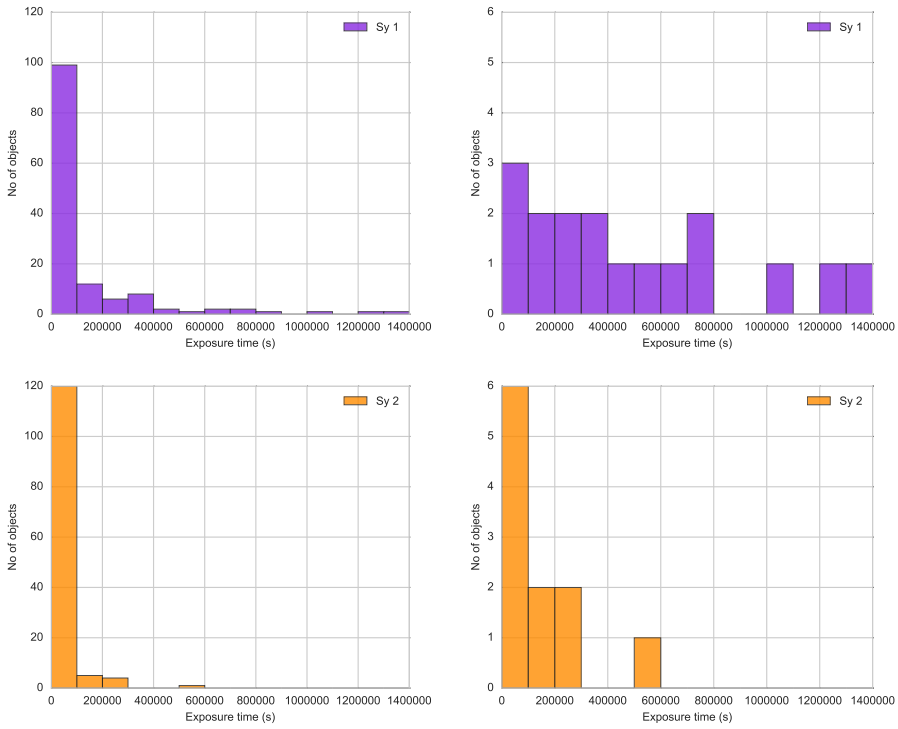

Fig. 7.4: Histograms showing the distribution of (RGS1 and RGS2 combined) exposure times for observations of Seyfert 1s (purple) and Seyfert 2s (orange). Left top: For the full sample, 137 Seyfert 1s. Left bottom: For the full sample, 130 Seyfert 2s. Right top: For those objects with 3σ emission line detections, 17 Seyfert 1s. Right bottom: For those objects with 3σ emission line detections, 11 Seyfert 2s.

Seyfert 2 objects is lower, and therefore the narrow emission lines should be easier to detect.

In this analysis, the detection rates for objects classed as Seyfert 1 and Seyfert 2 are 13% (17/136) and 9% (11/130) respectively, which is not what would be expected. Given that this sample is not uniformly selected it has a wide range of exposure times, which have been chosen for various reasons. Fig. 7.4 shows that very few Seyfert 2s have been observed for exposure times longer than 100 ks compared to Seyfert 1s, in both the full sample and those with line detections. Therefore this sample cannot be used to draw conclusions on the relative detection rates between objects because the exposure time coverage is not uniform.

The necessity of long observations for emission line detections means that the sample I am using is likely to be missing emission line detections for those

objects which have only been observed briefly by *XMM-Newton*. Given that *XMM-Newton* observations of AGN are performed for a variety of scientific reasons, for the remainder of this work I assume that this does not lead to a bias in velocities of the detected emission lines.

Fig. 7.3 shows the variety of classifications provided in NED. This wide range of names and types has been collected from the literature over many years, and is not uniformly organised or checked. Therefore there are differences in classification between NED and the current understanding of particular objects, especially for those classifications not commonly used. In order to test the main hypothesis of this work, I split the sample into two broad classifications of 'Type 1' and 'Type 2', with the 'Type 1' objects more likely to be at face on inclination, and the 'Type 2' objects more likely to be at edge on inclination. The Seyfert 1, 1.2, 1.5 and Narrow Line Seyfert 1 objects were placed in the 'Type 1' group, and the Seyfert 2, 1.9, 1.8 and Seyfert 1 h (Seyfert 2 objects with broad lines detected in polarised light) objects were placed in the 'Type 2' group. The unobscured Seyfert 2 objects were included in the 'Type 1' group, as their classification is for objects thought to be seen face on, but with no broad line emission (see Nicastro 2000; Laor 2003; Elitzur and Ho 2009). This was confirmed for the three objects with this classification (NGC 2992, NGC 6251 and NGC 7590) by Trippe et al. (2008), Bassani et al. (1999) and Evans et al. (2005) respectively.

This left 13 objects with NED classifications of LINER, Seyfert, Flat-Spectrum Radio Source, H II, H-α Emission Line Galaxy/Seyfert 1 or Interacting, which I looked at individually in more detail. Based on the literature, I classified 10 of these into the 'Type 1' and 'Type 2' groups, and determined that three of them were too uncertain to use. The details and references for these objects are included in Appendix C. The 'Type 1' and 'Type 2' groups contain 53 and 33 objects respectively.

The measured wavelength shifts of the O VII f lines have been converted into velocities (km s^{-1}) and will be used in this form from this point onwards in this chapter. Negative velocities represent movement towards us relative to the host galaxy, and positive velocities imply movement away from us relative

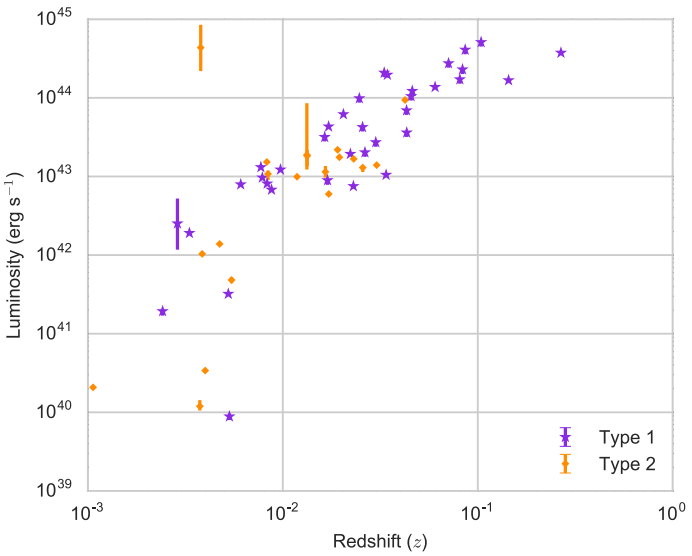

Fig. 7.5: 2-10 keV luminosity vs redshift for the objects with absorption corrected luminosities, when classified into 'Type 1' and 'Type 2'. For details of those classifications, see text.

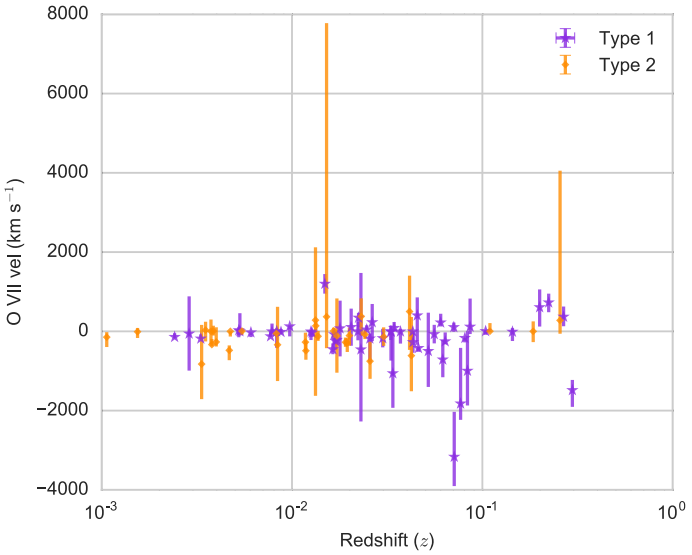

Fig. 7.6: O VII forbidden line velocity (in km s^{-1}) vs redshift for the objects when classified into 'Type 1' and 'Type 2'. For details of those classifications, see text.

to the host galaxy.

As this sample is not selected to be unbiased in redshift or intrinsic luminosity (see Fig. 7.5), I compared those parameters between the groups with the K-S test. The K-S test cannot reject the null hypothesis that the 2-10 keV luminosity distributions (corrected for intrinsic absorption) are drawn from the same parent distribution (with a probability of 13%), but does reject the hypothesis at a significant level (with a probability of 0.6%) that the redshift distributions of the two groups come from the same parent distribution. Fig. 7.6 suggests that there is no dependence of O VII f velocity on redshift, therefore the different redshift distributions of the groups should not be a problem for the results of this study.

Fig. 7.7 compares histograms of the O VII velocity shifts for the 'Type 1' and 'Type 2' objects. It appears that the 'Type 1' objects have O VII f velocity shifts distributed over a larger range and displaced towards the blueshift direction, but this does not take into account the varying uncertanties on each measurement. For example, the 'Type 1' measurement that falls in the -3500 to -3000 km s^{-1} bin actually has a 1σ uncertainty of $+1100$ km s^{-1} and -700 km s^{-1}, while one of the measurements that falls in the -1500 to -1000 km s^{-1} bin has a much smaller 1σ uncertainty of $+300$ km s^{-1} and -400 km s^{-1}. In the histogram uncertainties are not displayed, and therefore all measurements are treated as exact.

To avoid this problem, I created probability density functions for the distribution of measurements for each group using Kernel Density Estimation (KDE)[1] (Scott 2015). Each measurement is now represented by a *Gaussian* with the width determined by the uncertainty of that particular measurement. The probability density function for each group is made by summing these *Gaussian* kernels together, and the results are shown in Fig. 7.8. This method assumes that the 1σ uncertainties are symmetrical, which is not quite the case, although symmetry in the uncertainties is a reasonable assumption to make given that taking the uncertainties into account this way is more representative than not doing so at all.

[1] http://scikit-learn.org/stable/modules/density.html

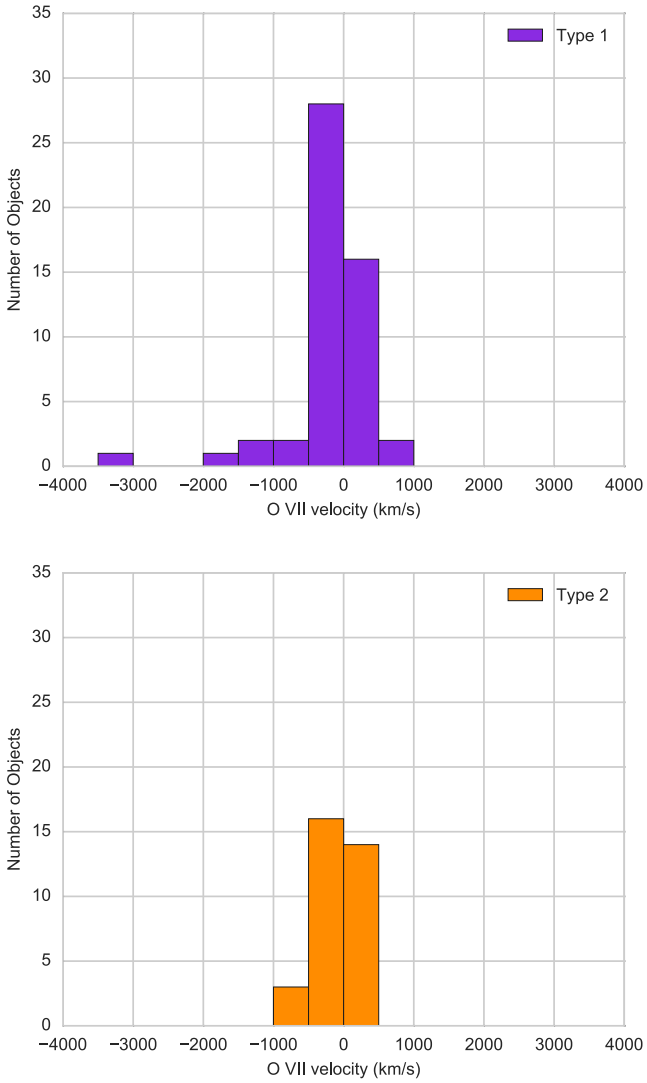

Fig. 7.7: Histograms (with bin widths of 500 km s^{-1}) showing the distribution of O VII f line wavelength shifts as velocities for the 'Type 1' group (top) and the 'Type 2' group (bottom)

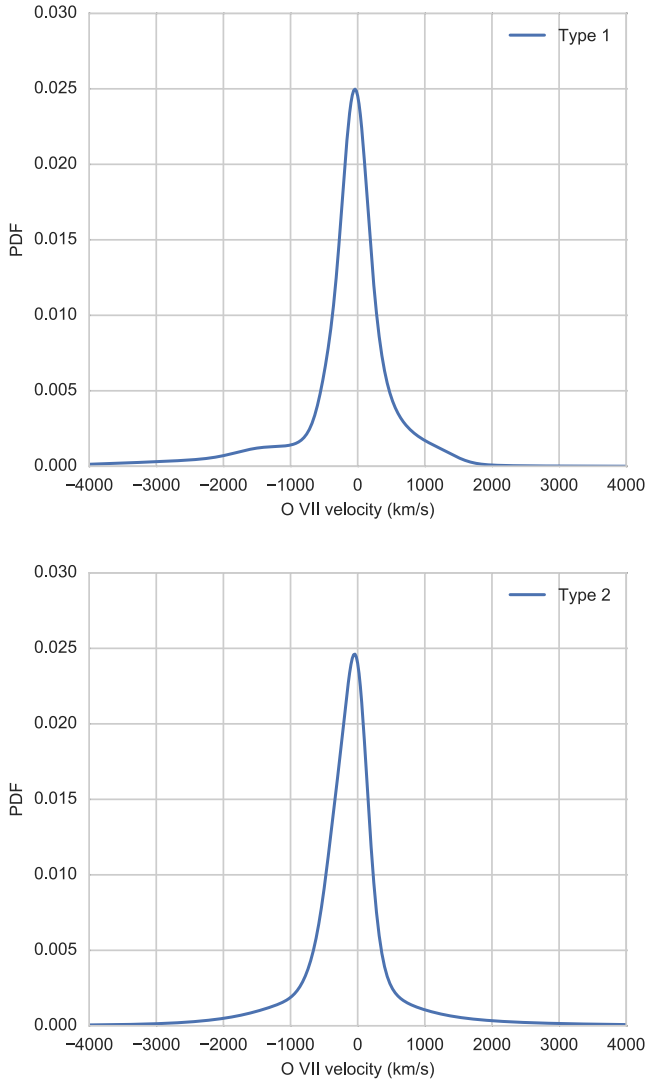

Fig. 7.8: Probability Density Function of the distribution of O VII f line wavelength shifts plotted as velocities for the 'Type 1' group (top) and the 'Type 2' group (bottom), taking into account the different uncertainties on the measurements.

The 'Type 1' distribution peaks at $-40 \pm 60\,\mathrm{km\ s^{-1}}$ with 68% of the distribution between $-500\,\mathrm{km\ s^{-1}}$ and $330\,\mathrm{km\ s^{-1}}$, while the 'Type 2' distribution also peaks at $-40 \pm 70\,\mathrm{km\ s^{-1}}$ with 68% of this distribution between $-550\,\mathrm{km\ s^{-1}}$ and $250\,\mathrm{km\ s^{-1}}$.

Both distributions also appear to prefer the blueshifted (negative) velocity values, with 56% and 62% of the distributions at velocities less than $0\,\mathrm{km\ s^{-1}}$, for 'Type 1' and 'Type 2' respectively.

A K-S test has been used to compare the two distributions, using the original samples. The null hypothesis that the two samples were drawn from the same parent distribution cannot be rejected, with a probability of 81%. Clearly this does not support the hypothesis that the O VII f line velocity distributions are different between 'Type 1' and 'Type 2' objects.

One complication with the K-S test is that the conversion of distance metric between cumulative distribution functions (D) to probability is dependent on sample size (n_1 and n_2; see Sect. 7.3.1). Therefore the same D can be considered non-significant with small samples, and significant with large samples.

In this case, if I make the simplifying assumption that the D value would remain the same, sample sizes of 190 objects in each group would be sufficient for the K-S test to establish that samples drawn from the same parent population would only differ this much $< 5\%$ of the time. A total number of 380 objects is more than four times greater than the number of objects with line detections in this work, and more than half the number of the initial sample of objects (599) analysed in this work.

The total uncertainties on the velocity measurements in this sample are very varied, ranging from $130\,\mathrm{km\ s^{-1}}$ to $4000\,\mathrm{km\ s^{-1}}$. To understand the effect the large uncertainties have on these results I repeated the above analysis with a sub-sample where the O VII f detections have total uncertainties of $\leq 500\,\mathrm{km\ s^{-1}}$, giving 35 objects in the 'Type 1' group and 21 objects in the 'Type 2' group. The results are essentially unchanged; the distribution peaks remain the same and both distributions still prefer blueshifted (negative) velocities, with the same percentages of the distributions at velocities less than

$0\,\mathrm{km\ s^{-1}}$. There are two minor differences, the first being that using more certain measurements (those with smaller uncertainties) gives a narrower distribution for both groups, indicating that the widths of the original distributions are artificially broadened by the uncertainties compared to the underlying physical distribution. The second difference is in the K-S test results; using more certain measurements reduces the probability that the two samples were drawn from the same parent population (from 81% to 30%), although the null hypothesis still cannot be rejected. If all uncertainties in the velocity measurements were $\leq 500\,\mathrm{km\ s^{-1}}$ and the D value would remain the same, then a sample size of 55 objects in each group would be sufficient for the K-S test to establish that samples drawn from the same parent population would only differ this much $< 5\%$ of the time.

The host galaxy redshifts in this sample have been collected using a variety of methods, including using optical emission lines, and optical line studies have shown that the [O III] λ5007 line is regularly blueshifted with respect to lower ionisation optical lines and to stellar absorption lines of the host galaxy. If the optical line derived redshifts are biased towards blueshifts relative to the host galaxy, then the O VII f line wavelength shifts measured in this work may be artificially altered. To quantify whether optical line derived redshifts in this sample are biasing the results, a sub sample of 39 objects with 21cm derived redshifts was used. A probability density function was calculated of the measured O VII f line velocities relative to the 21cm derived host galaxy redshifts. This was compared to the same plot (of the same 36 objects) using O VII f line velocities relative to optical emission line derived redshifts (see Fig. 7.9). While for individual objects the differently derived redshifts can be up to $\Delta z = 0.0015$ different from each other (see Fig. 7.10; corresponding to a difference of $\Delta v = 450\,\mathrm{km\ s^{-1}}$ in the O VII f line velocity), there is no major systematic shift between the Probability Density Functions (see Fig. 7.9). Therefore the two sample distributions are indistinguishable from each other, with both peaks at $-60 \pm 50\,\mathrm{km\ s^{-1}}$ and 68% of the 21cm and optically derived redshift distributions in the range -420-$240\,\mathrm{km\ s^{-1}}$ and -400-$240\,\mathrm{km\ s^{-1}}$ respectively.

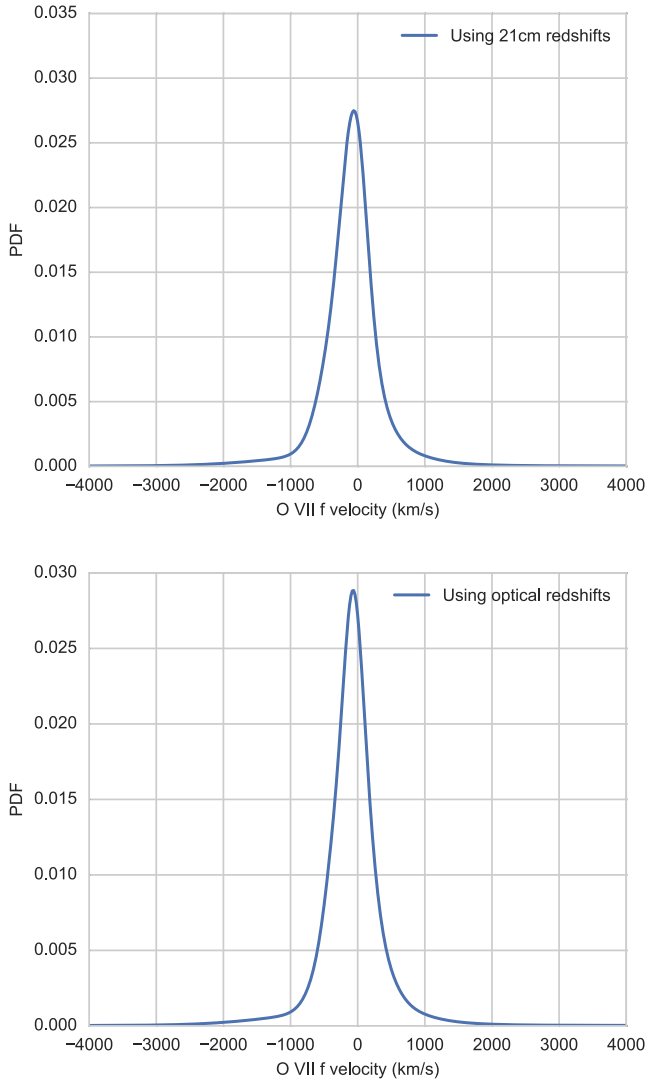

Fig. 7.9: Probability Density Function of the distribution of O VII f line wavelength shifts plotted as velocities for all objects with a 21cm derived host galaxy redshift, using the 21cm derived redshift as the reference (top) and using an optical emission line derived host galaxy redshift as reference (bottom).

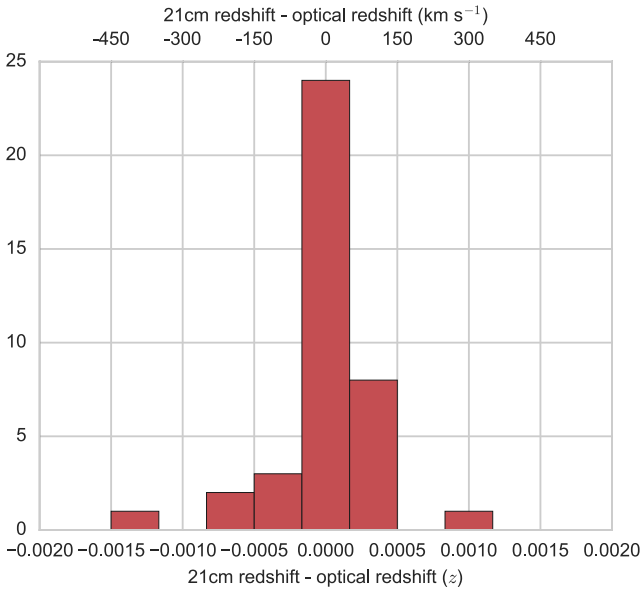

Fig. 7.10: Histogram showing the differences between 21cm and optically derived redshift values.

In the X-ray literature AGN are often classified by their level of intrinsic absorption, instead of the strength of their optical broad emission lines, and the relationship between these classifications systems is not simple (see e.g. Gonzalez-Martin et al. 2014). To investigate whether using the classification based on obscuration would alter the results, Fig. 7.11 shows the intrinsic absorption column density of the sources in the sample against their O VII f line velocity. There is no correlation between the two variables within this sample, and therefore using a classification system based on the level of intrinsic absorption would be unlikely to change the conclusions of this study.

Previous studies measuring optical emission line (O [III]) velocities have found that the blueshift of O [III] can be related to the Eddington ratio of the source (see Sect. 7.1) To explore whether similar behaviour occurs in this sample, Fig. 7.12 compares O VII f emission line velocity to Eddington ratio. This is done for all objects in the sample with a O VII f line detection, a luminosity (converted to a bolometric luminosity estimate, see Sect. 7.3) and a black hole mass (used to calculate the Eddington luminosity, see Sect. 7.3). This comparison does not show any correlation, but for both Fig. 7.11 and 7.12 the uncertainties on the O VII f velocities are too large to draw statistically

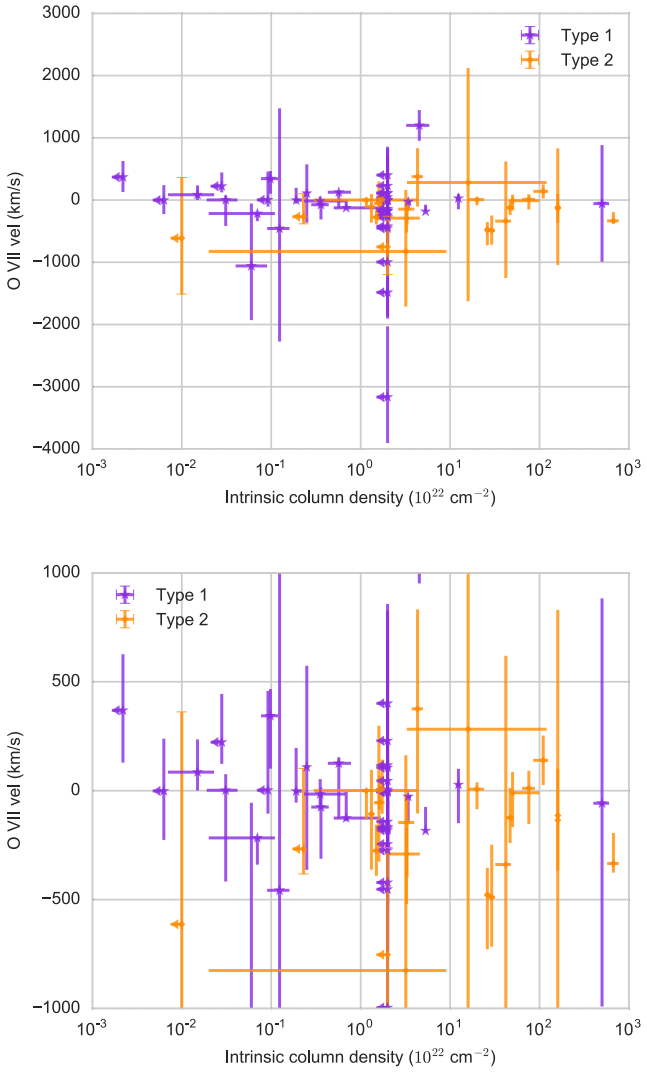

Fig. 7.11: Comparing intrinsic absorption column density to O VII f line wavelength shift (in velocity). The bottom plot is the same as the top one, but looks more closely at the $-1000\,\mathrm{km\ s^{-1}}$ to $1000\,\mathrm{km\ s^{-1}}$ range.

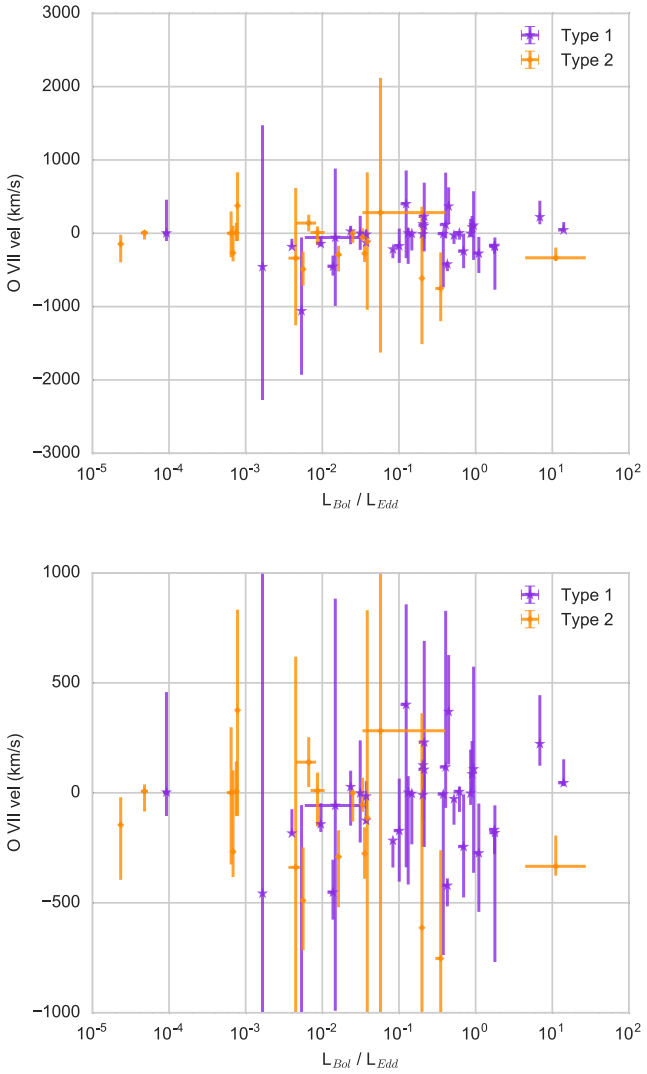

Fig. 7.12: Comparing Eddington ratio to O VII f line wavelength shift (in velocity). The bottom plot is the same as the top one, but looks more closely at the $-1000\,\mathrm{km\ s^{-1}}$ to $1000\,\mathrm{km\ s^{-1}}$ range.

significant conclusions that no correlation exists.

7.4.1 Comparison to the CIELO-AGN Sample

The CIELO-AGN sample by Guainazzi and Bianchi (2007) is the only systematic study of AGN soft X-ray emission lines found in the literature. CIELO-AGN only includes obscured Seyferts, with a classification of type $\geq$1.5 in NED, and *XMM-Newton*-RGS public data as of Sept 2006. Of the 69 objects in CIELO-AGN, the sample here includes 59. The 10 objects in the CIELO-AGN sample which are not in this work have not been included for the following reasons:

- Differences in current NED classification (eight objects)
- Redshift above applied z $<$ 0.65 cut (IRAS F10214+4724)
- Problem with *XMM-Newton* pipeline extraction of RGS1 spectra (NGC 7674); Guainazzi and Bianchi (2007) used the Observation Data Files (ODFs), not the Processing Pipeline Subsystem (PPS) products

The sample for this work includes O VII f line detections in 31/201 objects which now fulfil the CIELO-AGN criteria (NED classification and public *XMM-Newton* data). Within this work there are 16 objects which are not in the CIELO-AGN sample even though their *XMM-Newton* data were public at the time of that study. These objects were not classified as Seyferts of type $\geq$1.5 until late 2006 when 'A catalogue of quasars and active nuclei: 12th edition' was published by Véron-Cetty and Véron (2006), therefore these classifications were likely not to be present in NED at the time Guainazzi and Bianchi (2007) collected their CIELO-AGN sample.

The CIELO-AGN sample finds O VII f line detections in 23/69 objects, a significantly higher detection rate than in this work. One major difference between the two studies is the criterion for when an emission line is counted as 'detected'; Guainazzi and Bianchi (2007) considered a line detected if the flux is inconsistent with zero at the 1σ level, whereas this work has been more conservative and uses a 3σ restriction for this analysis. This explains why the O VII f detection rate is reduced for this work compared to Guainazzi and Bianchi (2007).

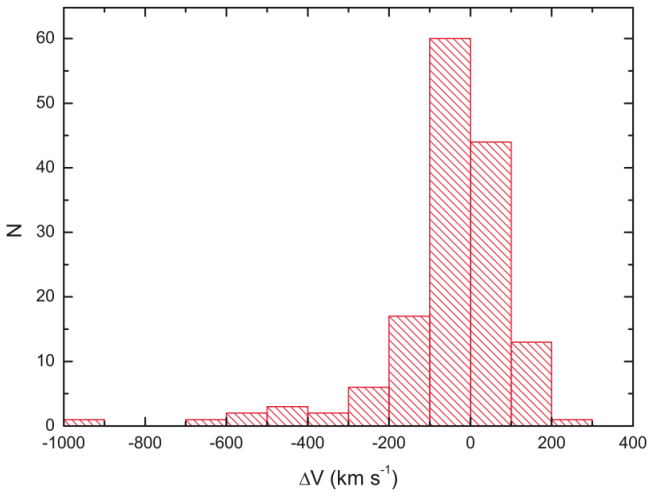

Fig. 7.13: From Bian et al. (2005). The distribution of the [O III] blueshift relative to Hβ (ΔV) in units of km s^{-1}

7.4.2 Comparison to Optical Emission Line Studies

The histogram of O VII f velocites found in 'Type 1' objects (Fig. 7.7) bears resemblance to the equivalent plot using [O III] λ5007 velocities of NL Seyfert 1s by Bian et al. (2005), shown in Fig. 7.13, and to a lesser extent to that from SDSS QSOs by Boroson (2005), shown in Fig. 7.14. The two optical line velocity histograms show an excess of negative velocities and a tail extending three times further in that direction, which are also seen in Fig. 7.7. Zhang et al. (2011) studied [O III] velocities of only Type 1 objects and found that the distribution peaks at -47 km s^{-1} with a standard deviation of 72 km s^{-1}, while Bae and Woo (2014) looked at only Type 2 objects and found their distribution peaks at 0 km s^{-1} with a standard deviation of 36 km s^{-1}. The 'Type 1' and 'Type 2' O VII f line velocity distributions in this work are both consistent with those [O III] values, as they peak at -40 ± 60 km s^{-1} and -40 ± 70 km s^{-1} respectively. The uncertainties on the O VII f line velocities measured here are too large to identify a velocity difference of the order (50 km s^{-1}) measured using [O III] λ5007.

The velocity difference of 50 km s^{-1} between Type 1 and Type 2 objects found using [O III] is a reasonable estimate for that expected from the O VII f velocity distributions because Bianchi et al. (2006) show that [O III] and O

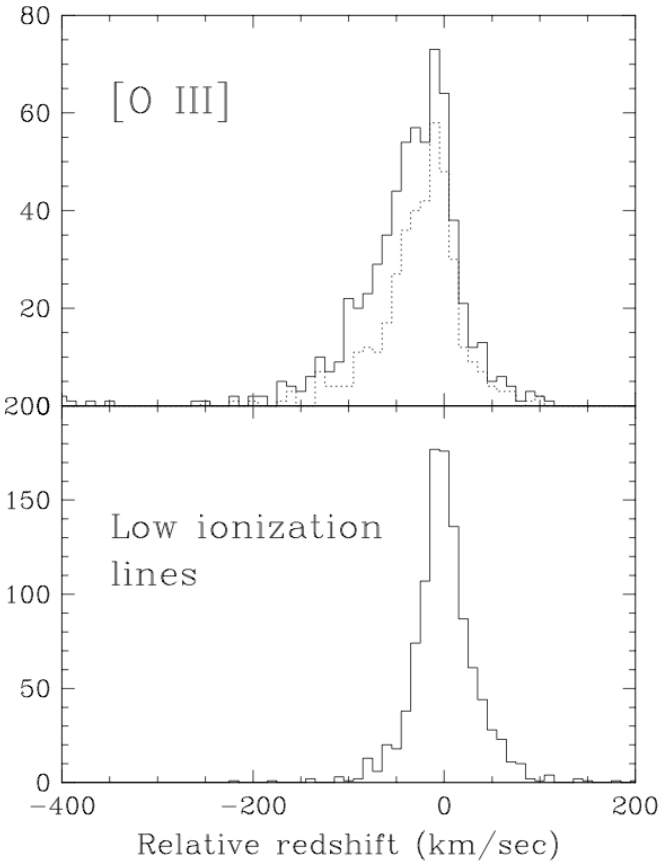

Fig. 7.14: From Boroson (2005). Relative redshift distributions for all measurements of low-ionisation lines (bottom) and for the [O III] λ5007 line (top). The dotted line in the top panel shows the objects for which two or more low-ionization species are used to calculate the systemic velocity.

VII line emitting gas are co-spatial in Seyfert 2 galaxies.

Bae and Woo (2014) also found that a lower percentage of Seyfert 2s (25-40%) had [O III] line velocities more blueshifted than $-50\,\mathrm{km\ s^{-1}}$ compared to literature results of Seyfert 1s (50%). That pattern is not followed within this work which shows a slightly higher proportion of velocities more blueshifted than $-50\,\mathrm{km\ s^{-1}}$ in the 'Type 2' distribution (51% and 57% for 'Type 1' and 'Type 2' respectively). The 'Type 2' distribution (Fig. 7.8) shows a higher proportion of velocities more blueshifted than $x\,\mathrm{km\ s^{-1}}$ than the 'Type 1' distribution, until x becomes $-700\,\mathrm{km\ s^{-1}}$, from which point the two distributions have comparable proportions.

7.5 Conclusion

Velocities of the O VII forbidden X-ray narrow emission line have been used to address the hypothesis that on average the emission-line gas associated with face on AGN should show wavelength blueshifts, i.e. velocity towards us, unlike the emission-line gas associated with edge on AGN. The work described in this chapter is the first to investigate O VII f emission line velocity differences across AGN types, and in the process has substantially increased the number of O VII forbidden line detections from a uniform analysis across different types of AGN.

No difference has been found between the two broadly classified AGN types, as the distributions of velocities for each type peak at $-40 \pm 60\,\mathrm{km\ s^{-1}}$ and $-40 \pm 70\,\mathrm{km\ s^{-1}}$ for the 'Type 1' and 'Type 2' groups respectively. If there is a velocity difference comparable to that of [O III] λ5007, previously measured to be around $50\,\mathrm{km\ s^{-1}}$, the uncertainties in this sample are too large for that difference to be detectable.

If designing an ideal sample to test this particular hypothesis again, one important step forward would be the use of a much larger sample size, of at least 200 objects with O VII forbidden line detections, and velocity measurements with total uncertainties of $\leq 500\,\mathrm{km\ s^{-1}}$, in each of the broad 'Type 1' and 'Type 2' groups. Much longer exposure times will be needed to achieve this, especially of 'Type 2' objects. More certain classifications would also

be beneficial, ideally derived the same way for all the sample objects. While 21cm derived host galaxy redshifts are expected to be more accurate relative to optical line derived redshifts, using one or the other does not appear to alter the results with this sample, because the differences are not systematically in one direction. This could be tested again once the SKA1 (first light: 2020) galaxy survey has been undertaken, as it is predicted to result in 21cm derived redshifts for 5×10^6 galaxies up to $z \sim 0.8$ (Santos et al. 2015).

The second important aspect to really investigate these potential velocity differences is a representative sample across both 'Type 1' and 'Type 2' groups. The confidence in any result would be greatly improved by systematically observing a selection of AGN in both groups rather than using existing observations with detectable O VII forbidden lines, as has been done here.

If, as is assumed, the line-emitting gas is outflowing from the central source within an ionisation cone, then any measured velocities will be an average of the line of sight velocity components over the whole volume of that gas. When looking directly face on to the ionisation cone, the largest line of sight velocities would be from the centre of the cone, where the full outflow velocity is in the line of sight. The gas towards the edges of the ionisation cone would have smaller line of sight velocities because some part of their velocity is perpendicular to the line of sight. If the gas outflow is radial and originates at the location of the background X-ray source, then for absorption features, when only gas in the line of sight can be seen, the measured velocity would always be the full velocity. For emission features, when gas outside the line of sight also contributes to the total emission, the velocity measured would be averaged over the line of sight velocities from all parts of the cone, reducing the total measured velocity of the gas.

Therefore the outflow velocities measured from both [O III] and O VII emission can be thought of as lower limits to the direct outflow velocity in each system, even for face on ('Type 1') objects. In this case, the average velocity in 'Type 1' objects is lower than the total outflow velocity, making any potential difference between 'Type 1' and 'Type 2' objects harder to detect.

If there really is no difference between the line-of-sight velocities of X-ray

emission line gas in each group, this would indicate that the simple orientation dependent AGN unified schemes are not representative of AGN throughout the nearby Universe. One solution could be to add further differences between the two main AGN types, for example the existence of different quantities of obscuring gas at varying distances complicates the simplest unification scenarios. The structure of any central torus is an additional factor which may affect line-of-sight velocity tests such as this. A clumpy torus, which allows radiation to escape to some extent in all directions (not just into ionisation cones) could cause outflows to exist at many varying locations around the central source. This would dilute any potential line-of-sight velocity differences from orientation angles.

Instead of altering orientation dependent unification schemes, it is possible that as the field develops further, these unification schemes will end up being left behind and alternative theories will be developed instead. Tests along the same lines as the one done in this chapter will have an important role to play in continually challenging and testing unification theories.

Chapter 8

Conclusions and Implications

"If we all did the things we are really capable of doing,
we would literally astound ourselves"
Thomas A. Edison

X-ray narrow emission lines can give insights into ionisation states, distances, velocities and abundances of gas intrinsic to AGN. Through the work in this thesis I have investigated these topics in both (normally) unobscured and obscured AGN.

I first investigated one object of each classification type in detail, NGC 5548 and NGC 1365. A sequence of observations of the usually unobscured AGN NGC 5548 showed an unexpectedly high level of intrinsic absorption, allowing a clear view of the X-ray narrow emission lines in this object for the first time. Through detailed analysis of the O VII He-like triplet (Chapter 5), I found evidence that these narrow emission lines are absorbed by at least one of the warm absorber phases known to be intrinsic to the object. Through modelling, I also provide an ionisation state and distance estimate for the emitting gas of $\log \xi = 1.45 \pm 0.05$ and 13.9 ± 0.6 pc respectively. This distance is consistent with those of the intrinsic WAs components, which have upper limits to their distances from < 2.2 pc to < 50 pc (Ebrero et al. 2016). Ionised absorption of AGN narrow emission lines has been discussed previously in the UV, when Kriss et al. (2003) found that the best fit to their Far Ultraviolet Spectroscopic Explorer (FUSE) data of NGC 7469 included absorption of the

narrow emission line components by the UV warm absorbers. Neutral absorption has also been invoked by Kraemer et al. (2011) to explain weaker O VII forbidden lines in Seyfert 2 galaxies compared to Seyfert 1s, although from examination of a small sample of objects.

Previous studies (e.g. Krolik and Kriss 1995; George et al. 1998; Sako et al. 2000; Blustin et al. 2003; Armentrout et al. 2007) have compared X-ray warm absorber parameters such as ionisation level, distance and column density, with those of the ionised X-ray narrow line-emitting gas in the same objects, and found potential connections between them, without conclusively proving that the emission and absorption come from the same gas. The work in Chapter 5 of this thesis adds more evidence to the concept that these emission and absorption phases should not be thought of and modelled separately. The two processes are occuring at very similar (potentially the same) distances from the central source and are being ionised by the same source, therefore a realistic physical model should consistently account for both.

Chapter 6 focuses on X-ray narrow emission lines from an obscured AGN, NGC 1365. Using data available from the *XMM-Newton* archive, I consistently modelled the 2004-2013 X-ray narrow emission lines from both the AGN and surrounding starburst region, with a combination of two collisionally ionised (kT = 220$\pm$10 and 570$\pm$15 eV) and three photoionised ($\log \xi$ of 1.5$\pm$0.2, 2.5$\pm$0.2, 1.1$\pm$0.2) phases of emitting gas. A higher (4.5$\pm$0.5$\times$) abundance of nitrogen is needed to fit the line ratios correctly, relative to other metals in the spectrum (e.g. oxygen, carbon and iron). An increased nitrogen abundance has been suggested previously for this AGN, using optical emission line ratios, supporting this interpretation of the X-ray spectrum. I tentatively suggest that this increase of nitrogen may originate from the Wolf-Rayet stars observed in the nuclear region (Phillips and Conti 1992).

Usual methods of determining metal abundances in AGN rely on UV broad emission lines in the rest frame of the galaxy, or narrow absorption lines in either the UV or X-ray. For obscured AGN, these methods are not applicable because the broad lines are not visible and the absorbed continuum is too low to show narrow absorption line signatures. In these cases being able to estimate

abundances from both optical and X-ray emission lines enables consistency checks across wavelengths and ionisation states, increasing confidence in the results, especially given their individual dependence on photoionisation codes.

Finally, Chapter 7 looks at X-ray narrow emission lines on a population level, comparing outflow velocity distributions of O VII f in type 1 and type 2 AGN. This is a natural extension of the work in Chapters 5 and 6, where I measured the O VII f line in NGC 5548 at a velocity of -300±30 km s^{-1}, and that in NGC 1365 as at rest (-30±70 km s^{-1}). These outflow velocities found for the two differently classified AGN are consistent with the hypothesis that traditional type 1 objects are viewed face on, with higher observed outflow velocities for their intrinsic gas, and type 2 objects are viewed side on, with lower observed outflow velocities for their intrinsic gas. The exploratory study in Chapter 7 significantly increased the number of O VII f emission lines detected in a uniform way across a sample (from 23 by Guainazzi and Bianchi 2007, in obscured AGN, to 89 in both obscured and unobscured AGN in this thesis), although with current uncertainties it is not possible to detect population velocity differences of the order seen in optical studies (around 50 km s^{-1}, see e.g. Zhang et al. 2011; Bae and Woo 2014).

8.1 Future Work

While the high-resolution grating spectrometers on *XMM-Newton* and *Chandra* continue to provide new insights into ionised gas associated with AGN, in both emission and absorption, using long and targeted campaigns, in my opinion the next major breakthroughs are likely to occur once new X-ray observatory satellites become operational.

A hint of this potential was given by *Hitomi* in mid-2016, before the spacecraft was lost. The SXS (Soft X-ray Spectrometer) spectra from the Perseus Cluster resolved the FeKα complex in far greater detail than possible before (Hitomi Collaboration 2016). With an energy resolution of 5 eV over the whole of its operational spectral band, SXS would not have increased the available spectral resolution over current instruments operating below 2 keV, although the effective area was greater than *XMM-Newton*-RGS by nearly a

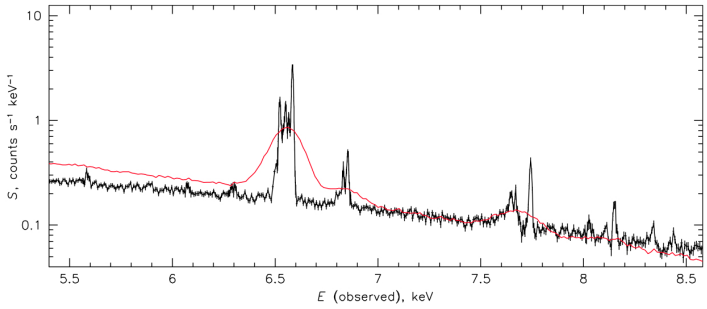

Fig. 8.1: *Hitomi* SXS spectrum (black line) of the full Perseus Cluster field overlaid with a CCD spectrum of the same region. The CCD spectrum is from data taken with the*Suzaku* X-ray imaging spectrometer (XIS) (red line); the difference in the continuum slope is due to differences in the effective areas of the instruments. From the Supplementary Material of Hitomi Collaboration (2016).

factor of two. However, achieving such a resolution over the entire SXS band of 0.3-12 keV (1-40 Å) represents an exceptional opportunity to expand 'high-resolution' X-ray studies to the hard X-ray regime for the first time. Fig. 8.1 shows the increase in spectral resolution from CCD based spectrometers (including *XMM-Newton*-EPIC) to microcalorimeters (such as SXS on *Hitomi*) between 5.5 and 8.5 keV. The successful demonstration of microcalorimeter technology within SXS is one positive outcome from the unintentionally short mission for*Hitomi*.

While the microcalorimeter (X-IFU) planned for ESA's *ATHENA* mission (launch date 2028; see Chapter 3) will not increase spectral resolution in the soft X-ray band compared to *XMM-Newton*-RGS, the expected energy resolution of 2.5 eV (up to 7 keV; Barret et al. 2016) will be an improvement over even the *Hitomi* SXS resolution. The increase in effective area of a factor of 200 from the *XMM-Newton* combined RGS chains (125 cm^2) to the *ATHENA* X-IFU ($\sim$ 2 m^2) will enable much larger samples of excellent quality spectra to be collected; a great advantage for studies such as those in Chapter 7 of this thesis.

If plans for *Astro-H2* and *ATHENA* are realised, then their microcalorimeter instruments should provide unparallelled energy resolution and effective area with which to investigate higher energy narrow emission and absorption features from the same AGN photoionised gas that RGS observes. Observing

higher ionisation states of ions and more elements will allow current photoionisation models to be constrained with more accuracy, and will also drive improvements to these models.

If the proposed NASA mission *Arcus* is implemented, then a reflection grating spectrometer operating over 8-50 Å with ten times the spectral resolution and more than four times the effective area of *XMM-Newton*-RGS could be launched as soon as 2023 (NASA 2016). Even compared to the spectral resolution of the grating spectrometers on *Chandra*, *Arcus* would have three times higher spectral resolution (and 70-100 times larger effective area at ∼20 Å) (Smith et al. 2016). Another grating spectrometer of similar resolution is expected to be part of the payload of the *X-ray Surveyor* mission, which is undergoing a concept study in preparation for the NASA 2020 Decadal Survey (see Chapter 3 for more details on future missions).

This thesis has explored ionised emission regions associated with AGN, how they relate to ionised absorbing gas in similar locations and how they may differ between AGN types. As a natural progression from the work in this thesis, I suggest the following aims for future studies of X-ray narrow emission lines around AGN.

8.1.1 Emission and Absorption Connections

The work in Chapter 5 would not have been possible without detailed warm absorber modelling achieved before the recent obscuration event in NGC 5548. The warm absorbers could be investigated when the observed continuum was sufficiently high (from lack of obscuration) for narrow absorption lines to be studied. On the other hand, the narrow emission lines could only be studied in detail during the obscuration event, when they were fully revealed over such an absorbed continuum.

Therefore further studies of this type, to explore if absorption of narrow emission lines is a common occurrence, and how their location of origin relates to that of the absorbers, should focus on objects with variable absorption and ideally follow the discovery of new obscuration events, like that seen in NGC 5548. The probability of a Type 1 AGN to undergo a similar event is estimated to be $0.006^{+0.160}_{-0.003}$ (Markowitz et al. 2014), translating to a probability of 3%

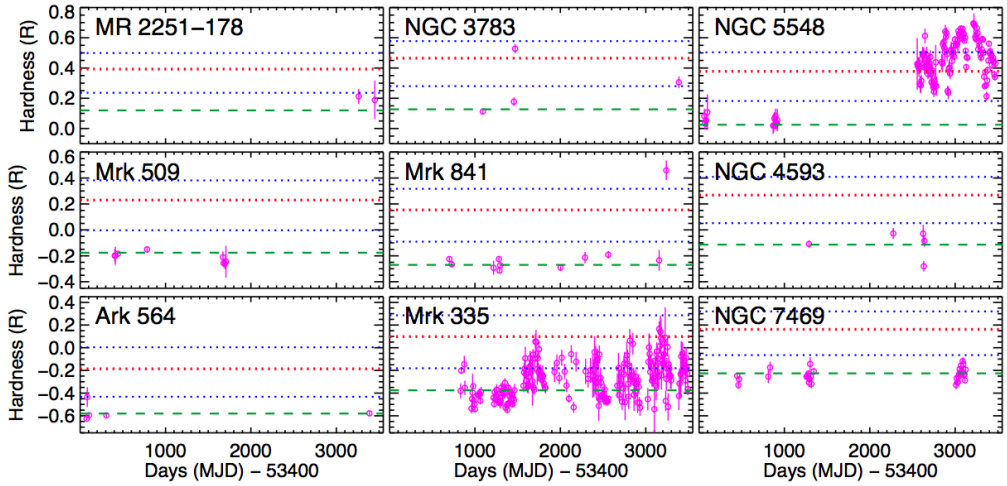

Fig. 8.2: Archival *Swift* observations of nine Type 1 AGN. These are the eight AGN (plus NGC 5548) being monitored by *Swift* (Mehdipour 2016) in order to trigger *XMM-Newton* observations if a new obscuration event takes place (Kaastra 2015). Dashed green line: average unobscured hardness ratio; dotted lines from bottom to top: average hardness ratio with an additional 10^{21}, 3×10^{21} (red), and $5 \times 10^{21}\,\mathrm{cm}^{-2}$ obscuring column density. From Kaastra (2015).

per year, per target, of an event with (almost neutral, $\log \xi = -1.2$) column density $> 3 \times 10^{21}\,\mathrm{cm}^{-2}$ (lower than the column density of the NGC 5548 obscuration, $10^{23}\,\mathrm{cm}^{-2}$; probability calculated for the *XMM-Newton* and *Swift* proposals by Kaastra (2015) and Mehdipour (2016) which have been approved and are currently being implemented).

One way these events can be found is by monitoring AGN using the *Swift* observatory and calculating the spectral hardness ratio. The Hardness Ratio (R) is defined as $R = \frac{(H-S)}{(H+S)}$, where H and S are the count rate fluxes in the hard ($1.5 - 10\,\mathrm{keV}$) and soft ($0.3 - 1.5\,\mathrm{keV}$) bands of *Swift*'s X-ray Telescope (XRT), respectively (see Chapter 5 and Mehdipour et al. 2016, for an example of its use). The hardness ratio increases as absorption in the soft X-ray band increases, giving a good indication of the column density of any obscuration events (see Fig. 8.2).

This strategy is being pursued by the collaboration that discovered the NGC 5548 obscuration event: following the *Swift* detection of an obscuration event, *XMM-Newton* RGS observations are triggered to examine the spectrum

in detail. Eight AGN (in addition to NGC 5548, see Fig. 8.2) have been chosen for monitoring because they have confirmed warm absorbers, are sufficiently bright to get excellent spectra with limited observing time in an obscured state and > 200 ks archival data with *XMM-Newton* or *Chandra* gratings. So far (Nov 2016), *Swift* observations have not met the triggering criteria since this particular monitoring programme began.

With good quality spectra of both the obscured and unobscured states, as for NGC 5548, the ionised gas seen in both emission and absorption can be modelled in detail, and the frequency of absorbed X-ray narrow emission lines can begin to be explored.

8.1.2 Comparing X-ray Narrow Emission Line Regions

As X-ray narrow emission lines in Type 1 objects begin to be studied in detail, they can then be compared to the X-ray narrow emission lines in Type 2 objects. The archetypal Type 2 high-resolution soft X-ray spectrum is that of NGC 1068 (Kinkhabwala et al. 2002), seen in Fig. 1.7, and others have been studied in depth since they were observed (see e.g. Marinucci et al. 2010; Armentrout et al. 2007). Comparing different aspects of Type 1 and Type 2 narrow emission lines would build on tests such as that in Chapter 7 of this thesis. In addition, undertaking the same style of test with different emission lines would begin to build up a picture of narrow line-emitting gas at varying ionisations. The forbidden lines of the N VI or Ne IX He-like triplets could be suitable for this.

Comparisons between the optical NLR for Type 1 and Type 2 objects have found that 'highly ionised' (e.g. [Fe VII] λ6087) emission lines, and those with higher critical densities (e.g. $3.3 \times 10^7\,\mathrm{cm}^{-3}$ for [O III] λ4363, compared to $7.0 \times 10^5\,\mathrm{cm}^{-3}$ for [O III] λ5007) are stronger in Type 1 than Type 2 objects (Murayama and Taniguchi 1998; Nagao et al. 2001). The interpretation of this is that the parts of the line-emission regions located closer to the nucleus have higher ionisations and higher densities (of the order of $10^7\,\mathrm{cm}^{-3}$), and are obscured from view in Type 2 objects (see e.g. Nagao et al. 2001). As X-ray emission lines are from more highly ionised ions (O VII compared to [O III]) and have higher critical densities (a few $\times 10^9$ cm^{-3} for O VII Porquet

et al. 2010 compared to a few $\times 10^{5-7}\,\mathrm{cm}^{-3}$) than optical emission lines, X-ray studies can contribute here.

Future X-ray studies should look to optical results such as this and explore whether similar differences as between Type 1 and Type 2 optical emission lines exist for X-ray emission lines. The *ATHENA* X-IFU will enable high quality spectra to be taken of fainter and more distant AGN than currently possible, therefore sampling different redshift and luminosity parameter space, as well as increasing the quality of spectra taken of current targets over relatively short observing time.

The different ionisation states probed by the two wavelength bands can give complementary results, as already seen in work such as that by Kraemer et al. (2011) and Bianchi et al. (2006). This would be an opportunity to bring the optical and X-ray AGN communities closer together, to exploit the synergy of optical and X-ray narrow emission line investigations, enabling the 'big picture' of AGN narrow emission line regions to be explored over a wide range of ionisation states.

Appendix A

Survey of O VII f Emission Line Velocities: Spectra

"The eye sees only what the mind is prepared to comprehend"

Robertson Davies

This Appendix contains plots of the O VII f line detections found through the work explained in Chapter 7. Each plot shows the data in black and the best fit model in red. Each model includes Galactic absorption of the continuum, which can be seen in some spectra as a narrow absorption feature. The features marked with a square containing a cross are artefacts from bad columns. The only emission lines fitted are the O VII resonance, intercombination and forbidden lines, so in each case the O VII f emission line is the Gaussian line with the longest wavelength.

The objects with multiple observations in the archive, and therefore stacked spectra, are labelled by their object name. Those with only one observation are labelled with their *XMM-Newton* Observation ID number, they are related to the relevant object name in Table A.1.

Table A.1: *XMM-Newton* Observation IDs and their associated objects, for objects which only had one observation in the *XMM-Newton* Science Archive.

Observation ID	Object Name	Observation ID	Object Name
0056340201	NGC 6251	0109130601	ESO 103-G35
0065940501	PKS 0921-213	0110930201	NGC 3079
0090050601	3C 445	0112551701	NGC 5273
0109080601	PG 1444+407	0152940101	NGC 5252
0140950201	NGC 1386	0200430701	UGC 1214
0201130301	CTS A08.12	0200431001	NGC 591
0201930201	MCG+8-11-11	0205390201	2MASX J02070218+2930459
0300910201	5C 3.100	0301650301	NGC 2655
0301450101	H 0439-272	0405340101	3C 234
0305920101	2XMM J010712.0+140844	0601740201	NGC 788
0502090201	ESO 511-G030	0112810101	NGC 3690
0654800501	NGC 613		

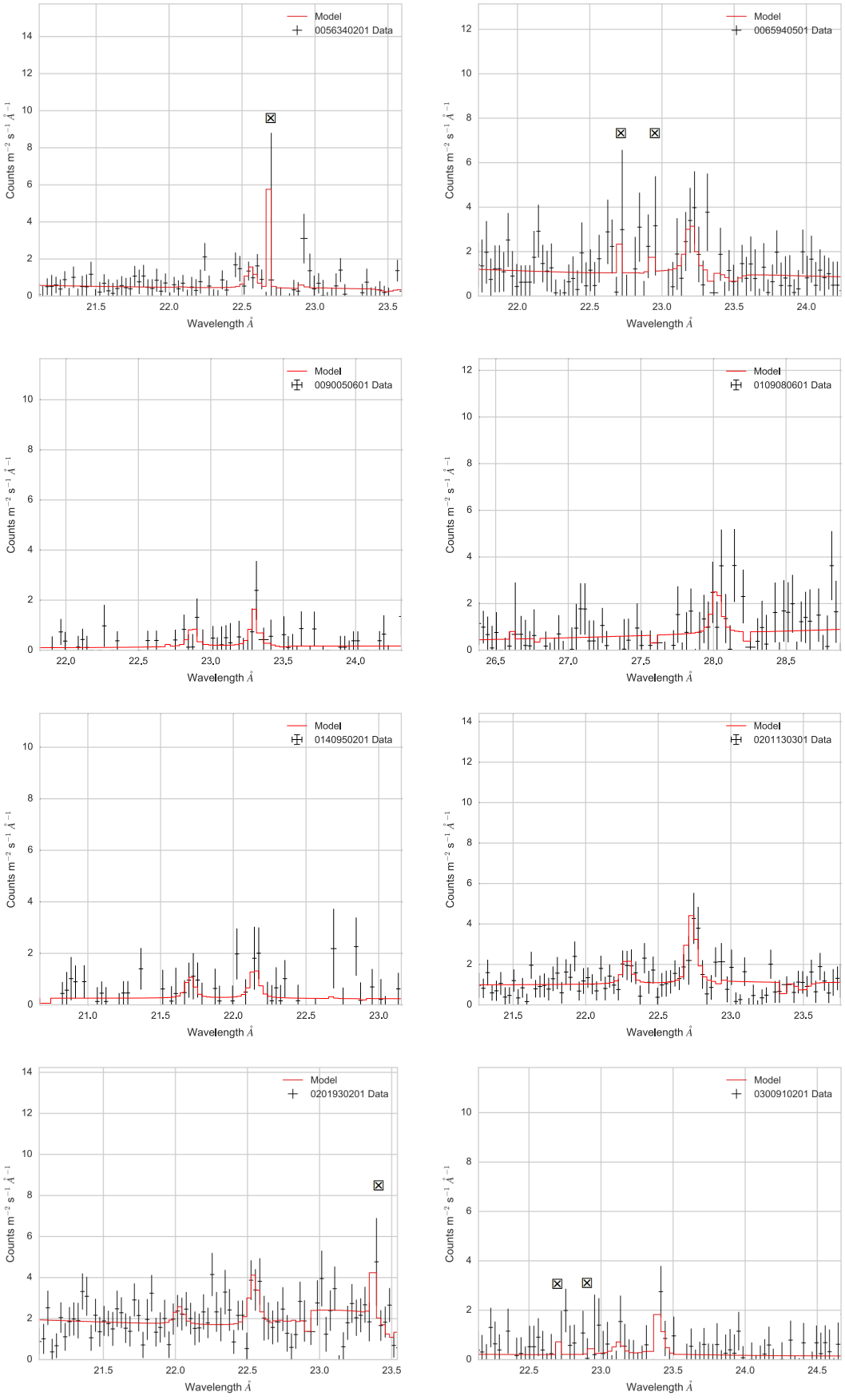

Fig. A.1: O VII f line detections used in the 'Type 1' analysis group.

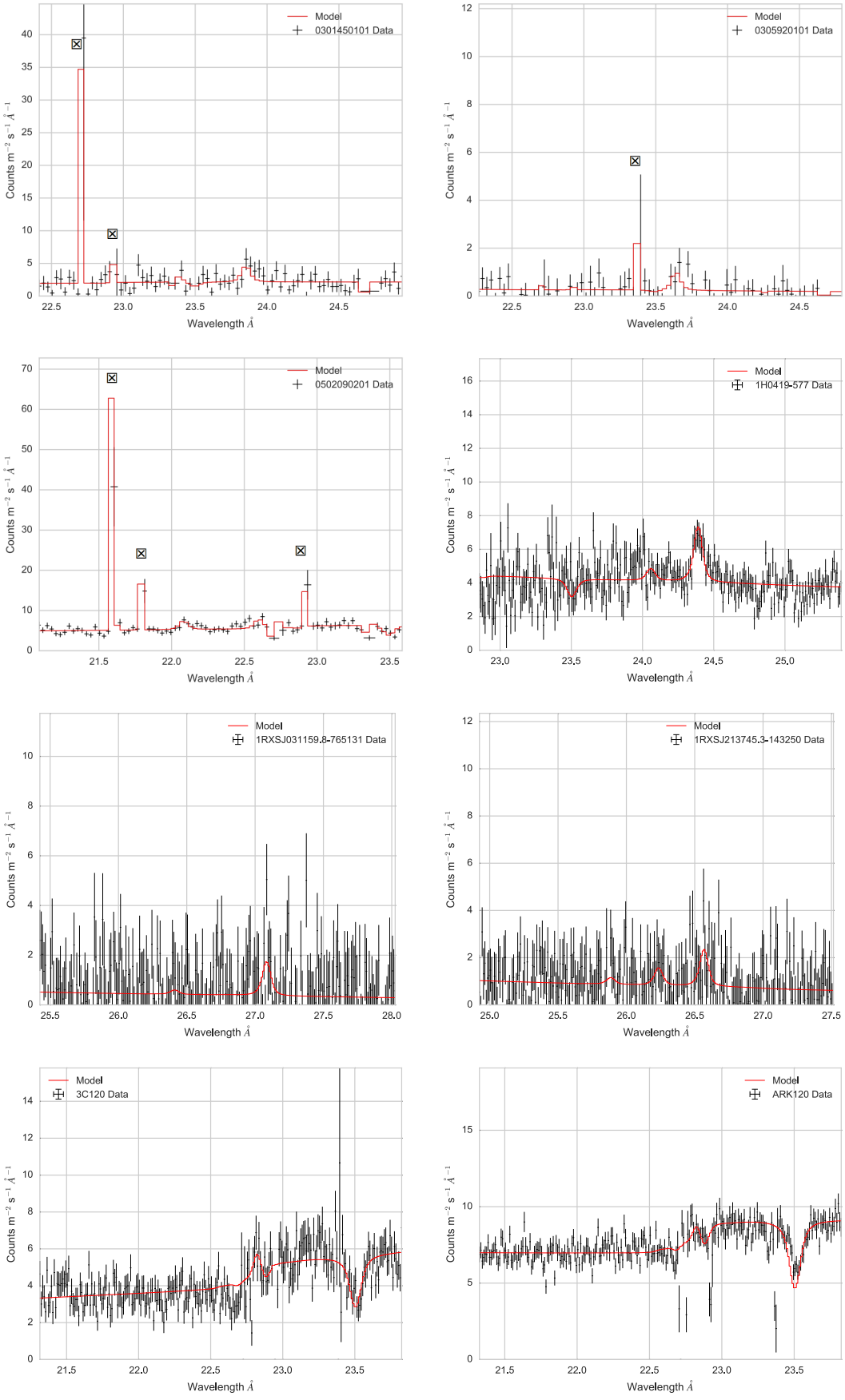

Fig. A.2: O VII f line detections used in the 'Type 1' analysis group.

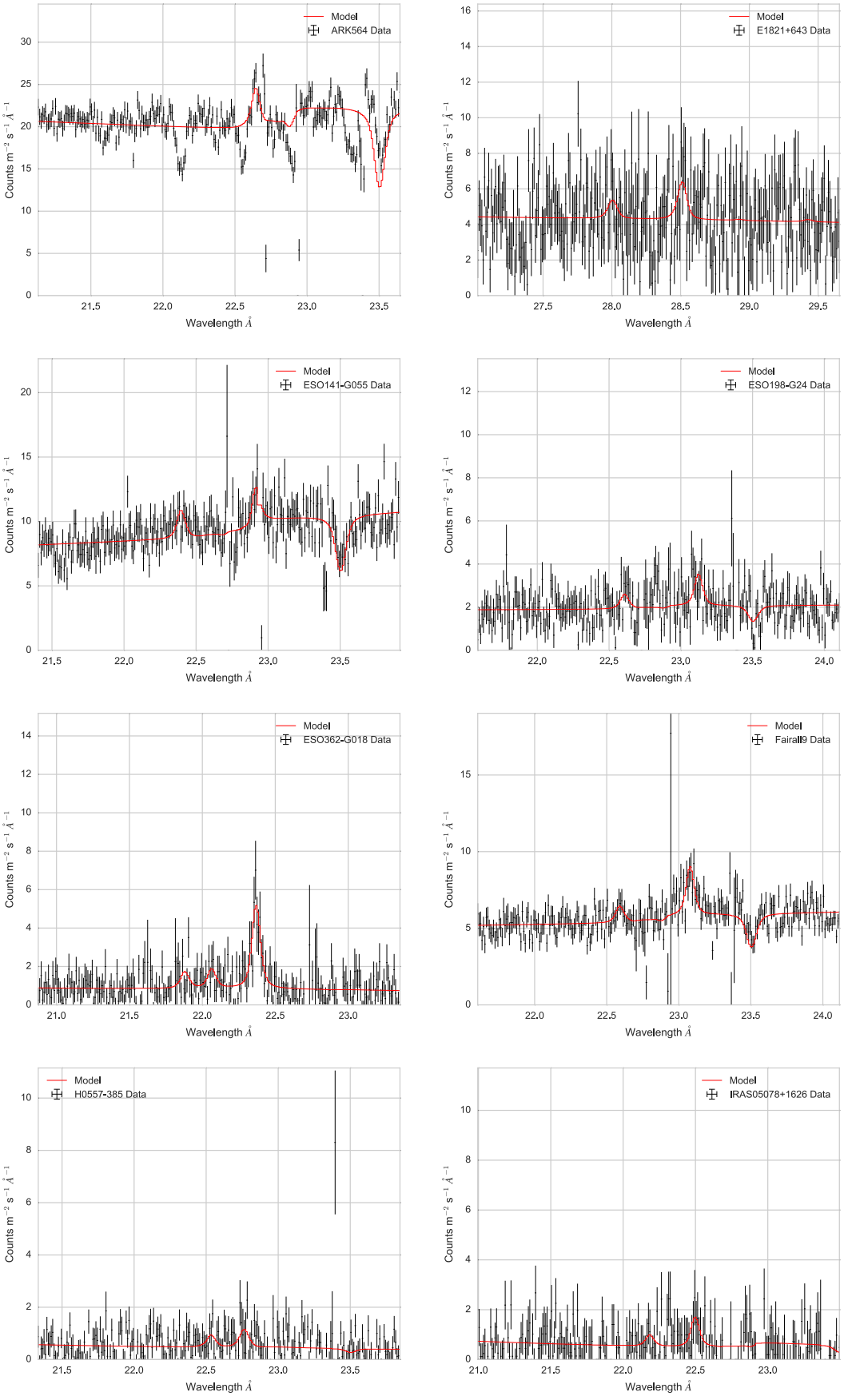

Fig. A.3: O VII f line detections used in the 'Type 1' analysis group.

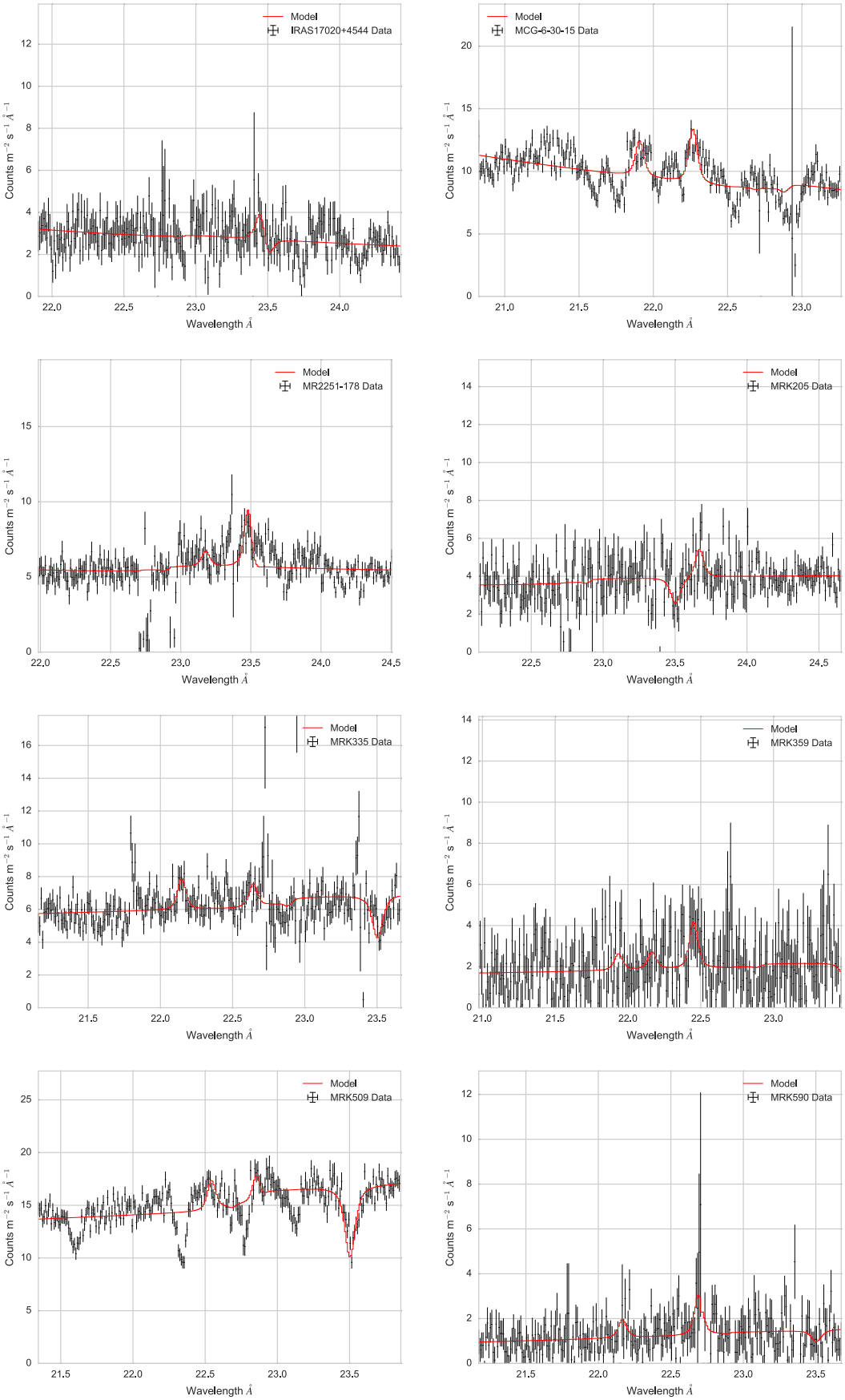

Fig. A.4: O VII f line detections used in the 'Type 1' analysis group.

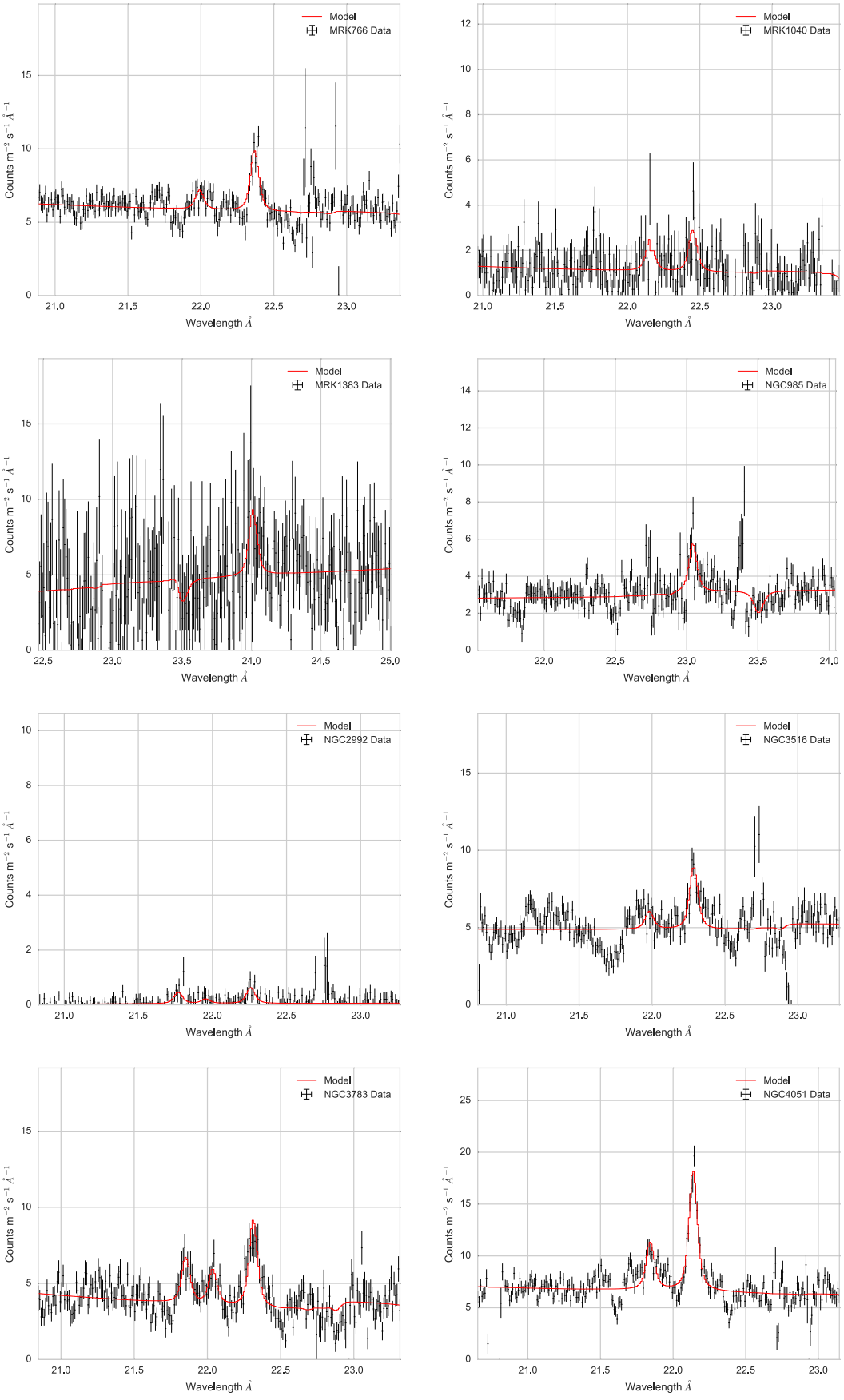

Fig. A.5: O VII f line detections used in the 'Type 1' analysis group.

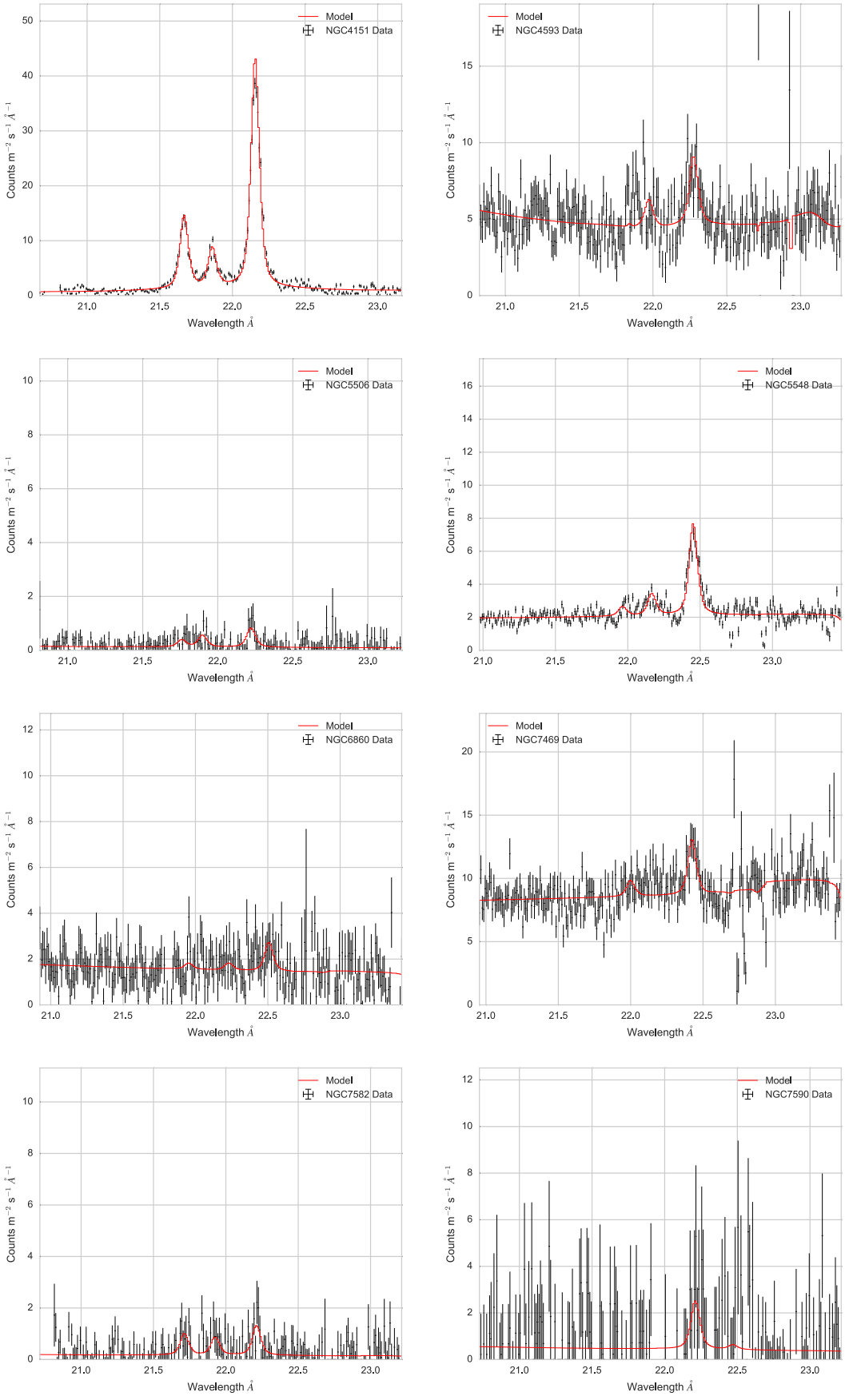

Fig. A.6: O VII f line detections used in the 'Type 1' analysis group.

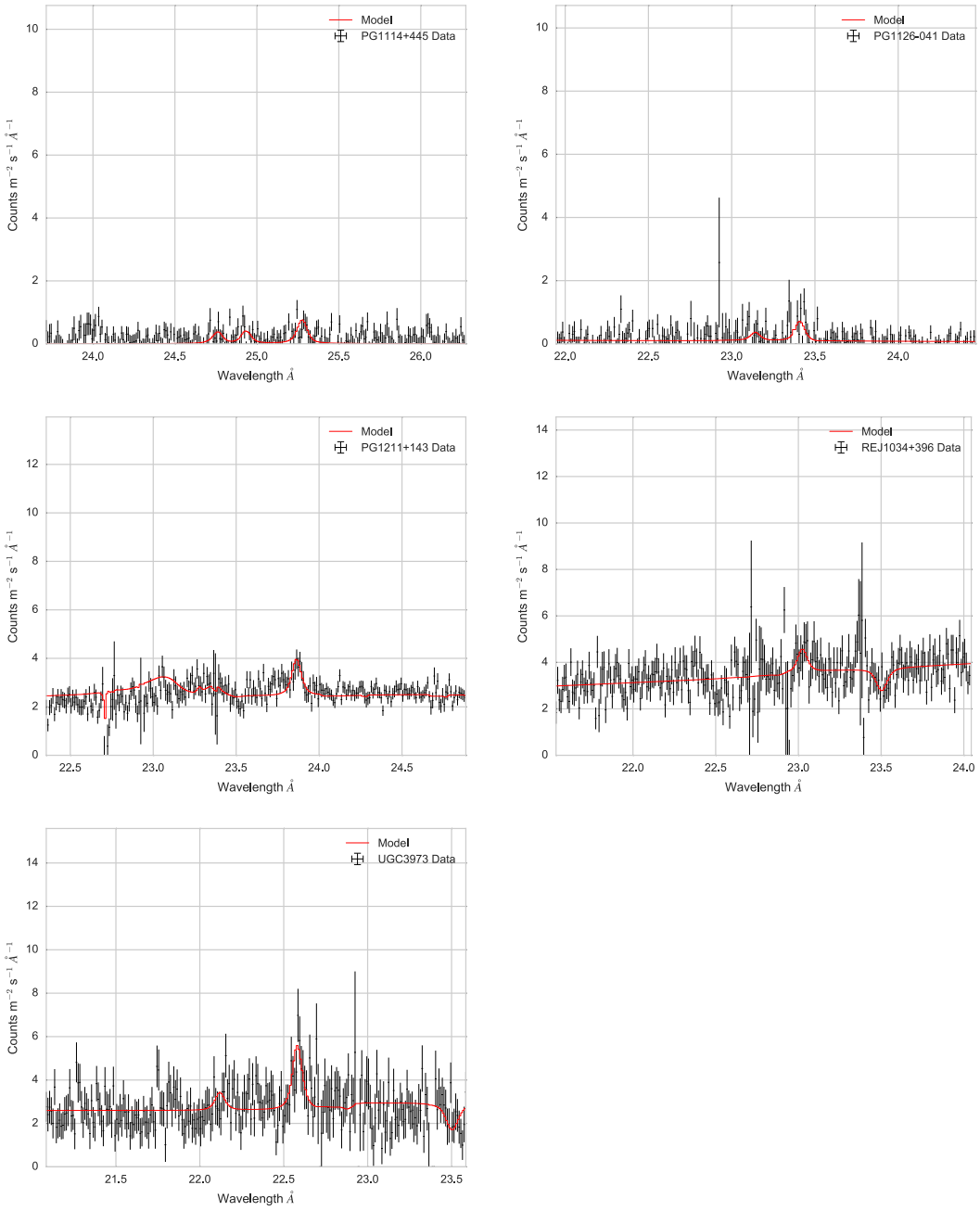

Fig. A.7: O VII f line detections used in the 'Type 1' analysis group.

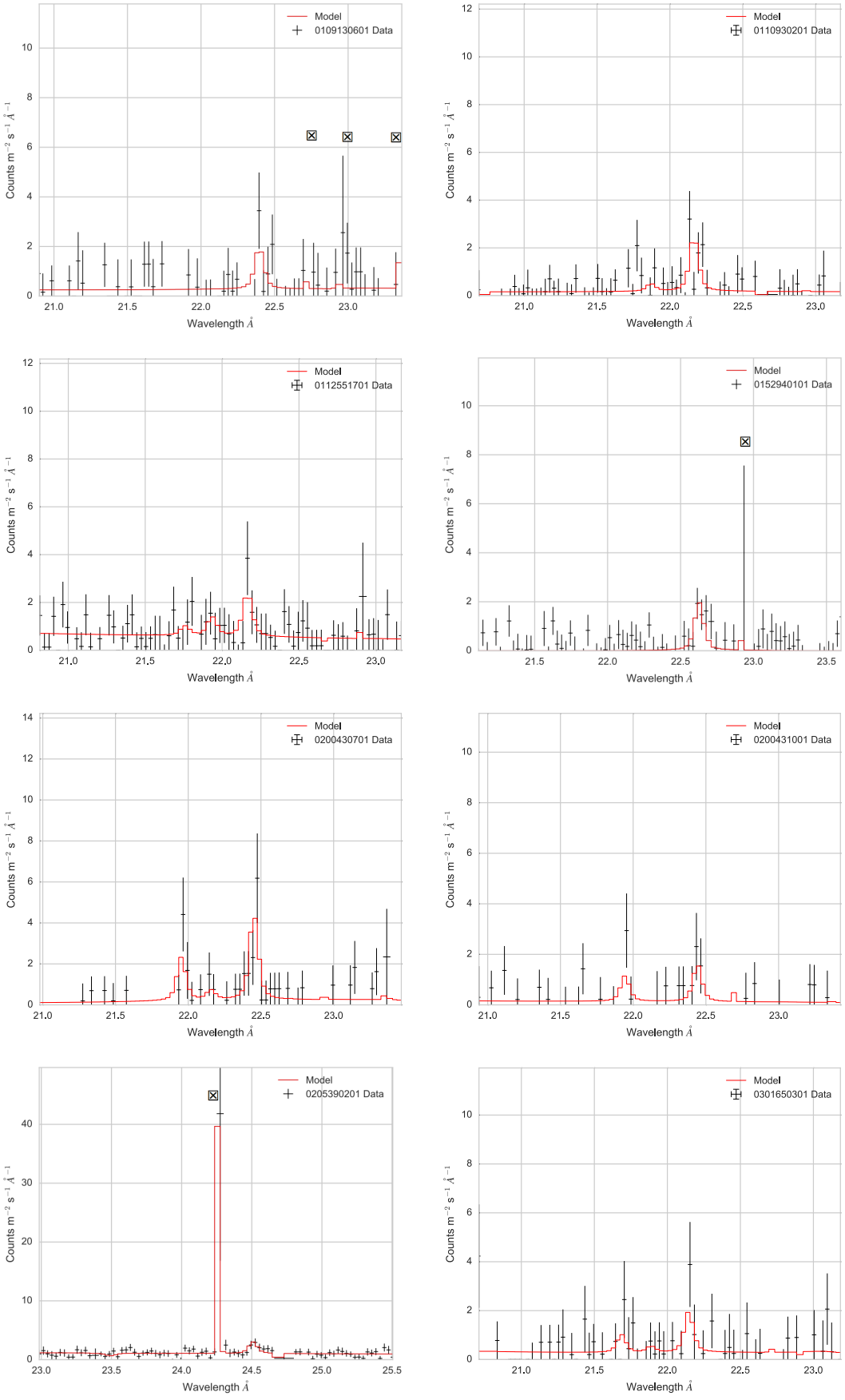

Fig. A.8: O VII f line detections used in the 'Type 2' analysis group.

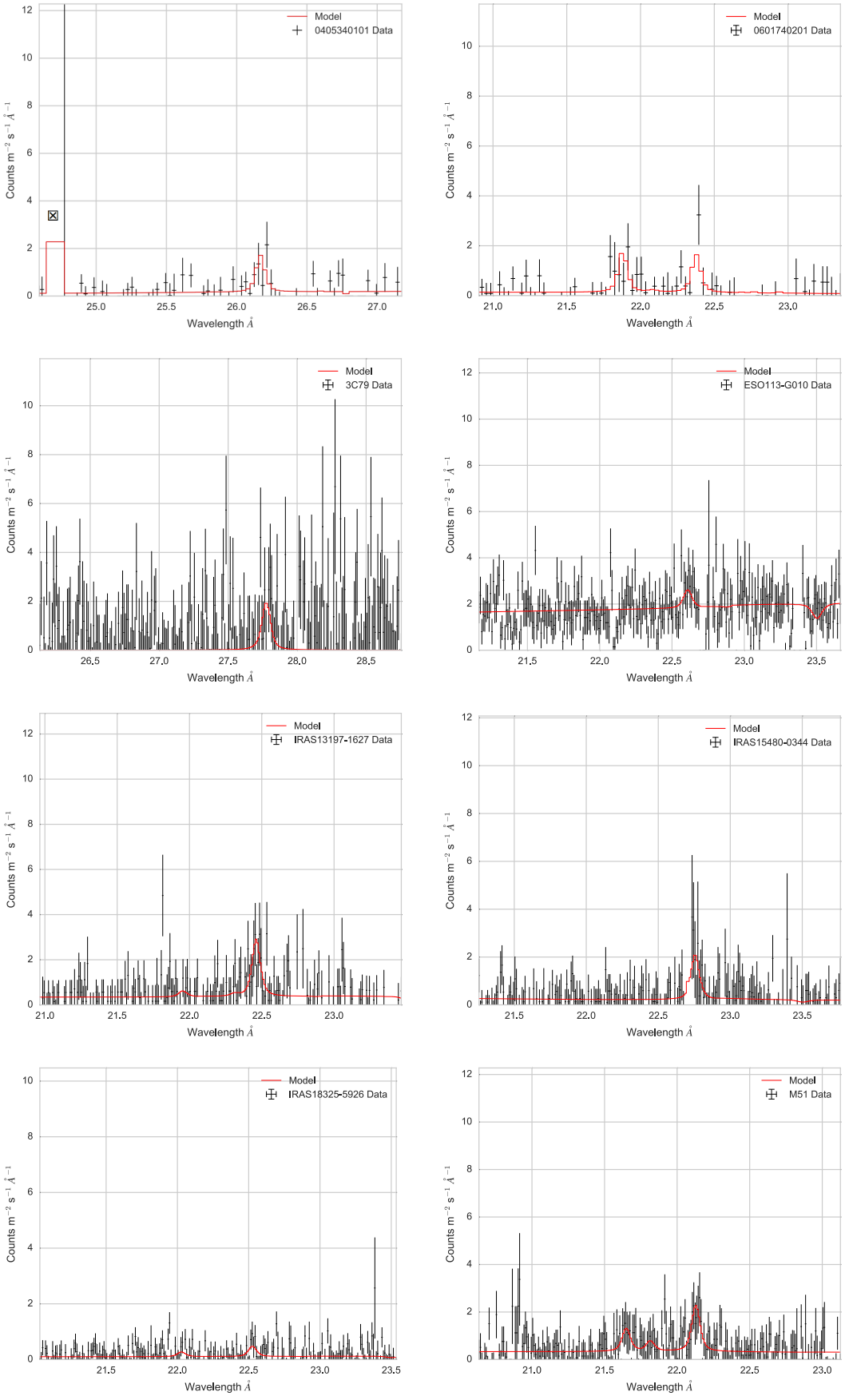

Fig. A.9: O VII f line detections used in the 'Type 2' analysis group.

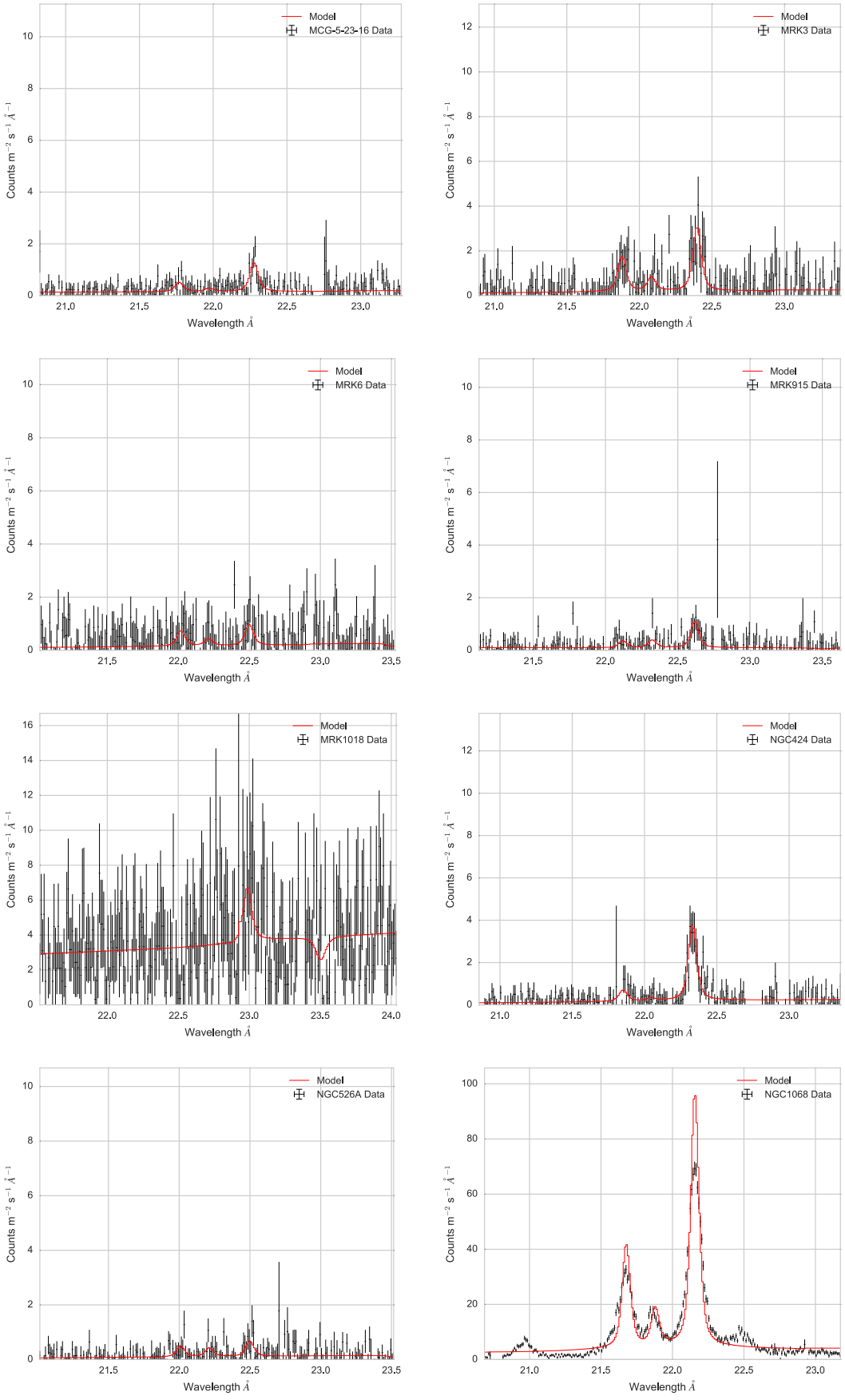

Fig. A.10: O VII f line detections used in the 'Type 2' analysis group.

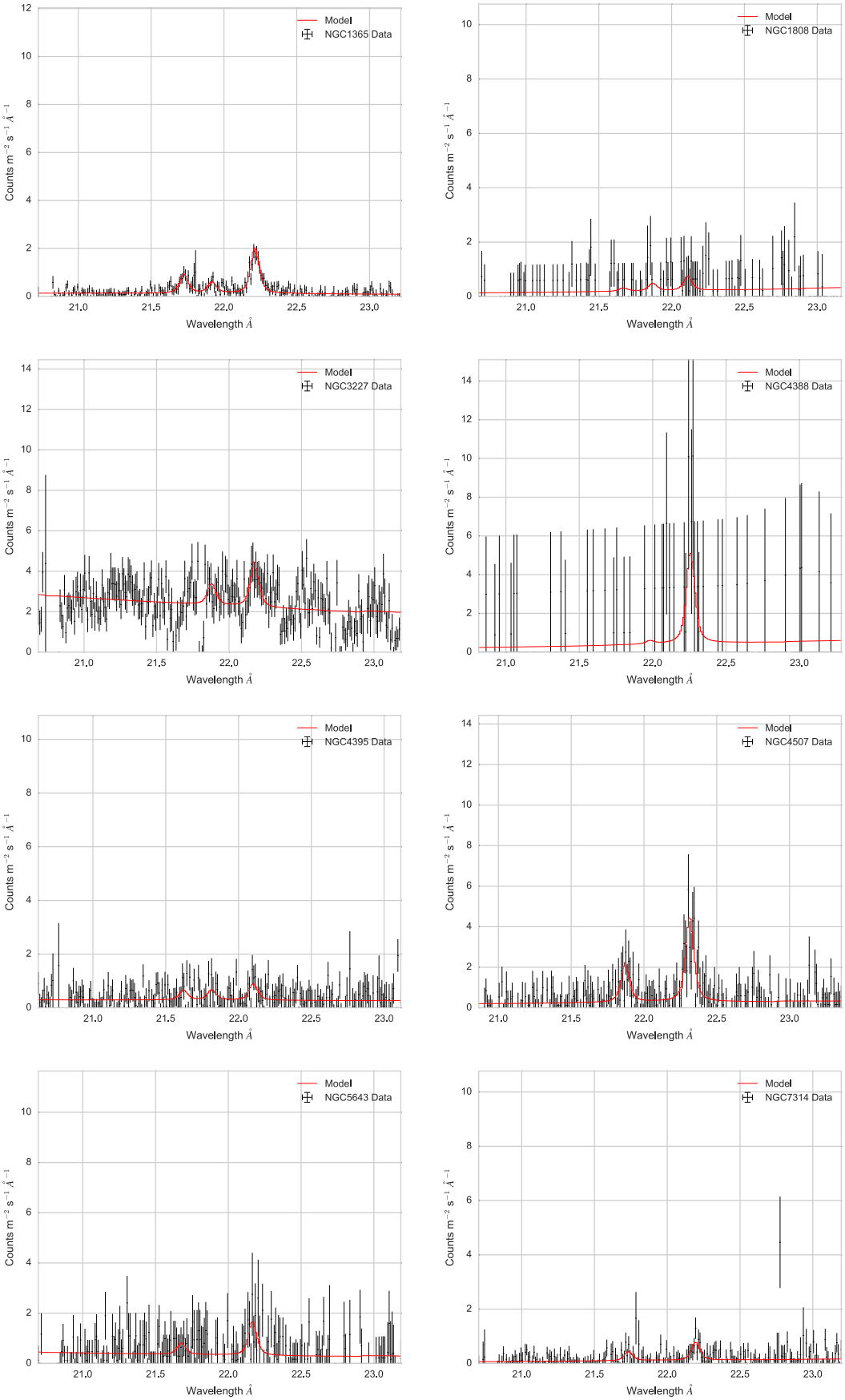

Fig. A.11: O VII f line detections used in the 'Type 2' analysis group.

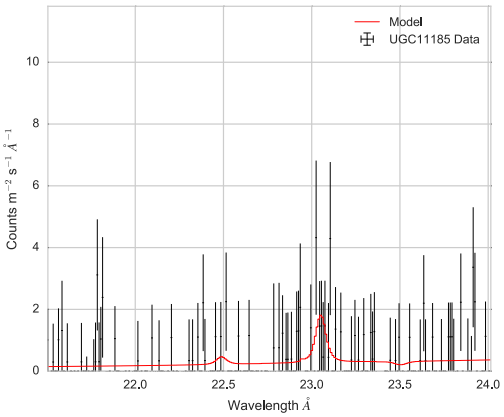

Fig. A.12: O VII f line detections used in the 'Type 2' analysis group.

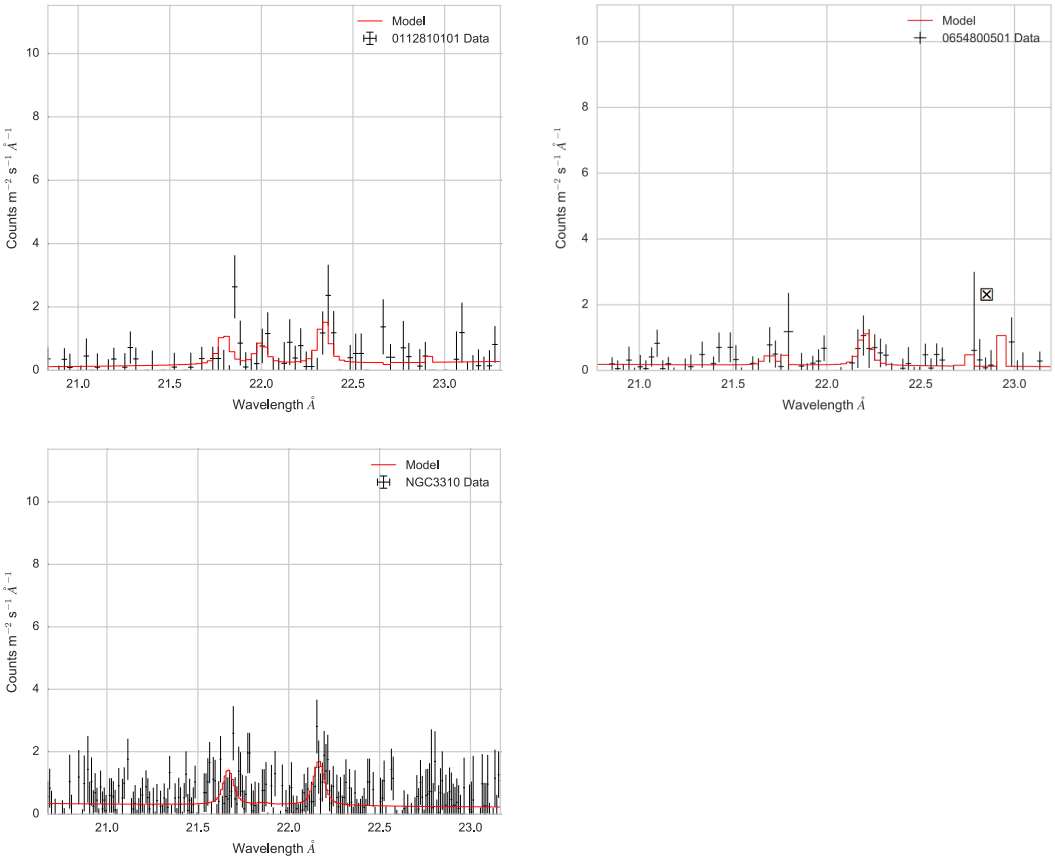

Fig. A.13: O VII f line detections not used in either 'Type 1' or 'Type 2' groups for analysis.

Appendix B

Survey of O VII f Emission Line Velocities: Tables

"Science is much more than a body of knowledge.
It is a way of thinking"
Carl Sagan

Table B.1: Basic information on the objects with O VII f line detections, used in Chapter 7. FSRS stands for Flat-Spectrum Radio Source.

Object Name	Galactic N_H	Classification	Redshift	Redshift Error	Redshift Type	Optical Redshift	Optical Redshift Error
Fairall 9	3.16e+20	Sy 1.2	0.046145	5.7e-05	OPTICAL		
NGC 1068	2.92e+20	Sy 2	0.003793	1e-05	21cm	0.003646	4.7e-05
NGC 1365	1.34e+20	Sy 1.8	0.005458	1.7e-05	21cm	0.005587	3.7e-05
NGC 2992	4.87e+20	unobscured Sy 2	0.007719	2e-05	21cm	0.007785	8e-05
NGC 3516	3.45e+20	Sy 1.5	0.008753	7e-05	OPTICAL		
NGC 4151	2.3e+20	Sy 1.5	0.003319	1e-05	21cm	0.003189	3.7e-05
NGC 4395	1.85e+20	Sy 1.8	0.001064	4e-06	21cm	0.001037	0.000217
NGC 526A	2.31e+20	Sy 1.9	0.019097	0.00013	OPTICAL		
PG 1211+143	2.74e+20	NL Sy 1	0.0809	0.0005	OPTICAL		
1RXS J031159.8-765131	8.57e+20	FSRS	0.223	0.001	OPTICAL		
3C 120	1.06e+21	FSRS	0.033056	6.3e-05	OPTICAL		
ARK 120	9.78e+20	Sy 1	0.03312	9.3e-05	OPTICAL		
E 1821+643	3.44e+20	Sy 1.2	0.297	0.0003	OPTICAL		
ESO 113-G010	2.08e+20	Sy 1.8	0.025701	0.0001	UNKNOWN		
ESO 141-G055	4.83e+20	Sy 1.2	0.037122	0.0002	OPTICAL		
ESO 198-G24	2.93e+20	Sy 1	0.0455	0.0	UNKNOWN		
ESO 362-G018	1.75e+20	Sy 1.5	0.012585	6.7e-05	OPTICAL		
H 0557-385	3.69e+20	Sy 1.2	0.03387	0.0006	UNKNOWN		
IRAS 05078+1626	1.88e+21	Sy 1.5	0.017879	7.7e-05	UNKNOWN		
IRAS 18325-5926	6.47e+20	Sy 1 h	0.020021	0.00015	OPTICAL		

Table B.2: Continued from Table B.1

Object Name	Galactic N_H	Classification	Redshift	Redshift Error	Redshift Type	Optical Redshift	Optical Redshift Error
M 51	1.81e+20	Sy 2	0.001544	0.0002	21cm	0.001544	4e-05
MRK 1383	2.6e+20	Sy 1	0.0862	0.0001	OPTICAL		
MRK 6	6.89e+20	Sy 2	0.019513	3.3e-05	21cm	0.018349	0.000107
MCG-6-30-15	3.92e+20	Sy 1.2	0.007852	0.000133	OPTICAL		
NGC 985	3.17e+20	Sy 1	0.043127	0.0001	OPTICAL		
MRK 205	2.8e+20	Sy 1	0.0708	0.0002	OPTICAL		
MRK 335	3.56e+20	Sy 1	0.025644	0.000103	OPTICAL		
MRK 509	4.25e+20	Sy 1.5	0.034397	4e-05	UNKNOWN		
MRK 590	2.65e+20	Sy 1	0.026385	4e-05	21cm	0.026889	0.0002
MRK 766	1.78e+20	Sy 1	0.012739	8.3e-05	OPTICAL		
MR 2251-178	2.42e+20	Sy 1.5	0.063777	0.00015	OPTICAL		
MRK 1040	6.64e+20	Sy 1	0.016642	5e-06	21cm	0.016391	0.000137
MRK 359	4.26e+20	Sy	0.016958	1.4e-05	21cm	0.016822	0.00012
MRK 915	5.35e+20	Sy	0.024177	3.7e-05	21cm	0.024043	0.0001
NGC 3783	9.91e+20	Sy 1.5	0.00973	7e-06	21cm	0.00976	9.3e-05
NGC 3227	1.99e+20	Sy 2	0.003859	1e-05	21cm	0.003819	6e-05
NGC 4051	1.15e+20	Sy 1	0.002418	1.7e-05	21cm	0.002295	4.3e-05
NGC 4593	1.89e+20	Sy	0.008312	2e-05	21cm	0.008879	0.000127
NGC 5548	1.55e+20	Sy 1.5	0.017175	2.3e-05	21cm	0.016765	8.7e-05
NGC 6860	3.15e+20	Sy 1.5	0.014884	8e-05	OPTICAL		

Table B.3: Continued from Table B.1

Object Name	Galactic N_H	Classification	Redshift	Redshift Error	Redshift Type	Optical Redshift	Optical Redshift Error
NGC 7469	4.45e+20	Sy 1	0.016398	2e-05	21cm	0.016165	3.3e-05
1RXS J213745.3-143250	4.38e+20	Sy 1.5	0.199928	0.00015	OPTICAL		
RE J1034+396	1.31e+20	NL Sy 1	0.0432	0.0001	OPTICAL		
UGC 3973	5.27e+20	Sy 1	0.022212	1.7e-05	21cm	0.021915	0.0001
1H 0419-577	1.26e+20	Sy 1.5	0.104	0.0	UNKNOWN		
ARK 564	5.34e+20	LINER	0.024684	6.7e-05	21cm	0.024994	0.00015
IRAS 17020+4544	2.01e+20	NL Sy 1	0.0604	0.0003	OPTICAL		
MRK 3	9.67e+20	Sy 2	0.013336	2e-05	21cm	0.013443	8e-05
MRK 1018	2.43e+20	Sy 1.9	0.042369	0.000113	OPTICAL		
NGC 1808	2.59e+20	H II	0.003352	3e-05	21cm	0.003382	5.7e-05
NGC 3310	1.35e+20	H II	0.003312	9e-06	21cm	0.003396	4e-05
NGC 424	1.56e+20	Sy 1 h	0.011764	3.1e-05	21cm	0.011508	0.000177
MCG-5-23-16	8.7e+20	Sy 1 i	0.008279	0.00014	OPTICAL		
NGC 5506	4.08e+20	Sy 1 i	0.006084	9e-06	21cm	0.006101	4e-05
NGC 7314	1.5e+20	Sy 1 h	0.004743	2e-05	21cm	0.005957	0.00016
3C 79	8.72e+20	Sy 2	0.2559	0.0	UNKNOWN		
IRAS 13197-1627	4.99e+20	Sy 1 h	0.016541	4e-05	21cm	0.016918	0.00015
IRAS 15480-0344	9.11e+20	Sy 1 h	0.0303	0.0003	UNKNOWN		
NGC 4388	2.58e+20	Sy 1 h	0.008396	1.3e-05	21cm	0.008466	8.7e-05

Table B.4: Continued from Table B.1

Object Name	Galactic N_H	Classification	Redshift	Redshift Error	Redshift Type	Optical Redshift	Optical Redshift Error
NGC 4507	7.04e+20	Sy 1 h	0.011829	3e-05	21cm	0.011671	9.7e-05
NGC 5643	8.01e+20	Sy 2	0.003999	7e-06	21cm	0.003879	7e-05
NGC 7582	1.33e+20	Sy 1 i	0.005254	2.3e-05	21cm	0.005217	7.3e-05
NGC 7590	1.4e+20	unobscured Sy 2	0.005324	2.3e-05	21cm	0.004887	0.000113
PG 1114+445	1.77e+20	Sy 1	0.143862	0.000351	OPTICAL		
PG 1126-041	4.35e+20	Sy 1	0.06196	0.00015	OPTICAL		
UGC 11185	3.14e+20	Sy 2	0.041449	8.7e-05	SIMBAD		
NGC 3079	8.85e+19	Sy 2	0.003753	2e-05	21cm	0.003673	9.7e-05
5C 3.100	8.09e+20	Sy 1	0.071149	0.0	UNKNOWN		
H 0439-272	2.59e+20	Sy 1.5	0.0835	0.0003	UNKNOWN		
MCG+8-11-11	1.84e+21	Sy 1.5	0.020457	5e-06	21cm	0.020644	0.000153
NGC 6251	5.57e+20	unobscured Sy 2	0.023016	0.00014	OPTICAL		
PG 1444+407	1.16e+20	Sy 1	0.26703	0.000365	OPTICAL		
2MASX J02070218+2930459	5.34e+20	Sy 1.8	0.1096	0.00067	UNKNOWN		
UGC 1214	2.52e+20	Sy 2	0.017212	3.5e-05	21cm	0.017032	9.3e-05
NGC 3690	9.01e+19	Interacting	0.009994	4.7e-05	OPTICAL		
CTS A08.12	3.52e+20	Sy 1.2	0.029974	0.00015	UNKNOWN		
3C 234	1.76e+20	Sy 1 h	0.184925	0.001086	OPTICAL		
3C 445	4.49e+20	Sy 1.5	0.055879	0.000183	UNKNOWN		
ESO 103-G35	5.71e+20	Sy 2	0.013286	0.000113	OPTICAL		

Table B.5: Continued from Table B.1

Object Name	Galactic N_H	Classification	Redshift	Redshift Error	Redshift Type	Optical Redshift	Optical Redshift Error
ESO 511-G030	4.69e+20	Sy 1	0.022365	2e-05	21cm	0.022292	0.000197
NGC 1386	1.31e+20	Sy 1 i	0.002882	5e-05	OPTICAL		
NGC 2655	2.18e+20	LINER	0.004683	1.7e-05	21cm	0.004693	0.000133
NGC 5252	2.14e+20	Sy 1.9	0.023093	5e-06	21cm	0.022983	0.00016
NGC 5273	9.16e+19	Sy 1.9	0.003516	0.000123	OPTICAL		
NGC 591	4.14e+20	Sy 1 h	0.015191	3e-05	21cm	0.014994	0.00012
NGC 613	1.65e+20	Sy	0.00492	1.7e-05	21cm	0.005037	5e-05
NGC 788	2.12e+20	Sy 1 h	0.013706	0.000137	OPTICAL		
PKS 0921-213	4.65e+20	FSRS	0.052	0.0	UNKNOWN		
2XMM J010712.0+140844	3.44e+20	NL Sy 1	0.076835	0.000572	OPTICAL		

Table B.6: Intrinsic column density and luminosity information on the objects with O VII f line detections, used in Chapter 7.

Object Name Object Name	Intrinsic Column Density $10^{22}\,\mathrm{cm}^{-2}$	2-10keV Luminosity $\mathrm{erg\,s}^{-1}$	Black Hole Mass $\log \mathrm{M}_{\odot}$	Bolometric Luminosity $\mathrm{erg\,s}^{-1}$	Eddington Ratio
Fairall 9	$2.0^{+0.0}_{-2.0}$	$1.2e{+}44^{+3.7e+41}_{-1.5e+43}$	7.91	$4.4e{+}45^{+1.7e+43}_{-6.9e+44}$	$0.43^{+0.0}_{-0.07}$
NGC 1068	$670.0^{+100.0}_{-100.0}$	$4.4e{+}44^{+4.1e+44}_{-2.2e+44}$	7.23	$2.4e{+}46^{+3.5e+46}_{-1.4e+46}$	$11.1^{+16.3}_{-6.7}$
NGC 1365	$20.0^{+4.0}_{-4.0}$	$4.8e{+}41^{+4.4e+40}_{-4.4e+40}$	8.88	$4.6e{+}42^{+4.8e+41}_{-4.8e+41}$	$4.8e{-}05^{+5.1e-06}_{-5.0e-06}$
NGC 2992	$0.69^{+0.99}_{-0.19}$	$1.3e{+}43^{+8.6e+41}_{-1.9e+41}$	7.72	$2.5e{+}44^{+2.0e+43}_{-4.4e+42}$	$0.04^{+0.00}_{-0.00}$
NGC 3516	$0.353^{+0.32}_{-0.12}$	$6.8e{+}42^{+1.6e+41}_{-6.4e+40}$	7.36	$1.1e{+}44^{+3.1e+42}_{-1.3e+42}$	$0.04^{+0.00}_{-0.00}$
NGC 4151	$5.32^{+0.07}_{-0.08}$	$1.9e{+}42^{+7.9e+39}_{-8.7e+39}$	7.66	$2.3e{+}43^{+1.1e+41}_{-1.3e+41}$	$0.004^{+0.00}_{-0.00}$
NGC 4395	$3.3^{+0.68}_{-0.67}$	$2.1e{+}40^{+7.7e+38}_{-7.7e+38}$	7.69	$1.4e{+}41^{+5.6e+39}_{-5.6e+39}$	$2.3e{-}05^{+9.1e-07}_{-9.1e-07}$
NGC 526A	$1.5^{+0.14}_{-0.14}$	$2.2e{+}43^{+2.4e+41}_{-2.4e+41}$	8.02	$4.7e{+}44^{+6.7e+42}_{-6.6e+42}$	$0.04^{+0.00}_{-0.00}$
PG 1211+143	$2.0^{+0.0}_{-2.0}$	$1.7e{+}44^{+2.8e+41}_{-2.1e+43}$	7.49	$6.9e{+}45^{+1.5e+43}_{-1.1e+45}$	$1.8^{+0.004}_{-0.276}$
1RXS J031159.8-765131					
3C 120			7.84		
ARK 120	$2.0^{+0.0}_{-2.0}$	$2.1e{+}44^{+3.4e+41}_{-2.5e+43}$	8.27	$8.9e{+}45^{+1.9e+43}_{-1.4e+45}$	$0.38^{+0.001}_{-0.059}$
E 1821+643	$2.0^{+0.0}_{-2.0}$				
ESO 113-G010	$2.0^{+0.0}_{-2.0}$	$1.3e{+}43^{+3.2e+40}_{-1.6e+42}$	6.74	$2.4e{+}44^{+7.6e+41}_{-3.6e+43}$	$0.351^{+0.001}_{-0.053}$
ESO 141-G055					
ESO 198-G24	$2.0^{+0.0}_{-2.0}$	$1.1e{+}44^{+2.3e+41}_{-1.3e+43}$	8.36	$3.6e{+}45^{+1.0e+43}_{-5.6e+44}$	$0.1242^{+0.0004}_{-0.0193}$
ESO 362-G018			9.0		
H 0557-385	$0.06^{+0.03}_{-0.02}$	$1.0e{+}43^{+1.0e+41}_{-9.6e+40}$	8.44	$1.9e{+}44^{+2.3e+42}_{-2.1e+42}$	$5.3e{-}03^{+6.7e-05}_{-6.2e-05}$
IRAS 05078+1626			7.55		
IRAS 18325-5926	$1.32^{+0.1}_{-0.1}$				

Table B.7: Continued from Table B.6

Object Name Object Name	Intrinsic Column Density $10^{22}\,\mathrm{cm}^{-2}$	2-10keV Luminosity $\mathrm{erg\,s}^{-1}$	Black Hole Mass $\log \mathrm{M}_{\odot}$	Bolometric Luminosity $\mathrm{erg\,s}^{-1}$	Eddington Ratio
M 51	$50.0\ ^{+50.0}_{0.0}$		6.95		
MRK 1383	$2.0\ ^{+0.0}_{-2.0}$	$4.1e{+}44^{+2.3e+42}_{-5.1e+43}$	8.63	$2.2e{+}46^{+1.7e+44}_{-3.6e+45}$	$0.407\ ^{+0.003}_{-0.066}$
MRK 6	$3.26\ ^{+1.33}_{-1.19}$	$1.8e{+}43^{+1.2e+42}_{-1.1e+42}$	8.24	$3.6e{+}44^{+3.1e+43}_{-2.9e+43}$	$0.016\ ^{+0.001}_{-0.001}$
MCG-6-30-15	$0.19\ ^{+0.03}_{-0.01}$	$9.7e{+}42^{+2.8e+40}_{-1.5e+40}$	6.19	$1.7e{+}44^{+6.1e+41}_{-3.2e+41}$	$0.861\ ^{+0.003}_{-0.002}$
NGC 985	$2.0\ ^{+0.0}_{-2.0}$	$6.9e{+}43^{+4.4e+41}_{-8.6e+42}$	8.05	$2.1e{+}45^{+1.7e+43}_{-3.3e+44}$	$0.147\ ^{+0.001}_{-0.023}$
MRK 205	$2.0\ ^{+0.0}_{-2.0}$	$2.8e{+}44^{+3.9e+41}_{-3.3e+43}$	8.68	$1.3e{+}46^{+2.4e+43}_{-2.0e+45}$	$0.2130\ ^{+0.0004}_{-0.0335}$
MRK 335	$2.0\ ^{+0.0}_{-2.0}$	$4.2e{+}43\ ^{+5.8e+40}_{-5.1e+42}$	6.69	$1.1e{+}45^{+1.9e+42}_{-1.7e+44}$	$1.784\ ^{+0.003}_{-0.271}$
MRK 509	$0.015\ ^{+0.008}_{-0.008}$	$2.0e{+}44^{+3.5e+41}_{-3.5e+41}$	7.86	$8.2e{+}45^{+2.0e+43}_{-1.9e+43}$	$0.899\ ^{+0.002}_{-0.002}$
MRK 590	$2.0\ ^{+0.0}_{-2.0}$	$2.0e{+}43^{+8.7e+40}_{-2.5e+42}$	7.2	$4.3e{+}44^{+2.3e+42}_{-6.5e+43}$	$0.214\ ^{+0.001}_{-0.033}$
MRK 766			6.28		
MR 2251-178					
MRK 1040	$0.36\ ^{+0.08}_{-0.08}$		7.64		
MRK 359	$2.0\ ^{+0.0}_{-2.0}$	$9{,}0e{+}42^{+7.6e+40}_{-1.1e+42}$	6.24	$1.5e{+}44^{+1.6e+42}_{-2.4e+43}$	$0.697\ ^{+0.007}_{-0.108}$
MRK 915					
NGC 3783	$0.57\ ^{+0.21}_{-0.14}$	$1.2e{+}43^{+1.9e+41}_{-1.3e+41}$	6.94	$2.3e{+}44^{+4.3e+42}_{-3.0e+42}$	$0.205\ ^{+0.004}_{-0.003}$
NGC 3227	$1.74\ ^{+0.12}_{-0.09}$	$1.0e{+}42^{+8.7e+39}_{-6.9e+39}$	8.07	$1.1e{+}43^{+1.1e+41}_{-8.8e+40}$	$7.5e{-}04^{+7.5e-06}_{-5.9e-06}$
NGC 4051	$2.0\ ^{+0.0}_{-2.0}$	$1.9e{+}41^{+5.7e+38}_{-2.4e+40}$	6.13	$1.6e{+}42^{+5.4e+39}_{-2.2e+41}$	$9.6e{-}03^{+3.2e-05}_{-1.3e-03}$
NGC 4593	$0.031\ ^{+0.011}_{-0.012}$	$8.1e{+}42^{+7.4e+40}_{-7.4e+40}$	6.91	$1.4e{+}44\ ^{+1.5e+42}_{-1.5e+42}$	$0.132\ ^{+0.001}_{-0.001}$
NGC 5548	$0.07\ ^{+0.04}_{-0.05}$	$4.3e{+}43^{+2.1e+41}_{-2.4e+41}$	8.03	$1.1e{+}45^{+7.0e+42}_{-8.0e+42}$	$0.0834\ ^{+0.0005}_{-0.0006}$
NGC 6860	$4.53\ ^{+1.33}_{-1.3}$		8.24		

Table B.8: Continued from Table B.6

Object Name Object Name	Intrinsic Column Density $10^{22}\,\mathrm{cm}^{-2}$	2-10keV Luminosity $\mathrm{erg\,s}^{-1}$	Black Hole Mass $\log \mathrm{M}_{\odot}$	Bolometric Luminosity $\mathrm{erg\,s}^{-1}$	Eddington Ratio
NGC 7469	$2.0\ ^{+0.0}_{-2.0}$	$3.2\mathrm{e}{+43}^{+8.7\mathrm{e}+40}_{-3.8\mathrm{e}+42}$	8.64	$7.6\mathrm{e}{+44}^{+2.7\mathrm{e}+42}_{-1.2\mathrm{e}+44}$	$0.0138\ ^{+4.8\mathrm{e}-05}_{-0.002}$
1RXS J213745.3-143250					
RE J1034+396	$2.0\ ^{+0.0}_{-2.0}$	$3.6\mathrm{e}{+43}^{+6.0\mathrm{e}+40}_{-4.4\mathrm{e}+42}$	6.81	$9.0\mathrm{e}{+44}^{+1.9\mathrm{e}+42}_{-1.4\mathrm{e}+44}$	$1.101\ ^{+0.002}_{-0.168}$
UGC 3973	$0.0063\ ^{+0.0}_{-0.0063}$	$1.9\mathrm{e}{+43}^{+5.7\mathrm{e}+40}_{-6.5\mathrm{e}+40}$	8.01	$4.0\mathrm{e}{+44}^{+1.5\mathrm{e}+42}_{-1.7\mathrm{e}+42}$	$0.0312\ ^{+0.0001}_{-0.0001}$
1H 0419-577	$2.0\ ^{+0.0}_{-2.0}$	$5.1\mathrm{e}{+44}^{+1.4\mathrm{e}+42}_{-6.2\mathrm{e}+43}$	8.58	$2.9\mathrm{e}{+46}^{+1.1\mathrm{e}+44}_{-4.7\mathrm{e}+45}$	$0.615\ ^{+0.002}_{-0.099}$
ARK 564	$2.0\ ^{+0.0}_{-2.0}$	$9.9\mathrm{e}{+43}^{+1.1\mathrm{e}+41}_{-1.2\mathrm{e}+43}$	6.27	$3.3\mathrm{e}{+45}^{+4.7\mathrm{e}+42}_{-5.1\mathrm{e}+44}$	$14.09\ ^{+0.020}_{-2.17}$
IRAS 17020+4544	$0.028\ ^{+0.0}_{-0.028}$	$1.4\mathrm{e}{+44}\ ^{+6.6\mathrm{e}+41}_{-9.3\mathrm{e}+41}$	6.77	$5.1\mathrm{e}{+45}^{+3.2\mathrm{e}+43}_{-4.6\mathrm{e}+43}$	$6.88\ ^{+0.04}_{-0.06}$
MRK 3	$110.0\ ^{+15.0}_{-25.0}$	$1.8\mathrm{e}{+43}^{+3.5\mathrm{e}+42}_{-4.8\mathrm{e}+42}$	8.65	$3.7\mathrm{e}{+44}^{+9.3\mathrm{e}+43}_{-1.2\mathrm{e}+44}$	$0.007\ ^{+0.002}_{-0.002}$
MRK 1018	$0.01\ ^{+0.0}_{-0.01}$	$9.4\mathrm{e}{+43}^{+5.8\mathrm{e}+41}_{-6.4\mathrm{e}+41}$	8.09	$3.1\mathrm{e}{+45}^{+2.5\mathrm{e}+43}_{-2.8\mathrm{e}+43}$	$0.199\ ^{+0.002}_{-0.002}$
NGC 1808	$3.2\ ^{+5.88}_{-3.18}$				
NGC 3310					
NGC 424			7.78		
MCG-5-23-16	$1.62\ ^{+0.23}_{-0.21}$	$1.5\mathrm{e}{+43}^{+2.2\mathrm{e}+41}_{-2.0\mathrm{e}+41}$	7.85	$3.0\mathrm{e}{+44}^{+5.4\mathrm{e}+42}_{-5.0\mathrm{e}+42}$	$0.0335\ ^{+0.0006}_{-0.0006}$
NGC 5506	$3.4\ ^{+0.26}_{-0.12}$	$7.9\mathrm{e}{+42}^{+1.1\mathrm{e}+41}_{-5.9\mathrm{e}+40}$	6.3	$1.3\mathrm{e}{+44}^{+2.3\mathrm{e}+42}_{-1.2\mathrm{e}+42}$	$0.522\ ^{+0.009}_{-0.005}$
NGC 7314	$1.16\ ^{+0.04}_{-0.13}$	$1.4\mathrm{e}{+42}^{+6.8\mathrm{e}+39}_{-1.5\mathrm{e}+40}$	6.7	$1.6\mathrm{e}{+43}^{+9.2\mathrm{e}+40}_{-2.0\mathrm{e}+41}$	$0.0250^{+0.0001}_{-0.0003}$
3C 79					
IRAS 13197-1627	$76.0\ ^{+13.0}_{-12.2}$	$1.1\mathrm{e}{+43}^{+2.1\mathrm{e}+42}_{-1.8\mathrm{e}+42}$	8.28	$2.1\mathrm{e}{+44}^{+4.9\mathrm{e}+43}_{-3.9\mathrm{e}+43}$	$0.009\ ^{+0.002}_{-0.002}$
IRAS 15480-0344	$160.0\ ^{+0.0}_{-0.0}$	$1.4\mathrm{e}{+43}^{+0.0}_{-1.4\mathrm{e}+42}$		$2.7\mathrm{e}{+44}^{+0.0}_{-3.3\mathrm{e}+43}$	
NGC 4388	$42.0\ ^{+6.0}_{-10.0}$	$1.1\mathrm{e}{+43}^{+1.1\mathrm{e}+42}_{-1.7\mathrm{e}+42}$	8.53	$1.9\mathrm{e}{+44}\ ^{+2.6\mathrm{e}+43}_{-3.8\mathrm{e}+43}$	$0.0045\ ^{0.0006}_{-0.0009}$
NGC 4507	$29.2\ ^{+2.3}_{-2.3}$	$9.9\mathrm{e}{+42}^{+4.7\mathrm{e}+41}_{-4.6\mathrm{e}+41}$	8.39	$1.7\mathrm{e}{+44}^{+1.0\mathrm{e}+43}_{-1.0\mathrm{e}+43}$	$0.0056\ ^{0.0003}_{-0.0003}$

Table B.9: Continued from Table B.6

Object Name Object Name	Intrinsic Column Density 10^{22} cm^{-2}	2-10keV Luminosity erg s^{-1}	Black Hole Mass log M$_\odot$	Bolometric Luminosity erg s^{-1}	Eddington Ratio
NGC 5643	$0.23\ ^{+0.0}_{-0.23}$	$3.4e{+}40^{+1.3e+39}_{-1.8e+39}$	6.45	$2.4e{+}41^{+9.7e+39}_{-1.4e+40}$	$6.9e{-}04^{+2.7e-05}_{-3.8e-05}$
NGC 7582	$12.4\ ^{+0.6}_{-0.8}$	$3.2e{+}41^{+7.3e+39}_{-9.1e+39}$	5.99	$2.9e{+}42\ ^{+7.5e+40}_{-9.2e+40}$	$0.0234\ ^{+0.0006}_{-0.0008}$
NGC 7590	$0.092\ ^{+0.0}_{-0.092}$	$8.9e{+}39^{+8.2e+38}_{-8.7e+38}$	6.71	$6.0e{+}40^{+5.6e+39}_{-6.0e+39}$	$9.3e{-}05^{+8.7e-06}_{-9.2e-06}$
PG 1114+445	$0.0\ ^{+0.0}_{0.0}$	$1.7e{+}44^{+1.3e+42}_{-1.3e+42}$	8.41	$6.6e{+}45^{+7.0e+43}_{-7.0e+43}$	$0.205\ ^{+0.002}_{-0.002}$
PG 1126-041					
UGC 11185					
NGC 3079	$1.6\ ^{+2.7}_{-1.3}$	$1.2e{+}40^{+2.4e+39}_{-1.4e+39}$	6.0	$8.1e{+}40^{+1.7e+40}_{-9.7e+39}$	$6.5e{-}04^{+1.3e-04}_{-0.7e-04}$
5C 3.100	$2.0\ ^{+0.0}_{-2.0}$				
H 0439-272	$2.0\ ^{+0.0}_{-2.0}$	$2.3e{+}44^{+1.8e+42}_{-2.9e+43}$		$1.0e{+}46^{+1.1e+44}_{-1.67e+45}$	
MCG+8-11-11	$0.25\ ^{+0.016}_{-0.015}$	$6.2e{+}43^{+4.2e+41}_{-4.1e+41}$	7.18	$1.9e{+}45^{+1.6e+43}_{-1.6e+43}$	$0.941\ ^{+0.008}_{-0.008}$
NGC 6251	$0.124\ ^{+0.036}_{-0.034}$	$7.5e{+}42^{+8.0e+40}_{-7.9e+40}$	8.77	$1.2e{+}44^{+1.6e+42}_{-1.6e+42}$	$0.00166^{+0.2e-04}_{-0.2e-04}$
PG 1444+407	$0.0022\ ^{+0.0}_{-0.0022}$	$3.7e{+}44^{+3.9e+42}_{-3.9e+42}$	8.54	$1.9e{+}46^{+2.7e+44}_{-2.7e+44}$	$0.444\ ^{+0.006}_{-0.006}$
2MASX J02070218+2930459					
UGC 1214	$160.0\ ^{+0.0}_{0.0}$	$6.0e{+}42^{+1.7e+41}_{-1.7e+41}$	7.28	$9.3e{+}43^{+3.3e+42}_{-3.3e+42}$	$0.039\ ^{+0.001}_{-0.001}$
NGC 3690					
CTS A08.12	$2.0\ ^{+0.0}_{-2.0}$	$2.7e{+}43^{+1.8e+41}_{-3.4e+42}$	7.69	$6.2e{+}44^{+5.2e+42}_{-9.7e+43}$	$0.1009\ ^{+0.0008}_{-0.0158}$
3C 234					
3C 445					
ESO 103-G35	$15.91\ ^{+104.1}_{-12.62}$	$1.9e{+}43^{+6.7e+43}_{-6.6e+42}$	7.73	$3.9e{+}44^{+2.3e+45}_{-1.6e+44}$	$0.057\ ^{+0.347}_{-0.024}$
ESO 511-G030	$0.098\ ^{+0.021}_{-0.021}$		8.66		

Table B.10: Continued from Table B.6

Object Name Object Name	Intrinsic Column Density $10^{22}\,\mathrm{cm}^{-2}$	2-10keV Luminosity $\mathrm{erg\,s}^{-1}$	Black Hole Mass $\log \mathrm{M}_{\odot}$	Bolometric Luminosity $\mathrm{erg\,s}^{-1}$	Eddington Ratio
NGC 1386	$500.0\ ^{+100.0}_{-100.0}$	$2.5e{+}42^{+2.7e+42}_{-1.4e+42}$	7.24	$3.2e{+}43^{+4.6e+43}_{-1.9e+43}$	$0.015\ ^{+0.021}_{-0.009}$
NGC 2655	$26.1\ ^{+2.7}_{-1.7}$		7.7		
NGC 5252	$4.33\ ^{+0.66}_{-0.61}$	$1.7e{+}43^{+5.8e+41}_{-5.5e+41}$	9.53	$3.3e{+}44\ ^{+1.5e+43}_{-1.4e+43}$	$7.8e{-}04^{+3.5e-05}_{-3.2e-05}$
NGC 5273			6.51		
NGC 591					
NGC 613					
NGC 788	$46.89\ ^{+4.68}_{-4.47}$		7.51		
PKS 0921-213			8.14		
2XMM J010712.0+140844					

Table B.11: Measured O VII f line velocities used in Chapter 7, for standard reference redshifts (column 2) and for optically derived redshifts (column 3). There is also 0.008 $\mathring{A}$ uncertainty on these values due to RGS absolute wavelength uncertainty

Object Name	O VII f line velocity (km s^{-1})	O VII f line velocity with optical redshift reference (km s^{-1})
Fairall 9	-421^{+32}_{-95}	
NGC 1068	-334^{+140}_{-42}	-290^{+140}_{-42}
NGC 1365	7^{+31}_{-92}	-32^{+31}_{-92}
NGC 2992	-126^{+121}_{-14}	-145^{+121}_{-14}
NGC 3516	-15^{+69}_{-58}	
NGC 4151	-184^{+109}_{-7}	-145^{+109}_{-7}
NGC 4395	-146^{+126}_{-250}	-138^{+126}_{-250}
NGC 526A	-276^{+119}_{-115}	
PG 1211+143	-168^{+2}_{-111}	
1RXS J031159.8-765131	$728\ ^{+223}_{-246}$	
3C 120	-2^{+147}_{-217}	
ARK 120	-6^{+12}_{-731}	
E 1821+643	-1483^{+257}_{-422}	
ESO 113-G010	-753^{+492}_{-445}	
ESO 141-G055	-5^{+62}_{-304}	
ESO 198-G24	401^{+456}_{-739}	
ESO 362-G018	-5^{+34}_{-214}	
H 0557-385	-1059^{+1003}_{-871}	
IRAS 05078+1626	76^{+699}_{-707}	
IRAS 18325-5926	-107^{+203}_{-255}	

Table B.12: Continued from Table B.11

Object Name	O VII f line velocity (km s^{-1})	O VII f line velocity with optical redshift reference (km s^{-1})
M 51	-10^{+95}_{-158}	-10^{+95}_{-158}
MRK 1383	117^{+710}_{-185}	
MRK 6	-291^{+121}_{-230}	58^{+120}_{-230}
MCG-6-30-15	-2^{+199}_{-52}	
NGC 985	-4^{+10}_{-231}	
MRK 205	106^{+116}_{-118}	
MRK 335	-182^{+125}_{-587}	
MRK 509	85^{+150}_{-85}	
MRK 590	229^{+461}_{-476}	78^{+461}_{-476}
MRK 766	-32^{+16}_{-109}	
MR 2251-178	-253^{+225}_{-74}	
MRK 1040	-75^{+90}_{-237}	0^{+90}_{-237}
MRK 359	-245^{+238}_{-230}	-204^{+238}_{-230}
MRK 915	-79^{+118}_{-116}	-39^{+118}_{-116}
NGC 3783	126^{+27}_{-252}	117^{+27}_{-252}
NGC 3227	8^{+135}_{-114}	20^{+135}_{-114}
NGC 4051	-142^{+95}_{-36}	-105^{+95}_{-36}
NGC 4593	2^{+74}_{-419}	-168^{+74}_{-419}
NGC 5548	-217^{+5}_{-123}	-94^{+5}_{-123}
NGC 6860	1199^{+246}_{-248}	

Table B.13: Continued from Table B.11

Object Name	O VII f line velocity (km s^{-1})	O VII f line velocity with optical redshift reference (km s^{-1})
NGC 7469	-452^{+148}_{-124}	-383^{+148}_{-124}
1RXS J213745.3-143250	609^{+449}_{-487}	
RE J1034+396	-274^{+225}_{-267}	
UGC 3973	-1^{+240}_{-225}	88^{+240}_{-225}
1H 0419-577	5^{+23}_{-92}	
ARK 564	45^{+107}_{-15}	-48^{+107}_{-15}
IRAS 17020+4544	223^{+221}_{-100}	
MRK 3	139^{+114}_{-114}	107^{+114}_{-114}
MRK 1018	-613^{+975}_{-899}	
NGC 1808	-826^{+988}_{-885}	-835^{+988}_{-885}
NGC 3310	-30^{+235}_{-234}	-55^{+235}_{-234}
NGC 424	-272^{+238}_{-230}	-195^{+238}_{-230}
MCG-5-23-16	-55^{+124}_{-32}	
NGC 5506	-27^{+5}_{-118}	-32^{+5}_{-118}
NGC 7314	0^{+7}_{-131}	-364^{+7}_{-131}
3C 79	277^{+3777}_{-337}	
IRAS 13197-1627	11^{+81}_{-164}	-102^{+81}_{-164}
IRAS 15480-0344	-135^{+236}_{-232}	
NGC 4388	-339^{+958}_{-916}	-360^{+958}_{-916}
NGC 4507	-490^{+242}_{-227}	-442^{+242}_{-227}

Table B.14: Continued from Table B.11

Object Name	O VII f line velocity (km s^{-1})	O VII f line velocity with optical redshift reference (km s^{-1})
NGC 5643	-267^{+370}_{-115}	-231^{+370}_{-115}
NGC 7582	28^{+73}_{-177}	39^{+73}_{-177}
NGC 7590	2^{+455}_{-108}	133^{+455}_{-108}
PG 1114+445	-10^{+92}_{-234}	
PG 1126-041	-712^{+491}_{-446}	
UGC 11185	500^{+906}_{-968}	
NGC 3079	1^{+297}_{-326}	25^{+297}_{-326}
5C 3.100	-3166^{+1135}_{-738}	
H 0439-272	-996^{+999}_{-875}	
MCG+8-11-11	108^{+465}_{-472}	52^{+465}_{-472}
NGC 6251	-457^{+1931}_{-1817}	
PG 1444+407	369^{+258}_{-240}	
2MASX J02070218+2930459	4^{+205}_{-22}	
UGC 1214	-114^{+944}_{-930}	-60^{+944}_{-930}
NGC 3690	429^{+3640}_{-3855}	
CTS A08.12	-172^{+237}_{-232}	
3C 234	1^{+251}_{-273}	
3C 445	-71^{+235}_{-233}	
ESO 103-G35	282^{+1838}_{-1909}	
ESO 511-G030	344^{+123}_{-242}	366^{+123}_{-242}

Table B.15: Continued from Table B.11

Object Name	O VII f line velocity (km s^{-1})	O VII f line velocity with optical redshift reference (km s^{-1})
NGC 1386	-58^{+940}_{-933}	
NGC 2655	-478^{+124}_{-250}	-481^{+124}_{-250}
NGC 5252	376^{+457}_{-480}	409^{+457}_{-480}
NGC 5273	31^{+211}_{-286}	
NGC 591	368^{+7409}_{-793}	427^{+7409}_{-793}
NGC 613	185^{+925}_{-948}	150^{+925}_{-948}
NGC 788	-124^{+137}_{-116}	
PKS 0921-213	-497^{+968}_{-906}	
2XMM J010712.0+140844	-1822^{+1404}_{-412}	

Appendix C

Survey of O VII f Emission Line Velocities: Notes

"It ain't what you don't know that gets you into trouble.
It's what you know for sure that just ain't so"
Josh Billings

The following objects which have line detections in this analysis and are not classified as Seyfert 1 (1 h, 1 i), 1.2, 1.5, 1.8, 1.9, 2, Narrow Line Seyfert 1 or unobscured Seyfert 2 in the NED database. More information was needed in order to classify these objects broadly as 'Type 1' or 'Type 2' for the analysis in this work, and here is a summary of that information.

Objects classified as 'Type 1':

Ark 564: Khanna et al. (2016) define it as NL Sy 1, as do Gliozzi et al. (2002); Papadakis et al. (2002); Marinello et al. (2016).

1RXS J031159.8-765131: Véron-Cetty and Véron (2006) classify it as Sy 1.2

3C 120: Ricci et al. (2014) include in their type 1 sample

PKS 0921-213: Véron-Cetty and Véron (2006) classify it as Sy 1

NGC 4593: Ricci et al. (2014) include it in their type 1 sample

Mrk 359: Ricci et al. (2014) include it in their type 1 sample

Objects classified as 'Type 2':

MCG-5-23-16: Simbad classification of Seyfert 2 and Baloković et al.

(2015) also classify it as Seyfert 1.9.

Mrk 915: Goodrich (1995) classify it as a Seyfert 1.8/1.9

NGC 2655: Gonzalez-Martin et al. (2015) classify it as an AGN-dominated LINER, not Compton-thick. Ho et al. (1997) also classify it as Seyfert 2

NGC 1808: Simbad classification of Seyfert 2, and Bassani et al. (1999) also classify as a Seyfert 2 with intrinsic column density of $N_H = 3.20 \times 10^{22}\,\mathrm{cm}^{-2}$

Objects not attributed to either group:

NGC 3310: Ho et al. (1997) classify it as H II region (non-AGN), using optical emission line ratios

NGC 613: Falcón-Barroso et al. (2014) classify it as a composite AGN (of unidentified type) with starburst, from photoionised and shock heated emission line ratios.

NGC 3690: Ho et al. (1997) classify it as an H II region (non-AGN), using optical emission line ratios

Bibliography

Abdo, A. A., Ackermann, M., Agudo, I., Ajello, M., Aller, H. D. and et al. (2010), The Spectral Energy Distribution of Fermi Bright Blazars, *The Astrophysical Journal* **716**(1), 30–70.

Alloin, D. (2006), Physics of Active Galactic Nuclei at all Scales, *Physics of Active Galactic Nuclei at all Scales* **693**.

Antonucci, R. R. J. and Miller, J. S. (1985), Spectropolarimetry and the nature of NGC 1068, *Astrophysical Journal* **297**, 621–632.

Arav, N., Chamberlain, C., Kriss, G. A., Kaastra, J. S., Cappi, M. and et al. (2015), Anatomy of the AGN in NGC 5548: II. The spatial, temporal, and physical nature of the outflow from HST/COS Observations, *Astronomy & Astrophysics* **577**, A37–27.

Arav, N., Gabel, J. R., Korista, K. T., Kaastra, J. S., Kriss, G. A., Behar, E. and et al. (2007), Chemical Abundances in an AGN Environment: X-Ray/UV Campaign on the Markarian 279 Outflow, *The Astrophysical Journal* **658**(2), 829–839.

Armentrout, B. K., Kraemer, S. B. and Turner, T. J. (2007), A Photoionization Model for the Soft X-Ray Spectrum of NGC 4151, *The Astrophysical Journal* **665**(1), 237–246.

Arnaud, K. A., Branduardi-Raymont, G., Culhane, J. L., Fabian, A. C., Hazard, C. and et al. (1985), EXOSAT observations of a strong soft X-ray excess in MKN 841, *Monthly Notices of the Royal Astronomical Society* **217**, 105–113.

Athena Science Working Group 2.3, Feedback in Local AGN and Star Forming Galaxies (2015).

Audard, M., Behar, E., G del, M., Raassen, A. J. J., Porquet, D. and et al. (2001), The XMM-Newton view of stellar coronae: High-resolution X-ray spectroscopy of Capella, *Astronomy & Astrophysics* **365**(1), L329–L335.

Bae, H.-J. and Woo, J.-H. (2014), A Census of Gas Outflows in Type 2 Active Galactic Nuclei, *The Astrophysical Journal* **795**(1), 30–11.

Baldwin, J. A., Hamann, F., Korista, K. T., Ferland, G. J., Dietrich, M. and et al. (2003), Chemical Abundances in Broad Emission Line Regions: The "Nitrogen-loud" Quasi-Stellar Object Q0353-383, *The Astrophysical Journal* **583**(2), 649–658.

Baloković, M., Matt, G., Harrison, F. A., Zoghbi, A., Ballantyne, D. R. and et al. (2015), Coronal Properties of the Seyfert 1.9 Galaxy MCG-05-23-016 Determined from Hard X-ray Spectroscopy with NuSTAR, *The Astrophysical Journal* **800**(1), 62–7.

Barret, D., den Herder, J. W., Piro, L., Ravera, L., den Hartog, R. and et al. (2013), The Hot and Energetic Universe: The X-ray Integral Field Unit (X-IFU) for Athena+, *arXiv:1308.6784* .

Barret, D., Lam Trong, T., den Herder, J.-W., Piro, L., Barcons, X. and et al. (2016), The Athena X-ray Integral Field Unit (X-IFU), *in* J.-W. A. den Herder, T. Takahashi and M. Bautz (eds.), *SPIE Astronomical Telescopes + Instrumentation*, SPIE.

Bassani, L., Dadina, M., Maiolino, R., Salvati, M., Risaliti, G. and et al. (1999), A Three-dimensional Diagnostic Diagram for Seyfert 2 Galaxies: Probing X-Ray Absorption and Compton Thickness, *The Astrophysical Journal Supplement Series* **121**(2), 473–482.

Beck, R., Fletcher, A., Shukurov, A., Snodin, A., Sokoloff, D. D. and et al. (2005), Magnetic fields in barred galaxies, *Astronomy & Astrophysics* **444**(3), 739–765.

Behar, E., Kinkhabwala, A., Sako, M., Paerels, F., Kahn, S. M. and et al. (2002), A Physically-Consistent Model for X-ray Emission by Seyfert 2 Galaxies Demonstrated using NGC 1068, *Mass Outflow in Active Galactic Nuclei: New Perspectives* **255**, 43.

Behar, E., Rasmussen, A. P., Blustin, A. J., Sako, M., Kahn, S. M. and et al. (2003), A Long Look at NGC 3783 with the XMM-Newton Reflection Grating Spectrometer, *The Astrophysical Journal* **598**(1), 232–241.

Bentz, M. C., Denney, K. D., Cackett, E. M., Dietrich, M., Fogel, J. K. J. and et al. (2007), NGC 5548 in a Low-Luminosity State: Implications for the Broad-Line Region, *The Astrophysical Journal* **662**(1), 205–212.

Bian, W., Yuan, Q. and Zhao, Y. (2005), The blueshift of the [O III] emission line in narrow-line Seyfert 1 galaxies, *Monthly Notices of the Royal Astronomical Society* **364**(1), 187–194.

Bianchi, S., Chiaberge, M., Evans, D. A., Guainazzi, M., Baldi, R. D. and et al. (2010), High-resolution X-ray spectroscopy and imaging of Mrk 573, *Monthly Notices of the Royal Astronomical Society* **405**(1), 553–563.

Bianchi, S., Guainazzi, M. and Chiaberge, M. (2006), The soft X-ray/NLR connection: a single photoionized medium?, *Astronomy & Astrophysics* **448**(2), 499–511.

Blandford, R. D. and Rees, M. J. (1978), Some comments on radiation mechanisms in Lacertids, *in* A. M. Wolfe (ed.), *BL Lac Objects*, pp.328–341.

Blustin, A. J., Branduardi-Raymont, G., Behar, E., Kaastra, J. S., Kahn, S. M. and et al. (2002), Multi-wavelength study of the Seyfert 1 galaxy NGC3783 with XMM-Newton, *Astronomy & Astrophysics* **392**(2), 453–467.

Blustin, A. J., Branduardi-Raymont, G., Behar, E., Kaastra, J. S., Kriss, G. A. and et al. (2003), Multiwavelength studies of the Seyfert 1 galaxy NGC 7469 II. X-ray and UV observations with XMM-Newton, *Astronomy & Astrophysics* **403**(2), 481–492.

Blustin, A. J., Page, M. J., Fuerst, S. V., Branduardi-Raymont, G. and Ashton, C. E. (2005), The nature and origin of Seyfert warm absorbers, *Astronomy & Astrophysics* **431**(1), 111–125.

Bohm, G. and Zech, G. (2010), *Introduction to Statistics and Data Analysis for Physicists*, Verlag Deutsches Elektronen-Synchrotron.

Boller, T., Brandt, W. N. and Fink, H. (1996), Soft X-ray properties of narrow-line Seyfert 1 galaxies., *Astronomy & Astrophysics* **305**, 53–.

Borguet, B. C. J., Arav, N., Edmonds, D., Chamberlain, C. and Benn, C. (2012), Major Contributor to AGN Feedback: VLT X-Shooter Observations of S IV BALQSO Outflows, *The Astrophysical Journal* **762**(1), 49–13.

Boroson, T. (2005), Blueshifted [O iii] Emission: Indications of a Dynamic Narrow-Line Region, *The Astronomical Journal* **130**(2), 381–386.

Boroson, T. (2011), A New Orientation Indicator for Radio-Quiet Quasars, *The Astrophysical Journal* **735**(1), L14–4.

Böttcher, M. (2007), Modeling the emission processes in blazars, *Astrophysics and Space Science* **309**(1-4), 95–104.

Bottorff, M. C., Korista, K. T. and Shlosman, I. (2000), Dynamics of Warm Absorbing Gas in Seyfert Galaxies: NGC 5548, *The Astrophysical Journal* **537**(1), 134–151.

Braito, V., Reeves, J. N., Gofford, J., Nardini, E., Porquet, D. and et al. (2014), NGC 1365: A Low Column Density State Unveiling a Low Ionization Disk Wind, *The Astrophysical Journal* **795**(1), 87–13.

Branduardi-Raymont, G. (1989), EXOSAT Observations of Flux and Spectral Variability in the Seyfert Galaxy NGC 5548, *in* D. E. Osterbrock and J. S. Miller (eds.), *Active Galactic Nuclei: proceedings of the 134th Symposium of the International Astronomical Union*, *International Astronomical Union* **134**, Kluwer Academic Publishers, Dordrecht, pp.177–178.

Brenneman, L. W., Risaliti, G., Elvis, M. and Nardini, E. (2013), An examination of the spectral variability in NGC 1365 with Suzaku, *Monthly Notices of the Royal Astronomical Society* **429**(3), 2662–2676.

Bresolin, F., Schaerer, D., González Delgado, R. M. and Stasińska, G. (2005), A VLT study of metal-rich extragalactic HII regions, *Astronomy & Astrophysics* **441**(3), 981–997.

Bridle, A. H. and Perley, R. A. (1984), Extragalactic Radio Jets, *Annual Review of Astronomy and Astrophysics* **22**(1), 319–358.

Brinchmann, J., Kunth, D. and Durret, F. (2008), Galaxies with Wolf-Rayet signatures in the low-redshift Universe, *Astronomy & Astrophysics* **485**(3), 657–677.

Brinkman, A., Aarts, H., den Boggende, A., Bootsma, T., Dubbeldam, L. and et al. (1998), The Reflection Grating Spectrometer onboard XMM, *Science with XMM* p.2.

Brinkman, A. C., Kaastra, J. S., van der Meer, R. L. J., Kinkhabwala, A., Behar, E. and et al. (2002), The soft X-ray spectrum from NGC 1068 observed with LETGS on Chandra, *Astronomy & Astrophysics* **396**, 761–772.

Cappi, M. (2006), Relativistic blue- and red-shifted absorption lines in AGNs, *Astronomische Nachrichten* **327**(10), 1012–1019.

Cappi, M., De Marco, B., Ponti, G., Ursini, F., Petrucci, P.-O. and et al. (2016), Anatomy of the AGN in NGC 5548. VIII. XMM-Newton's EPIC detailed view of an unexpected variable multilayer absorber, *Astronomy & Astrophysics* **592**, A27.

Cappi, M., Done, C., Behar, E., Bianchi, S., Braito, V. and et al. (2013), The Hot and Energetic Universe: Astrophysics of feedback in local AGN, *arXiv:1306.2330* .

Cash, W. (1979), Parameter estimation in astronomy through application of the likelihood ratio, *The Astrophysical Journal* **228**(228), 939–947.

Chiang, J., Reynolds, C. S., Blaes, O. M., Nowak, M. A., Murray, N. and et al. (2000), Simultaneous EUVE/ASCA/RXTE Observations of NGC 5548, *The Astrophysical Journal* **528**(1), 292–305.

Cicone, C., Maiolino, R., Sturm, E., Graciá-Carpio, J., Feruglio, C. and et al. (2014), Massive molecular outflows and evidence for AGN feedback from CO observations, *Astronomy & Astrophysics* **562**, A21–25.

Connolly, S. D., McHardy, I. M. and Dwelly, T. (2014), Long-term wind-driven X-ray spectral variability of NGC 1365 with Swift, *Monthly Notices of the Royal Astronomical Society* **440**(4), 3503–3510.

Costantini, E. (2010), The Ultraviolet-X-Ray Connection in AGN Outflows, *Space Science Reviews* **157**(1-4), 265–277.

Cottam, J., Kahn, S. M., Brinkman, A. C., den Herder, J. W. and Erd, C. (2001), High-resolution spectroscopy of the low-mass X-ray binary EXO 0748-67, *Astronomy & Astrophysics* **365**(1), L277–L281.

Crenshaw, D. M., Kraemer, S. B. and George, I. M. (2003), Mass Loss from the Nuclei of Active Galaxies, *Annual Review of Astronomy and Astrophysics* **41**(1), 117–167.

Croston, J. H., Sanders, J. S., Heinz, S., Hardcastle, M. J., Zhuravleva, I. and et al. (2013), The Hot and Energetic Universe: AGN feedback in galaxy clusters and groups, *arXiv:1306.2323* .

de Vaucouleurs, G., de Vaucouleurs, A., Corwin, Jr., H. G., Buta, R. J., Paturel, G. and et al. (1991), *Third Reference Catalogue of Bright Galaxies. Volume I: Explanations and references. Volume II: Data for galaxies between 0^h and 12^h. Volume III: Data for galaxies between 12^h and 24^h.*, Springer, New York, USA.

de Vries, C. P., den Herder, J. W., Gabriel, C., Gonzalez-Riestra, R., Ibarra, A. and et al. (2015), Calibration and in-orbit performance of the reflection grating spectrometer onboard XMM-Newton, *Astronomy & Astrophysics* **573**, A128–29.

de Vries, C. P., den Herder, J. W., Kaastra, J. S., Paerels, F. B., den Boggende, A. J. and et al. (2003), The interstellar oxygen-K absorption edge as observed by XMM-Newton. Separation of instrumental and interstellar components, *Astronomy & Astrophysics* **404**(3), 959–967.

den Herder, J. W., Bagnali, D., Bandler, S., Barbera, M., Barcons, X. and et al. (2012), The X-ray microcalorimeter spectrometer onboard Athena, *in* T. Takahashi, S. S. Murray and J.-W. A. den Herder (eds.), *SPIE Astronomical Telescopes + Instrumentation*, SPIE, pp.84432B–12.

den Herder, J. W., Brinkman, A. C., Kahn, S. M., Branduardi-Raymont, G., Thomsen, K. and et al. (2001), The Reflection Grating Spectrometer on board XMM-Newton, *Astronomy & Astrophysics* **365**(1), L7–L17.

Dennerl, K. (2010), Charge Transfer Reactions, *Space Science Reviews* **157**(1-4), 57–91.

Dennerl, K., Lisse, C. M., Bhardwaj, A., Burwitz, V., Englhauser, J. and et al. (2006), First observation of Mars with XMM-Newton, *Astronomy & Astrophysics* **451**(2), 709–722.

Denney, K. D., De Rosa, G., Croxall, K., Gupta, A., Bentz, M. C. and et al. (2014), The Typecasting of Active Galactic Nuclei: Mrk 590 No Longer Fits the Role, *The Astrophysical Journal* **796**(2), 134–13.

Detmers, R. G., Kaastra, J. S., Costantini, E., McHardy, I. M. and Verbunt, F. (2008), The warm absorber in NGC 5548, *Astronomy & Astrophysics* **488**(1), 67–72.

Detmers, R. G., Kaastra, J. S. and McHardy, I. M. (2009), X-ray narrow line region variability as a geometry probe, *Astronomy & Astrophysics* **504**(2), 409–414.

Di Gesu, L., Costantini, E., Ebrero, J., Mehdipour, M., Kaastra, J. S. and et al. (2015), Anatomy of the AGN in NGC 5548. IV. The short-term variability of the outflows, *Astronomy & Astrophysics* **579**, A42.

Di Matteo, T., Springel, V. and Hernquist, L. (2005), Energy input from quasars regulates the growth and activity of black holes and their host galaxies, *Nature* **433**(7), 604–607.

Doroshenko, V. T., Lyutyi, V. M. and Shenavrin, V. I. (1998), Surface brightness distributions of four Seyfert galaxies based on multi-aperture UBV photometry, *Astronomy Letters* **24**(2), 160–170.

Ebrero, J., Kaastra, J. S., Kriss, G. A., Di Gesu, L., Costantini, E. and et al. (2016), Anatomy of the AGN in NGC 5548. VI. Long-term variability of the warm absorber, *Astronomy & Astrophysics* **587**, A129.

Eddington, A. S. (1925), A limiting case in the theory of radiative equilibrium, *Monthly Notices of the Royal Astronomical Society* **85**(5), 408–.

Edge, D. O., Shakeshaft, J. R., McAdam, W. B., Baldwin, J. E. and Archer, S. (1959), A survey of radio sources at a frequency of 159 Mc/s., *Memoirs of the Royal Astronomical Society* **68**, 37–60.

Elitzur, M. and Ho, L. C. (2009), On the Dissapearance of the Broad-Line Region in Low-Luminosity Active Galactic Nuclei, *The Astrophysical Journal* **701**(2), L91–L94.

Elvis, M. (2000), A Structure for Quasars, *The Astrophysical Journal* **545**(1), 63–76.

ESA XMM-Newton SOC (2016), *XMM-Newton Users Handbook*.

Evans, D. A., Hardcastle, M. J., Croston, J. H., Worrall, D. M. and Birkinshaw, M. (2005), Chandra and XMM-Newton observations of NGC 6251, *Monthly Notices of the Royal Astronomical Society* **359**(1), 363–382.

Fabian, A. C. (2012), Observational Evidence of Active Galactic Nuclei Feedback, *Annual Review of Astronomy and Astrophysics* **50**(1), 455–489.

Fabian, A. C., Guilbert, P. W., Blandford, R. D., Phinney, E. S. and Cuellar, L. (1986), Pair-induced spectral changes and variability in compact X-ray

sources, *Monthly Notices of the Royal Astronomical Society* **221**(4), 931–945.

Fabian, A. C. and Ross, R. R. (2010), X-ray Reflection, *Space Science Reviews* **157**(1-4), 167–176.

Falcón-Barroso, J., Ramos Almeida, C., Boker, T., Schinnerer, E., Knapen, J. H. and et al. (2014), The circumnuclear environment of NGC 613: a nuclear starburst caught in the act?, *Monthly Notices of the Royal Astronomical Society* **438**(1), 329–340.

Fanaroff, B. L. and Riley, J. M. (1974), The morphology of extragalactic radio sources of high and low luminosity, *Monthly Notices of the Royal Astronomical Society* **167**(1), 31P–36P.

Fardal, M. A., Katz, N., Weinberg, D. H. and Dave, R. (2007), On the evolutionary history of stars and their fossil mass and light, *Monthly Notices of the Royal Astronomical Society* **379**(3), 985–1002.

Ferland, G. J., Porter, R. L., van Hoof, P. A. M., Williams, R. J. R., Abel, N. P. and et al. (2013), The 2013 Release of Cloudy, *Revista Mexicana de Astronomía y Astrofísica Vol. 49* **49**, 137–163.

Ferrarese, L. and Merritt, D. (2000), A Fundamental Relation between Supermassive Black Holes and Their Host Galaxies, *The Astrophysical Journal* **539**(1), L9–L12.

Gabel, J. R., Arav, N. and Kim, T.-S. (2006), The AGN Outflow in the HDF-S Target QSO J2233-606 from a High-Resolution VLT UVES Spectrum, *The Astrophysical Journal* **646**(2), 742–753.

Gabriel, A. H. and Jordan, C. (1969), Interpretation of solar helium-like ion line intensities, *Monthly Notices of the Royal Astronomical Society* **145**, 241.

Gebhardt, K., Bender, R., Bower, G., Dressler, A., Faber, S. M. and et al. (2000), A Relationship between Nuclear Black Hole Mass and Galaxy Velocity Dispersion, *The Astrophysical Journal* **539**(1), L13–L16.

George, I. M., Turner, T. J., Netzer, H., Nandra, K., Mushotzky, R. F. and et al. (1998), ASCA Observations of Seyfert 1 Galaxies. III. The Evidence for Absorption and Emission Due to Photoionized Gas, *The Astrophysical Journal Supplement Series* **114**(1), 73–120.

Ghisellini, G., Tavecchio, F., Foschini, L. and Ghirlanda, G. (2011), The transition between BL Lac objects and flat spectrum radio quasars, *Monthly Notices of the Royal Astronomical Society* **414**(3), 2674–2689.

Gierlinski, M. and Done, C. (2004), Is the soft excess in active galactic nuclei real?, *Monthly Notices of the Royal Astronomical Society* **349**(1), L7–L11.

Gliozzi, M., Brinkmann, W., Räth, C., Papadakis, I. E., Negoro, H. and et al. (2002), On the nature of X-ray variability in Ark 564, *Astronomy & Astrophysics* **391**(3), 875–886.

Gonzalez-Martin, O., Díaz-González, D., Acosta-Pulido, J. A., Masegosa, J., Papadakis, I. E. and et al. (2014), Synapses of active galactic nuclei: Comparing X-ray and optical classifications using artificial neural networks, *Astronomy & Astrophysics* **567**, A92–23.

Gonzalez-Martin, O., Masegosa, J., Márquez, I., Guerrero, M. A. and Dultzin-Hacyan, D. (2006), X-ray nature of the LINER nuclear sources, *Astronomy & Astrophysics* **460**(1), 45–57.

Gonzalez-Martin, O., Masegosa, J., Márquez, I., Rodriguez-Espinosa, J. M., Acosta-Pulido, J. A. and et al. (2015), Nuclear obscuration in LINERs, *Astronomy & Astrophysics* **578**, A74–19.

Goodrich, R. W. (1995), Dust in the broad-line regions of Seyfert galaxies, *Astrophysical Journal* **440**, 141–150.

Groves, B. A., Heckman, T. M. and Kauffmann, G. (2006), Emission-line diagnostics of low-metallicity active galactic nuclei, *Monthly Notices of the Royal Astronomical Society* **371**(4), 1559–1569.

Guainazzi, M. and Bianchi, S. (2007), On the origin of soft X-rays in obscured AGN: answers from high-resolution spectroscopy with XMM-Newton, *Monthly Notices of the Royal Astronomical Society* **374**(4), 1290–1302.

Guainazzi, M., Risaliti, G., Nucita, A., Wang, J., Bianchi, S. and et al. (2009), AGN/starburst connection in action: the half million second RGS spectrum of NGC 1365, *Astronomy & Astrophysics* **505**(2), 589–600.

Halpern, J. P. (1984), Variable X-ray absorption in the QSO MR 2251 - 178, *Astrophysical Journal* **281**, 90–94.

Hamann, F., Korista, K. T., Ferland, G. J., Warner, C. and Baldwin, J. (2002), Metallicities and Abundance Ratios from Quasar Broad Emission Lines, *The Astrophysical Journal* **564**(2), 592–603.

Hamann, F., Warner, C., Dietrich, M. and Ferland, G. (2007), Quasar Metal Abundances and Host Galaxy Evolution, *The Central Engine of Active Galactic Nuclei* **373**, 653–.

Heckman, T. M. (1980), An optical and radio survey of the nuclei of bright galaxies - Activity in normal galactic nuclei, *Astronomy & Astrophysics* **87**, 152–164.

Heckman, T. M. (1987), The Nature of Liners, *in Observational Evidence of Activity in Galaxies: Proceedings of the 121st Symposium of the International Astronomical Union*, pp.421–.

Hitomi Collaboration (2016), The quiescent intracluster medium in the core of the Perseus cluster, *Nature* **535**(7), 117–121.

Ho, L. C., Filippenko, A. V. and Sargent, W. L. W. (1997), A Search for "Dwarf" Seyfert Nuclei. III. Spectroscopic Parameters and Properties of the Host Galaxies, *The Astrophysical Journal Supplement Series* **112**(2), 315–390.

Hopkins, A. M. and Beacom, J. F. (2006), On the Normalization of the Cosmic Star Formation History, *The Astrophysical Journal* **651**(1), 142–154.

Hopkins, P. F. and Elvis, M. (2010), Quasar feedback: more bang for your buck, *Monthly Notices of the Royal Astronomical Society* **401**(1), 7–14.

Humphrey, P. J., Liu, W. and Buote, D. A. (2009), χ^2 and Poissonian Data: Biases even in the High-Count Regime and How to Avoid Them, *The Astrophysical Journal* **693**(1), 822–829.

Jansen, F., Lumb, D., Altieri, B., Clavel, J., Ehle, M. and et al. (2001), XMM-Newton observatory, *Astronomy & Astrophysics* **365**(1), L1–L6.

Jimenez-Garate, M. A. and Khu, T. (2004), Using the X-Ray Emission Lines of Seyfert 2 AGN to Measure Abundance Ratios, *in Multiwavelength AGN Surveys. Proceedings of the Guillermo Haro Conference 2003. Held 8-12 December 2003 in Cozumel*, MIT Center for Space Research, 70 Vassar St., NE80-6009 Cambridge, MA, 02139, USA mario@space.mit.edu, World Scientific, pp.191–192.

Kaastra, J. (2015), Shining light on obscured AGN outflows: XMM-Newton Proposal.

Kaastra, J. S., de Vries, C. P., Steenbrugge, K. C., Detmers, R. G., Ebrero, J. and et al. (2011), Multiwavelength campaign on Mrk 509: II. Analysis of high-quality Reflection Grating Spectrometer spectra, *Astronomy & Astrophysics* **534**, A37.

Kaastra, J. S., Kriss, G. A., Cappi, M., Mehdipour, M., Petrucci, P. O. and et al. (2014), A fast and long-lived outflow from the supermassive black hole in NGC 5548, *Science* **345**(6192), 64–68.

Kaastra, J. S., Mewe, R. and Nieuwenhuijzen, H. (1996), SPEX: a new code for spectral analysis of X & UV spectra., *11th Colloquium on UV and X-ray Spectroscopy of Astrophysical and Laboratory Plasmas* pp.411–414.

Kaastra, J. S., Mewe, R., Liedahl, D. A. and Brinkman, A. C. (2000), X-ray absorption lines in the Seyfert 1 galaxy NGC 5548 discovered with Chandra-LETGS, *Astronomy & Astrophysics* **354**, L83–L86.

Kaastra, J. S., Steenbrugge, K. C., Raassen, A. J. J., van der Meer, R. L. J., Brinkman, A. C. and et al. (2002), X-ray spectroscopy of NGC 5548, *Astronomy & Astrophysics* **386**(2), 427–445.

Kahn, S. M., Behar, E., Kinkhabwala, A. and Savin, D. W. (2002), X-ray spectroscopy of astrophysical plasmas, *Philosophical Transactions of the Royal Society A: Mathematical, Physical and Engineering Sciences* **360**(1798), 1923–1933.

Kalberla, P. M. W., Burton, W. B., Hartmann, D., Arnal, E. M., Bajaja, E. and et al. (2005), The Leiden/Argentine/Bonn (LAB) Survey of Galactic HI, *Astronomy & Astrophysics* **440**(2), 775–782.

Keel, B. (2002), Optical Spectra of Active Galactic Nuclei: http://pages.astronomy.ua.edu/keel/agn/spectra.gif.

Khachikian, E. Y. and Weedman, D. W. (1974), An atlas of Seyfert galaxies, *The Astrophysical Journal* **192**, 581–589.

Khanna, S., Kaastra, J. S. and Mehdipour, M. (2016), Probing the photoionised outflow in the NLS1 Arakelian 564: An XMM-Newton view, *Astronomy & Astrophysics* **586**, A2–10.

King, A. (2003), Black Holes, Galaxy Formation, and the MBH-σ Relation, *The Astrophysical Journal* **596**(1), L27–L29.

Kinkhabwala, A., Behar, E., Sako, M., Gu, M. F., Kahn, S. M. and et al. (2003), Atomic Calculations and Spectral Models of X-ray Absorption and Emission Features From Astrophysical Photoionized Plasmas, *arXiv:0304.332* .

Kinkhabwala, A., Sako, M., Behar, E., Kahn, S. M., Paerels, F. and et al. (2002), XMM-Newton Reflection Grating Spectrometer Observations of Discrete Soft X-Ray Emission Features from NGC 1068, *The Astrophysical Journal* **575**(2), 732–746.

Koratkar, A. and Blaes, O. (1999), Invited Review: The Ultraviolet and Optical Continuum Emission in Active Galactic Nuclei: The Status of Accretion

Disks, *Publications of the Astronomical Society of the Pacific* **111**(755), 1–30.

Korista, K. T., Alloin, D., Barr, P., Clavel, J., Cohen, R. D. and et al. (1995), Steps toward determination of the size and structure of the broad-line region in active galatic nuclei. 8: an intensive HST, IUE, and ground-based study of NGC 5548, *Astrophysical Journal Supplement Series* **97**, 285–330.

Kormendy, J. (2001), Supermassive Black Holes in Disk Galaxies, *in Galaxy Disks and Disk Galaxies* **230**, 247–256.

Kormendy, J. and Ho, L. C. (2013), Coevolution (Or Not) of Supermassive Black Holes and Host Galaxies, *Annual Review of Astronomy and Astrophysics* **51**(1), 511–653.

Kraemer, S. B., Crenshaw, D. M., Filippenko, A. V. and Peterson, B. M. (1998), Evidence for a Physically Compact Narrow-Line Region in the Seyfert 1 Galaxy NGC 5548, *The Astrophysical Journal* **499**(2), 719–727.

Kraemer, S. B., Schmitt, H. R., Crenshaw, D. M., Meléndez, M., Turner, T. J. and et al. (2011), Multi-Wavelength Probes of Obscuration Toward the Narrow-Line Region in Seyfert Galaxies, *The Astrophysical Journal* **727**(2), 130–11.

Kriss, G. A. (2001), Far-Ultraviolet Spectra of AGN: First Results from FUSE, *Probing the Physics of Active Galactic Nuclei* **224**, 45–.

Kriss, G. A., Blustin, A., Branduardi-Raymont, G., Green, R. F., Hutchings, J. and et al. (2003), Multiwavelength studies of the Seyfert 1 galaxy NGC7469 I. Far UV observations with FUSE, *Astronomy & Astrophysics* **403**(2), 473–479.

Kristen, H., Jorsater, S., Lindblad, P. O. and Boksenberg, A. (1997), Imaging the nuclear environment of NGC 1365 with the Hubble Space Telescope, *Astronomy & Astrophysics* **328**, 483–492.

Krolik, J. H. (1999), *Active Galactic Nuclei: From the Central Black Hole*

to the Galactic Environment, Princeton University Press, Princeton, New Jersey, USA.

Krolik, J. H. and Kriss, G. A. (1995), Observable Properties of X-Ray–heated Winds in Active Galactic Nuclei: Warm Reflectors and Warm Absorbers, *The Astrophysical Journal* **447**, 512–14.

Krolik, J. H. and Kriss, G. A. (2001), Warm Absorbers in Active Galactic Nuclei: A Multitemperature Wind, *The Astrophysical Journal* **561**(2), 684–690.

Kutner, Marc. L (2003), *Astronomy: A Physical Perspective*, Cambridge University Press, Cambridge, UK.

Laha, S., Guainazzi, M., Dewangan, G. C., Chakravorty, S. and Kembhavi, A. K. (2014), Warm absorbers in X-rays (WAX), a comprehensive high-resolution grating spectral study of a sample of Seyfert galaxies - I. A global view and frequency of occurrence of warm absorbers., *Monthly Notices of the Royal Astronomical Society* **441**(3), 2613–2643.

Laor, A. (2003), On the Nature of Low-Luminosity Narrow-Line Active Galactic Nuclei, *The Astrophysical Journal* **590**(1), 86–94.

Liu, J.-R. and Mao, S.-D. (2015), On the diffuse soft X-ray emission from the nuclear region of M51, *Research in Astronomy and Astrophysics* **15**(1), 2164–2172.

Lodders, K., Palme, H. and Gail, H. P. (2009), Abundances of the Elements in the Solar System, *"Landolt-Börnstein - Group VI Astronomy and Astrophysics Numerical Data and Functional Relationships in Science and Technology Volume* **4B**(Chapter 34), 712–770.

Longinotti, A. L., Nucita, A., Santos-Lleo, M. and Guainazzi, M. (2008), The Seyfert 1 Galaxy Mrk 335 at a very low flux state: mapping the soft X-ray photoionised gas, *Astronomy & Astrophysics* **484**(2), 311–315.

Maiolino, R. and Rieke, G. H. (1995), Low-Luminosity and Obscured Seyfert Nuclei in Nearby Galaxies, *Astrophysical Journal v.454* **454**, 95.

Marconi, A., Risaliti, G., Gilli, R., Hunt, L. K., Maiolino, R. and et al. (2004), Local supermassive black holes, relics of active galactic nuclei and the X-ray background, *Monthly Notices of the Royal Astronomical Society* **351**(1), 169–185.

Marinello, M., Rodríguez-Ardila, A., Garcia-Rissmann, A., Sigut, T. A. A. and Pradhan, A. K. (2016), The Fe ii Emission in Active Galactic Nuclei: Excitation Mechanisms and Location of the Emitting Region, *The Astrophysical Journal* **820**(2), 1–22.

Marinucci, A., Bianchi, S., Matt, G., Fabian, A. C., Iwasawa, K. and et al. (2010), The X-ray spectral signatures from the complex circumnuclear regions in the Compton thick AGN NGC 424, *Astronomy & Astrophysics* **526**, A36.

Markowitz, A. G., Krumpe, M. and Nikutta, R. (2014), First X-ray-based statistical tests for clumpy-torus models: eclipse events from 230 years of monitoring of Seyfert AGN, *Monthly Notices of the Royal Astronomical Society* **439**(2), 1403–1458.

Mason, K. O., Breeveld, A., Much, R., Carter, M., Cordova, F. A. and et al. (2001), The XMM-Newton optical/UV monitor telescope, *Astronomy & Astrophysics* **365**(1), L36–L44.

Matt, G., Guainazzi, M. and Maiolino, R. (2003), Changing look: from Compton-thick to Compton-thin, or the rebirth of fossil active galactic nuclei, *Monthly Notice of the Royal Astronomical Society* **342**(2), 422–426.

Mehdipour, M. (2016), Continuing the Search for X-ray Obscuring Disk Winds in AGN: Swift proposal.

Mehdipour, M., Branduardi-Raymont, G. and Page, M. J. (2010), The warm absorber and X-ray variability of the Seyfert 1 galaxy NGC3516 as seen by the XMM-Newton RGS, *Astronomy & Astrophysics* **514**, A100.

Mehdipour, M., Branduardi-Raymont, G., Kaastra, J. S., Petrucci, P. O., Kriss, G. A. and et al. (2011), Multiwavelength campaign on Mrk 509: IV.

Optical-UV-X-ray variability and the nature of the soft X-ray excess, *Astronomy & Astrophysics* **534**, A39.

Mehdipour, M., Kaastra, J. S., Kriss, G. A., Cappi, M., Petrucci, P. O. and et al. (2015), Anatomy of the AGN in NGC 5548: I. A global model for the broadband spectral energy distribution, *Astronomy & Astrophysics* **575**, A22–18.

Mehdipour, M., Kaastra, J. S., Kriss, G. A., Cappi, M., Petrucci, P. O. and et al. (2016), Anatomy of the AGN in NGC 5548: VII. Swift study of obscuration and broadband continuum variability, *Astronomy & Astrophysics* **588**, A139–12.

Miller, J. S., Goodrich, R. W. and Mathews, W. G. (1991), Multidirectional views of the active nucleus of NGC 1068, *Astrophysical Journal* **378**, 47–64.

Miller, L. and Turner, T. J. (2013), The Hard X-Ray Spectrum of NGC 1365: Scattered Light, Not Black Hole Spin, *The Astrophysical Journal Letters* **773**(1), L5.

Mingo, B., Watson, M. G., Rosen, S. R., Hardcastle, M. J., Ruiz, A. and et al. (2016), The MIXR sample: AGN activity versus star formation across the cross-correlation of WISE, 3XMM, and FIRST/NVSS, *Monthly Notices of the Royal Astronomical Society* **462**(3), 2631–2667.

Mo, H., van den Bosch, F. and White, S. (2010), *Galaxy Formation and Evolution*, Cambridge University Press, Cambridge, UK.

Mukai, K., Kinkhabwala, A., Peterson, J. R., Kahn, S. M. and Paerels, F. (2003), Two Types of X-Ray Spectra in Cataclysmic Variables, *The Astrophysical Journal* **586**(1), L77–L80.

Murayama, T. and Taniguchi, Y. (1998), Where Is the Coronal Line Region in Active Galactic Nuclei?, *The Astrophysical Journal* **497**(1), L9–L12.

Murdin, P. (2001), *Encyclopedia of Astronomy and Astrophysics*, Institute of Physics Publishing.

Nagao, T., Murayama, T. and Taniguchi, Y. (2001), Where is the [O III]4363 Emitting Region in Active Galactic Nuclei?, *The Astrophysical Journal* **549**, 155–171.

Nahar, S. N. and Pradhan, A. K. (2003), Electron-Ion Recombination Rate Coefficients and Photoionization Cross Sections for Astrophysically Abundant Elements. VII. Relativistic Calculations for O VI and O VII f or Ultraviolet and X-Ray Modeling, *The Astrophysical Journal Supplement Series* **149**(1), 239–249.

Nandra, K., Barcons, X., den Herder, J.-W., Watson, M., Barret, D. and et al. (2014), Athena Mission Proposal, Technical Report.

Nardini, E., Fabian, A. C., Reis, R. C. and Walton, D. J. (2011), A reflection origin for the soft and hard X-ray excess of Ark 120, *Monthly Notices of the Royal Astronomical Society* **410**(2), 1251–1261.

Nardini, E., Gofford, J., Reeves, J. N., Braito, V., Risaliti, G. and et al. (2015), The Chandra/HETG view of NGC 1365 in a Compton-thick state, *Monthly Notices of the Royal Astronomical Society* **453**(3), 2558–2568.

NASA (2016), Announcement of Opportunity. Astrophysics Explorers Program: 2016 Medium Explorer (MIDEX), pp.1–124.

Netzer, H. (2006), Active Galactic Nuclei: Basic Physics and Main Components, in *Physics of Active Galactic Nuclei at all Scales* (Alloin 2006), pp.1–38.

Netzer, H. (2015), Revisiting the Unified Model of Active Galactic Nuclei, *Annual Review of Astronomy and Astrophysics* **53**(1), 365–408.

Nicastro, F. (2000), Broad Emission Line Regions in Active Galactic Nuclei: The Link with the Accretion Power, *The Astrophysical Journal* **530**(2), L65–L68.

Nucita, A. A., Guainazzi, M., Longinotti, A. L., Santos-Lleo, M., Maruccia, Y. and et al. (2010), A characterization of the NGC 4051 soft X-ray spectrum as observed by XMM-Newton, *Astronomy & Astrophysics* **515**, A47.

Origlia, L., Ranalli, P., Comastri, A. and Maiolino, R. (2004), Stellar and Gaseous Abundances in M82, *The Astrophysical Journal* **606**(2), 862–868.

Osterbrock, D. E. (1981), Seyfert galaxies with weak broad H alpha emission lines, *Astrophysical Journal* **249**, 462–470.

Osterbrock, D. E. and Ferland, G. J. (2006), *Astrophysics of Gaseous Nebulae and Active Galactic Nuclei*, University Science Books, Sausalito, California, USA.

Pagel, B. E. J. (2009), *Nucleosynthesis and Chemical Evolution of Galaxies*, Nucleosynthesis and Chemical Evolution of Galaxies.

Pancoast, A., Brewer, B. J., Treu, T., Park, D., Barth, A. J. and et al. (2013), Modeling reverberation mapping data II: dynamical modeling of the Lick AGN Monitoring Project 2008 dataset, *Monthly Notices of the Royal Astronomical Society* pp.1–20.

Papadakis, I. E., Brinkmann, W., Negoro, H. and Gliozzi, M. (2002), Detection of a high frequency break in the X-ray power spectrum of Ark 564, *Astronomy & Astrophysics* **382**(1), L1–L4.

Parker, M. L., Walton, D. J., Fabian, A. C. and Risaliti, G. (2014), PCA of PCA: principal component analysis of partial covering absorption in NGC 1365, *Monthly Notices of the Royal Astronomical Society* **441**(2), 1817–1824.

Peterson, B. M. (1993), Reverberation Mapping of Active Galactic Nuclei, *Publications of the Astronomical Society of the Pacific* **105**(685), 247–268.

Peterson, B. M. (1999), *An Introduction To Active Galactic Nuclei*, Cambridge University Press, Cambridge, UK.

Peterson, B. M., Berlind, P., Bertram, R., Bochkarev, N. G., Bond, D. and et al. (1994), Steps toward determination of the size and structure of the broad-line region in active nuclei. 7: Variability of the optical spectrum of NGC 5548 over years, *The Astrophysical Journal* **425**, 622–634.

Peterson, B. M., Denney, K. D., De Rosa, G., Grier, C. J., Pogge, R. W. and et al. (2013), The Size of the Narrow-Line-Emitting Region in the Seyfert 1 Galaxy NGC 5548 From Emission-Line Variability, *The Astrophysical Journal* **779**(2), 109–14.

Phillips, A. C. and Conti, P. S. (1992), Detection of WC9 stars in NGC 1365, *Astrophysical Journal* **395**, L91–L93.

Porquet, D., Dubau, J. and Grosso, N. (2010), He-like Ions as Practical Astrophysical Plasma Diagnostics: From Stellar Coronae to Active Galactic Nuclei, *Space Science Reviews* **157**(1), 103–134.

Porquet, D. and Dubau, J. (2000), X-ray photoionized plasma diagnostics with helium-like ions. Application to warm absorber-emitter in active galactic nuclei, *Astronomy and Astrophysics Supplement Series* **143**(3), 495–514.

Porter, F. S. and Brown, G. V. and Cottam, J. (2005), *Cryogenic Particle Detection*, Cambridge University Press, Cambridge, UK.

Porter, R. L. and Ferland, G. J. (2007), Revisiting He-like X-Ray Emission-Line Plasma Diagnostics, *The Astrophysical Journal* **664**(1), 586–595.

Pounds, K. A., Done, C. and Osborne, J. P. (1995), RE 1034+39: a high-state Seyfert galaxy?, *Monthly Notices of the Royal Astronomical Society* **277**(1), L5–L10.

Pounds, K. A., Turner, T. J. and Warwick, R. S. (1986), Rapid X-ray variability of the Seyfert galaxy MCG-6-30-15, *Monthly Notices of the Royal Astronomical Society* **221**, 7P–12P.

Read, A. M. and Stevens, I. R. (2002), XMM-Newton Reflection Grating Spectrometer observations of the prototypical starburst galaxy M82, *Monthly Notices of the Royal Astronomical Society* **335**(1), L36–L40.

Reeves, J. N., Braito, V., Nardini, E., Behar, E., O'Brien, P. T. and et al. (2016a), Discovery of broad soft X-ray absorption lines from the quasar wind in PDS 456, *The Astrophysical Journal* **824**(1), 1–18.

Reeves, J. N., Porquet, D., Braito, V., Nardini, E., Lobban, A. and Turner, T. J. (2016b), A Deep X-ray View of the Bare AGN ARK 120. I. Revealing the Soft X-ray Line Emission, *The Astrophysical Journal* **828**(2), 98–42.

Reynolds, C. S. (1997), An X-ray spectral study of 24 type 1 active galactic nuclei, *Monthly Notices of the Royal Astronomical Society* **286**(3), 513–537.

Ricci, C., Ueda, Y., Paltani, S., Ichikawa, K., Gandhi, P. and et al. (2014), Iron K emission in type-I and type-II active galactic nuclei, *Monthly Notices of the Royal Astronomical Society* **441**(4), 3622–3633.

Risaliti, G., Bianchi, S., Matt, G., Baldi, A., Elvis, M. and et al. (2005a), Highly Ionized Iron Absorption Lines from Outflowing Gas in the X-Ray Spectrum of NGC 1365, *The Astrophysical Journal* **630**(2), L129–L132.

Risaliti, G., Elvis, M., Fabbiano, G., Baldi, A. and Zezas, A. (2005b), Rapid Compton-thick/Compton-thin Transitions in the Seyfert 2 Galaxy NGC 1365, *The Astrophysical Journal* **623**(2), L93–L96.

Risaliti, G., Elvis, M., Fabbiano, G., Baldi, A., Zezas, A. and et al. (2007), Occultation Measurement of the Size of the X-Ray-emitting Region in the Active Galactic Nucleus of NGC 1365, *The Astrophysical Journal* **659**(2), L111–L114.

Risaliti, G., Harrison, F. A., Madsen, K. K., Walton, D. J., Boggs, S. E. and et al. (2013), A rapidly spinning supermassive black hole at the centre of NGC 1365, *Nature* **494**(7), 449–451.

Risaliti, G., Miniutti, G., Elvis, M., Fabbiano, G., Salvati, M. and et al. (2009a), Variable Partial Covering and a Relativistic Iron Line in NGC 1365, *The Astrophysical Journal* **696**(1), 160–171.

Risaliti, G., Salvati, M., Elvis, M., Fabbiano, G., Baldi, A. and et al. (2009b), The XMM-Newton long look of NGC 1365: uncovering of the obscured X-ray source, *Monthly Notices of the Royal Astronomical Society: Letters* **393**(1), L1–L5.

Rivers, E., Risaliti, G., Walton, D. J., Harrison, F., Arevalo, P. and et al. (2015), The Multi-Layer Variable Absorbers in NGC 1365 Revealed by XMM-Newton and NuSTAR, *The Astrophysical Journal* **804**(2), 1–11.

Rosen, S., Watson, M., Pye, J., Webb, N., Schwope, A. and et al. (2015), The 3XMM-DR4 Catalogue, *Astronomical Data Analysis Software an Systems XXIV (ADASS XXIV)* **495**, 319–.

Ross, R. R. and Fabian, A. C. (2005), A comprehensive range of X-ray ionized-reflection models, *Monthly Notices of the Royal Astronomical Society* **358**(1), 211–216.

Rybicki, G. B. and Lightman, A. P. (1979), *Radiative Processes in Astrophysics*, John Wiley and Sons, Inc.

Sako, M. (2003), Carbon-Nitrogen-Oxygen Line Radiation and the X-Ray Bowen Fluorescence Mechanism in Optically Thick, Highly Ionized Media, *The Astrophysical Journal* **594**(2), 1108–1114.

Sako, M., Kahn, S. M., Paerels, F. and Liedahl, D. A. (2000), The Chandra High-Energy Transmission Grating Observation of an X-Ray Ionization Cone in Markarian 3, *The Astrophysical Journal* **543**(2), L115–L118.

Sako, M., Liedahl, D. A., Kahn, S. M. and Paerels, F. (1999), The X-Ray Spectrum and Global Structure of the Stellar Wind in VELA X-1, *The Astrophysical Journal* **525**(2), 921–934.

Santos, M., Alonso, D., Bull, P., Silva, M. B. and Yahya, S. (2015), HI galaxy simulations for the SKA: number counts and bias, *in Proceedings of Advancing Astrophysics with the Square Kilometre Array (AASKA14). 9 -13 June*, p.21.

Schild, H., G del, M., Mewe, R., Schmutz, W., Raassen, A. J. J. and et al. (2004), Wind clumping and the wind-wind collision zone in the Wolf-Rayet binary γ^2 Velorum, *Astronomy & Astrophysics* **422**(1), 177–191.

Schulz, H., Komossa, S., Schmitz, C. and Mücke, A. (1999), Clues on the

obscured active nucleus of NGC 1365, *Astronomy & Astrophysics* **346**, 764–768.

Scott, D. W. (2015), *Multivariate Density Estimation: Theory, Practice, and Visualization*, John Wiley and Sons, Inc.

Seyfert, C. K. (1943), Nuclear Emission in Spiral Nebulae., *Astrophysical Journal* **97**, 28.

Shankar, F., Weinberg, D. H. and Miralda-Escudé, J. (2008), Self-Consistent Models of the AGN and Black Hole Populations: Duty Cycles, Accretion Rates, and the Mean Radiative Efficiency, *The Astrophysical Journal* **690**(1), 20–41.

Shuder, J. M. and Osterbrock, D. E. (1981), Empirical results from a study of active galactic nuclei, *Astrophysical Journal* **250**, 55–65.

Silk, J. and Rees, M. J. (1998), Quasars and galaxy formation, *Astronomy & Astrophysics* **331**, L1–L4.

Singh, R., van de Ven, G., Jahnke, K., Lyubenova, M., the CALIFA collaboration and et al. (2013), The nature of LINER galaxies:, *Astronomy & Astrophysics* **558**, A43–8.

Smith, R. K., Abraham, M. H., Allured, R., Bautz, M., Bookbinder, J. and et al. (2016), Arcus: the x-ray grating spectrometer explorer, *in* J.-W. A. den Herder, T. Takahashi and M. Bautz (eds.), *SPIE Astronomical Telescopes + Instrumentation*, SPIE.

Sramek, R. A. and Weedman, D. W. (1980), The radio properties of optically discovered quasars, *Astrophysical Journal* **238**, 435–444.

Steenbrugge, K. C., Kaastra, J. S., Crenshaw, D. M., Kraemer, S. B., Arav, N. and et al. (2005), Simultaneous X-ray and UV spectroscopy of the Seyfert galaxy NGC 5548, *Astronomy & Astrophysics* **434**(2), 569–584.

Steenbrugge, K. C., Kaastra, J. S., de Vries, C. P. and Edelson, R. (2003), XMM-Newton High resolution spectroscopy of NGC 5548, *Astronomy & Astrophysics* **402**(2), 477–486.

Steenbrugge, K. C., Kaastra, J. S., Detmers, R. G., Ebrero, J., Ponti, G. and et al. (2011), Multiwavelength campaign on Mrk 509: VII. Relative abundances of the warm absorber, *Astronomy & Astrophysics* **534**, A42–10.

Stocke, J. T., Morris, S. L., Weymann, R. J. and Foltz, C. B. (1992), The radio properties of the broad-absorption-line QSOs, *Astrophysical Journal* **396**, 487–503.

Strüder, L., Briel, U., Dennerl, K., Hartmann, R., Kendziorra, E. and et al. (2001), The European Photon Imaging Camera on XMM-Newton: The pn-CCD camera, *Astronomy & Astrophysics* **365**(1), L18–L26.

Symeonidis, M., Georgakakis, A., Page, M. J., Bock, J., Bonzini, M. and et al. (2014), Linking the X-ray and infrared properties of star-forming galaxies at z ¡ 1.5, *Monthly Notices of the Royal Astronomical Society* **443**(4), 3728–3740.

Tabatabaei, F. S., Weiß, A., Combes, F., Henkel, C., Menten, K. M. and et al. (2013), Cold dust in the giant barred galaxy NGC 1365, *Astronomy & Astrophysics* **555**, A128–11.

Tadhunter, C. and Tsvetanov, Z. (1989), Anisotropic ionizing radiation in NGC 5252, *Nature* **341**(6241), 422–424.

Takahashi, T., Mitsuda, K., Kelley, R., Aharonian, F., Akamatsu, H. and et al. (2014), The ASTRO-H X-ray astronomy satellite, *in* T. Takahashi, J.-W. A. den Herder and M. Bautz (eds.), *SPIE Astronomical Telescopes + Instrumentation*.

Tarter, C. B., Tucker, W. H. and Salpeter, E. E. (1969), The Interaction of X-Ray Sources with Optically Thin Environments, *The Astrophysical Journal* **156**, 943–10.

Tombesi, F., Cappi, M., Reeves, J. N. and Braito, V. (2012), Evidence for ultrafast outflows in radio-quiet AGNs - III. Location and energetics, *Monthly Notices of the Royal Astronomical Society: Letters* **422**(1), L1–L5.

Tombesi, F., Cappi, M., Reeves, J. N., Nemmen, R. S., Braito, V. and et al. (2013), Unification of X-ray winds in Seyfert galaxies: from ultra-fast outflows to warm absorbers, *Monthly Notices of the Royal Astronomical Society* **430**(2), 1102–1117.

Tombesi, F., Cappi, M., Reeves, J. N., Palumbo, G. G. C., Yaqoob, T. and et al. (2010), Evidence for ultra-fast outflows in radio-quiet AGNs, *Astronomy & Astrophysics* **521**, A57–35.

Tran, H. D. (2001), Hidden Broad-Line Seyfert 2 Galaxies in the CFA and 12 μM Samples, *The Astrophysical Journal* **554**(1), L19–L23.

Trippe, M. L., Crenshaw, D. M., Deo, R. and Dietrich, M. (2008), Long-Term Variability in the Optical Spectrum of the Seyfert Galaxy NGC 2992, *The Astronomical Journal* **135**(6), 2048–2054.

Tueller, J., Baumgartner, W. H., Markwardt, C. B., Skinner, G. K., Mushotzky, R. F. and et al. (2010), The 22 Month Swift-BAT All-Sky Hard X-ray Survey, *The Astrophysical Journal Supplement* **186**(2), 378–405.

Turner, M. J. L., Abbey, A., Arnaud, M., Balasini, M., Barbera, M. and et al. (2001), The European Photon Imaging Camera on XMM-Newton: The MOS cameras, *Astronomy & Astrophysics* **365**(1), L27–L35.

Turner, T. J., Urry, C. M. and Mushotzky, R. F. (1993), Position Sensitive Proportional Counter Soft X-Ray Observations of Seyfert 2 Galaxies, *The Astrophysical Journal* **418**, 653.

Urry, C. M. and Padovani, P. (1995), Unified Schemes for Radio-Loud Active Galactic Nuclei, *Publications of the Astronomical Society of the Pacific* **107**, 803.

Ursini, F., Boissay, R., Petrucci, P.-O., Matt, G., Cappi, M. and et al. (2015), Anatomy of the AGN in NGC 5548. III. The high-energy view with NuSTAR and INTEGRAL, *Astronomy & Astrophysics* **577**, A38.

Veilleux, S., Shopbell, P. L., Rupke, D. S., Bland-Hawthorn, J. and Cecil, G.

(2003), A Search for Very Extended Ionized Gas in Nearby Starburst and Active Galaxies, *The Astronomical Journal* **126**(5), 2185–2208.

Véron-Cetty, M. P. and Véron, P. (2006), A catalogue of quasars and active nuclei: 12th edition, *Astronomy & Astrophysics* **455**(2), 773–777.

Véron-Cetty, M. P., Véron, P. and Gonçalves, A. C. (2001), A spectrophotometric atlas of Narrow-Line Seyfert 1 galaxies, *Astronomy & Astrophysics* **372**(3), 730–754.

Véron, P., Lindblad, P. O., Zuiderwijk, E. J., Veron, M. P. and Adam, G. (1980), On the nature of the so-called narrow-line X-ray galaxies, *Astronomy & Astrophysics* **87**, 245–249.

Wakker, B. P., Lockman, F. J. and Brown, J. M. (2011), Measuring Turbulence in the Interstellar Medium by Comparing(H I; Lyα) and N(H I; 21 cm), *The Astrophysical Journal* **728**(2), 159–25.

Walton, D. J., Risaliti, G., Harrison, F. A., Fabian, A. C., Miller, J. M. and et al. (2014), NuSTAR and XMM-Newton Observations of NGC 1365: Extreme Absorption Variability and a Constant Inner Accretion Disk, *The Astrophysical Journal* **788**(1), 76–12.

Wang, J., Fabbiano, G., Elvis, M., Risaliti, G., Mazzarella, J. M. and et al. (2009), Imaging the Circumnuclear Region of NGC 1365 with Chandra, *The Astrophysical Journal* **694**(2), 718–733.

Wang, Q. D. and Liu, J. (2012), Spectroscopic evidence of charge exchange X-ray emission from galaxies, *Astronomische Nachrichten* **333**(4), 373–377.

Wargelin, B. J., Beiersdorfer, P. and Brown, G. V. (2008), EBIT charge-exchange measurements and astrophysical applications, *Canadian Journal of Physics* **86**(1), 151–169.

Watson, M. G., Schröder, A. C., Fyfe, D., Page, C. G., Lamer, G. and et al. (2009), The XMM-Newton serendipitous survey, *Astronomy & Astrophysics* **493**(1), 339–373.

Whewell, M., Branduardi-Raymont, G. and Page, M. J. (2016), X-ray narrow emission lines from the nuclear region of NGC 1365, *Astronomy & Astrophysics* **595**, A85–15.

Whewell, M., Branduardi-Raymont, G., Kaastra, J. S., Mehdipour, M., Steenbrugge, K. C. and et al. (2015), Anatomy of the AGN in NGC5548: V. A clear view of the X-ray narrow emission lines, *Astronomy & Astrophysics* **581**, A79–14.

Willingale, R., Pareschi, G., Christensen, F. and den Herder, J.-W. (2013), The Hot and Energetic Universe: The Optical Design of the Athena+ Mirror, *arXiv:1307.1709* .

Winter, L. M., Lewis, K. T., Koss, M., Veilleux, S., Keeney, B. and et al. (2010), Optical Spectral Properties of Swift Burst Alert Telescope Hard X-Ray-Selected Active Galactic Nuclei Sources, *The Astrophysical Journal* **710**(1), 503–539.

Worrall, D. M. (2009), The X-ray jets of active galaxies, *The Astronomy and Astrophysics Review* **17**(1), 1–46.

XMM-Newton Science Operations Centre Team (2014), XMM-Newton: The Users Guide.

Zhang, K., Dong, X.-B., Wang, T.-G. and Gaskell, C. M. (2011), The Blueshifting and Baldwin Efeects for the [O III] λ5007 Emission Line in Type 1 Active Galactic Nuclei, *The Astrophysical Journal* **737**(2), 71–9.